Low Mach Number CFD for Wind Turbine Analysis

by

Marina Carrión

A thesis submitted in partial
fulfillment of the requirements for
the degree of Doctor of Philosophy
University of Liverpool
School of Engineering
May 2014

Declaration

I hereby declare that this dissertation is a record of work carried out in the School of Engineering at the University of Liverpool during the period from July 2011 to May 2014. The dissertation is original in content except where otherwise indicated.

May 2014

.....
(Marina Carrión)

Abstract

To maximise the amount of energy extracted from wind turbines, the rotor diameter has increased, reaching values of 160m in some cases. Large scale wind turbines are working at high Reynolds numbers and a wide range of flow conditions, with virtually incompressible flow present at the root and mildly compressible near the blade tips, where the Mach numbers can reach locally 0.48 for the largest wind turbines employed to date. In traditional aerodynamics, most CFD methods were designed to cope with high Mach number flows and consequently solve the compressible Navier-Stokes equations. This is the case of the Helicopter Multi-Block (HMB2) CFD method from Liverpool University.

The present PhD thesis aims to provide an all-Mach-number capability to the HMB2 method, by implementing modified Roe schemes to account for low-Mach flows. For 2D cases, the modified Roe schemes showed great improvement in the convergence and the quality of the solution, when compared with the Original Roe and Osher schemes, and the Low-Mach Roe scheme showed the best performance.

With the low-Mach capability included in the compressible solver, both MEXICO and NREL Annex XX experiments were simulated. A detailed analysis of the velocity field behind the MEXICO rotor was performed, where the low-Mach scheme (LM-Roe) showed less sensitivity on the grid size than the Osher scheme.

Accurate prediction of wind turbine wake breakdown is also important for the performance analysis of the turbines and their optimal positioning within tightly-spaced wind farms. Using a fine mesh able to preserve the vortices up to 8R downstream the MEXICO rotor plane, the instabilities on the wake leading to vortex pairing were captured. FFTs of the axial velocity component enabled to identify the main harmonics in the wake. In the stable region, the wake was a perfect spiral and the main frequency was the blade-passing one. An approximate exponential growth was then observed and in the region where instabilities were present, higher frequencies dominated, leading an oscillatory pattern. Simple wake models were also investigated and a combination between a kinematic model to account for the wake initial expansion and a field model to account for the far wake decay was proposed, showing good agreement with the CFD solution. With the correct set of constants, it was proved that this simple model can be used to approximate the behaviour of wind turbine wakes with minimal computational cost.

Another consequence of the increased size of wind turbines is that their stiffness lowers and aeroelasticity therefore plays an important role, since the blades can suffer great deformations. To account for the blade deformations, a tightly coupled CFD-CSD method was employed to analyse the MEXICO and NREL Annex XX wind turbines. For the latter, the tower and nacelle were considered as stiff bodies and the blades were allowed to deform. As a result of the aeroelastic calculations, the blades showed deformation in bending (towards the tower). The maximum deflections were present after the blades had passed in front of the tower, and maximum amplitudes of 0.59%R, at 20m/s were observed.

Publications

Journals Papers

M. Carrión, M. Woodgate, R. Steijl and G. Barakos, Implementation of All-Mach Roe-type Schemes in Fully Implicit CFD Solvers - Demonstration for Wind Turbine Flows, *International Journal for Numerical Methods in Fluids*, vol. 73, num. 8, p 693-728, 2013.

M. Carrión, M. Woodgate, R. Steijl, G. Barakos, S. Gomez-Iradi and X. Munduate, Computational Fluid Dynamics Analysis of the Wake behind the MEXICO Rotor in Axial Flow Conditions, *Wind Energy*, 2014, DOI: 10.1002/we.1745.

M. Carrión, M. Woodgate, R. Steijl, G. Barakos, S. Gomez-Iradi and X. Munduate, Understanding Wind Turbine Wake Breakdown using CFD, *AIAA Journal*, Accepted May 2014.

M. Carrión, M. Woodgate, R. Steijl, G. Barakos, S. Gomez-Iradi and X. Munduate, Aeroelastic Analysis of Wind Turbines using a Tightly Coupled CFD-CSD Method, *Journal of Fluids and Structures*, Accepted July 2014.

M. Carrión, M. Woodgate, R. Steijl and G. Barakos, Breakdown of the Swirling Wake Behind a Wind Turbine, *ERFCOFTAC Bulletin*, Bulletin 98, March 2014.

Papers in Conference Proceedings

The Science of Making Torque from Wind, CFD and Aeroelastic Analysis of the MEXICO Wind Turbine, M. Carrión, M. Woodgate, R. Steijl, G. Barakos S. Gomez-Iradi and X. Munduate, Oldenburg, Germany, October 9-11, 2012.

9th PhD Seminar on Wind Energy in Europe, Understanding Wind Turbine Wake Breakdown using CFD, M. Carrión, M. Woodgate, R. Steijl, G. Barakos, S. Gomez-Iradi and X. Munduate, Uppsala University Campus Gotland, Sweden, September 18-20, 2013.

AHS 70th Annual Forum, Understanding Wind Turbine Wake Breakdown using CFD, M. Carrión, M. Woodgate, R. Steijl and G. Barakos, Montréal, Québec, Canada, May 20-22, 2014.

6th European Conference on Computational Fluid Dynamics (ECFD VI), Coupled CFD/CSD Method for Wind Turbines, M. Carrión, M. Woodgate, R. Steijl, G. Barakos, S. Gomez-Iradi and X. Munduate, Barcelona, Spain, July 20-25, 2014.

Presentations without Proceedings

Wind Engineering Research Day, Institute of Civil Engineering, Nottingham, United Kingdom, 19 October 2011.

MareWint 1st Technical Workshop, National Center of Renewable Energies of Spain (CENER), Pamplona, Spain, 23-27 September 2013.

Technical Notes

TN12-004, Explicit RK4 Calculation.

TN13-002, Correction for low-Mach flows.

TN13-003, Computations of Wind Turbine Cases with HMB2.

TN14-003, Incompressible Solver.

Acknowledgements

Firstly, I would like to thank my first supervisor Prof. George Barakos for his guidance and constant support throughout the PhD. His technical knowledge and advise was crucial for this work and his contagious enthusiasm was a source of motivation. I am also very grateful to my second supervisor Dr. Rene Steijl, who advised me and shared his knowledge at all moments. Special thanks for Dr. Mark Woodgate for sharing his expertise in numerical methods and providing me with valuable advise.

Many thanks have to be granted to Dr. Sugoi Gómez and Dr. Xabier Munduate from the Renewable Energy Centre of Spain (CENER), whose contributions helped to make this work possible.

The financial support by CENER and the School of Engineering of Liverpool University is gratefully acknowledged, as well as the access to the N8 HPC facility, Polaris, and the Chadwick system of the University of Liverpool. The use of the MEXICO and NREL Annex XX wind tunnel data is also acknowledged.

I would like to extend my gratitude to all the members of the CFD Lab, for creating a stimulating work environment and making me feel at home.

Last but not the least, I would like to thank my family and friends from Sabadell, whose unconditional support and understanding gave me the strength to keep going.

Contents

List of Figures

List of Tables

Nomenclature

Acronyms

ABL	Atmospheric Boundary Layer
AD	Actuator Disk
AL	Actuator Line
ALE-VMS	Arbitrary LagrangianEulerian Variational Multiscale
AOA	Angle Of Attack
AS	Actuator Surface
A-Roe	All-Mach Roe scheme
A-J	All-Mach Roe Jacobian
AUSM	Advection Upstream Splitting Method
BEM	Blade-Element Momentum
BILU	Block Incomplete Lower-Upper
CFD	Computational Fluid Dynamics
CFL	Courant-Friedrichs-Lewy condition
COMB-J	Combined Jacobian
CSD	Computational Structural Dynamics
CVT	Constant Volume Tetrahedron
DES	Detached Eddy Simulation
DFW	Direct Free Wake
DOF	Degree Of Freedom
DTU	Denmark Technical University
EAL	Exact Arithmetics Library
EWEA	European Wind Energy Association
FAST	Fatigue, Aerodynamics, Structures and Turbulence
FEM	Finite Element Method
FFT	Fast Fourier Transform
FP5	Fifth Framework Programme
FR	Full Rotor
HAWT	Horizontal Axis Wind Turbines
HMB2	Helicopter Multi-Block
IFW	Inverse Free Wake
LES	Large Eddy Simulation
LM-Roe	Low-Mach Roe scheme
LM-J	Low-Mach Roe Jacobian
MEXICO	Model EXperiments In COntrolled conditions

MGIV	Modified GIVens methd
MUSCL	Monotone Upwind Schemes for Scalar Conservation Laws
MVBB	Minimum Volume Bounding Box
NREL	National Renewable Energy Laboratory
NS	Navier-Stokes
O-J	Original Roe Jacobian
OMS	Overset Mesh Search
O-Roe	Original Roe scheme
PDE	Partial Differential Equation
PIV	Particle Image Velocimetry
P-Roe	Preconditioned Roe scheme
RANS	Reynolds-Averaged Navier-Stokes
RK4	Runge-Kutta 4 stage
RWT	Reference Wind Turbine
rms	Root mean square
SA	Spring Analogy
S-A	Spalart-Allmaras
SAS	Scale-Adaptative Simulation
SB	Single Blade
SPL	Sound Pressure Level
SST	Shear Stress Transport
TFI	Transfinite Interpolation
T-J	Thornber's Roe Jacobian
T-Roe	Thornber's Roe scheme
TVD	Total Variation Diminishing
URANS	Unsteady Reynolds-Averaged Navier-Stokes
VISCEL	Viscous and Aeroelastic Effects on Wind Turbine Blades
WDC	Wake Decay Constant
WMB	Wind Multi-Block
W.T.	Wind Turbine

Symbols

A	Signal amplitude, Area of the beam cross section
a	Speed of sound, Wave speed
b	Wake width
B	Number of blades
c	Speed of sound, Chord
c_p	Specific heat for a constant pressure
c_v	Specific heat for a constant volume
C_D	Drag coefficient of the blade/rotor
C_d	Drag coefficient of the aerofoil
C_L	Lift coefficient of the blade/rotor
C_l	Lift coefficient of the aerofoil
C_M	Moment coefficient of the blade/rotor
C_m	Moment coefficient of the aerofoil
C_P	Pressure coefficient of the blade/rotor
C_p	Pressure coefficient of the aerofoil

C_Q	Torque coefficient of the blade/rotor
C_q	Torque coefficient of the aerofoil
C_T	Thrust coefficient of the blade/rotor
C_t	Thrust coefficient of the aerofoil
D	Rotor diameter
dm	Linear mass distribution
e	Specific energy
E	Total energy
F	Flux vector in x direction
$f(M)$	Scaling function
f_i^s	Modal forcing in the i-th mode
G	Flux vector in y direction
h	Enthalpy
H	Flux vector in z direction
I_1	Edgewise (chordwise) moment of inertia
I_2	Flapwise moment of inertia
J	Torsional stiffness
J	Jacobian matrix
k	Reduced frequency, Heat transfer coefficient
L	Left eigenvector
M	Local Mach number
M_∞	Free-stream Mach number
M_{tip}	Tip Mach number
M_{ref}	Reference Mach number
N	Vector of normal components
n_i	normal vector in i direction
P	Vector of primitive variables
P	Preconditioning matrix
p	Local pressure
p_∞	Free-stream pressure
p_{ref}	Reference pressure
q^2	Kinematic energy per unit mass
Q	Torque
r	Radial position
R	Right eigenvector, Residual
R	Blade radius, Specific gas constant
Re	Reynolds number
R_g	Radius of gyration
Re_T	Turbulence Reynolds number
S	Entropy, Source term
t	Physical time-step
T_u	Turbulence intensity
tol	Tolerance
T	Temperature, Thrust, Period
T_ref	Reference temperature

T_S	Sutherland temperature
u	Velocity in x direction
u_n	Normal velocity to the cell face
u_i	Velocity vector
v	Velocity in y direction
v_w	Wind velocity
$v_w ind$	Wind velocity
V	Cell volume
w	Velocity in z direction
$\mathbf{W}$	Vector of conservative variables
x_i	Position vector

Greek symbols

α	Parametric coefficient, Incidence angle
α_{eff}	Effective geometric angle of attack
α_i	Modal amplitude
β	Artificial compressibility parameter
γ	Specific heat ratio
$\mathbf{\Gamma}$	Preconditioning matrix
δ	Parametric coefficient, Flapping/Bending deflection
Δ	Increment, Difference between left and right states
ϕ	Pitch angle
κ	Condition number
λ	Tip speed ratio, Weight factor for interpolation
λ_1	Negative acoustic eigenvalue
λ_2	Convective eigenvalue, Second real Eigenvalue of the vorticity-strain matrix
λ_3	Positive acoustic eigenvalue
$\mathbf{\Lambda}$	Matrix of eigenvalues
μ	Molecular viscosity
ω	Rotational speed, Vorticity
ω_i	Eigen-frequency
ω_n	Maximum vorticity normal to the plane
Ψ	Azimuthal position
ρ	Local density
ρ_∞	Free-stream density
τ	Viscous stress tensor, Computational time-step
θ	Global cut-off parameter, Torsional deflection
ϕ	Fluid property, Pitch angle
ζ_i	Damping coefficient

Subscripts and superscripts

ϕ_i, ϕ_l	Left state
ϕ_{i+1}, ϕ_r	Right state
$\overline{\phi}$, $\phi_{i+1/2}$	Roe's averaged value
$\tilde{\phi}$	Normalised value for the Preconditioned-Roe
ϕ_n	Normal to the cell face

ϕ_c	Convective part of ϕ
ϕ_d	Diffusive part of ϕ
ϕ_{ref}	reference value of ϕ
ϕ_∞	Free-stream value of ϕ

Chapter 1

Introduction

1.1 Motivation

In the age of growth of renewable energies, wind energy is playing an important role. In 2013, more wind power was installed than any other power generating technology in Europe, accounting for 32% of total power capacity installations. Currently, 8% of the European Union's electricity is provided by wind energy from an installed capacity of 117.3 GW (110.7 GW onshore and 6.6 GW offshore), as published by the European Wind Energy Association, EWEA[1]. The rest of the world has followed a similar trend, with continuous growth of almost 10% every year. Moreover, EWEA targets 230 GW of installed capacity (190 GW onshore and 40 GW offshore) by 2020 and 400 GW (250 GW onshore and 150 GW offshore) by 2030.

Due to the increasing development of this field, there is a need to optimise the performance of wind turbines, in order to maximise their power production and reduce cost. Computational Fluid Dynamics (CFD) is a very versatile tool that, although traditionally used for aerospace applications, is recently gaining interest by the wind energy community, since it enables detailed analysis of the flow features around the wind turbine that simpler methods cannot deal with. Currently, CFD is employed in a wide range of areas within the wind energy field. This includes blade design and prediction of extreme loads for certification, along with extraction of angles of attack to create aerofoil data for input for reduced order models. Simulation of complex terrains is also possible with CFD, since it avoids expensive experimental tests and enables the testing in atmospheric and wind conditions difficult to measure *in situ*. Although loads and velocity field

predictions are in reasonable agreement with experiments, and on many occasions better results are obtained than with reduced order models, CFD of wind turbines has still limitations and there is a range of problems that have not been fully understood yet.

The motivation behind the present PhD thesis is to improve and validate a CFD method for the analysis of horizontal axis wind turbines (HAWT) and provide a better understanding of their performance.

1.2 Literature survey

The search has been firstly focused on the basic principles of wind turbine aerodynamics, including the momentum theory applied to the rotor and the complexity of the wake aerodynamics.

An overview of the engineering models employed by the wind energy community for design and performance prediction is provided, which include Blade Element Momentum and panel methods, as well as lifting-line, vortex-wake and simple wake models.

The third area of research focuses on the application of Computational Fluid Dynamics (CFD) to wind turbines and the methods employed to model the rotor and the wake. Emphasis is also put on the treatment of low-speed flows when employing compressible CFD codes. This includes the understanding of the low-Mach problem, as well as the different approaches to solve it (preconditioning techniques, artificial compressibility methods and all-Mach schemes). A description of the CFD solvers currently employed for the analysis of wind turbines is also provided.

The MEXICO project (Model Experiments in Controlled Conditions) is of great importance for the present PhD thesis, since it provides experimental data related to blade pressure and loads and the flow field around the rotor and in the near wake. A description of the experiments is provided, along with a deep analysis of the works in the literature published so far.

Finally, two very challenging problems present in the literature are analysed in detail. Firstly, a review on the attempts on the prediction of wind turbine wake instabilities and breakdown is provided. Secondly, the methods for predicting fluid-structure interaction are presented and the most relevant works in the literature summarised.

1.2.1 Principles of wind turbine aerodynamics

Momentum theory

The rotor of a wind turbine can be simplified as a disk of area A_d that extracts momentum from the free-stream flow, as shown in the diagram of Figure 1.1. Hence, a fluid element passing through the rotor losses part of its kinetic energy and therefore slows down from the free-stream velocity (U_∞) to a lower velocity in the wake ($U_{wake} < U_\infty$). Likewise, the static pressure increases in front of the rotor disk from the free-stream value (p_∞) to p_d^+, drops behind the disk to p_d^- and recovers the free-stream value downstream. For a one-dimensional problem and under the assumption of axial flow conditions, a force on the disk (thrust) is generated as a result of this difference of pressures.

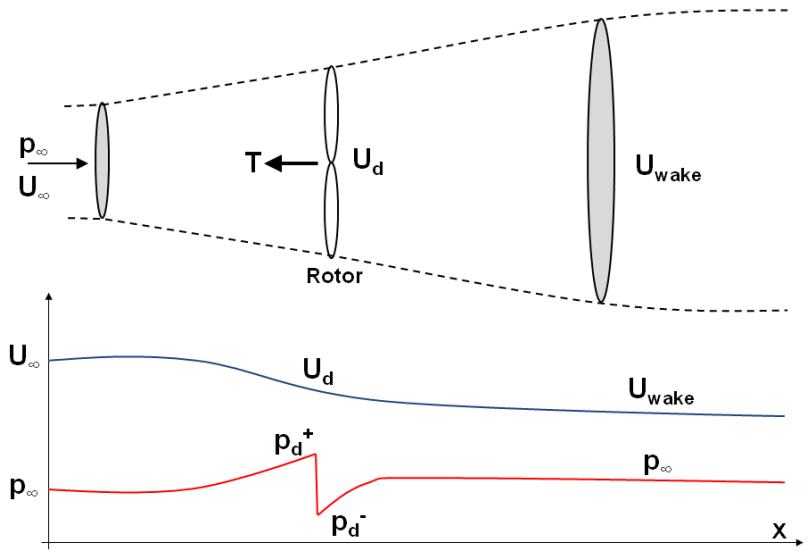

Figure 1.1: Schematic of the one-dimensional flow through a rotor disk, including the deficit of velocity ($U_d, U_{wake} < U_\infty$) and the change in pressure at the rotor disk.

In reality, however, the rotor consists of several blades that, additionally, convert the energy of the wind into rotational energy, which is dictated by rotational frequency (Ω), as the schematic on Figure 1.2 shows. A reaction torque (Q) is also generated, which makes the flow to rotate in opposite direction to the rotor. In the total velocity, therefore, the tangential component due to the blades rotation (Ωr) and the tangential velocity component due to this reaction torque acting on the flow (U_t) should be considered.

The addition of the rotational kinetic energy to the translational one results into a lower power extraction than the ideal case and the thrust and torque are expressed as a combination of the lift (L) and drag (D) forces.

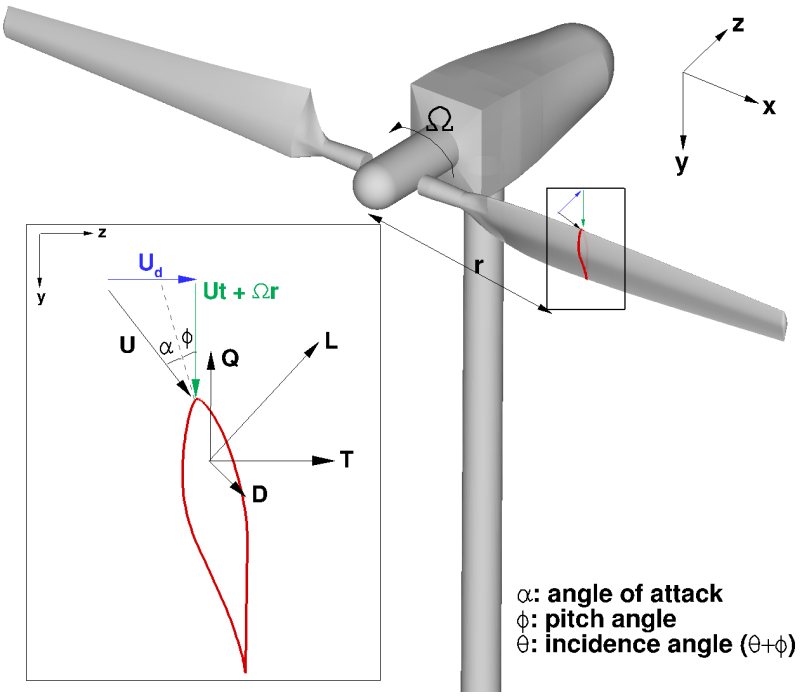

Figure 1.2: Relative angles and forces on a section of the wind turbine blade. *L: Lift, D: Drag, T:Thrust, Q: Torque, U_d: Velocity at the rotor disk, U_t: Tangential velocity component due to the reaction torque.*

A theoretical threshold, known as Betz limit, states that wind turbines cannot convert more than 59.3% of the energy in the wind into usable power, and was demonstrated by Bergey [17]. Sorensen *et al.* [138] found out that when applying the general momentum theory in a closed volume that contains the rotor and the wake behind it, both pressure and friction effects cannot be neglected. Otherwise, at low tip speed ratios (λ), the obtained power coefficient has unphysical values.

Power control

Wind turbines are designed to withstand extreme winds when they are parked; however, they are not designed for extreme rotational torques or speeds. At very large aerodynamic torque or rotational speed, the forces on the blades (and other parts of the wind turbine) are substantial and could seriously damage them. That is why a cut–out speed is employed, above which the rotor is stopped. A typical power curve of a wind turbine is shown in Figure 1.3. Region I consists of low wind speeds, below the rated power, where the

wind turbine runs with maximum efficiency. Region II is a transition region and region III consists of high wind speeds, below the cut–out speed. For this range of wind speeds various control strategies are employed to prevent the wind turbine to get damaged. These strategies can be classified as active and passive load controls [11].

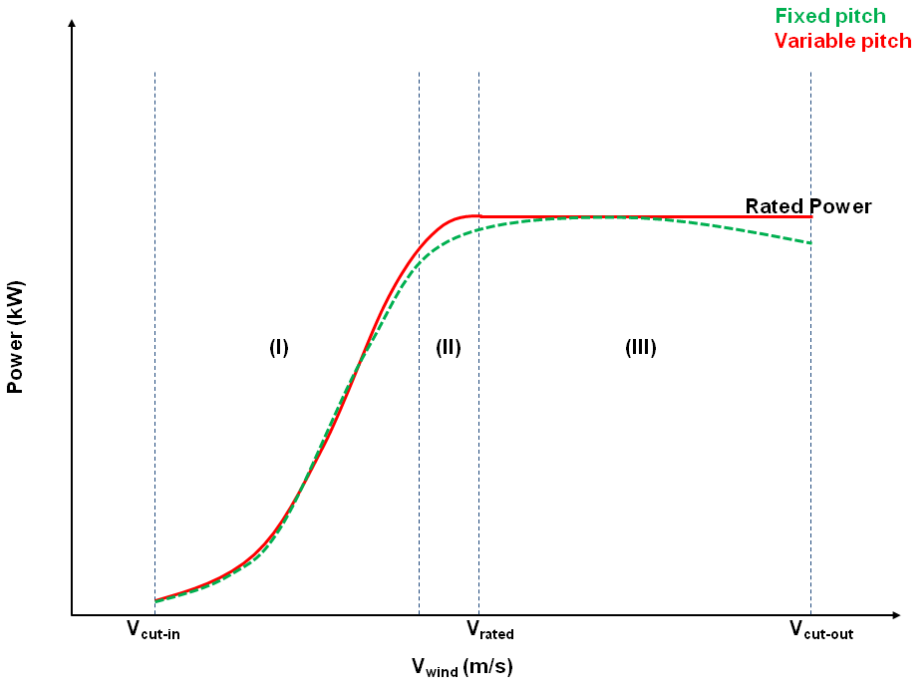

Figure 1.3: Typical power curve of a wind turbine, with and without pitch control.

The first approach consists adapting the blade loads by adjusting the aerodynamic properties of the blades, based on sensor inputs. Pitch-regulation systems fall in this category, where the pitch angle is changed to decrease the torque produced by the blades in fixed-speed wind turbines and to decrease the rotational speed in variable-speed wind turbines. For wind speeds higher than that of the rated power, the blades will pitch so that there is less lift and more drag due to increasing flow separation along the blade length. This will reduce the rotational speed or the torque transferred to the shaft, so that the rotational speed or the torque is kept constant below a set threshold. Pitch regulated turbines see increasing power until the rated wind speed, beyond which it sees constant power until the cut-out speed, as can be seen in Figure 1.3.

On the other hand, stall-regulation belongs to the passive control strategy for power regulation. In this case, the blades are designed so that when wind speeds are high, the rotational speed or the aerodynamic torque, hence the power production, decreases with increasing wind speed above a certain value. The

decrease in power with increasing wind speeds is due to aerodynamic effects on the turbine blades: regions of the blade are stalled, starting from the root and moving outwards with increasing wind speeds. The blades are designed so that they will perform worse (in terms of energy extraction) in high wind speeds to protect the wind turbine without the need for active controls. Stall-regulation systems are simpler and require lower maintenance than pitch-regulation. However, active control techniques offer significantly more flexibility, especially when dealing with unsteady changes in the flow [11].

Wake aerodynamics

The flow around a wind turbine is highly complex and a number of factors play a role, as the schematic of Figure 1.4 shows. To begin with, wind turbines operate in the lowest part of the Earth's atmospheric boundary layer (ABL), which influences the atmospheric turbulence intensity, and wind shear effects are present. The atmospheric boundary layer can be unstable, stable or neutral [124]. Strong winds are present when it is neutral, which is the most extreme situation that can be considered.

As a result of the difference in pressure at the tip of the blade between the lower and the upper surfaces, a tip vortex is generated and convected downstream in a helical path that rotates opposite to the rotor. The wake developed behind a wind turbine can be divided into a near-wake ($<$1D) and far-wake ($>$1D) [161]. In the near wake, the properties of the rotor determine the flow field; in the far wake, conversely, the effect of the rotor is less important. The difference in velocity between the air inside and outside the wind turbine wake results in a shear layer, that thickens when moving downstream, and turbulent eddies are formed [124]. As the wake expands, there is a mixing between the low velocity fluid inside the wake and the high velocity fluid outside. When the shear layer reaches the wind turbine axis, the end of the near wake is reached. Further downstream, the tip vortices start to interact and eventually break down. The tower will also create a wake, which will be interacting with the rotor one.

Since wind turbines are normally installed within wind farms, the effect of wake interaction is very important, as the power loss of a downstream turbine can be up to 40% [124] in full-wake conditions. In offshore wind turbines the wake effects are specially important, since in the sea both roughness and ambient turbulence levels are much lower leading to more persistent wakes [124].

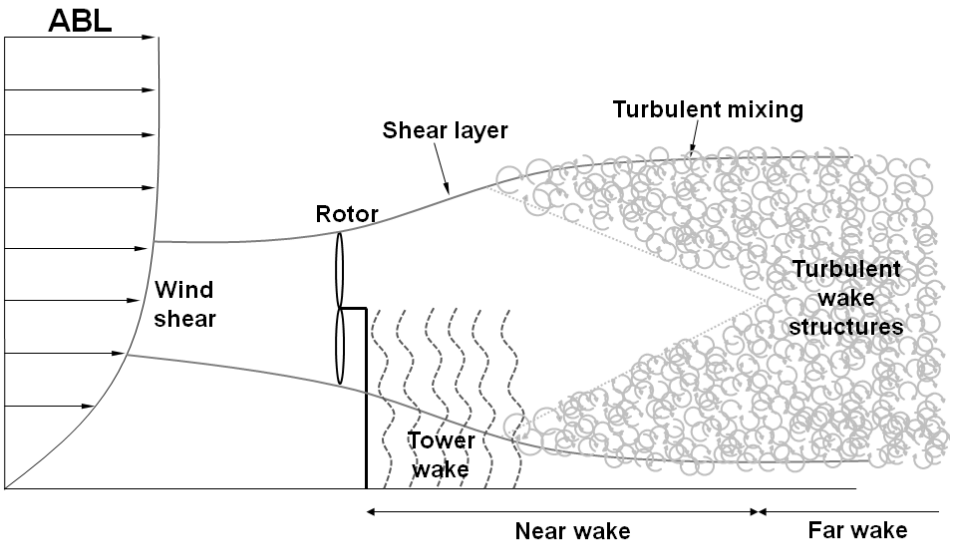

Figure 1.4: Schematic of the evolution of the flow crossing a wind turbine, showing the complexity of the flow and different factors that play a role.

The review paper of Vermeer *et al.* [161] provides a description of both near and far wake experiments and computations carried out until the year 2003. To date there are three main projects that stand out for the availability of experimental wake data. Firstly, MEXICO (Model Experiments in Controlled Conditions), where PIV measurements of the near-wake were performed and a full description is provided in Section 1.2.5. Secondly, experiments from Chamorra and Porté-Agel in atmospheric wind tunnel. Finally, experiments on wake meandering in the atmospheric boundary layer wind tunnel at the University of Orléans.

1.2.2 Overview of Engineering Models

For designing wind turbine blades and estimating the wake, reduced order methods known as *Engineering Models* are traditionally employed in the wind energy industry, due to the small computational power and time they require. Among others, these include the Blade Element Momentum (BEM), panel methods, lifting-line, vortex-wake and wake models. In the following, descriptions of these methods are provided.

Blade Element Momentum method

The BEM method is extensively used in the literature as a model for wind turbine design, due to its simplicity. It consists of splitting the blade into small elements and summing the contribution of all of them. For each element, lift and drag can be obtained using two-dimensional tabular aerofoil data. As reported by Sanderse's review paper [124], throughout the last years several improvements have been applied in order to account for tip loss (Prandtl's tip loss factor), yaw misalignment, turbulent wake, unsteadiness of the flow field and rotational effects. However, it has still several limitations, related to the fact that it is hard to model atmospheric turbulence, wind shear due to ground effect, deep stall and the effect of neighbouring turbines. A variation of BEM, known as BEMT (Blade Element Momentum Theory), was developed to account for aeroelastic effects.

Using BEM, Amano *et al.* [7] provided two main approaches to increase the efficiency of the blades at high wind speeds while maintaining efficiency at lower wind speeds. The first one was the use of a straight edge blade, which optimises the angle of attack and chord length for a given aerofoil cross section along the blade. The second approach was a swept edge blade, which aimed to accommodate the span-wise velocity component and delay the stall point of the rotor. Hence, a sweep angle was applied to the straight edge blade, maintaining all the other properties. The experimental data from NTK500/41 commercial wind turbine with LM19.1 blades was used for validation and good agreement was found until 12m/s, when the blades began to stall. It was proved that the swept geometry produced 20% increase in power for speeds higher than 20m/s.

Panel methods

Panel methods are used under the assumption of incompressible, inviscid, irrotational flow. In this case, the blade is discretised in panels, which consist of singularities and viscous effects can be taken into account if a boundary layer is superposed. A comparison of different potential flow methods to model the blade-tower interaction for upwind-oriented rotors was presented by Lackner *et al.* [76]. They claimed that 3D models of tower interference are only accurate in the absence of nacelle, since they take into account tower end effects.

Lifting-line and Vortex-wake methods

Both Lifting-line and Vortex-wake methods assume that the flow is incompressible and inviscid and are used to obtain the velocity induced by vortex lines. The former represents the wind turbine blades by bound vortex lines, whose strength or circulation (Γ) depends on the lift coefficient, which is extracted from tabulated data. The latter models the vorticity in the wake by a distribution of vortex singularities. Unlike BEM methods, Vortex-wake models do not rely on global momentum balance, hence, can be used in unsteady conditions and with yaw misalignment. That is the reason why they are usually used to correct BEM models.

Mast *et al.* [92] presented a vortex model to reconstruct the circulation over a two-bladed rotor, with NACA 0012 aerofoil sections, using wind tunnel data. The circulation distribution was calculated from the induced velocity in the wake ($\vec{v}_{induced} = \vec{v}_{measured} - \vec{v}_{\infty}$), using the Biot-Savart law. An optimisation scheme was added to approximate the induced velocities, and the total induced velocity was obtained by summing the contribution of each part of the vortex model (Figure 1.5). The velocities over the blade compared well with the measured ones, especially when considering the average induced velocity for all measured positions. However, there was a difference in the peak-to-peak values, which was attributed to the representation of the blade as a line, as opposed to a blade with chord length and thickness. The results were also compared with BEM results and the latter showed an underestimation and overestimation of the circulation near the root and at the tip, respectively.

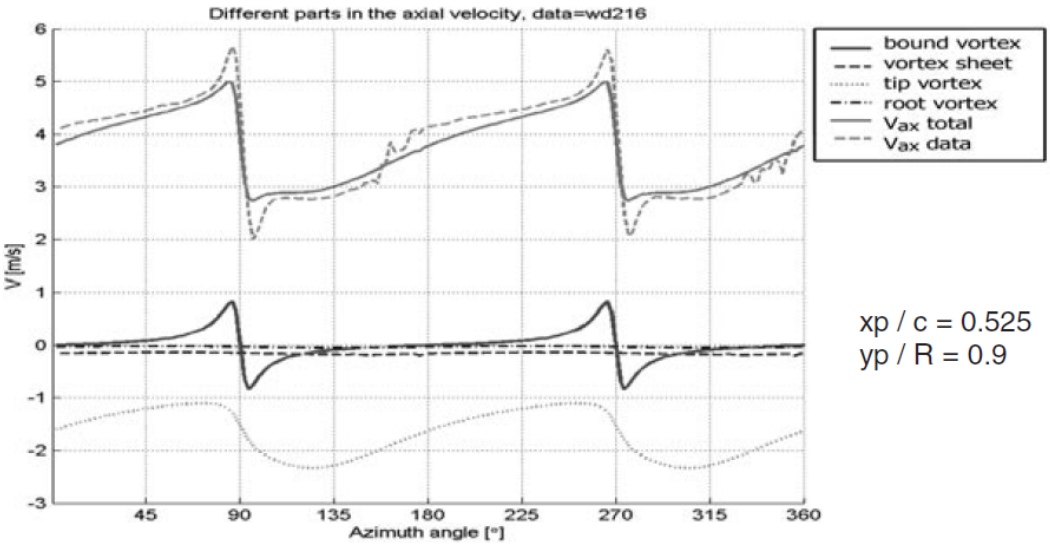

Figure 1.5: Induced velocity (close to the blade tip) generated by different parts of the vortex model. Source: Mast *et al.* [92].

Wake models

For the study of wind turbine wake interaction within a wind farm, simple methods known as *wake models* are traditionally employed in the wind energy industry, since they do not require much computational effort. In the review papers by Crespo *et al.* [30] and Vermeer *et al.* [161], three families of wake models are presented. Firstly, in the kinematic models the deficit of the wake behind the wind turbine is obtained from global momentum conservation and using as input the thrust coefficient (C_T). These models do not consider the initial wake expansion and any change in turbulence intensity. The models from Katic *et al.* [72] in the *WAsP* and *WindFarmer* solvers, where it is assumed that the wake expands linearly with the velocity deficit, and Larsen [77] in the *WindPro* solver, which uses Prandtl's mixing length theory, fall in this category. The second family are the field models, where the Reynolds-averaged Navier-Stokes equations are solved, with a turbulence model for closure. A well-known 2D field model is the one by Ainslie [6], which is used in the *WindPro*, *OpenWind*, *WindFarmer* and *FLaP* solvers. It uses the axisymmetrical, time averaged form of the incompressible Navier-Stokes equations, with eddy viscosity closure, and the assumption that the pressure gradients are negligible in the wake. For the wake up to $2D$ downstream, a Gaussian profile dependent on the velocity deficit is employed, which serves as the initial conditions for the N-S equations. Finally, the last category includes the boundary layer wake models, like the 3D model *WAKEFARM*. It was developed by ECN, based on the *UPMWAKE* model by Crespo *et al.* [31], and does not assume axial symmetry and uses the k-ε turbulence model. Like the previous model, the pressure gradients are neglected, which makes it not applicable in the near wake. The contribution of the pressure gradient in the near wake was included via a boundary layer analogy. The main disadvantage of the wake models is that they need analytical expressions for the expansion region and the near wake region, which are employed as boundary conditions. In addition, they incorporate a set of constants that are adjusted to match experimental data.

In Reference.[114], validation of different wake models was presented, using wind farm and wind tunnel data. The model by Larsen [77] was found to be the poorest, since the estimated wakes were too wide. It also showed high sensitivity to the the employed turbulence model. On the other hand, the Ainslie model [6] performed consistently and showed little dependency on the turbulence model. However, the wake losses were slightly under-predicted.

1.2.3 Computational Fluid Dynamics

CFD methods, which rely on the principles of conservation of mass, momentum and energy (Navier-Stokes equations), are more sophisticated than the Engineering models, since they can cope with compressibility effects, viscosity, turbulence and unsteadiness. That is why the use of CFD applied to wind turbines has increased in recent years. Summer *et al.* [145] reviewed the evolution of the application of CFD to wind turbines, from 2D flows around aerofoils to an entire wind farm, emphasising that one of the current challenges in this field is the modelling of turbulence and flow separation.

Many authors in the literature have come across the problem of properly capturing the separated flow when studying the NREL Phase VI wind turbine [56] at high wind speeds [147, 151, 46] and yawed flow conditions [130]. Likewise, Chaviaropoulos *et al.* [24] performed a parametric investigation for the LM 17.0 and LM 19.1 blades [110], using five CFD solvers, and the results showed good agreement with the experiments at low wind speeds, but strong over-prediction of the power output at wind speeds higher than 12m/s, when the flow was separated, as observed in Figure 1.6. With this regard, Sorensen [139] implemented the critical momentum thickness Reynolds number ($\tilde{Re}_\theta$) and transition length factor [97] in the empirical correlation-based transition model of the EllipSys2D/3D CFD code [100]. Computations were performed varying the turbulence intensity from 0.1 to 0.5 and the wind speed from 5 to 25m/s. Comparison with experimental values and the fully turbulent case showed that the implemented transition model improved the prediction of stall at the inboard part of the blade. Likewise, Rinehart *et al.* [118] employed a GPU-accelerated compressible Navier-Stokes flow solver for the computation of wind turbine aerofoils (S809 [136] and S827 [137]). The lift prediction was improved at high angles of attack, using an adverse gradient pressure correction (APG) to the Spalart-Allmaras (S-A) turbulence model [143]. The drag over-prediction at low angles of attack, was reduced with an improved $\gamma - Re_{\theta_t}$ S-A transition model [94].

Another difficulty related to the CFD study of wind turbines is modelling turbulent flows, due to the wide range of time and length scales for the presence of non-linearities [125]. As a result, both boundary layers on the turbine blades and all the turbulent structures in the wake cannot be resolved at the same time, if reasonable grid sizes and computational power are employed. Methods to simplify the rotor and/or the wake have been therefore formulated and used in the literature and are briefly described in the following paragraphs.

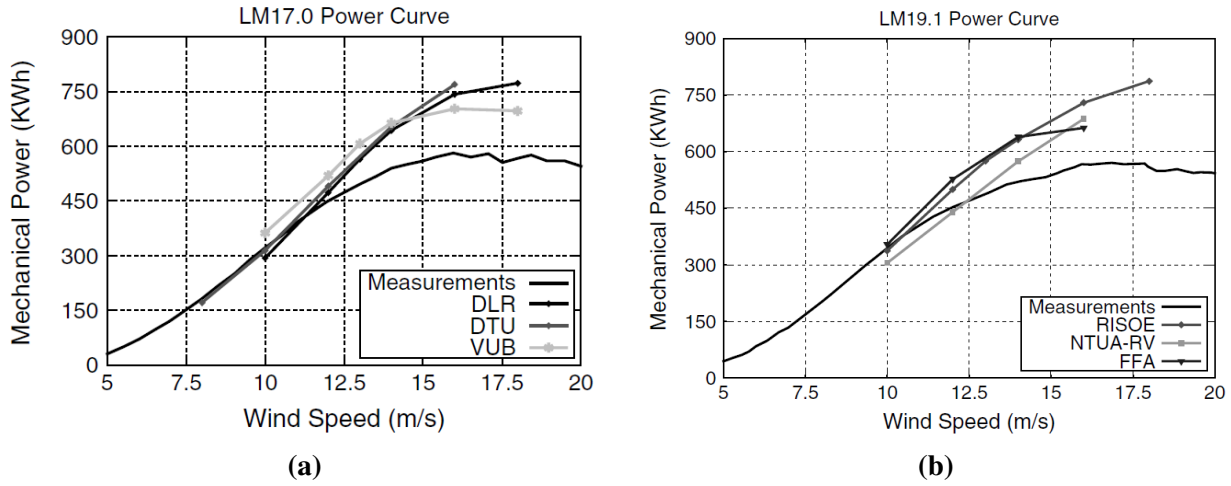

Figure 1.6: Comparison of the mechanical power predicted by several Navier-Stokes codes against measured values, for the **(a)** LM 17.0 and **(b)** LM 19.1 blades. Source: VISCEL Project, Part I [24].

Rotor modelling

The most common approaches regarding the modelling of the rotor are the direct or full rotor representation and the simplified models, which include the actuator disk, actuator line and actuator surface methods. On one hand, the direct approach consists of discretising the geometry of the blade on a computational mesh, which requires the calculation of its boundary layer. On the other hand, the actuator disk represents the blades by an averaged force, which acts on the flow extracting momentum. As input, it requires both lift and drag coefficients from aerofoil tabular data. The actuator line is a more complex method, where the forces act on rotating lines representing the blades, instead of being averaged over the entire disk. Finally, the actuator surface represents the aerofoil sections as a plate with distributed forces. Figure 1.7 shows a representation of these four approaches.

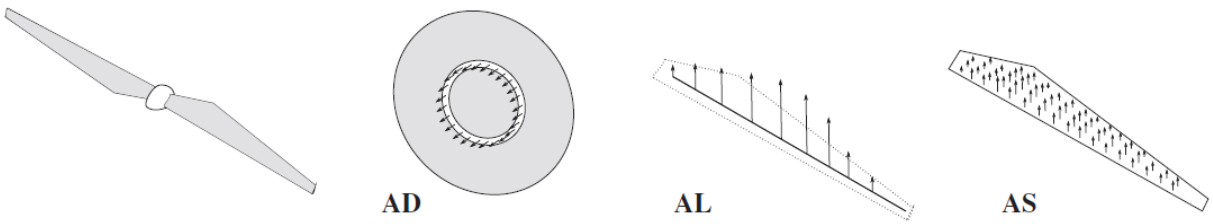

Figure 1.7: Direct rotor representation, Actuator disk (AD), Actuator Line (AL) and Actuator Surface (AS). Source: Sanderse *et al.* [125]

Wake modelling

Although Large Eddy Simulation (LES) approaches are able to better predict the unsteady, anisotropic turbulent atmosphere, since more scales are resolved, the use of Reynolds-Averaged Navier-Stokes (RANS) is more common, as the computational effort associated is lower. Three main RANS approaches are present in the literature regarding the modelling of the wake: elliptic models, which solve the pressure Poisson equation; parabolic models, which neglect diffusion and pressure gradient in the stream-wise direction; and linearised models, which solve the linearised Navier-Stokes equations, combined with a spectral method and tables with velocity profiles.

Detached Eddy Simulation (DES) [142] and Delayed Detached Eddy Simulation (DDES) [141] computations, which switch from RANS to LES depending on the length of the turbulent scales, are found to depict the wake in a better way than fully RANS, only when modelling the full rotor geometry, as seen at the top of Figure 1.8 by Troldborg *et al.* [154]. That is due to the fact that, for a particular grid, RANS adds more dissipation which can lead to a faster smear of the wake. If the actuator disk technique is employed to model the rotor, however, the detailed wake characteristics cannot be easily identified, even if DES is used, as seen at the bottom of Figure 1.8.

Troldborg *et al.* [152] studied the wake interaction between two 2MW NM80 wind turbines, employing LES with actuator line combined with a simplified model of wind shear and ambient turbulence, and using an incompressible solver. Several simulations were performed, covering different mutual positions between rotors and from laminar to turbulent inflow ($T_u = 0.1$ at hub height). Mean velocities, power deficit, contours of stream-wise velocity and absolute vorticity, as well as aerodynamic loading along the blades of each turbine, were compared with the experiments, obtaining good agreement with experiments at the near wake, but poor at the far wake. Ambient turbulence was found to have a significant impact on the characteristics of the aerodynamic interaction between rotors and it was observed that wake rotation causes a rotationally non-symmetric development of the upstream wake, clear in the laminar cases but small in the turbulent ones.

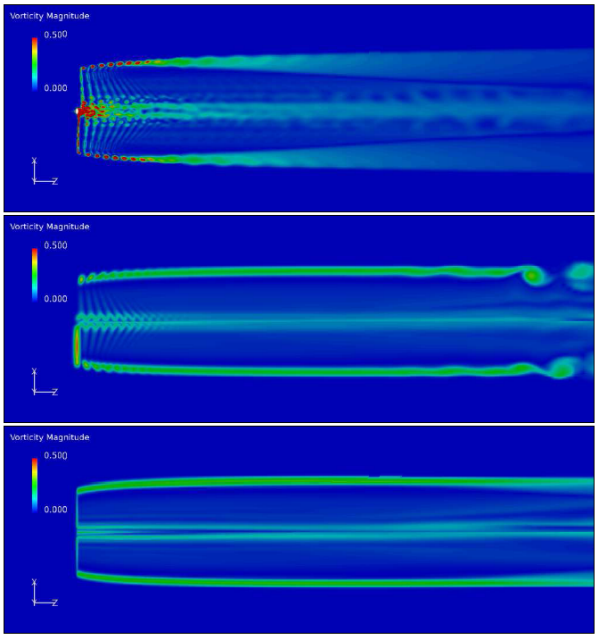

(a) RANS computation.

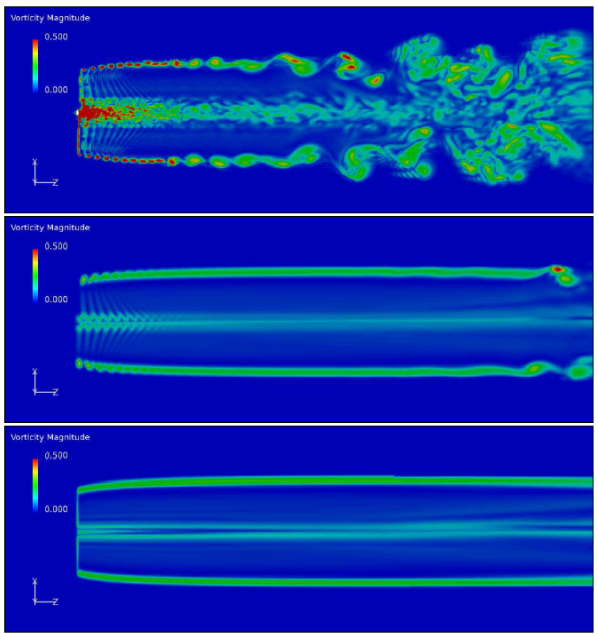

(b) DES computation.

Figure 1.8: Early breakdown prediction of NREL 5MW wake at $1D$, obtained with RANS and DES computations, due to the coarseness of the grid employed (minimum cell size of $R/126$). The wind speed was 8m/s ($\lambda = 7.6$). Top: Full rotor representation; Middle: Actuator Line; Bottom: Actuator Disk. Source: Troldborg *et al.* [154].

Blade design and optimisation and rotor-tower interaction with CFD

CFD is a tool popular in the literature for the design and optimisation of wind turbine blades. Among others, Amano *et al.* [7] used CFD to investigate different geometry configurations (straight and swept edges) for the NTK500/41 blades, obtaining an increase of 20% in produced power with the swept edge geometry. Gómez-Iradi *et al.* [42] performed a CFD investigation of some wind turbine rotor design parameters, including the tip and root sections, blade aspect ratio and pitch angle. Variations of the root and tip geometries were considered and the results were validated against experimental data of the NREL/NASA-Ames Phase VI wind tunnel campaign [56]. The main differences appeared if a root section and/or a hub were included in the CFD calculations. The overall agreement was strong and it was confirmed that the pitch and blade aspect ratio are the fundamental parameters to be taken into account in the blade aerodynamic design. In fact, when the pitch was increased by 0.5 deg. the torque was reduced by 2.6%.

Blade-tower interaction of horizontal axis wind turbines is important since it introduces transient loads on the blades, especially when the rotor size increases. Due to the proximity of the rotor to the tower of the NREL Phase VI wind turbine [56], of 5m of radius, there are several works in the literature where the interaction was studied. This is the case of Zhale *et al.* [170], who used the Ellipsys3D CFD solver with an overset grid method at three wind speeds in axial flow conditions and for the downwind configuration. Good agreement with the experiments was observed, although some deviations were observed at high wind speeds. Kim *et al.* [73] used a non-linear vortex correction method with time-marching free wake and found that the interaction with the rotor was higher when the radius of the rotor increased, rather than reducing the tower clearance or increasing the yaw or wind shear inflow conditions.

The full wind turbine in upwind configuration was considered by Gomez-Iradi *et al.* [46], who obtained good agreement with the experimental data at 7m/s wind speed with a compressible CFD solver, see Figure 1.9. Likewise, Li *et al.* [85] presented RANS and DES computations and studied the sensitivity on the wind speed and the blade pitch angle. They found that DES computations predicted the pressure transient fluctuations better than the RANS computations and, at large angles of attack, the thrust was over-predicted and the torque under-predicted. Wang *et al.* [162] employed the OpenFOAM code coupled with arbitrary mesh interface (AMI) to assess the blade-tower interaction with URANS computations (Unsteady Reynolds-Averaged Navier-Stokes). Comparison of time histories of thrust and pressure distribution showed small influence of the tower on the aerodynamic performance of the wind turbine. In addition, a huge drop of the tower pressure was observed at azimuthal angle of 180 degrees, which was also observed in Ref. [46]. Hsu *et al.* [59] proposed an Arbitrary LagrangianEulerian Variational Multiscale (ALE-VMS) formulation with weakly enforced non-slip boundary conditions and employed sliding planes. In all cases, all of them found a reduction in the blade loads of less than 10% due to the interaction with the tower.

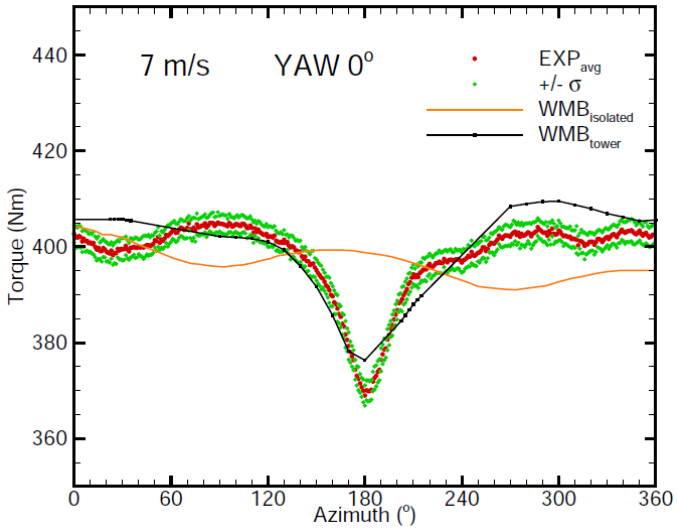

Figure 1.9: Comparison between NREL Phase VI experiments and computed single-blade torque during a full revolution (rotor tower and isolated rotor configurations), at 7m/s. Source: Gomez-Iradi *et al.* [46].

1.2.4 CFD for low-Mach flows [1]

In the literature, there are two main families of methods for incompressible flow analysis with CFD. On one hand, we have compressible methods with a fix to account for low-Mach flows, and on the other, purely incompressible solvers, such as the pressure-based methods. The first family covers three main approaches. Firstly, steady-state preconditioners, that include the work of Turkel [156]. They basically consist of pre-multiplying the pseudo-time derivative of the transport equations by the inverse of a preconditioning matrix ($\mathbf{\Gamma}$), dependent on the Mach number, to help reaching convergence. A preconditioner typically employed in the literature [36, 41] was the one proposed by Choi-Merkle [156] and shown in Equation 1.1.

$$\mathbf{\Gamma_{CM}} = \begin{pmatrix} \beta^2 & 0 & 0 & -\beta^2\delta \\ -\frac{\alpha u}{a} & 1 & 0 & \frac{\alpha u}{a}\delta \\ -\frac{\alpha v}{a} & 0 & 1 & \frac{\alpha v}{a}\delta \\ 0 & 0 & 0 & 1 \end{pmatrix}, \tag{1.1}$$

where α, β and δ are parameters to be chosen by the user. To eliminate the preconditioning for supersonic flows, $\alpha = 0$, $\beta = 1$ and $\delta = 0$. β should be proportional to the Mach number M in order to have a condition number close to 1.

[1] Full citation of: M. Carrión *et al.* , Implementation of All-Mach Roe-type Schemes in Fully Implicit CFD Solvers - Demonstration for Wind Turbine Flows, *International Journal for Numerical Methods in Fluids*, vol. 73, num. 8, p 693-728, 2013.

Preconditioning techniques have also been applied to flux splitting methods used to solve the Riemann problem, such as Roe's schemes [61, 49] and Godunov-type schemes [52, 50] and for double-phase flows [51]. Likewise, Campobasso [23] implemented a preconditioning matrix to the Navier-Stokes equations in harmonic balance formulation to an explicit solver.

A disadvantage of the use of preconditioning is that for unsteady problems it can only be used if the scale of the time dependence is slow compared with the convective speed of the fluid [107]. In addition, as the system of equations changes, the characteristics of the system also change too; hence, the boundary conditions of the preconditioned system need to be modified, as Turkel reports in his review paper [156]. Depcik *et al.* [35] also demonstrated, by means of a dispersion analysis, that most of the preconditioners present an unstable mode for certain combinations of low Reynolds and low Mach numbers. Finally, when creating a preconditioning matrix, special consideration is needed to avoid singularities at the incompressibility limit ($M = 0$) and stagnation points, as Zaccanti *et al.* report in Ref. [169]. For this purpose, Turkel [156] proposed a global cut-off, Lee *et al.* derived a "stagnation-friendly" all-purpose preconditioner for Euler [80] and the Navier-Stokes equations [79] and Campobasso [23] suggested several cut-off parameters related to the local pressure gradient, cell Reynolds number and physical time-step.

Artificial compressibility is the second approach, which is based on Chorin's method [26]. It introduces an artificial time derivative of density into the incompressible, steady state, continuity equation. Hence, an artificial transient solution is carried out with the objective of reaching the steady state solution. The new parameter β introduced in this method is normally related to an artificial speed of sound. The advantage of this method is that it is easy to implement in a compressible CFD solver; however, it is hard to solve for unsteady flow problems, since mass conservation is only guaranteed at the limit of convergence and the transient solution may be limited by the choice of time step. Moreover, when both compressibility and incompressibility effects need to be taken into account, this method is not suitable.

The third method is the use of all-Mach schemes, which calculate the fluxes by solving the approximate Riemann problem at each cell of the domain. For this, they are split into a convective or central term, which is generally an averaged value between the left and right states, and an artificial dissipation term. Among others, the family of Roe's solver[121, 117, 83] and the AUSM (Advection Upstream Splitting Method) scheme [88, 86, 87, 133] are popular in the literature. To overcome the low-Mach problem, the dissipation term

is generally modified by means of a scaling function, dependent on the local Mach number. In the review paper by Li *et al.* [83], modified Roe-type schemes - including preconditioned Roe, All-Speed Roe, Thornber's Roe and LM-Roe - were compared in an explicit solver. Numerical experiments - lid-driven cavity laminar flow, Euler flow past a cylinder, Euler flow pass a turbine blade and Sod's shock tube - revealed that, with regard to avoiding the checkerboard problem, the preconditioned Roe scheme was the best to perform, the All-Speed Roe was the worst and the Thornber's Roe and LM-Roe schemes were in-between.

The advantage of these schemes is that their explicit implementation is relatively easy; however, for implicit solvers this is more difficult. That is due to the fact that the all-Mach solvers are not always continuously differentiable, like the original Osher scheme [106]. Besides, the apparition of "expansion shocks" is common, requiring the use of an entropy fix. This fix consists of scaling the acoustic wave speeds ($|u_n + c|$ and $|u_n - c|$) in a way that the entropy condition is always satisfied at both sides of the shock wave. A comparative study of different schemes - Original Roe, Preconditioned-Roe, All-Speed-Roe, AUSM$^+$, AUSM$^+$ -up, SHUS and SLAU was performed by Kitamura *et al.* [74], using the implicit time integration method LU-SGS (Lower-Upper Symmetric Gauss Seidel) and a preconditioned version of it (pLU-SGS). The inviscid and viscous flow over the NACA0012 aerofoil was studied, for a range of Mach numbers. Figure 1.10 shows the drag convergence history obtained for the different combinations of methods and the inviscid case, and Table 1.1 summarises the results. In the lowest Mach number limit studied ($M = 0.001$), SLAU was found to be the only scheme that converged with physical results when using LU-SGS time integration method. When pLU-SGS was employed, Preconditioned-Roe, All-Speed-Roe, AUSM$^+$-up and SLAU succeed, obtaining the best results with All-Speed-Roe. They finally claimed that the recommended lower limit of non-preconditioned methods is Mach number 0.1.

Pressure-Poisson methods, firstly developed by Harlow and Welch [58], are used for purely incompressible solvers. They solve the Navier-Stokes equations in their incompressible form. As for incompressible flows density is not related to pressure, this leads to the resolution of only one equation for the pressure. However, in order to satisfy continuity in the velocity field considerable effort must be expended in solving the resulting Poisson equation.

Table 1.1: Summary of computed results by Kitamura *et al.* [74].

Implicit Schemes	**Baseline (Roe, AUSM$^+$, SHUS)**	**Low Dissipation (P-Roe, A-Roe, AUSM$^+$-up, SLAU)**
LU-SGS	**U**	**S** (slow convergence,SLAU) or **F** (other fluxes)
pLU-SGS	**F**	**S** (fast convergence)

S: successful, U: unphysical or oscillatory, F: Failure, diverged.

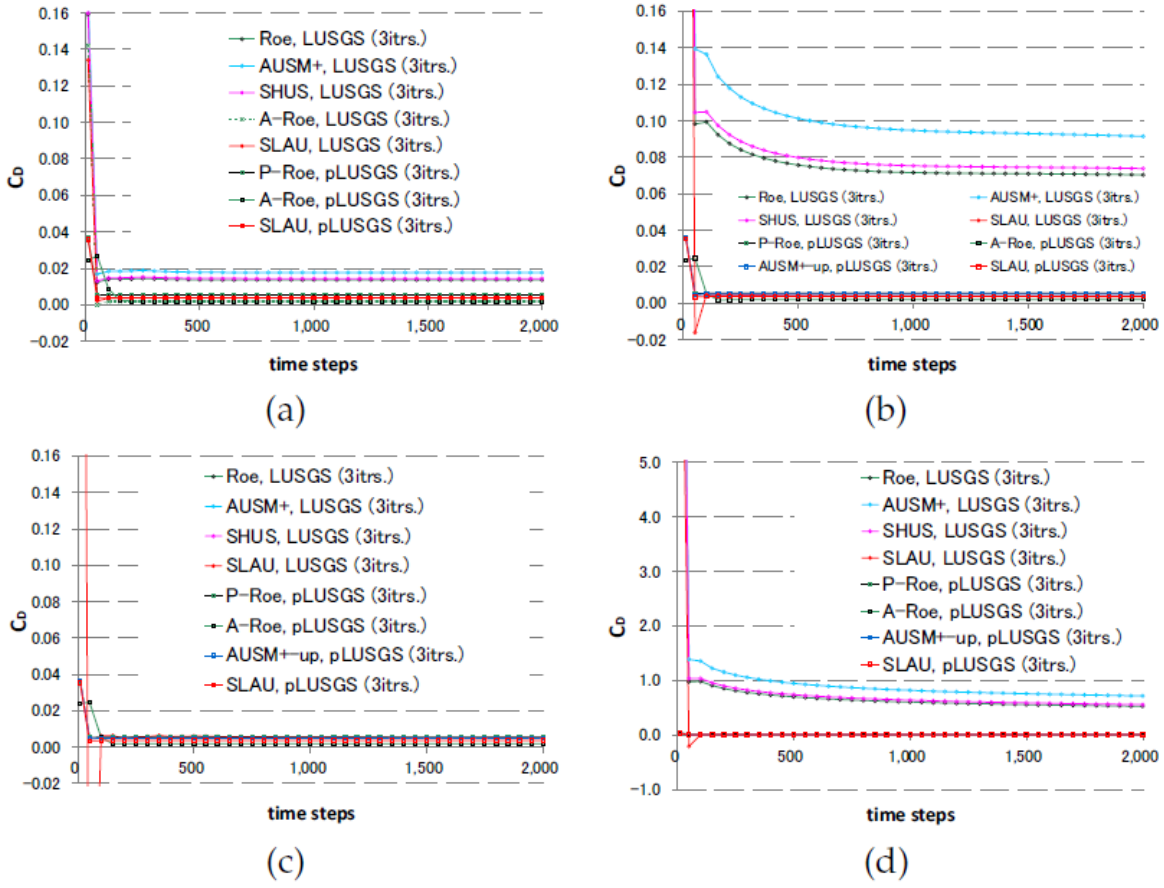

Figure 1.10: Drag convergence history of different low-Mach schemes for **(a)** $M_\infty = 0.1$, **(b)** $M_\infty = 0.01$ and **(c)**, **(d)** $M_\infty = 0.001$, including more detailed solution with wider scale on the vertical axis. Source: Kitamura *et al.* [74].

Solvers employed in Wind Turbine analysis

The majority of CFD solvers employed for wind turbine analysis are incompressible. This is the case for the *EllipSys3D* [100, 101] solver, that has been extensively used for the NREL wind turbine case [56], as well as for the MEXICO case [135]. In addition, the *AVL SWIFT* [12] solver is employed using unstructured grids, while the *CFD-ACE* [164, 3] is used with structured. Commercial solvers include *CFX* [128, 63], *FLUENT* [40] developed by ANSYS and AcuSolve [5] developed by Altair. They have the capability of modelling compressible and incompressible flows, although the incompressible formulation (pressure-based methods) has been used for the analysis of wind turbines [128, 63, 28]. There are other incompressible codes, based on engineering models; such as the *AWSM* [158] solver, which is based on lifting line theory and developed by ECN. Likewise, *UPMWAKE* was developed by Crespo *et al.* [29] for wake modelling.

With the current trend of increasing the size of wind turbine blades and the high tip speeds that they can reach (up to Mach 0.4), compressible solvers have also been used for wind turbine analysis. Table 1.2 lists the solvers employed in the literature. Likewise, it is worth mentioning the *Euranus* [120] solver, developed by FOI, which solves the viscous RANS equations in multi-block grids, and the *FLOWer* [113] and *TAU*[75] solvers developed under the MEGAFLOW project by DLR, Airbus and EADS. Both solvers are based on a finite-volume formulation for structured and unstructured grids, respectively. Moreover, NASA developed *ARC2D* [65], *OVERFLOW* [108] and more recently *Helios* [134, 126]. The latter employs an unstructured grid in the flow near the body and a block-Cartesian grid for the off-body flow.

In the VISCEL Project [24, 25], *Euranus* and *FLOWer* solvers, as well as the incompressible *EllipSys3D* and other solvers, were employed for the analysis of viscous and aeroelastic effects on the LM19.1 and LM17.0 blades. All showed torque over-prediction for wind speeds above 12m/s.

Note that, to date, the compressible solvers for wind turbine analysis employed in the literature only incorporate a preconditioning matrix in order to account for low-speed flows. To the best of the author's knowledge, no all-Mach Roe-type schemes applied to wind turbines have been published. Likewise, these schemes have been mainly implemented in explicit time-marching methods.

Table 1.2: Compressible solvers for Wind Turbine analysis employed in the literature.

Solver	Developed by	Flux evaluation	L.M. Precond. (Y/N)	W.T. cases
ARC2D[65, 62]	NASA	Central van Leer/2nd ord. Limiter	-	other W.T.
Overflow-D2[108]	NASA	Central	Y (1)	NREL
Helios[134, 126]	NASA / AFDD / Wyoming / Stanford	Central	Y(1)	NREL
elsA[78]	ONERA & CERFACS	van Leer/Roe/ Coquel-Liou HUS/AUSM	Y (1)	NREL
Euranus[120]	FOI	Central/Upwind	Y(1)	VISCEL
NSMB[19, 2]	EPFL, KTH & CERFACS	Roe/AUSM+/HLLE	Y (1)	
FLOWer[113, 75]	DLR, Airbus & EADS	Central/Upwind	Y (1)	VISCEL, MEXICO
TAU[75]	DLR, Airbus & EADS	Central/Upwind	Y (1)	NREL
PUMA2[71, 22]	Penn State University	Roe/van Leer/ 2nd ord. Limiter	-	NREL
HMB,**WMB**[46]	Liverpool University	Osher/Roe	Y (2)	NREL, MEXICO

L.M.: Low Mach, Precond.: Preconditioning, Y.: Yes, N.: No, W.T: Wind Turbine. Preconditioning methods: (1) Preconditioning matrix, (2) All-Mach scheme. The Central scheme refers to Jameson's method with artificial dissipation, WMB: Wind Multi-Block.

1.2.5 Studies on the MEXICO wind turbine

Description of the experiments

First details of the MEXICO project (Model Experiments in Controlled Conditions) experiment were given by Vermeer *et al.* in the review paper [161]. Snel [135] and Pascal [109] described this project in more detail and presented the first analysis of the results. The MEXICO project was a FP5, partly financed by the European Commission, with a duration of 6 years. A three-bladed wind turbine of 4.5m diameter was designed and tested in the wind tunnel of opened section ($9.5mx9.5m$) of the German-Dutch Wind tunnel facility.

The MEXICO blade geometry consists of three aerofoil families, whose arrangement along the blade can be seen in Figure 1.11. DU 91-W2-250 aerofoil is placed in the root, from 20 to 45% span, at the mid span (from 55 to 65%) there is the RISØA1-21 and, finally, the NACA 64-418 is found in the tip of the blade, from 70 to 100%. Between these three aerofoils sections, the blade has a constant section. Its length is 2.25m and the maximum aerodynamic chord measures 0.24m. In Figure 1.11, the dimensions are based on the chord at the root.

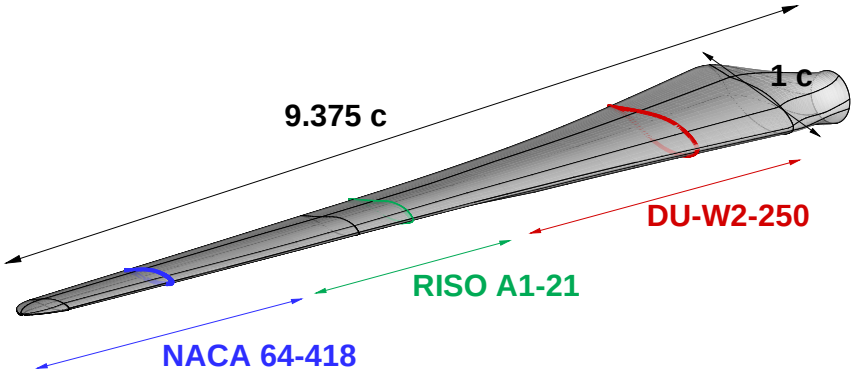

Figure 1.11: MEXICO blade geometry. The DU 91-W2-250 aerofoil is placed from 20 to 45% span, RISØA1-21 from 55 to 65% and NACA 64-418 from 70 to 100%. The length of the maximum aerodynamic chord (c) is 0.24m.

The rotor was pitch controlled and turned at constant speed of 424.5rpm. The design wind speed was 15m/s, corresponding to a speed ratio of $\lambda = 6.67$, tip speed of 100m/s and tip Mach number just below 0.3. The rotor instrumentation consisted of 148 Kulite dynamic pressure sensors distributed over 5 span-wise sections of the blades (25%, 35%, 60%, 82% and 92%), 2 strain gauge bridges at each of the three blade roots, and a thermometer to monitor the blade temperature. Three forces and three moments at the foot of the tower were also measured, to quantify the axial and sideways forces, and the yawing, tilting and rolling moments. Pressure and loads were measured at wind speeds ranging from 5 to 30m/s and tip speeds of 76 and 100m/s, with changes in the pitch angle from -2.3deg. (nose up) to 5deg. (nose down). Axial flow conditions were considered, as well as yaw angles of $+/-45$deg.

Flow field mapping of the three velocity components was performed with stereo PIV measurements, employing two cameras focusing on the PIV sheets (which were located horizontally in the symmetry plane of the rotor) and 950 velocity (x, y and z components) data points were obtained. The PIV measurements were taken within the rotor plane as radial traverses (*Priority 1*); as axial traverses from -1 to 1.5 diameters downstream at two span-wise stations (*Priority 2* at 60% R and *Priority 4* at 80% R); and the tip vortices were tracked (*Priority 3*). The PIV samples were rotor-phase locked and each PIV data point consisted of 30-100 samples. Within the Mexnext project [127], velocity averaged results were investigated. Measurements were taken at 10, 15 and 24m/s, for axial flow conditions and yaw angles of $+/-30$deg. Figures 1.12 to

1.14 show the relative position of the blades with respect to the PIV windows for each azimuthal angle and for the different measurements. The PIV frames were always located at nine o'clock and the rotor spinned clock-wise. Azimuth 0 degrees indicates that a reference blade is positioned at twelve o'clock (Figure 1.12 (a)).

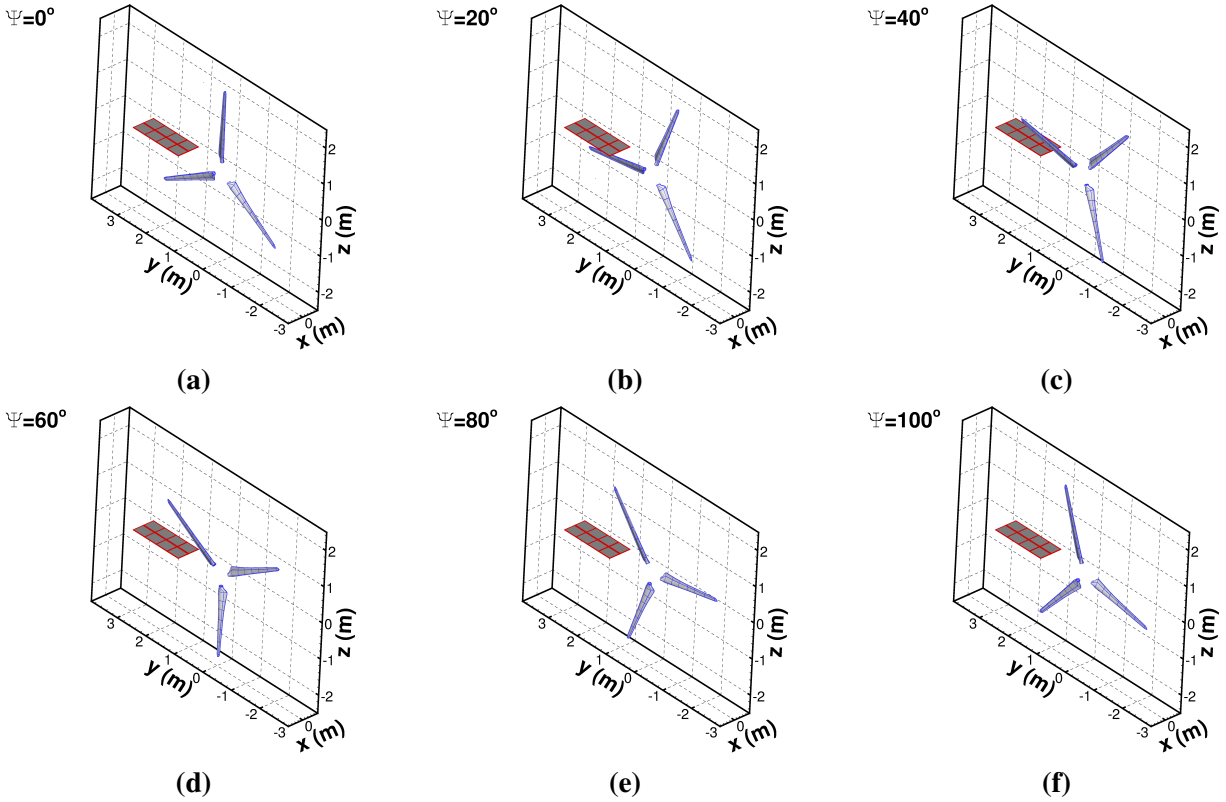

Figure 1.12: PIV configurations near the MEXICO rotor plane (*Priority 1*), for the different azimuth angle positions. The PIV frames are always set at nine o'clock and the rotor spins clock-wise. The azimuth angle is measured relative to the twelve o'clock initial position.

Measurements in parked conditions were also performed, in order to simulate storm conditions (with high wind speed) when the blades of the wind turbine are feathered. The tunnel wind speed was 30m/s and the pitch angles were varied from -2.3 to 87 degrees. Pressure and loads were measured, but no PIV measurements were performed. It should be noted that the pressure transducers for stations 25% and 35% R were found to be erroneous and not reliable at 60% R, as reported by Gomez-Iradi *et al.* [45].

The following section presents all the numerical simulations employing the MEXICO wind turbine published in the literature, along with the main conclusions reported in the MexNext final report [127].

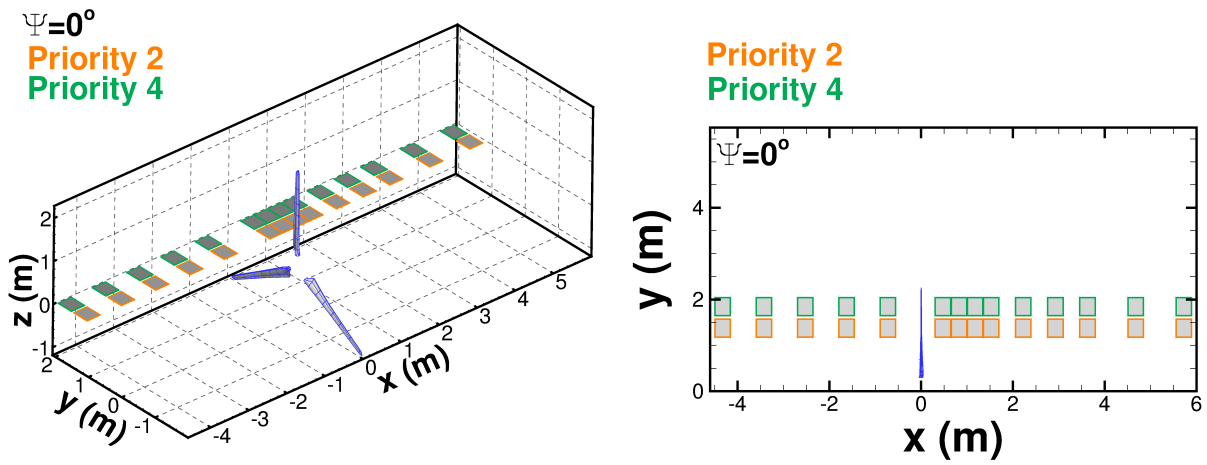

(a) 3D view. **(b)** Top view.

Figure 1.13: PIV windows configurations for MEXICO velocity mapping. Orange and green windows are located at 60%R (*Priority 2*) and 82%R (*Priority 4*) radial stations, respectively. The azimuth angle is always 0 degrees (reference blade at 12 o'clock). Note that the rotor spins clock-wise.

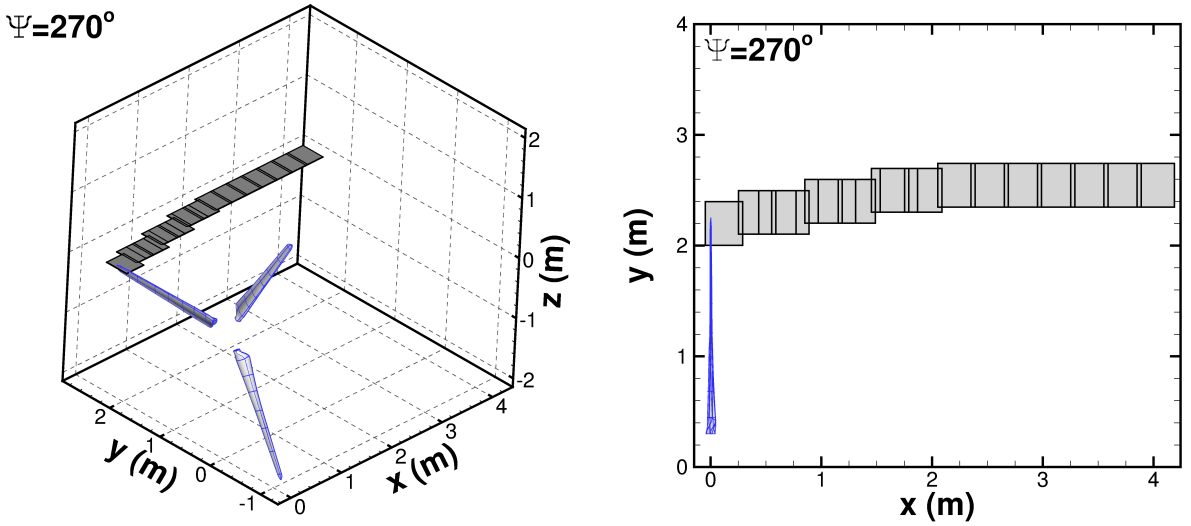

(a) 3D view. **(b)** Top view.

Figure 1.14: PIV windows configurations for MEXICO vortex tracking (*Priority 3*). The azimuth angle is always 270 degrees (reference blade at 9 o'clock). Note that the rotor spins clock-wise.

Numerical simulations

Since the results of the MEXICO project were released[135, 127], several authors have used the data to validate computational methods. The most popular test case is at 15m/s wind speed, zero-yaw, and pitch angle of -2.3 degrees rotating at 424.5rpm. Yawed conditions have also been considered by some authors[47, 99, 111, 140]. Published papers regarding the MEXICO experiment include the work of Bechmann *et al.* [16], who used the incompressible solver *EllipSys3D*. The isolated three-bladed rotor was considered and differences in the loads were observed between experiments and CFD results, at all wind speeds studied. The discrepancies were attributed to the fact that the computations were run fully turbulent. Among all cases, they found better agreement with the pressure distributions at the outer sections of the blade than the inner ones, and for 15m/s wind speed, see Figure 1.15. The same authors, in a limited wake study, reported reasonable agreement of the axial velocity component one rotor diameter downstream.

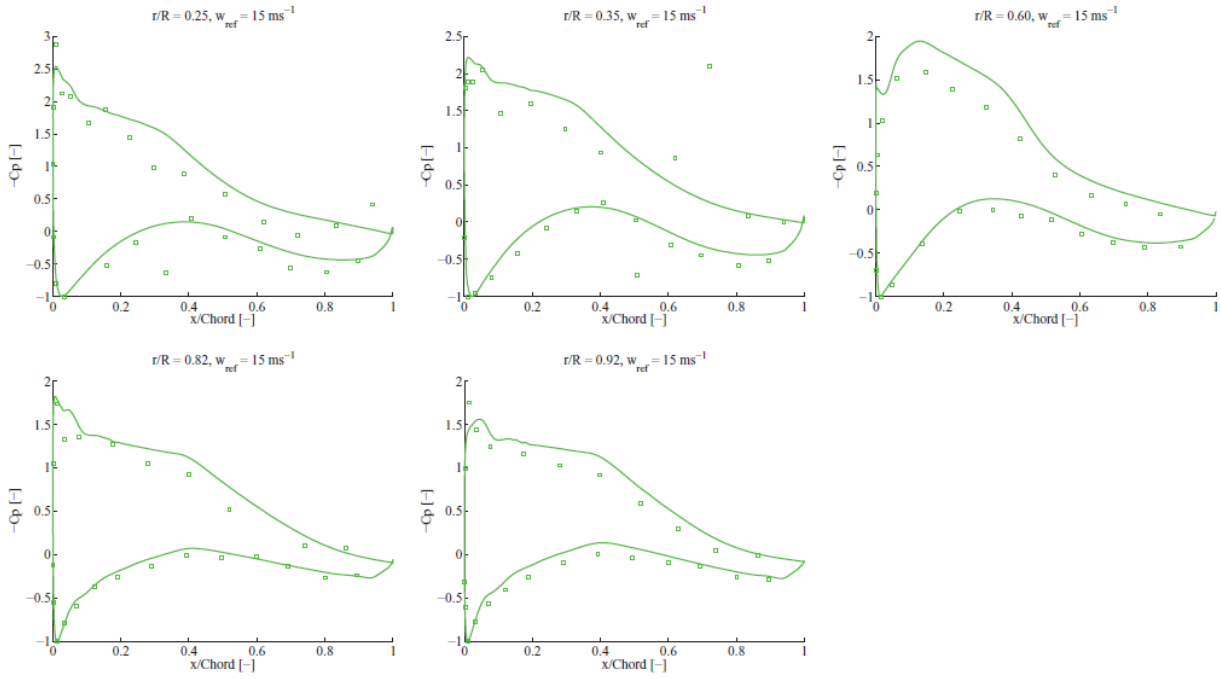

Figure 1.15: Computed pressure coefficient distribution of the MEXICO blade, non-yawed and at wind speed of 15m/s, by Bechmann *et al.* [16].

Shen *et al.* [132] used also the *EllipSys3D* solver to model the MEXICO rotor inside the wind tunnel, by a combination of an actuator line to model the blades and LES computations, using grids with finest cell size of R/30 (31%c). To determine the body forces on the rotor blades, they employed a blade element

approach combined with 2D aerofoil data, either directly extracted from the experiments or corrected for tip effects[132]. Comparisons of blade loadings showed that the technique where the tip effects were corrected was in better agreement with the measurements than with the original 2D aerofoil data; however, no perfect matching with the experimental loads was achieved. In addition, comparisons of detailed near-wake velocities showed good agreement. However, the oscillatory pattern due to the blade passage was not captured (see Figure 1.16). With the employed coarse grid, the authors concluded that tunnel effects were not significant.

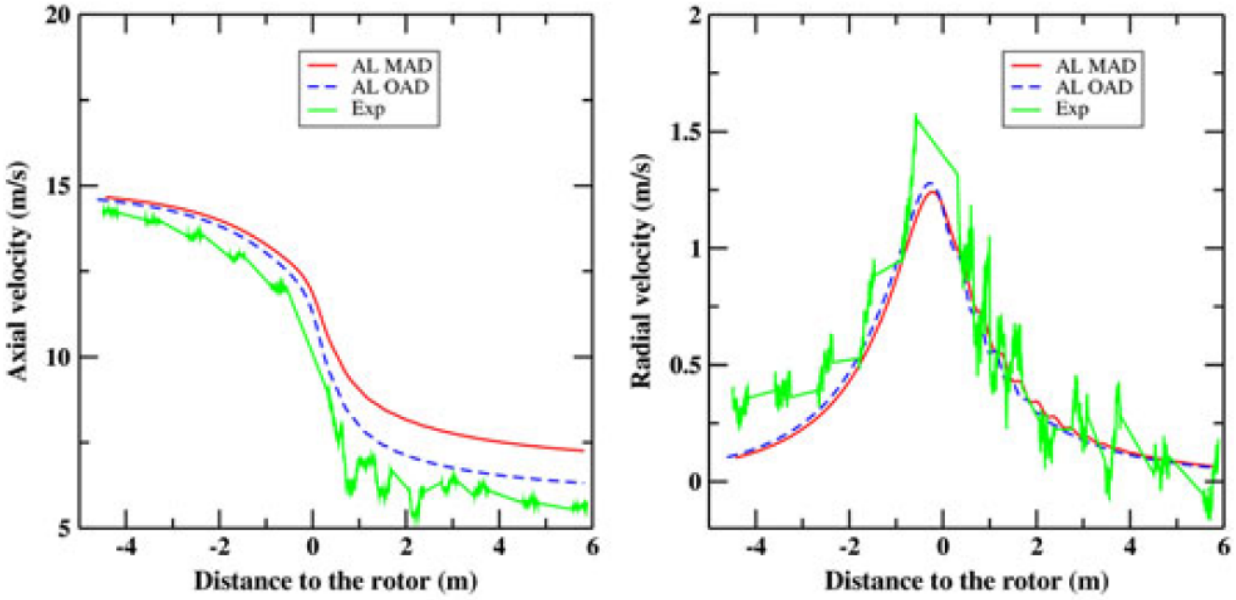

Figure 1.16: Computed axial and radial velocities at 61.2%R, non-yawed and at wind speed of 15m/s, by Shen *et al.* [132]. LES computations were performed, with actuator line. OAD: 2D aerofoil data; MAD: modified aerofoil data (tip effects).

Pressure and PIV data were used by Yang *et al.* [166] to determine the angle of attack and aerofoil data from the MEXICO blade, by subtracting the induced velocity created by bound circulation from the PIV measurements. The derived aerofoil data was used in a BEM code. They found that using the original 2D aerofoil data in the BEM code, the rotor loading was over-predicted, possibly due to strong 3D effects not accounted for in the analysis. Micallef *et al.* [99] carried out an investigation of the radial velocities close to the rotor plane, using a 3D unsteady potential panel method. They found that radial velocities were higher near the tip region than the root. Likewise, close to the blade, the radial flow velocity was not entirely due to the blade vorticity, but wake-induced radial velocities became important and had to be taken into account. The main discrepancies in the velocities were concentrated at the mid-span stations.

The location of the computed first tip vortices agreed well with the experiments, although a much faster wake convection was observed in the computations than in the experiments. Breton *et al.* [21] used the PIV data to compare URANS CFD results of the compressible *WMB* solver [46] with the full rotor representation and an actuator disk model. The vortex position, radius and strength were obtained using three methods. Firstly, representing the asymptotic behaviour of the circulation as a function of the radius. Secondly, performing a quadratic average of the distances from the maximum vorticity normal to the plane (ω_n) and the position where the vorticity reaches $0.2\omega_n$. In the third method, they employed λ_2-criterion [70], performing a quadratic average of the distances from λ_2 reached a peak to the points at the limit region where $\lambda_2 < 0$. It was found that the method employed in the calculation of the radius and strength of the vortices strongly influenced the results. In the simulations, the grid coarseness lead to high numerical dissipation, making the identification of vortices difficult. In fact, the wake expansion was under-predicted and the vortex radius was over-predicted by 250% using the first method, by 700% using the second and third methods, as can be observed in Figure 1.17. In Ref.[105], Nilsson *et al.* assessed the validation of the actuator line technique to predict the blade tip vortices. An off-set of $0.025R$ (5cm) in the vortex positions (in both radial and axial directions), with respect to the experimental values, was observed and the vortex size was largely overpredicted (5 times larger than in the experiments). Likewise, poor agreement was observed in the bound circulation around the vortex at 24m/s and better agreement at 10m/s and 15m/s. Comparisons of streamwise and radial velocities at 15m/s showed over-predictions for the former and good agreement for the latter.

A comparison between axial and yawed (30deg.) wind conditions was presented by Tsalicoglou *et al.* [155]. RANS simulations were performed using the commercial solver *CFX* and the full configuration was considered, including rotor, nacelle and tower. For the studied 15m/s wind speed, 21% less deficit in the wake was obtained for the yawed case with respect to the uniform one and less wake expansion was reported: while in axial flow conditions the wake expanded 127%D at 1D downstream, for yawed flow the expansion was 114%D. Likewise, the distance between vortices in the yawed case was found to be 20% shorter than in the uniform one.

Xudong *et al.* [165] implemented a tool for optimising wind turbine blades, consisting of an aeroelastic model and a BEM method, with a tip-loss correction model [131]. The design variables employed were the chord, twist and relative thickness. Aerodynamic results for the axial and tangential forces, were

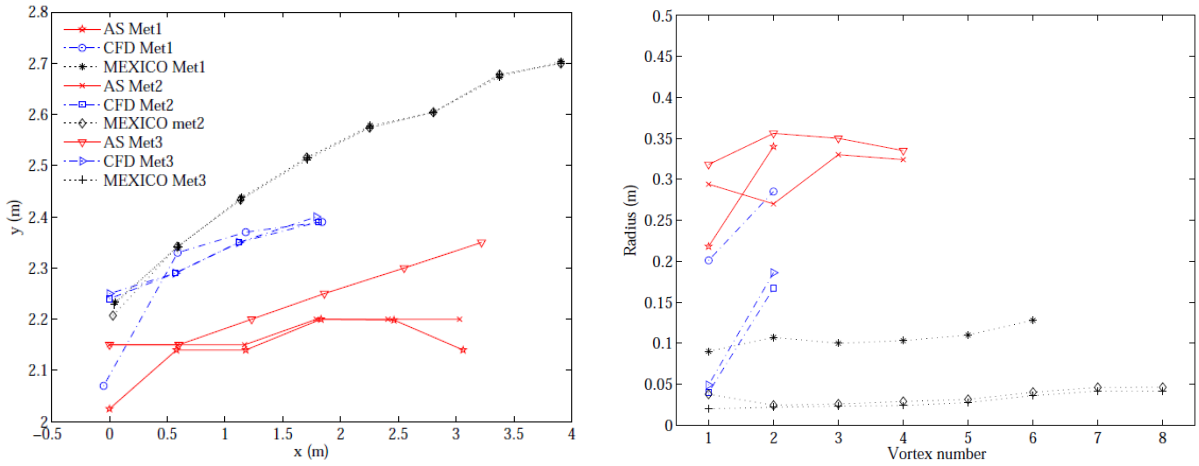

(a) Vortex position. **(b)** Vortex radius.

Figure 1.17: Position and radius of vortices in the wake of the MEXICO turbine at wind speed of 15m/s by Breton *et al.* [21]. Comparison between actuator surface model (AS), full rotor CFD computation (CFD) and experiments (MEXICO). Met1: circulation from integrals of tangential velocities, Met2: vorticity magnitude, Met3: λ_2-criterion [70]. The plots are shown in Chapter 5, with results from the present study.

compared with MEXICO data with aeroelastic effects accounted for. Flapwise and edgewise deflections were compared between the original and optimised rotors, and a small correction of the chord near the tip was reported to increase the aerodynamic performance by an additional 1.15%. Pereira *et al.* [111] adapted the Beddoes-Leishman dynamic stall model [81] for incompressible flows around wind turbines and implemented it into a BEM code. Normal force coefficients at different azimuth angles were compared with the experiments at wind speed of 24m/s and at different yaw flow angles. Due to the changes in angle of attack over a rotor revolution, dynamic stall was expected to occur in the inboard blade sections (25% and 35%), where larger angles of attack were present. In general, the dynamic stall model showed better agreement with experiments than the static BEM method, although an overprediction of 18% was obtained. At high yaw angles ($+/-45$deg.), however, poor agreement was observed.

Overall, and regarding the predicted loads, all authors have encountered discrepancies with the experiments. This was also reported in the MexNext report [127], where a comparison between different CFD solvers and engineering models against the experiments was presented, see Figure 1.18. At the design wind speed case (15m/s), an over-prediction at the inboard (25% and 35% R) and mid-span (60% R) sections was always observed. For the low-speed case (10m/s), over-predictions at the same span-wise sections were also present. For the highest wind speed case (24m/s), the pressure side was in good agreement with the exper-

iments, while the suction side was over-predicted at all the blade stations. These trends were also observed by Bechmann *et al.* [16] in the pressure distributions. Shen *et al.* [132], Guntur *et al.* [54] and Tsalicoglou *et al.* [155] reported an over-prediction in the integrated loads too. Finally, regarding the parked rotor at wind speed of 30m/s, uncertainties in the experiments at the inboard sections were reported by Gomez-Iradi *et al.* [45], while similar trends to the CFD computations were observed at the outer regions of the blade.

To date, there is no clear understanding about the discrepancies between the results obtained with CFD, BEM models or other lifting line codes and the MEXICO pressure data. In Ref. [127], three possible reasons are given to explain these discrepancies: differences in pitch and/or local twist; the thickness of the tripping tape caused a thicker and hence more decambering boundary layer; and inaccuracies on the sensitivity of the absolute pressure sensors.

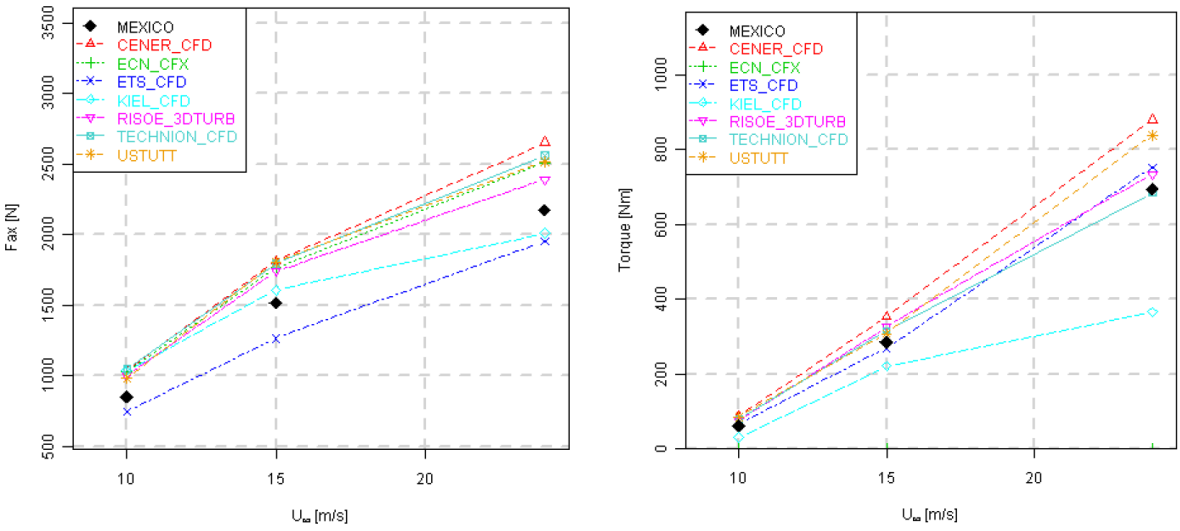

(a) Predicted thrust. **(b)** Predicted torque.

Figure 1.18: Comparison of the integrated thrust and torque between MEXICO experiments and different CFD codes. Source: MexNext final report [127].

Regarding the axial velocity, although the 24m/s was in good agreement, all the authors reported an offset for 10 and 15m/s wind speeds, see Figure 1.19 (a). To avoid this, Bechmann *et al.* [16] employed a correction of 0.7m/s in the experiments. For the other velocity components, better agreement with experiments was reported, although coarse grids did not capture the oscillatory pattern due to the blade passage (Figure 1.19 (b)). In yaw conditions, Sorensen *et al.* [140] studied the near rotor flow and reported a strong influence

of the shadow of the large nacelle in the velocities and, hence, should be included in yaw studies. Finally, the position and radius of the vortices were studied by Breton *et al.* [21] and Nilsson *et al.* [105]. The axial position was well predicted, while the wake showed more contraction than in the experiments, with 5cm of off-set; likewise, the computed vortex core radii were highly over-predicted in both publications. This was also published in the MexNext final report [127].

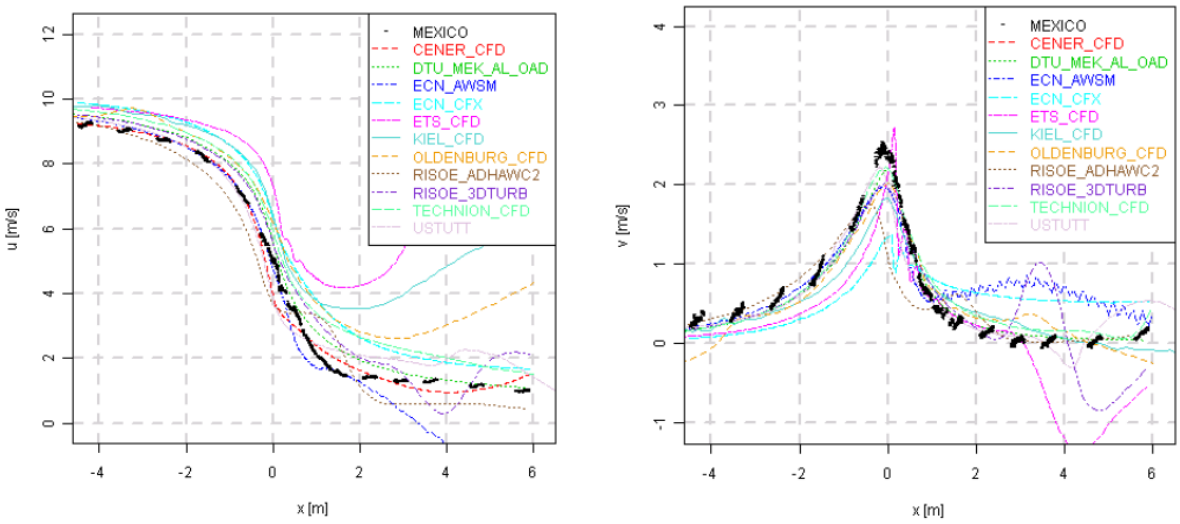

(a) Axial velocity. **(b)** Radial velocity.

Figure 1.19: Comparison of the axial and radial velocity components between MEXICO experiments and different CFD codes, at 10m/s wind speed. Source: MexNext final report [127].

Table 1.3 summarises the works on the MEXICO wind turbine. Details of the employed solvers, geometry and flow conditions are given, as well as an indication of whether the pressure (P) and/or the velocity field (PIV) were studied.

Table 1.3: Numerical computations on the MEXICO wind turbine (continued over).

Reported by	Solver	Model	Turbulence Model	Geometry	Mesh size	Flow	ω (rpm)	v_{wind} (m/s)	ϕ (°)	P	PIV
Bechman[16]	EllipSys3D	st.RANS	$k-\omega$ SST	R	16M	A	425.5	10,15,24	-2.3	y	y
Yang[166]	-	IFW +BEM	-	B	-	A	[324.4,424.4]	[10,24]	[-5.3,1.7]	y	y
Réthoré[115, 116]	EllipSys3D	st.RANS un.RANS st./un.RANS/DES	$k-\omega$ SST	WT R WT+R	12M 14M 26M	A	-	10,15,24	-2.3	y	y
Grasso[47]	AWSM	LLT + FV	-	R	-	A Y (30°)	-	10,15,24 15	-2.3	n	y
Shen[132]	EllipSys3D	AL/un.LES	-	R WT+R	11.8M 26.2M	A	424.5	10,15,24	-2.3	y	y
Lutz[90]	FLOWer	st. RANS un.RANS un.RANS	$k-\omega$	R+N R+N R+N+T	17.1M 9.1M 9.1M	A	-	10,15,24	-2.3	n	y
Micallef[98]	-	IFW DFW BEM	-	R	21 elem. 18 elem. -	Y ($^{+}/_{-}30°$)	-	15	-2.3	n	y
Micallef[99]	-	un.PM+FV	-	R+N	3908 pan.	A, Y ($^{+}/_{-}30°$)	424.5	15	-2.3	n	y
Schreck[129]	-	IFW	-	B	-	A	325	[5.4,30]	-2.3	y	n
Xudong[165]	-	BEM + Aero-elastic	-	R	20 elem.	A	424.5	15,25	-2.3,0.7	y	n
Guntur[54]	-	BEM + 3D ST	-	R	50 elem.	A	425	[5,30]	-2.3	y	n

R: Rotor, B: Single blade, N: Nacelle, T: Tower, WT: Wind Tunnel, A: Axial, Y: Yawed, st.: steady, un.: unsteady, AL: Actuator Line, LLT: Lifting Line Theory, FV: Free Vortex, DFW: Direct Free Wake, IFW: Inverse Free Wake, PM: Panel Method, ST: Stall Model, DST: Dynamic Stall Model, pan.: panels, ω: Rotational speed, ϕ: Pitch angle, P: Pressure, PIV: Particle Image Velocimetry, n: no, y: yes.

Table 1.3: Numerical computations on the MEXICO wind turbine (concluded).

Reported by	Solver	Model	Turbulence Model	Geometry	Mesh size	Flow	ω (rpm)	v_{wind} (m/s)	ϕ (°)	P	PIV
Breton[21]	- WMB	AS+CVFEM URANS	- $k-\omega$ SST	R	0.54M 25M	A	424.5	10,15,24	-2.3	n	y
Gomez-Iradi[45]	FAST WMB WMB	BEM+LLT URANS URANS	- $k-\omega$ SST $k-\omega$ SST	R	26 elem. 5.7M 11.5M	A	0	30	[90,-2.3]	y	n
Gomez-Iradi[44]	WMB	URANS	$k-\omega$/SST	NACA64-418 DU91-W2-250 RISO-A1-21	60k	-	-	-	-	y	n
Pereira[111]	-	DST+BEM	-	R	15 elem.	Y (30°,45°)	-	24	-2.3	y	n
Sorensen[140]	EllipSys3D	RANS / URANS	$k-\omega$ SST	R	28.3M	A / Y (30°)	425.5	15	-2.3	y	y
Tsalicoglou[155]	CFX	RANS	$k-\omega$ SST	R+N+T	15.5M	A Y (30°)	425.5	10,15,24 15	-2.3	y	y
Nilsson[105]	EllipSys3D	AL/un.LES	-	B	21M	A	425.5	10,15,24	-2.3	y	y
Present work	HMB2	st.RANS+Aeroel. st.RANS	$k-\omega$	B	2.6M 10M/64M	A	424.5	10,15,24	-2.3	y y	n y

R: Rotor, B: Single blade, N: Nacelle, T: Tower, WT: Wind Tunnel, A: Axial, Y: Yawed, st.: steady, un.: unsteady, AL: Actuator Line, LLT: Lifting Line Theory, FV: Free Vortex, DFW: Direct Free Wake, IFW: Inverse Free Wake, PM: Panel Method, ST: Stall Model, DST: Dynamic Stall Model, pan.: panels, ω: Rotational speed, ϕ: Pitch angle, P: Pressure, PIV: Particle Image Velocimetry, n: no, y: yes.

1.2.6 Prediction of wind turbine wake instability [2]

Accurate predictions of wind turbine wakes are important for the performance analysis of the turbines and their optimal positioning within tightly-spaced wind farms. In the past, CFD was considered a tool confined to the near-wake analysis due to the inherent numerical dissipation of CFD solvers. With progress, however, in numerical methods and mesh density, CFD is emerging as a good tool for the analysis of the wakes since it can accurately capture the development of core instabilities that will lead to the wake breakdown.

Ivanell *et al.* [64] studied the stability of tip vortices in an azimuthally periodic domain using the actuator-line method (one blade was simulated with spatial periodicity assumed). Perturbations were added to the solution and it was found that when the oscillations of vortices from one spiral to the next were out of phase the instabilities were larger than for in-phase modes. Likewise, the non-linear development of the wake instability resulted in vortex pairing. They also correlated the length of the stable wake with turbulence intensity at the free-stream.

Troldborg *et al.* [153] studied the wake behind the Tjaereborg wind turbine with LES and for different tip speed ratios. At high tip speed ratio (λ=11.78), the wake broke shortly downstream of the rotor, while at λ=7.07 the instabilities were present at 10R. In Troldborg *et al.* [154], they compared the wake behind the NREL 5MW wind turbine (126m diameter) with RANS and DES computations, employing the full rotor geometry as well as actuator line and actuator disc methods. The RANS results with the three representations of the rotor were very similar. However, DES computations showed that the use of an actuator line or disc methods are not optimal for a good wake capture when the inflow is laminar. Due to the coarseness of the employed grid (minimum cell size of 500mm), the results presented an early wake breakdown at approximately one diameter downstream, see Figure 1.8. There was a jump from finer to coarser grid and, therefore, the wake breakdown might be attributed to numerical dissipation.

LES computations, using the commercial CFD solver *FLUENT*, were performed by Mo *et al.* [103] for the NREL Phase VI wind turbine (10m diameter) inside a wind tunnel at 7m/s wind speed ($\lambda = 5.42$), with grid cell sizes of 250mm on the wake. An increase in the turbulent intensity was observed from the

[2] Full citation of: M. Carrión *et al.* , Understanding Wind Turbine Wake Breakdown using CFD, *AIAA Journal*, Accepted May 2014.

rotor plane to three diameters downstream and a gradual decrease in the region where the wake started to be unstable (at approximately 4D downstream). It finally broke down at 5D downstream and, as a result, the turbulence levels increased again. They also demonstrated that a deficit of velocity was noticeable at downstream distances of 20D. The same authors studied the effect of the wind speed on the wake instability [102], keeping a constant rotational speed of 72rpm. They found that the instability started to develop later in time and further downstream when the wind speed, and therefore the tip speed ratio, increased: while at 7m/s the instability region was located at 4D, at 10m/s it was located at 6D and at 15m/s it was at 11D downstream. Gundling *et al.* [53] used a free-vortex wake model coupled with a growth/diffusion vortex model for the prediction of wind turbine far wakes. The NREL Phase VI and WPS–30 wind turbines were used and the results were compared with actuator line LES (*FLOWYO* solver) and full-rotor DES (*HELIOS* solver) simulations, using adaptive mesh refinement. For laminar inflow and wind speed of 10m/s ($\lambda = 3.77$), the free-vortex wake model only captured the vortices up to 4R and were dissipated downstream, since high levels of dissipation were added for stability reasons, see Figure 1.20 (a). Employing the full-rotor representation, however, wake instabilities were predicted between 8R and 10R downstream (Figure 1.20 (c)). Additionally, the actuator line captured the wake very poorly, see Figure 1.20 (b).

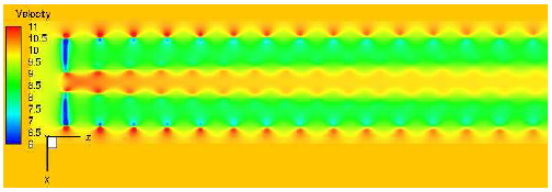

(a) Free-vortex model.

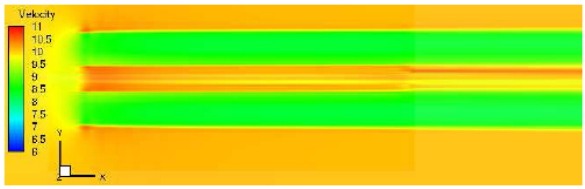

(b) Actuator Line.

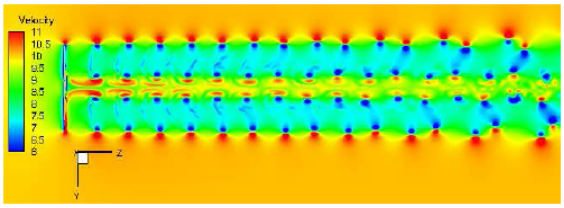

(c) Full Rotor representation.

Figure 1.20: Prediction of wake instabilities using a **(a)** Free-vortex model, and DES with **(b)** actuator line and **(c)** full rotor representation, with adaptative grid refinement method, by Gundling[53]. The wind speed was 10m/s ($\lambda = 3.77$) and the inflow was uniform.

Table 1.4 lists the conditions and grids employed in the works in the literature, as well as the location of the predicted instabilities.

Table 1.4: Wind turbine wake breakdown computations in the literature.

Reported by	Wind Turbine	Turb. Model	Rotor Model	Tu int. (%)	Mesh size	Wake res. (mm)	λ	Ins. (R)
Current work	MEXICO	RANS	F.R. (P)	2.58	860M	6	6.67	4.5
			F.R. (P)		860M		10	1.25
			F.R.		2B		10	1.25
Ivanell [64]	Tjaereborg	LES	AL (P)	1.0	10M	435	7.07	4
Troldborg [153]	Tjaereborg	LES	AL	0.0	8.4M	1000	3.21	-
							5.05	-
							7.07	5
							11.78	2
Troldborg [154]	NREL 5MW	RANS	AL	0.0	23M	500	7.6	7
			AD					-
			F.R.					-
Troldborg [154]	NREL 5MW	DES	AL	0.0	23M	500	7.6	7
			AD					-
			F.R.					2
Troldborg [154]	NREL 5MW	DES	AL	6.0	23M	500	7.6	2
			AD					-
			F.R.					2
Gundling [53]	NREL Phase VI	FV	BEM	0.0	-	N.A.	3.77 / 7.53	- / -
		LES	AL		5.9M	N.A.		- / -
		DES	F.R.		33M	N.A.		8 / 2
Gundling [53]	WPS-30	FV	BEM	13.0	-	N.A.		-
		LES	AL		5.9M	N.A.		-
		DES	F.R.		33M	N.A.		-
Mo [102]	NREL Phase VI	LES	F.R.	0.2	3.6M	250	2.51	22
							2.89	18
							3.79	12
							5.41	8

F.R.: Full Rotor representation; F.R. (P): Full Rotor representation with azimuthally periodic domain; AD: Actuator Disk; AL: Actuator Line; Tu int.: Turbulence intensity at the inflow; Wake res.: resolution of the cells at the wake in mm; Ins.: Relative location from the rotor plane where the instability is predicted; FV: Free-Vortex Wake method; BEM: Blade Element Model; N.A.: Information not available.

1.2.7 Fluid-structure interaction

Analysing large diameter wind turbines [10], aeroelasticity plays an important role, since the blades are less stiff and can suffer large deformations, changing therefore their aerodynamic performance. As Hansen *et al.* explain in their review paper [57], wind turbines suffer from aeroelastic instabilities, such as edgewise blade vibration, usually encountered in parked rotors, and flutter, due to the interplay between unsteady aerodynamic loads and the wind turbine structure. In order to study the interaction between the flow and the structure of the wind turbine, aeroelastic methods have been developed over the years, where the aerodynamic and structural information is exchanged.

For the structural analysis, Finite Element Method (FEM) and modal approach are typically employed. In FEM, the blade is modelled as a beam, and non-linear beam theory is employed, where the 3D structure is reduced to a 1D structure concentrated along the elastic axis of the beam, as shown in Figure 1.21. In traditional wind turbine analysis, and under the assumption of small deformations, almost all structural models are based on classical beam theory (Euler-Bernoulli or Timoshenko) [57], avoiding non-linear terms in the stiffness and loading matrices. Nowadays, however, there is an increase interest in non-linear models [18], due to the increasing size of the wind turbine blades over the last years. For more complex geometries, Finite Volume Methods (FVM) can also be employed, where the blade structure is modelled as a 3D element and therefore more complex structural behaviour can be predicted. Composite modelling procedures have also been recently employed [15, 60], since composite materials are used in modern wind turbine blades to reduce the rotor mass and preserve stiffness. The modal approach is also popular in the literature, and consists of a linear combination of the low frequency eigen-modes of the blade in order to define the blade shape, i.e. the blade deflection. This method assumes that the loads and the damping of the system do not excite the eigen-modes associated with higher frequencies, and typically the first 3 or 4 eigen-modes are employed in the model. The advantage of FEM with respect to modal approach methods is that FEM are able to work with fully non-linear rigid body dynamics and hence much more complex blade deformations can be obtained. The disadvantage is that the number of DOF in the system is much higher and, therefore, it requires higher computational effort than the modal approach [57].

To model the full wind turbine, multi-body dynamics formulations are also popular in the literature [119]. In this method, each component is separately considered, whose elastic DOF are defined as local elastic displacements to which rigid body motions are added through kinematic boundary conditions, see Figure 1.21 (c).

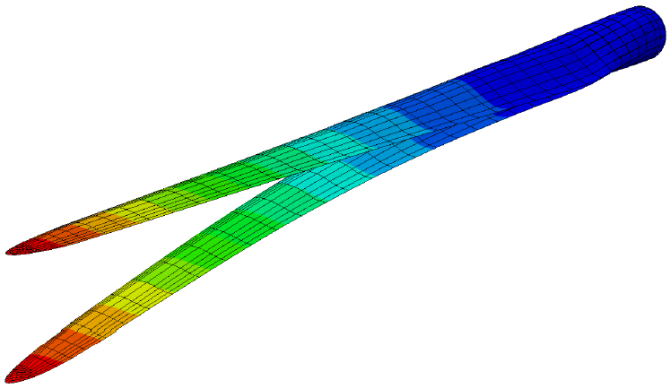

(a) Finite element model (FEM) of the NREL 5MW blade, by Motta-Mena *et al.* [104].

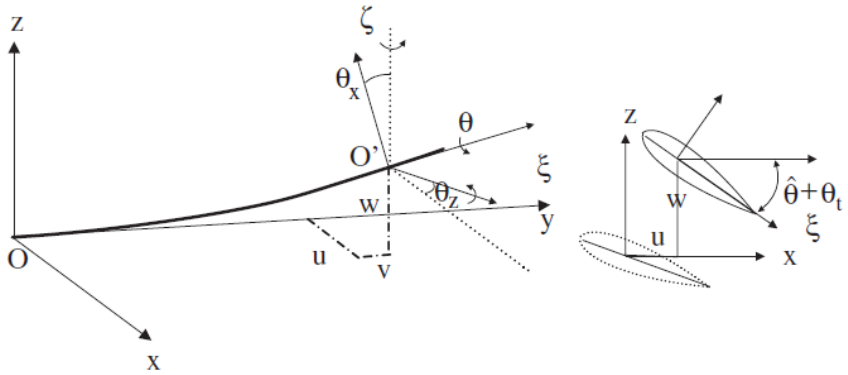

(b) Classical beam model of a blade, by Hansen *et al.* [57].

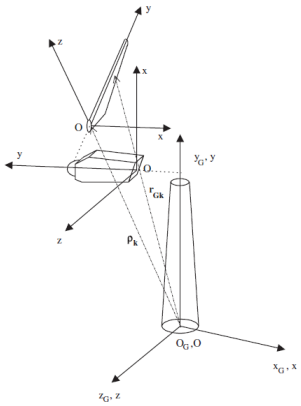

(c) Multi-body representation of a wind turbine, by Hansen *et al.* [57].

Figure 1.21: **(a)** Finite Element model and **(b)** classical beam model of a wind turbine blade. **(c)** Multi-body representation of a wind turbine.

To obtain the aerodynamic loads, BEM-based methods have been extensively used in the literature, since they do not require much computational effort. With this regard, in part II of the *VISCEL* project, Chaviaropoulos *et al.* [25] presented a comparison of 2D aeroelastic codes for the prediction of the aeroelastic behaviour of the NACA0015 aerofoil. Two problems were approached, including classical flutter (bending and pitching considered) and stall-induced flap-lag flutter, which is a combination of flapping and lead-lagging. The aeroelastic models for these two problems were combined with a simple linear aerodynamic model and it was found that high wind speeds and lighter blades have a destabilising effect. However, all the solvers from the VISCEL partners predicted a stable response when the blades were lighter and they claimed that linear analysis tends to over-predict instabilities. Classical flutter was studied also by Baxevanou *et al.* [13] with an upwind TVD scheme and an implicit coupling scheme and similar conclusions to Ref.[25] were reached. McTavish *et al.* [93] presented an analysis of the NREL Phase VI blade (5m radius), using a vortex particle potential flow method coupled with a non-linear structural beam model. Maximum deflections of 1cm were observed.

An analysis of the blade curvature in pre-bend and pre-sweep of the 5MW three-bladed Reference Wind Turbine (RWT) of 63m radius, was presented by Riziotis *et al.* [119], using two aeroelastic methods based on Euler-Bernoulli formulation: a second order beam and a multi-body model, which showed consistency. It was found that forward bending reduces torsion loads and increases blade stability, besides preventing blade collisions with the tower. In addition, the fatigue loads were reduced when an aft pre-sweep was applied, since the tendency of the blade was nose down torsion. The effect of the tower in the 5MW RWT was studied by Hsu *et al.* [60], who employed an isogeometric rotation-free shell formulation for the structural modelling of the composites blade coupled with a low-order finite-element technique for the aerodynamics. For the rigid case, a drop in the torque of 10–12% was observed when the blade passed in front of the tower. In the flexible case, deflections in bending were mainly observed, with amplitudes of 5%R approximately. The same wind turbine case was studied by Zhang *et al.* [171], using a potential flow method coupled with a quasi-steady one-dimensional FEM model to discretise the blades and the tower. A mean flapping amplitude of 10%R was predicted and, as a result of the blade passing in front of the tower, oscillations of $+/-3\%$ were observed, which led to an increase in the drop of the output power (5.65% and 7.49% for the rigid and elastic cases, respectively). They also reduced the length of the shaft (the rotor

was closer to the tower) and found that the flapping amplitudes and therefore the fluctuations on the loads increased drastically. In the limit case of a shaft 30% shorter, they predicted a collision of the blade into the tower.

Potential flow and BEM-based models, however, have limitations when simulating more realistic flows, which are three-dimensional and unsteady. That is the reason why the development and application of CFD-CSD coupling methods for wind turbine analysis have been increasing recently. With this regard, several methods can be found in the literature. Bazilevs *et al.* [15] employed a CFD solver to compute the Navier-Stokes equations and a CSD solver based on rotation-free thin shell formulation for the structural analysis of composite blades. Information between the two solvers was exchanged at each time-step. The 5MW RWT was the focus of their analysis. Only one blade was considered, imposing spatial periodicity, and a maximum deflection in flapping of 10%R and torsion of 2 deg. were reported. They also proposed a method to prebend the blades in Ref. [14], consisting of a decoupled method, where the wind loads were obtained with CFD computations on the rigid blades followed by a series of non-linear structural mechanics simulations to determine the stress-free prebent shape of the blade. Yu *et al.* [167, 168] used an incompressible Navier-Stokes CFD solver based on unstructured meshes loosely coupled with a FEM CSD solver (based on non-linear flap-lag-torsion beam theory) to obtain the blade deformations of the 5MW RWT case at rated wind speed. For static cases, the exchange of information between the CFD and CSD solvers was done once the loads were converged. For unsteady cases, the exchange was done only once per revolution, under the assumption of loads periodicity. For the single-blade static case, a torsion at the tip of 3.1 deg. (nose-down) was obtained and deflections in lead-lag and flapwise of 10%R and 7.5%R, respectively, leading to a significant reduction in thrust and torque. The unsteady computation considering the full machine showed similar averaged values to the static one and a reduction in the tower clearance of 40% for the elastic blades was observed (Figure 1.22), along with a substantial reduction on the loads.

Guo *et al.* [55] presented a CFD-CSD coupled method, where the N-S equations were solved along with the modal amplitudes at each solution update, using a predictor-corrector scheme. The interpolation from structural to aerodynamic nodes was performed with a linear interpolation scheme, since the blade was simplified as a one-dimensional beam. For validation of the method, they used the blades of the NH1500 wind turbine of 40.5m radius and obtained the main flapwise response close to its natural frequency, and

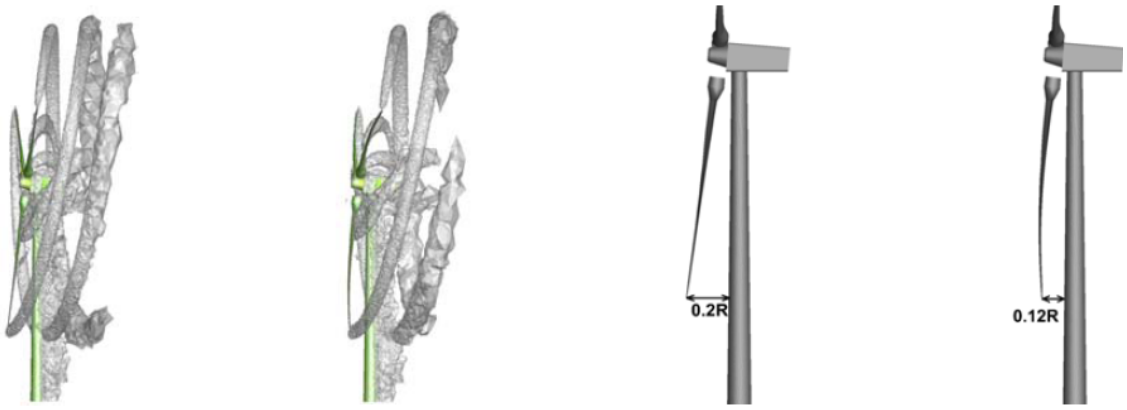

(a) Wake structure (left: CFD-only, right: CFD-CSD)

(b) Tower clearance (left: CFD-only, right: CFD-CSD)

Figure 1.22: Comparison of wake structure and tower clearance between rigid and elastic blades of the 5MW Reference Wind Turbine, when the reference blade is at an azimuth angle of 180 degrees. CFD-CSD computation performed by Yu *et al.* [167]

an additional edgewise response corresponding to the rotation frequency. Motta-Mena *et al.* [104] presented an actuator line method (implemented in the OpenFOAM CFD solver) loosely coupled with a modal-based structural dynamics solver, where the mode shapes and structural frequencies were defined using an Abaqus model. At each time-step, the displacements were computed based on the loads obtained using the velocity field, which was re-calculated considering the effects of the deformed structure. When the displacements converged within a particular time-step, the solver advanced to the next time-step until the end of the computation. For the 5MW RWT, the first flapwise mode was found to be the dominant one and a maximum tip displacement of 7%R was obtained, which lead to a decrease of 1.5% in the generated power. Likewise, the use of a very low structural damping ($\zeta = 0.005$) led to large oscillations that persisted for many cycles.

Corson *et al.* [28] presented an aeroelastic analysis for the Sandia's 100m reference blade model [48], using the Practical Fluid-Structure Interaction (P-FSI) package of the commercial CFD solver *AcuSolve*. The blade was modelled using a modal approach and a Multi-Iterative Coupling (MIC) method was employed for the exchange of the aerodynamic and structural information, where the fluid and structure were solved simultaneously and iterated to convergence before advancing to the next step. A single-blade domain was employed, applying periodicity, and the blade was modelled as a composite, using shell elements. Steady-state results were compared with the *FAST* and *WT_Perf* codes, showing some deviations in thrust, bending moment and tip displacement with the former and good agreement with the latter. Unsteady computations

were employed to study flutter on the blade, where the rotor speed was fixed and the blade was displaced using a pulse to excite the structure. However, the oscillations decayed and they no indications of flutter were observed.

Table 1.5 lists the CFD-CSD methods applied to wind turbines present in the literature. As can be observed, beam models remain by far the most popular approach for the structural modelling of the blades, since they are relatively easy to couple with CFD methods. Likewise, for dynamic computations, the modal approach in the CSD solver is extensively employed, since allows for savings in computational effort.

Table 1.5: CFD-CSD coupling methods for wind turbine aeroelastic analysis employed in the literature.

Reported by	Wind Turbine	CFD Solver	CSD Solver	Struct. Model	Coupling type	S/D	Geom.	Mesh size
Current work	MEXICO	RANS	FEM	Beam (NASTRAN)	Loose	S	B(P)	2.6M
	NREL XX	RANS	FEM	Beam	Loose	S	B(P)	5M
		URANS	Modal	(NASTRAN)	Tight	D	F.WT	18M
Bazilevs [15]	5MW RWT	RBVMS	RF shell	LPT	Loose	D	B(P) (NURBS)	1.5M
Bazilevs [14]	5MW RWT	RBVMS	RF shell	LPT	Decoupled	S	B(P) (NURBS)	1.5M
Yu [167, 168]	5MW RWT	RANS	FEM	Beam	Decoupled	S	B(P)	2.1M
		URANS			Loose	D	R	4.2M
		URANS			Loose	D	F.WT	4.3M
Guo [55]	NH1500	DES S-A	Modal	Beam	Tight (P.-C.)	D	R	-
Motta-Mena [104]	5MW RWT	PISO (ALM)	Modal	Beam (Abaqus)	Loose	D	R	0.3M
Corson [28]	Sandia's 100m	RANS S-A	Modal	Beam	Tight	S	B(P)	7.6M
		DDES S-A		(RADIOSS)		D		

NREL XX: NREL Annex XX wind turbine; 5MW RWT: 5 Mega Watt NREL Reference Wind Turbine; ALM: Actuator Line Method; R: Rotor; DES S-A: Detached Eddy Simulation with Spalart Allmaras; P.-C.: Predictor-Corrector Scheme; RF: Rotation-free thin shell; B(P): Single-blade azimuthally periodic domain; S/D: Static or Dynamic analysis; NURBS: Non-uniform rational B-splines; F.WT: Full wind turbine; RBVMS: Residual-based variational multiscale formulation of the N-S equations; LPT: Laminated plate theory for composite ply layout; PISO: Pressure implicit with splitting of operator.

1.2.8 Outcomes

Based on the literature survey, CFD analyses of wind turbines face a number of challenges, since large scale wind turbines are running at high Reynolds numbers, with high tip speeds, but at low wind speed conditions. Firstly, traditional CFD methods were developed for aerospace applications, where transonic speeds were expected. Compressible solvers running at very low-speed flows, such as wind turbines, present the well-known ”low-Mach problem”. The literature provides different approaches to overcome this problem, including preconditioning techniques, artificial compressibility and low-Mach schemes. Low-Mach Roe-type schemes seem to be popular in the literature and have only been applied to 2D problems and implemented in explicit solvers.

The MEXICO experiments are very valuable, since they provide both pressure on the blades and wake data. However, they should be used carefully, since many uncertainties were reported in the literature. On one hand, a systematic over-prediction of loads has been reported, which could be attributed to inaccuracies of the pressure transducers, but also transition could be an important effect that the numerical models did not properly capture. Since the MEXICO wind turbine was pitch-controlled, there could be additional issues regarding the under-prediction of stall on the blades, which could lead to the aforementioned over-predicted loads. On the other hand, the wake data seemed to be in much better agreement with the numerical results, although some discrepancies were reported, such as higher axial velocity levels at some wind speed conditions and differences in the wake expansion. In this case, inaccuracies regarding the position of the PIV windows with respect to the wake could lead to differences between experiments and computations.

The study of the wake behind wind turbines, including their breakdown mechanism, is a challenge that has not been fully addressed in the literature. To the best of the authors' knowledge, a full CFD study of the breakdown mechanism of wind turbines, in terms of considering the full geometry of the blades and fully resolving the tip vortices, has not been published yet. Although in several works of the literature it is claimed to fully capture the wake until its breakdown, in some works an azimuthally periodic domain was employed, restricting therefore the azimuthal wave number of the instabilities to be multiple of the number of blades. Likewise, in many publications the actuator line or actuator disk techniques were employed instead of the full blade representation. With the latter, no individual vortices can be captured and both

blade models require very detailed tabulated data, which makes the wake breakdown study very difficult. It was also found that most works lack the grid resolution required for wake study. This, along with the numerical dissipation, tends to trigger artificial wake decay. For a detailed wake study, the grid needs to be sufficiently fine to capture individual vortices with several cells across their diameter, and it should be uniform without any sudden changes, to have minimal numerical dissipation.

Aeroelasticity also plays an important role, since the bigger the blades the lower their stiffness and the larger their deformations. Most of the aeroelastic methods for wind turbine applications in the literature rely on simple BEM-based methods. However, due to their limitations in complex flows, there is an increase interest in coupled CFD-CSD techniques. To the best author's knowledge, in the methods presented in the literature applied to a full wind turbine the exchange of aerodynamic/structural information is done in a either fully decoupled or loosely coupled manner, assuming periodicity of the solution. Likewise, the assessment and validation of aeroelastic effects in the literature is limited, because of the lack of aeroelastic experimental data. Additionally, the difficulty in measuring the blade structural properties leads to uncertainties in its structural model definition. There is therefore a clear need for full-scale wind turbine experiments, where aeroelasticity measurements should be included.

1.3 Aims of the thesis

The aims of the present research project are listed below.

- Implementation of all-Mach Roe-type schemes into the compressible Helicopter Multi-Block (HMB2) CFD solver of Liverpool University.
- Comparison and validation of the implemented all-Mach Roe-type schemes for a range of problems and application to wind turbine cases.
- Study of the near wake behind the MEXICO rotor, for a range of wind speeds.
- Study of the breakdown mechanism of the wake developed behind the MEXICO rotor, with sensitivity studies on the wind speed and spatial periodicity.

- Aeroelasticity studies for two wind turbine cases:
  - Static analysis on the MEXICO blade, including sensitivity studies on the wind speed and torsional stiffness.
  - Static and dynamic analysis on the NREL Annex XX full wind turbine, including sensitivity studies on the wind speed.

1.4 Outline

The present PhD thesis is divided as follows:

Chapter 1 introduces the motivation behind the present work and provides the state-of-the-art on Computational Fluid Dynamics of wind turbines, as well as the challenges it involves. The objectives of the thesis are also presented.

Chapter 2 provides theoretical background of the employed numerical method, including the mathematical and turbulence model, parallel method, description of two mesh techniques (sliding planes and chimera) and the static and dynamic aeroelastic methods coupled with the CFD solver.

Chapter 3 presents the low-Mach problem, using a simple 2D example, and details the implementation of five variants of Roe's Riemann solver to account for low-speed flows in compressible solvers, known as all-Mach Roe-type schemes. Full description of the implementation of fluxes (explicit part) and the Jacobians (implicit part) is given.

Chapter 4 presents validation and analysis of the implemented all-Mach Roe-type schemes. This includes sensitivity studies on some numerical parameters (linear solver accuracy and CFL number), and for a number of 2D and 3D steady/unsteady problems, the different schemes are compared in terms of accuracy of the solution and convergence.

Chapter 5 studies the near wake developed behind the MEXICO rotor, in axial flow conditions and for three wind speeds. A preliminary study is firstly presented, where the effect of the blade's pitch angle and the employed turbulence model in the blade loads is assessed and a loads convergence is provided. The wake is then visualised with different techniques (λ_2-criterion, velocity contours and vorticity) and the

computed vortices are compared with experimental data, in terms of their size, position and vorticity. The three velocity components in the near wake and at the rotor plane are also compared with the experiments. Finally, the effect of the mesh density in the capability to resolve the vortex structure is assessed, employing comparisons of vorticity, velocity across the vortex and an empirical model.

Chapter 6 explores the wake breakdown behind the MEXICO rotor, for two wind speed cases. The effect of the wake resolution on the blade loads is first presented and the vortices are identified. A stability analysis is also provided to characterise in more detail the breakdown mechanism and the effect of using spatial periodicity is studied. The CFD results are compared with the experiments, in terms of vorticity and velocity across the vortices, and they are also compared with a semi-empirical model for the averaged turbulence intensity in the wake. Simple wake models are also explored and a combined kinematic-field model is proposed to match the CFD results. The last section of this chapter provides an aeroacoustic analysis for one of the wind speed cases.

Chapter 7 presents aeroelastic analysis on the MEXICO and the NREL Annex XX wind turbines. Firstly, a static analysis for the MEXICO blade is performed, where a sensitivity study on the torsional stiffness is provided for three wind speed cases. For the NREL Annex XX case, both static and a dynamic aeroelastic analyses are presented, where the tower and nacelle is rigid and the blades are allowed to deform. In the dynamic case, two wind speeds were selected, with significant differences in the type of flow. The blade deformations are analysed, along with their effect in the blade loads and tower. A sensitivity study of the structural damping is finally provided.

Chapter 8 details the main conclusions extracted from the different subjects covered in this work, along with recommendations and future work.

Chapter 2

HMB2 Solver

All computations were performed using the Helicopter Multi-Block (HMB2) flow solver developed at University of Liverpool. The flow solver has been revised and updated over a number of years and has been successfully applied to a variety of problems including cavity flows, helicopters, transonic wings, flutter, delta wing flows and wind turbines, amongst others.

2.1 Governing equations

The Navier-Stokes equations consist of Partial Differential Equations (PDEs) describing the laws of conservation for:

- Mass (continuity equation).
- Momentum (Newton's 2nd Law).
- Energy (1st Law of Thermodynamics).

The continuity equation states that the mass must be conserved. In Cartesian coordinates, x_i, this is written as

$$\frac{\partial \rho}{\partial t} + \frac{\partial \left(\rho u_i\right)}{\partial x_i} = 0, \tag{2.1}$$

where ρ is the density of the fluid, t is the time and u_i is the velocity vector. In the above, Einstein's notation is used, which implies summation for repeated indices.

The second conservation principle states that momentum must be conserved. It is written in Cartesian coordinates as

$$\frac{\partial(\rho u_i)}{\partial t} + \frac{\partial(\rho u_i u_j)}{\partial x_j} = \rho f_i - \frac{\partial p}{\partial x_i} + \frac{\partial \tau_{ij}}{\partial x_j} \tag{2.2}$$

where f_i represents the body forces, p the pressure and τ_{ij} the viscous stress tensor, which is defined as

$$\tau_{ij} = \mu\left[\left(\frac{\partial u_i}{\partial x_j} + \frac{\partial u_j}{\partial x_i}\right) - \frac{2}{3}\delta_{ij}\frac{\partial u_k}{\partial x_k}\right] \tag{2.3}$$

μ is the molecular viscosity and δ_{ij} represents the Kronecker delta, which is defined as

$$\delta_{ij} = \begin{cases} 1 & \text{if i=j} \\ 0 & \text{otherwise} \end{cases} \tag{2.4}$$

For the viscosity, Sutherland's law [146] is employed,

$$\mu = \mu_{ref}\left(\frac{T}{T_{ref}}\right)^{3/2}\frac{T_{ref}+T_S}{T+T_S}, \tag{2.5}$$

where T is the temperature of the fluid, T_{ref} is a reference temperature ($T_{ref} = 273.15K$), μ_{ref} is the viscosity at that reference temperature ($\mu_{ref} = 1.716\cdot 10^{-5} kg/ms$) and T_S is the Sutherland temperature ($T_S = 110.4K$).

The third principle of Energy conservation can be written in Cartesian coordinates as

$$\frac{\partial \rho E}{\partial t} + \frac{\partial}{\partial x_j}\left[u_i(\rho E + p)\right] - \frac{\partial}{\partial x_j}\left(u_i\tau_{ij} - q_j\right) = 0. \tag{2.6}$$

where E is the total energy of the fluid, defined as

$$E = \left[e + \frac{1}{2}u_i u_i\right] \tag{2.7}$$

and e is the specific internal energy with $u_i u_i$ representing the kinetic energy. The heat flux vector, q_i, is calculated using Fourier's Law

$$q_i = -k\frac{\partial T}{\partial x_i} \tag{2.8}$$

where k is the heat transfer coefficient. An ideal gas approximation is used, with the adiabatic index set to $\gamma = 1.4$, and the pressure is related to density as,

$$p = \rho RT, \tag{2.9}$$

where R is the specific gas constant $R = c_p - c_v = 287.058 Jkg^{-1}K^{-1}$.

2.1.1 Vector form of the conservation laws

These three laws of conservation can be combined and written in the equation shown below, which is referred to as the Navier-Stokes equation of viscous flow. For brevity, vector notation is used

$$\frac{\partial \mathbf{W}}{\partial t} + \frac{\partial \left(\mathbf{F}^i + \mathbf{F}^v\right)}{\partial x} + \frac{\partial \left(\mathbf{G}^i + \mathbf{G}^v\right)}{\partial y} + \frac{\partial \left(\mathbf{H}^i + \mathbf{H}^v\right)}{\partial z} = \mathbf{S} \tag{2.10}$$

where $\mathbf{W}$ is the vector of conserved variables and is defined by

$$\mathbf{W} = (\rho, \rho u, \rho v, \rho w, \rho E)^T \tag{2.11}$$

with the variables ρ, u, v, w, p and E having their usual meaning of density, the three components of velocity, pressure and total energy, respectively. The superscripts i and v in Equation (2.10) denote the inviscid and viscid components of the flux vectors $\mathbf{F}$ (in the x-direction), $\mathbf{G}$ (in the y-direction) and $\mathbf{H}$ (in the z-direction). The inviscid flux vectors, $\mathbf{F}^i$, $\mathbf{G}^i$ and $\mathbf{H}^i$, are given by

$$\begin{aligned}
\mathbf{F}^i &= \left(\rho u, \rho u^2 + p, \rho uv, \rho uw, u\left(\rho E + p\right)\right)^T, \\
\mathbf{G}^i &= \left(\rho v, \rho uv, \rho v^2 + p, \rho vw, v\left(\rho E + p\right)\right)^T, \\
\mathbf{H}^i &= \left(\rho w, \rho uw, \rho vw, \rho w^2 + p, w\left(\rho E + p\right)\right)^T.
\end{aligned} \tag{2.12}$$

while the viscous flux vectors, $\mathbf{F}^v$, $\mathbf{G}^v$ and $\mathbf{H}^v$, contain terms for the heat flux and viscous forces exerted on the body and can be represented by

$$\begin{aligned}
\mathbf{F}^v &= \frac{1}{\mathrm{Re}}\left(0, \tau_{xx}, \tau_{xy}, \tau_{xz}, u\tau_{xx} + v\tau_{xy} + w\tau_{xz} + q_x\right)^T, \\
\mathbf{G}^v &= \frac{1}{\mathrm{Re}}\left(0, \tau_{xy}, \tau_{yy}, \tau_{yz}, u\tau_{xy} + v\tau_{yy} + w\tau_{yz} + q_y\right)^T, \\
\mathbf{H}^v &= \frac{1}{\mathrm{Re}}\left(0, \tau_{xz}, \tau_{yz}, \tau_{zz}, u\tau_{xz} + v\tau_{yz} + w\tau_{zz} + q_z\right)^T.
\end{aligned} \tag{2.13}$$

where the term τ_{ij} represents the viscous stress tensor and q_i the heat flux vector. S is the source term. In most calculations, this term is set to 0, however, for rotors in axial flight configuration, a fixed grid approach is used and a source term is then added. A description of how this is done is presented in Section 2.4.

Although the Navier-Stokes equations completely describe turbulent flows, the large number of temporal and spatial turbulent scales associated with high Reynolds numbers make it difficult to resolve all the turbulent scales computationally. In such circumstances, the number of turbulent scales are reduced by time averaging the Navier-Stokes equations to give the Reynolds-Averaged Navier-Stokes equations (RANS).

This results in additional unknowns (called Reynolds stresses) which must be modelled. The viscous stress tensor mentioned in Equation (2.13) is then approximated by Boussinesq's hypothesis [20].

2.2 Turbulence modelling

In the present PhD thesis, RANS (Reynolds Averaged Navier-Stokes) and URANS computations were performed. In RANS, all the scales are modelled and this method has the limitation of being too diffusive if the grid employed is not fine enough. LES is also popular in the literature; it is based on filtering the scales larger than the grid cells and modelling the smaller ones with a sub-grid model. For a proper use of the LES method, however, both the grid and the time-step sizes should be very small, otherwise all the scales will be modelled instead of being resolved. LES leads to very expensive computations.

The $k-\omega$ turbulence model by Wilcox [163] was employed in most of the cases, due to its stability and the presence of attached flow on the blades for most of the studied wind speed cases. Spalart-Allmaras [143] turbulence model and variations to the $k-\omega$ model were employed in a sensitivity study presented in Chapter 5. This includes Menter's $k-\omega$ BSL [95] and $k-\omega$ SST [95], which consists of a hybridisation of the $k-\omega$ model with the $k-\varepsilon$ model.

Turbulence transport equations used in the formulation of the $k-\omega$ models are given by the following.

$$\frac{\partial}{\partial t}(\rho k)+\frac{\partial}{\partial x_j}(\rho U_j k) = \frac{\partial}{\partial x_j}\left[\left(\mu+\frac{\mu_t}{\sigma_k}\right)\frac{\partial k}{\partial x_j}\right]+\rho\left(P_k-\beta^*\omega k\right) \tag{2.14}$$

$$\frac{\partial}{\partial t}(\rho \omega)+\frac{\partial}{\partial x_j}(\rho U_j \omega) = \frac{\partial}{\partial x_j}\left[\left(\mu+\frac{\mu_t}{\sigma_\omega}\right)\frac{\partial \omega}{\partial x_j}\right]+\rho\left(\frac{\alpha}{\nu_t}P_\omega-\frac{\beta}{\beta^*\omega^2}\right)+\rho S_l \tag{2.15}$$

In the transport equation for k and ω above, the production of turbulence, P_k, and the dissipation rate specific to k , P_ω, is defined by

$$P_k=\tau_{ij}^R\frac{\partial u_i}{\partial x_j}, \qquad P_\omega=\rho\frac{\alpha}{\nu_t}P_k. \tag{2.16}$$

The SST model places an additional vorticity-dependent limiter on the shear stress and uses a slightly different value of σ_k.

In cases where stalled flow was expected, Menter's Scale-Adaptative Simulation [38, 96] was employed. SAS was introduced as a modification to the SST-RANS model [95] and is based on the use of a

second mechanical scale (in the form of second derivatives of velocity) in the source terms of the underlying turbulence model. Hence, an additional term Q_{SAS} is added in the transport equation for the specific dissipation rate ω (Equation (2.15)),

$$Q_{SAS} = max\left[\rho\zeta_2\kappa S^2\left(\frac{l}{l_{vK}}\right) - C\frac{2\rho k}{\sigma_\Phi} max\left(\frac{|\nabla\omega|^2}{\omega^2}, \frac{|\nabla k|^2}{k^2}\right), 0\right], \tag{2.17}$$

where l is the length scale and l_{vK} is the von Karman length scale in classic boundary layer definition,

$$l = \frac{\sqrt{k}}{c_\mu^{1/4}\omega}, \tag{2.18}$$

$$l_{vK} = \kappa\frac{U'(y)}{U''(y)}, \tag{2.19}$$

and the constants $\zeta_2 = 3.51$, $\sigma_\Phi = 2/3$ and $C = 2$.

SAS is a hybrid RANS/LES model which can produce spectral content for unstable flows, adjusting the turbulence length scale to the local flow inhomogeneities and balancing the contributions of modelled and resolved parts of the turbulent stresses. For stationary flows, it acts as a RANS model and for flows with transient instabilities like those with massive separation, the model reduces its eddy viscosity according to the locally resolved vortex size represented by the von Karman length scale. The SAS model can resolve the turbulent spectrum down to the grid limit and avoids RANS-typical single-mode vortex structure.

2.3 Numerical method

The Navier-Stokes (NS) equations are discretised using a cell-centred finite volume approach. The computational domain is divided into a finite number of non-overlapping control-volumes, and the governing equations are applied in integral-conservation form at each cell. The spatial discretisation of the NS equations leads to a set of ordinary differential equations in time,

$$\frac{d}{dt}(\mathbf{W}_{i,j,k}V_{i,j,k}) = -\mathbf{R}_{i,j,k}(\mathbf{W}) \tag{2.20}$$

where i, j, k represent spatial components. Note that no transformation into a cartesian domain is done and the governing equations are solved in the i, j, k spatial domain. $\mathbf{W}$ and $\mathbf{R}$ are the vectors of the cell conserved variables and residuals, respectively. Osher's [106] upwind scheme is used to discretise the convective terms

and MUSCL [159] variable interpolation is used to provide higher order accuracy. The Van Albada limiter [157] is used to prevent the oscillations near large changes of gradients, like shocks.

Using a fully implicit time discretisation and approximating the time derivative by a second order backward difference, Equation (2.20) becomes

$$\mathbf{R}^*{}_{i,j,k} = \frac{3V_{i,j,k}^{n+1}\mathbf{W}_{i,j,k}^{n+1} - 4V_{i,j,k}^{n}\mathbf{W}_{i,j,k}^{n} + V_{i,j,k}^{n-1}\mathbf{W}_{i,j,k}^{n-1}}{2\Delta t} + \mathbf{R}_{i,j,k}(\mathbf{W}^{n+1}) = \mathbf{0}. \tag{2.21}$$

Equation (2.21) is non-linear in $\mathbf{W}_{i,j,k}^{n+1}$ and cannot be solved analytically. This equation is defined to be the unsteady residual $\mathbf{R}^*{}_{i,j,k}$. Following the original implicit dual-time approach introduced by Jameson [66], Equation (2.21) is solved by iteration in pseudo-time t^*. This permits the acceleration techniques of steady state flow solvers to be used to obtain the updated solution and allows the real time step to be chosen based on accuracy requirements and without stability restrictions. Using an implicit time discretisation on the pseudo-time t^*,

$$\frac{\mathbf{W}_{i,j,k}^{m+1} - \mathbf{W}_{i,j,k}^{m}}{\Delta t^*} = -\frac{1}{V_{i,j,k}}\mathbf{R}^*{}_{i,j,k}(\mathbf{W}_{i,j,k}^{m+1}), \tag{2.22}$$

where the superscript $m+1$ denotes the time level $(m+1)\Delta t^*$ in pseudo-time. In Equation (2.22) the flux residual on the right hand side is evaluated at the new time level $m+1$ and is therefore expressed in terms of the unknown solution at this new time level. The unsteady flux residual $\mathbf{R}_{i,j,k}(\mathbf{W}_{i,j,k}^{m+1})$ is linearised in the pseudo-time variable t^* as follows,

$$\begin{aligned}
\mathbf{R}^*{}_{i,j,k}\left(\mathbf{W}^{m+1}\right) &= \mathbf{R}^*{}_{i,j,k}\left(\mathbf{W}^{m}\right) + \frac{\partial \mathbf{R}^*{}_{i,j,k}}{\partial t^*}\Delta t^* + O(\Delta t^{*2}) \\
&\approx \mathbf{R}^*{}_{i,j,k}\left(\mathbf{W}^{m}\right) + \frac{\partial \mathbf{R}^*{}_{i,j,k}}{\partial \mathbf{W}_{i,j,k}}\frac{\partial \mathbf{W}_{i,j,k}}{\partial t^*}\Delta t^* \\
&\approx \mathbf{R}^*{}_{i,j,k}\left(\mathbf{W}^{m}\right) + \frac{\partial \mathbf{R}^*{}_{i,j,k}}{\partial \mathbf{W}_{i,j,k}}\Delta \mathbf{W}_{i,j,k},
\end{aligned} \tag{2.23}$$

where $\Delta \mathbf{W}_{i,j,k} = \mathbf{W}_{i,j,k}^{m+1} - \mathbf{W}_{i,j,k}^{m}$. Using the definition of the unsteady residual,

$$\frac{\partial \mathbf{R}^*{}_{i,j,k}}{\partial \mathbf{W}_{i,j,k}} = \frac{\partial \mathbf{R}_{i,j,k}}{\partial \mathbf{W}_{i,j,k}} + \frac{3V_{i,j,k}}{2\Delta t}\mathbf{I}, \tag{2.24}$$

where $\mathbf{I}$ is the identity matrix. Substituting Equations (2.23) and (2.24) into Equation (2.22), and rewriting it in terms of the primitive variables $\mathbf{P}$, the fully implicit system to be solved is as follows,

$$\left[\left(\frac{V_{i,j,k}}{\Delta t^*} + \frac{3V_{i,j,k}}{2\Delta t}\right)\frac{\partial \mathbf{W}_{i,j,k}}{\partial \mathbf{P}_{i,j,k}} + \frac{\partial \mathbf{R}_{i,j,k}}{\partial \mathbf{P}_{i,j,k}}\right]\Delta \mathbf{P}_{i,j,k} = -\mathbf{R}^*{}_{i,j,k}(\mathbf{W}^{m}). \tag{2.25}$$

Note that the system is solved in the primitive variables formulation for simplicity and stability reasons.

The full system of equations, including the fluxes and the turbulence equations, are solved at once in a coupled manner. However, the contribution of the turbulence kinetic energy (k) is not included in the transport equation for energy, see Equations (2.6) and (2.7). As can be seen in Figure 2.1, good convergence behaviour is observed in the implicit method, for both fluxes and turbulence model.

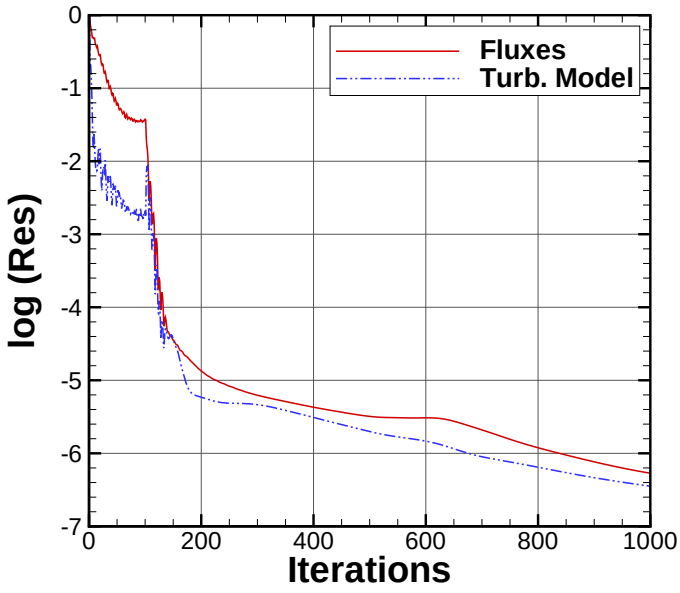

Figure 2.1: Convergence behaviour of the fluxes and turbulence model (k–ω), for a viscous NACA 0012 aerofoil case, at zero incidence angle.

2.3.1 Explicit scheme: four stage Runge-Kutta

As an explicit time-marching method, the four stage Runge-Kutta method (RK4) by Jameson *et al.* [67] is also available in HMB2. The iterative process is as follows,

$$\begin{aligned}
\mathbf{W}_i^0 &= \mathbf{W}_i^n \\
\mathbf{W}_i^1 &= \mathbf{W}_i^n - a_1 \Delta\tau \mathbf{R}_i(\mathbf{W}^0) \\
\mathbf{W}_i^2 &= \mathbf{W}_i^n - a_2 \Delta\tau \mathbf{R}_i(\mathbf{W}^1) \\
\mathbf{W}_i^3 &= \mathbf{W}_i^n - a_3 \Delta\tau \mathbf{R}_i(\mathbf{W}^2) \\
\mathbf{W}_i^{n+1} &= \mathbf{W}_i^n - \Delta\tau \mathbf{R}_i(\mathbf{W}^3)
\end{aligned} \tag{2.26}$$

Where $\mathbf{W}$ is the vector of conservative variables, n is the iteration number, $\Delta\tau$ denotes the local pseudo-time step, $\mathbf{R}_i$ is the residual in the ith stage and a is the weighting factor, whose value at each stage is $a_1 = 1/4$, $a_2 = 1/3$ and $a_3 = 1/2$. The local pseudo-time step ($\Delta\tau$) is computed at each cell of the domain as

$$\Delta\tau = \frac{CFL \cdot V_{i,j,k}}{|\overline{u}_n + c|}, \tag{2.27}$$

where the CFL number is constant in all the domain, $V_{i,j,k}$ is the cell volume and $|\overline{u}_n + c|$ is the acoustic wave speed.

Figure 2.2 shows a comparison of the convergence using this explicit scheme and the implicit one, for steady and pitching NACA 0012 aerofoil, at free-stream Mach number of 0.15. In both cases, a CFL of 1 is employed. For the steady computation (Figure 2.2 (a)), the RK4 scheme uses 300 more iterations than the implicit scheme. However, regarding the computational time, the former takes 24% less time. Nevertheless, one should bear in mind that the implicit scheme permits the use of much higher CFL (even a few hundreds for this case), which leads to much faster computations. Regarding the unsteady case (Figure 2.2 (b)), the number of iterations using the implicit method is reduced four times.

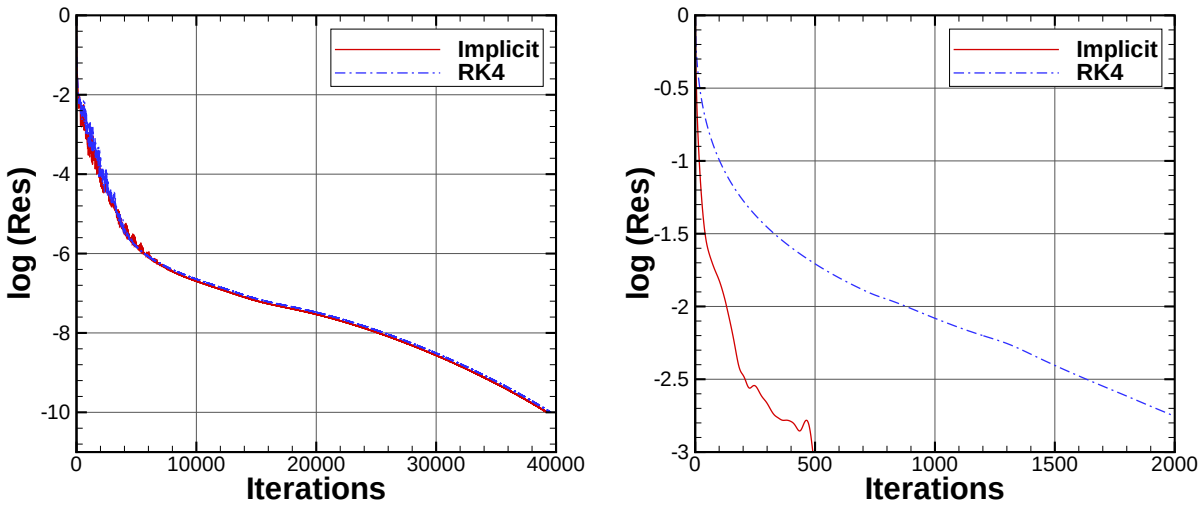

(a) Steady computation (76%). **(b)** Step 180 of unsteady computation (27.7%).

Figure 2.2: Comparison of the convergence behaviour between using the Osher's implicit and explicit (RK4) schemes, for (a) steady and (b) pitching NACA 0012 aerofoil at $M_\infty = 0.15$. In both cases, the CFL employed is 1.0. In parenthesis, percentage of CPU time that the RK4 takes, compared with the implicit one.

2.3.2 Flux evaluation: Roe's and Osher's Riemann solvers

At present, one of the most widely used approximate Riemann solver in the literature is Roe's [121]. In its definition, the fluxes are calculated by the sum of a convective and a dissipative term,

$$\mathbf{F}^{Roe}_{i+1/2} = \mathbf{F}^{Roe}_{c_{i+1/2}} + \mathbf{F}^{Roe}_{d_{i+1/2}} \tag{2.28}$$

The central or convective term is usually obtained by averaging the left and right states at each cell of the domain. On the other hand, the dissipation term is evaluated taking into account the matrix of eigenvalues, right and left eigenvectors at the cell interface, and the difference between right and left conservative variables.

$$\mathbf{F}^{Roe}_{i+1/2} = \frac{1}{2}(\mathbf{F}_i + \mathbf{F}_{i+1}) - \frac{1}{2}\mathbf{R}^{Roe}_{i+1/2}|\mathbf{\Lambda}^{Roe}_{i+1/2}|(\mathbf{R}^{Roe}_{i+1/2})^{-1}(\mathbf{W}_{i+1} - \mathbf{W}_i) \tag{2.29}$$

Osher's scheme [106] is also used in HMB2 and is continuously differentiable.

$$\mathbf{F}^{Osher}_{i+1/2} = \frac{1}{2}(\mathbf{F}_i + \mathbf{F}_{i+1}) + \frac{1}{2}\int_{\mathbf{W}_i}^{\mathbf{W}_{i+1}} |\mathbf{A}^{Osher}|(\mathbf{W})d\mathbf{W} \tag{2.30}$$

where the matrix,

$$|\mathbf{A}^{Osher}| = \mathbf{R}(\mathbf{W})\mathbf{\Lambda}^{-}(\mathbf{W})\mathbf{R}^{-1}(\mathbf{W}) - \mathbf{R}(\mathbf{W})\mathbf{\Lambda}^{+}(\mathbf{W})\mathbf{R}^{-1}(\mathbf{W}) \tag{2.31}$$

where $\mathbf{\Lambda}^{-}$ and $\mathbf{\Lambda}^{+}$ the matrices of negative and positive eigen values, respectively.

2.3.3 Variable extrapolation - MUSCL

The Monotone Upstream-Centred Scheme for Conservation Laws (MUSCL) was introduced by Van Leer [159]. It is a compact scheme which is used to discretise the convective part of the Navier-Stokes equations. In one dimension using a uniform spacing, the extrapolation to both sides of the face at $i+1/2$ is

$$\mathbf{F}^{L}_{i+1/2} = \mathbf{F}_i + \frac{\phi(r_i)}{4}\left[(1-\chi)\Delta_{-}\mathbf{F}_i + (1+\chi)\Delta_{+}\mathbf{F}_i\right] \tag{2.32}$$

$$\mathbf{F}^{R}_{i+1/2} = \mathbf{F}_{i+1} - \frac{\phi(r_{i+1})}{4}\left[(1-\chi)\Delta_{+}\mathbf{F}_{i+1} + (1+\chi)\Delta_{-}\mathbf{F}_{i+1}\right] \tag{2.33}$$

where $\Delta_{+}\mathbf{F}_i = \mathbf{F}_{i+1} - \mathbf{F}_i$, $\Delta_{-}\mathbf{F}_i = \mathbf{F}_i - \mathbf{F}_{i-1}$, $\phi(r_i)$ is the limiter and $r_i = \Delta_{-}\mathbf{F}_i/\Delta_{+}\mathbf{F}_i$. If $\phi(r_i) = 0$ then this is only a first order scheme but if $\phi(r_i) = 1$ then higher order schemes are activated which are at least second order for all values of χ.

The current scheme in HMB2 uses the alternative form of the van Albada limiter [157] namely

$$\phi(r) = \frac{2r}{r^2+1} \tag{2.34}$$

it should be noted that this limiter is not second order TVD since for any $r \in (1,2)$, $\phi(r) < 1$. Then value of χ is set to zero giving the final formulation

$$\mathbf{F}^L_{i+1/2} = \mathbf{F}_i + \frac{\Delta_-\mathbf{F}_i\Delta_+\mathbf{F}_i}{2(\Delta_+\mathbf{F}_i^2+\Delta_-\mathbf{F}_i^2)}\left[\Delta_-\mathbf{F}_i+\Delta_+\mathbf{F}_i\right]. \tag{2.35}$$

2.3.4 Jacobian Formulation

For a block-structured mesh, Equation (2.25) represents a large, sparse matrix which arises from the implicit discretisation in pseudo-time. The Jacobian matrix is calculated analytically by repeated application of the chain rule. The residual for one cell is built up as a summation of the fluxes through the cell faces. Considering the inviscid part of the residual of the cell face, denoted by $F_{i+1/2}$, and following the usual approach for Riemann solvers,

$$\mathbf{F}_{i+1/2} = \mathbf{F}_{i+1/2}(\mathbf{P}_l, \mathbf{P}_r) \tag{2.36}$$

where $\mathbf{P}_l$ and $\mathbf{P}_r$ are the left and right states of the Riemann problem. Applying MUSCL interpolation, both states are $\mathbf{P}_l = \mathbf{P}_l(\mathbf{P}_{i-1}, \mathbf{P}_i, \mathbf{P}_{i+1})$ and $\mathbf{P}_r = \mathbf{P}_r(\mathbf{P}_i, \mathbf{P}_{i+}, \mathbf{P}_{i+2})$, respectively. $\mathbf{F}_{i-1/2}$ is then computed using Osher's [106] or Roe's [121] approximate Riemann solvers.

For the cell face $i+1/2$ there are four contributions to the Jacobian matrix arising from

$$\frac{\partial \mathbf{F}_i}{\partial \mathbf{P}_{i-1}}, \quad \frac{\partial \mathbf{F}_i}{\partial \mathbf{P}_{i+1}}, \quad \frac{\partial \mathbf{F}_i}{\partial \mathbf{P}_i}, \quad \frac{\partial \mathbf{F}_i}{\partial \mathbf{P}_{i+2}}. \tag{2.37}$$

To avoid ill-conditioning the exact Jacobian matrix, is approximated by removing the dependence in the MUSCL interpolation. Therefore, a first order Jacobian is employed, which is very important with respect to parallelisation, as mentioned in Section 2.5.

$$\frac{\partial \mathbf{F}_i}{\partial \mathbf{P}_{i-1}} \approx \mathbf{0}; \quad \frac{\partial \mathbf{F}_i}{\partial \mathbf{P}_i} \approx \frac{\partial \mathbf{F}_i}{\partial \mathbf{P}_l}; \quad \frac{\partial \mathbf{F}_i}{\partial \mathbf{P}_{i+1}} \approx \frac{\partial \mathbf{F}_i}{\partial \mathbf{P}_r}; \quad \frac{\partial \mathbf{F}_i}{\partial \mathbf{P}_{i+2}} \approx \mathbf{0}. \tag{2.38}$$

With this approximation the number of non-zero contributions arising from each flux calculation is reduced from four to two. This scheme is similar to calculating the exact Jacobian matrix for a first order

spatial discretisation, with the modification that the MUSCL interpolated values at the interface are used in the evaluation rather than the cell values that would be used for a first order spatial scheme. In fact these approximations are exact for a first order spatial discretisation where $\mathbf{P}_l = \mathbf{P}_i$ and $\mathbf{P}_r = \mathbf{P}_{i+1}$.

The Jacobian matrix is sparse and, assuming the connectivity of the mesh does not change, its sparsity pattern is fixed. For an approximate first order spatial discretisation in 3D, there are 7 non zero blocks for each cell residual. Which columns these 7 blocks are in for any given row depends on the numbering scheme used, but in the current kij ordering in HMB2 a general row of the matrix looks like

$$\left[.,\frac{\partial R_{i,j,k}}{\partial P_{i,j,k-1}},...,\frac{\partial R_{i,j,k}}{\partial P_{i-1,j,k}},...,\frac{\partial R_{i,j,k}}{\partial P_{i,j-1,k}},\frac{\partial R_{i,j,k}}{\partial P_{i,j,k}}+\left(\frac{V_{i,j,k}}{\Delta t^*}+\frac{3V_{i,j,k}}{2\Delta t}\right)\frac{W_{i,j,k}}{\partial P_{i,j,k}},\frac{\partial R_{i,j,k}}{\partial P_{i,j+1,k}},...,\frac{\partial R_{i,j,k}}{\partial P_{i+1,j,k}},...,\frac{\partial R_{i,j,k}}{\partial P_{i,j,k+1}},.\right]$$

This shows the effect of the time-step on the Jacobian matrix. As Δt is increased, which means having a larger CFL number, the matrix becomes less diagonally dominant and hence harder to solve.

It is highly desirable not to expand this non-zero pattern when adding in the viscous terms to the Jacobian. For viscous fluxes, the gradients are required at the centre of the cell faces. Consider the two dimensional case in Figure 2.3. The gradient at P is calculated by integrating around the dashed volume using the mid point rule. The values at A and B are cell centre values while U and L are interpolated from the 4 neighbouring points. This would lead to a 9 point stencil for the viscous terms in two dimensions and a 19 point stencil for the viscous terms in three dimensions. To overcome the enlarging of the sparsity pattern of the Jacobian, a thin shear layer type approximation is used when forming the Jacobian terms. Hence, only the contributions from cell centres A and B are added into the Jacobian and the terms from C,D,E and F are ignored.

2.4 Axial flow formulation

Assuming that the wake shed from the rotor is steady, the flow around a rotor of a wind turbine can be treated as a steady-state problem. Likewise, periodicity of the flow in the azimuthal direction can be used to reduce the computational expense, since the grid can be reduced from an n-bladed rotor domain to a $1/n$ single-blade domain. In HMB2, the grid is not rotating and a non-inertial frame of reference is used to account for the blade motion. Both centripetal and Coriolis acceleration terms in the momentum equations

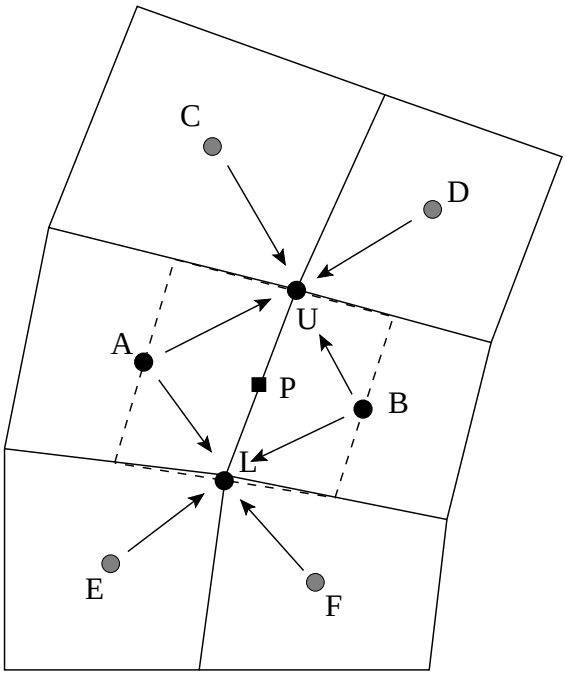

Figure 2.3: Calculation of the gradient at the mid point of the edge/face (*P*).

are accounted for by adding a mesh velocity ($\boldsymbol{u_{ref}}$) in the formulation of the Navier-Stokes equations, which corresponds to the mesh rotation in the direction of the rotor,

$$\boldsymbol{u_{ref}} = \omega \times \boldsymbol{r}, \tag{2.39}$$

where $\boldsymbol{\omega}$ is the rotation speed and $\boldsymbol{r}$ is the position vector of each cell. However, the addition of $\boldsymbol{u_{ref}}$ in the system of equations only adds a partial contribution of Coriolis. To have its full contribution, a source term for the momentum equations ($\boldsymbol{S}$) is therefore introduced,

$$\boldsymbol{S} = [0, -\rho\boldsymbol{\omega} \times \boldsymbol{u_h}, 0]^T, \tag{2.40}$$

where $\boldsymbol{\omega}$ is the rotation vector and $\boldsymbol{u_h}$ is the local velocity field in the rotor-fixed frame of reference.

By changing the velocities, the turbulence model is also modified and therefore is consistent with this steady-flow formulation. However, the extra source term added in the momentum equations is not considered. Further details on the implementation and validation of the axial flow are given in Ref.[112].

2.5 Parallel flow solver

There are two main advantages in using a first order approximate Jacobian when it comes to the parallel implementation. Firstly, only one row of halo cells is required for a matrix-vector multiplication. Additionally, due to the approximations made (Equation (2.38)) completing the matrix-vector multiplication is carried out at a lower level of precision compared to the residual evaluation. That is, while in the residuals double precision is employed, in the matrix-vector multiplication single precision is used. This reduces the amount of communication bandwidth needed by a factor of 4.

The BILU(k) preconditioner [8] is not amenable to parallelisation due to its sequentiality. This was partially overcome in Ref. [9] by preconditioning on the block sub-domains which were the same as the blocks in the multi-block grid. The drawback of this method is that as the number of sub-domains increases the resulting preconditioner degrades the convergence of the linear system. This partitioning of all the blocks into sub-domains was carried out regardless of whether two blocks had a common face on the same processor. A new idea is put forward here that groups all the sub-domains on the current process together and hence is independent of the number of blocks used to create a given sub-domain. This does introduce one obvious complication when considering parallel performance: for a fixed mesh, as the number of processors is increased the size of the sub-domains is reduced, since the same number is retained, which potentially reduces the effectiveness of the preconditioner. When there is a large number of blocks and a low number of parallel cores, it then becomes important how the partition of blocks is done, not only from the communication side of the matrix vector multiplication but also the effectiveness of the preconditioner.

2.5.1 Renumbering the final matrix

The sparse matrix vector product $A\mathbf{x} = \mathbf{y}$ is one of the major kernel operations of a Krylov subspace linear solver [39]. To perform this operation in parallel the vectors $\mathbf{x}$ and $\mathbf{y}$ as well as the matrix A must be distributed across processors. This distribution then has to be renumbered and three possible schemes are shown in Figure 2.4. The first scheme does not take boundary conditions into account. The second ordering numbers all the halo cells last so making the copying of halo data into the solution vector easier, since it requires no shifting. It does not however improve the parallel efficiently since cell 1 (in Figure 2.4) still requires

halo data to compute. The last method removes this problem by renumbering all the internal cells that can be updated without the communication from other processors first, $n_i = (1,2,\ldots,16)$, then numbers the boundary cells $n_b = (17,18,\ldots,25)$ followed lastly by the halo cells $n_h = (26,27,\ldots,36)$. It is now possible to do all the n_i updates without the need of halo data and so these calculations can overlap the communication of the halo data that is needed to compute the boundary terms. It should be noted that the numbering of the halo in the second and the third method are in fact the same. This means that exactly the same halo vector copy can be used for message passing during parallel execution. The default ordering in HMB2 is currently the second option since there is no communication/computation overlap. All three schemes are nonetheless available.

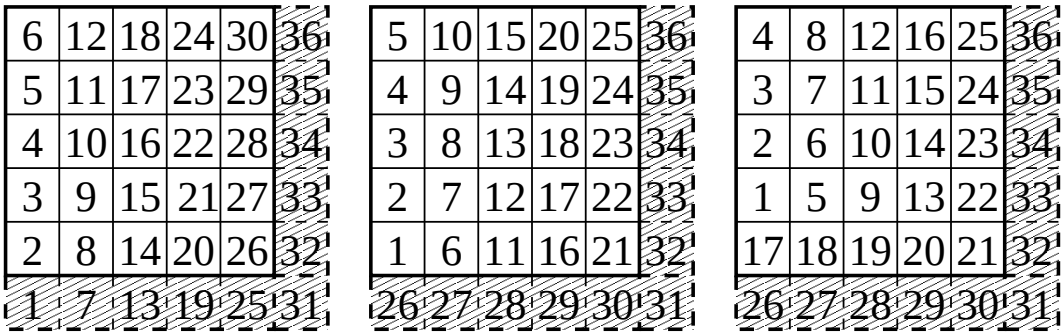

Figure 2.4: Three matrix renumbering methods. Left: No boundary conditions are taken into account, Centre: Halo cells are calculated last, Right: First internal cells are calculated, then the boundaries and finally the halo ones.

2.5.2 Scalability

Most computations undertaken in this work have been performed on the Beowulf cluster of Liverpool (Pentium 4 CH2). For very large grids, however, calculations were conducted on different HPC facilities. Firstly, the N8 HPC Facility 'Polaris' of Leeds University was used, where each CPU is composed by 8 cores of Intel@ Xeon E5-2670 type. The "Blue Joule" system of the Hartree HPC Centre of UK was also employed, where each processor rack contains 1,024 16-core, 64 bit, 1.60 GHz A2 PowerPC processors of IBM Blue Gene/Q type. For a single core job, the A2 process of BG/Q was found to be 8.5 times slower than the Intel@ Xeon process.

Figure 2.5 shows speedup curves of HMB2 with computations performed in the Blue Joule system, for grid sizes of 40 million and 1 billion (62,568 blocks) and using from 256 to 16,384 cores. As can be seen, for the smaller grid (Figure 2.5 (a)), excellent scaling is obtained. For the bigger case, a very good scaling is also achieved. Even though using 16,384 cores there was an imbalance between the maximum and minimum loaded nodes of 29.45%, a speedup of 3.5 was achieved, see Figure 2.5 (b).

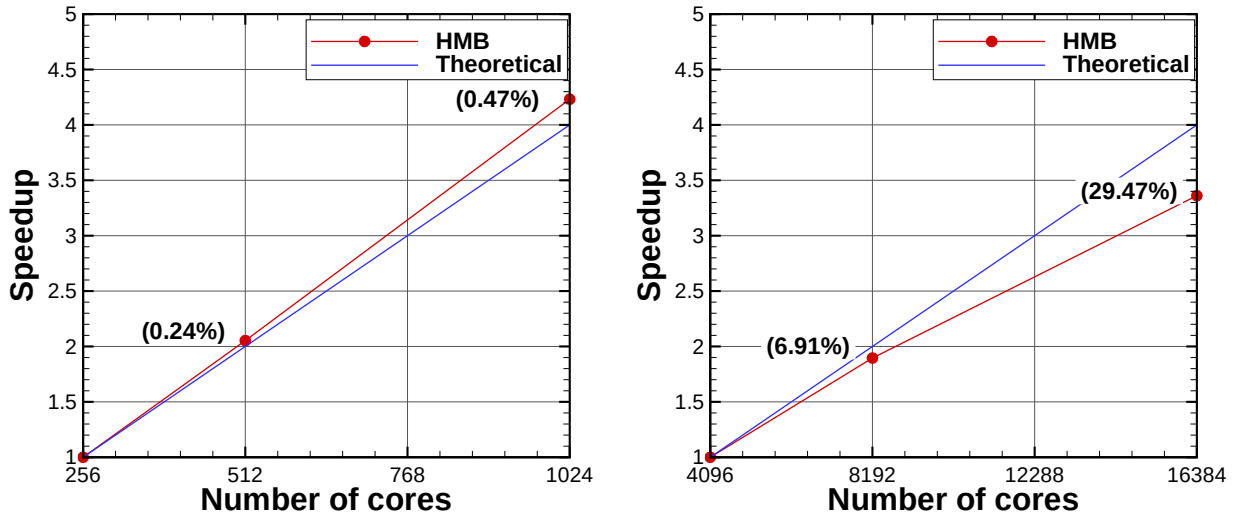

(a) 40 million cells. **(b)** 1 billion cells.

Figure 2.5: Speedup curves of HMB, employing a **(a)** 40 million and **(b)** 1 billion cells grids, with 62,568 blocks. The imbalance between the maximum and minimum loaded cores is included in parenthesis.

2.6 Mesh generation techniques

In HMB2, structured multi-block grids are employed, which are generated with ICEM-Hexa^{TM}of ANSYS [4]. Apart from fully matched grids, sliding planes and chimera meshes can be employed in HMB2. A description of these two methods is provided in the following sections.

2.6.1 Sliding planes method

The sliding plane algorithm enables the computation of grids where there is relative motion between components, like the case shown in Figure 2.6, where the rotor of the wind turbine rotates while the nacelle and tower are fixed.

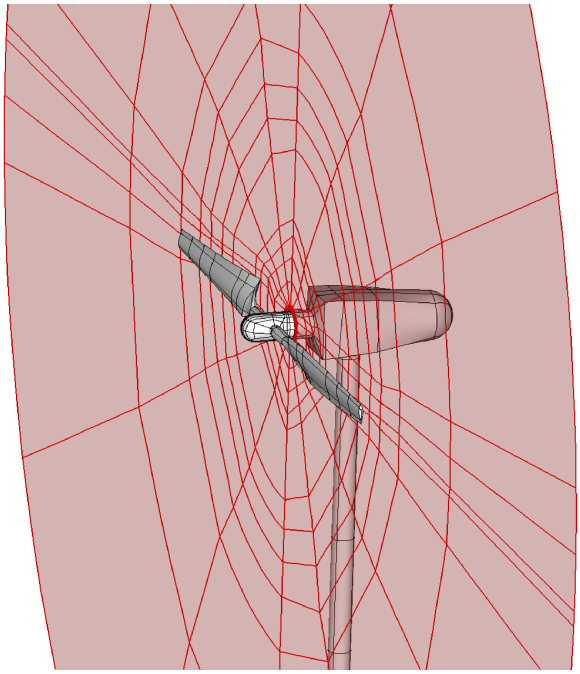

Figure 2.6: Sliding plane located between the rotor and the nacelle for the NREL Annex XX wind turbine.

The underlying idea behind the sliding-mesh approach and the implementation into HMB2 are explained in Ref.[144]. Figure 2.7 (a) shows the definition of two layers of halo cells around the boundary surface of each block, where the two adjacent blocks have non-matching cell faces. If the halo cells of each block are populated with interpolated values of the flow field variables, the solver will have no difficulty in updating the flow solution. The application of the sliding-plane algorithm to non-matching grids as well as grids in relative motion will result in non-matching cell faces as sketched in Figure 2.7 (a). For each pair of adjacent sliding planes, there are three main steps involved in populating the halo cells: i) identification of the neighbouring cells for each halo-cell, ii) interpolation of the solution at the centroids of the halo cells and iii) exchange of information between blocks associated with different processors. The last step is important for computations on distributed-memory machines only. Regardless of the identification and interpolation methods employed, the halo-cell values are computed using:

$$\phi_{halo} = \sum_{i=1}^{i=n} w_i \phi_i, \tag{2.41}$$

where ϕ represents any flow field variable, w_i is the weight associated with the ith neighbour of the halo cell and n is the number of neighbours.

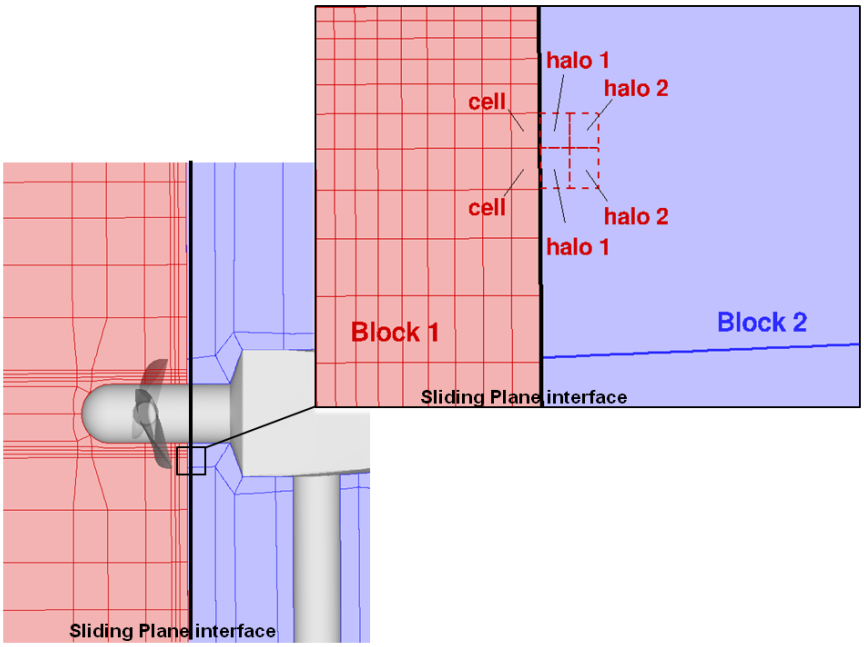

(a) Halo cells along the sliding plane interface.

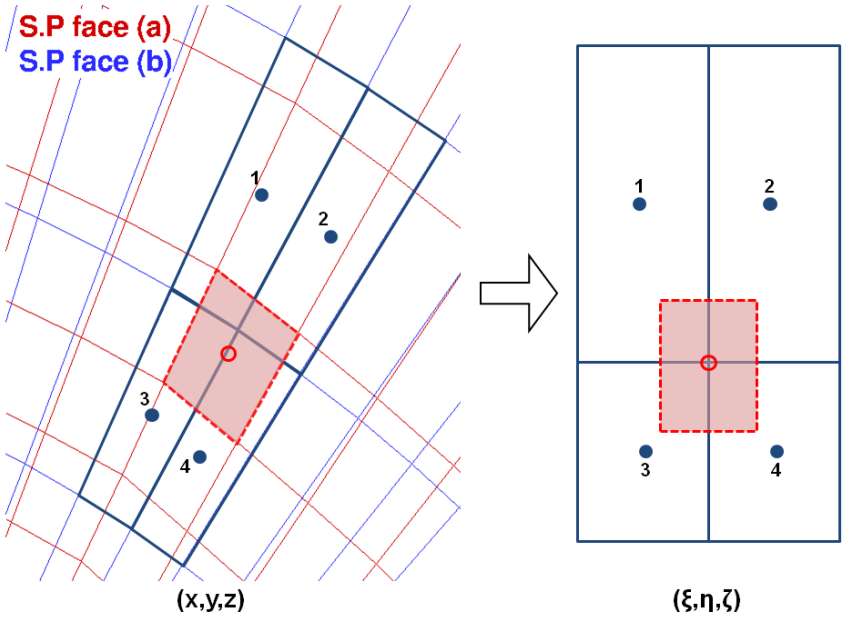

(b) Area-weighed interpolation.

Figure 2.7: Sliding plane interface with non-matching cell faces: **(a)** halo cells along the interface; **(b)** sketch of cell-area weighted interpolation.

The algorithm implemented in HMB2 is based on the cell-face overlap interpolation method presented in Figure 2.7 (b), where the weight of each neighbour is directly proportional to the fraction of the projected overlapping cell face area. Sliding-mesh interfaces can be of arbitrary shape and for this reason the contributing cell surfaces are projected on the curvilinear ξ, η, ζ axes as used in the solver. This step can be combined with a transformation from primitive to conservative variables so that flux-weighted summations can also be computed.

Two layers of halo cells are set for each cell on the sliding plane(s). For non-planar sliding interfaces, cells are projected on a plane before computing the area overlaps with their counterpart plane. The cell faces of the adjacent mesh that overlap are the neighbours. For each neighbour, the fraction of the overlap corresponds to the interpolation weight. The above procedure has been tested in validation test cases involving planar, cylindrical as well as spherical sliding plane interfaces. Also, the method has been implemented to handle an arbitrary number of sliding planes. This enables simulation of test cases at high level of geometric complexity.

2.6.2 Chimera method

The chimera method [69] is based on composite grids, consisting of independently generated, overlapping non-matching sub-domains. Each of these sub-domains is referred to as *Level* and they are sorted hierarchically, with higher levels having priority. The exchange of information between sub-domains is done by interpolation and following the level hierarchy. As an example, Figure 2.8 presents a three-level chimera grid for the MEXICO blade. *Level 0* covers the background domain; *Level 1* covers a small part of the computational domain for capturing the tip vortices; *Level 2* includes the grid around the blade. A view of how these three levels are combined is shown in Figure 2.8 (d).

To minimise the number of searches in the interpolation from one level to the other, a localisation procedure is carried out before the computation of the flow field starts. The localisation identifies the cells that require interpolated flow information from the grid they overlap with and provides interpolation weights for them. For this, approximate minimum volume bounding boxes (MVBBs) around each solid in the grid are constructed, based on the second moment of area matrix.

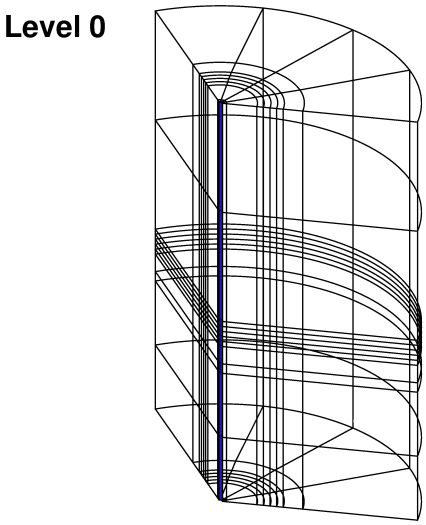

(a) Background (*Level 0*).

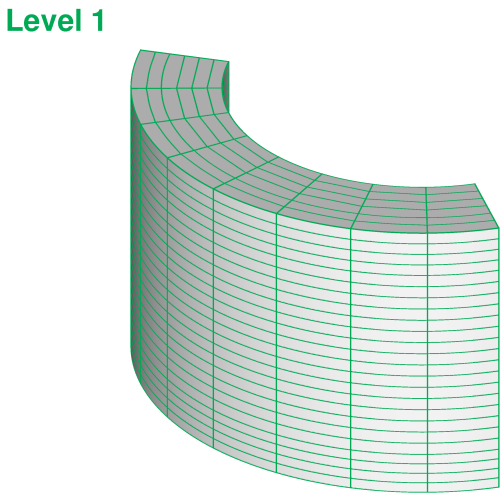

(b) Ring for vortex capture (*Level 1*).

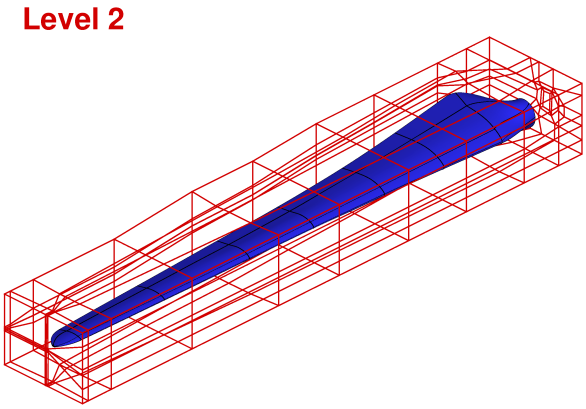

(c) Blade (*Level 2*).

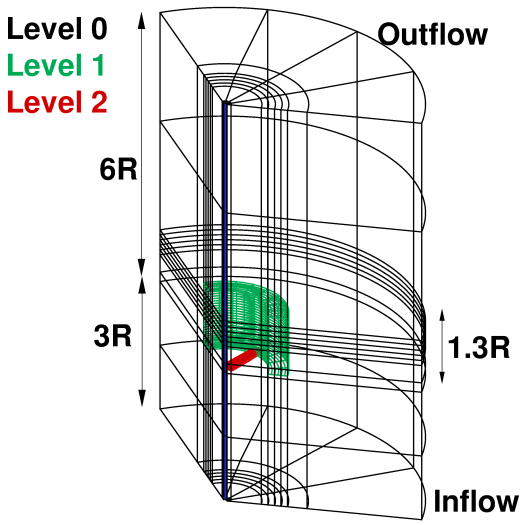

(d) View of all the combined sub-domains.

Figure 2.8: Chimera grid with three levels: **(a)** background grid, **(b)** ring for vortex capture, **(c)** grid around the blade. **(d)** View of all the combined sub-domains.

An overset mesh search (OMS) is then performed. By means of a range-tree algorithm, the points located inside the MVBB are identified and exact arithmetics library (EAL) is used to guarantee that any point can only be located in one cell of a level it is localised against. The cells are then classified in three groups:

- *holes*: do not need interpolation because overlap either with a hierarchically higher level cell or a solid,
- *interpolation cells*: those that require interpolated flow information from the grid they overlap,
- *normal or computational cells*: do not need any special treatment.

To illustrate this, Figure 2.9 (a) shows the localisation for *Level 0* (background). The computational cells are green; the red cells indicate the last layer of computational cells (the chimera fringe); and the yellow cells are the ones that need interpolated information. It should be mentioned that the interpolation cells are always flagged based on the viscous MUSCL stencil, regardless of the CFD model employed (inviscid or viscous). That is why there are two layers of interpolation cells in Figure 2.9. The holes are indicated in blue: light blue marks the holes overlapping with a higher level grid (the ring and the grid around the blade) and dark blue those intersecting solid parts (the surface of the blade). In a similar manner, the localisation is done for *Level 1* (ring), see Figure 2.9 (b).

Three interpolation methods are available in HMB2: zero order method, least square method and inverse distance method. In the first one, the nearest neighbours value are copied to the interpolation cell. The second method uses a quadratic polynomial for the interpolation. The latter considers a cloud of nearest points and assigns larger weights to those closer to the interpolation cell and it is the approach employed in this work. Further details of the method and its implementation in HMB2 are provided in Reference [69].

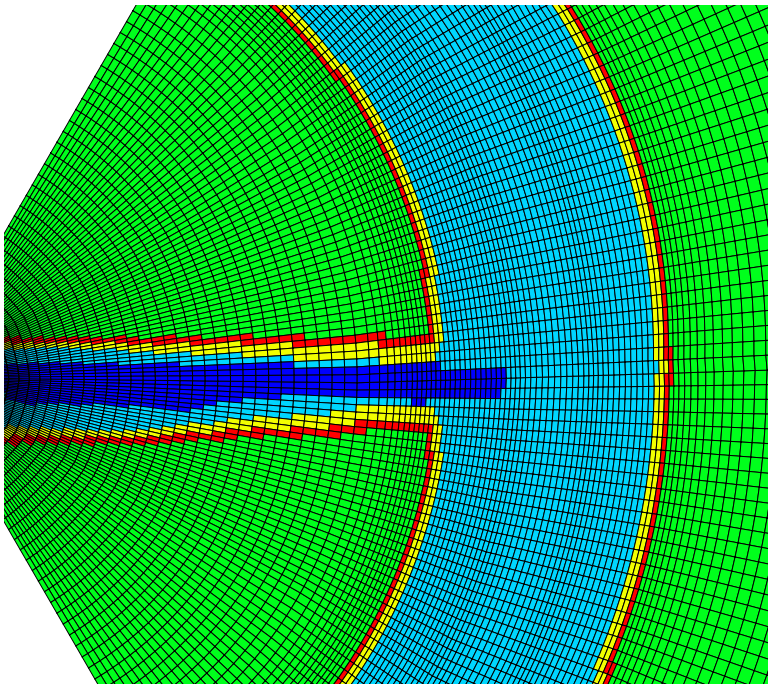

(a) Triple overlap background-ring-blade.

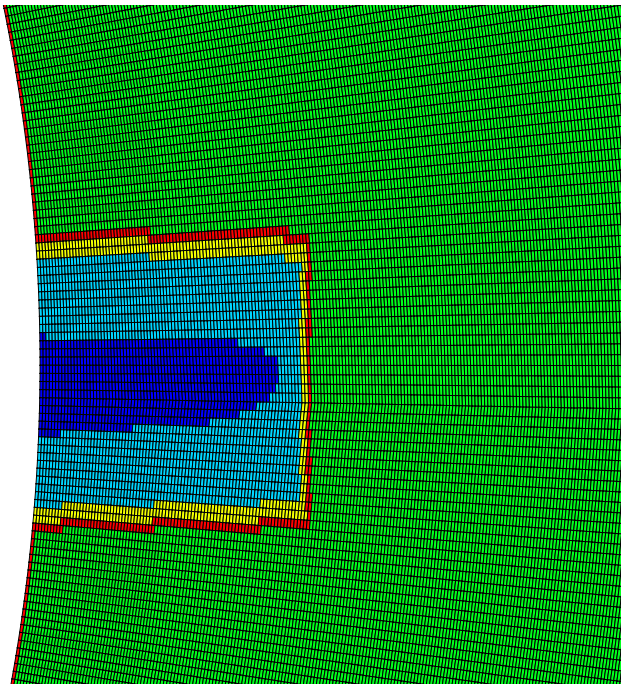

(b) Overlap between ring and blade.

Figure 2.9: Localisation for **(a)** *Level 0* (background) and **(b)** *Level 1* ring. In green, the normal cells; the red cells indicate the chimera fringe; the yellow cells are the ones that need interpolated information. In light blue, the cells overlapping with the ring and the grid around the blade and in dark blue those intersecting the surface of the blade.

2.7 CSD Solver

2.7.1 Blade structural model

Under the assumption that the blade structural properties are mainly distributed in the span-wise direction and that its span is much larger than its chord and aerofoil thickness, the blade can be modelled as a beam, where bending and torsion are coupled. In NASTRAN[27], the beam is divided into CBEAM-type elements, like the one presented in Figure 2.10, that contain PBEAM structural properties. Typically, the following properties are included in the blade's structural model:

- area of the beam cross section (A),
- chordwise (or edgewise) and flapwise area moment of inertia (I_1, I_2),
- torsional stiffness (J),
- linear mass distribution (dm),
- location of the shear centre compared to the actual node location ($\overrightarrow{w_a}$, $\overrightarrow{w_b}$) allows for the structural model to be located on the quarter chord line,
- mass centre position relative to the shear centre (y_{ma}, z_{ma}, y_{mb}, z_{mb}),
- neutral axis relative to the shear centre (y_{na}, z_{na}, y_{nb}, z_{nb}),
- radius of gyration (R_g).

All structural properties are defined at each end of the beam and, in between, linear variation is assumed. Inertial forces, centrifugal forces and an arbitrary loading could be introduced in the model using RFORCE and PLOAD entries, respectively. Likewise, a different material (MAT) for each CBEAM element could be employed. RBAR elements without any structural properties are connected to the CBEAM elements in the chordwise direction, which are used for interpolating the beam model deformation to the blade surface, which is then used for deforming the fluid grid.

In Chapter 7, the structural models for the MEXICO blade and the NREL Annex XX blade are provided.

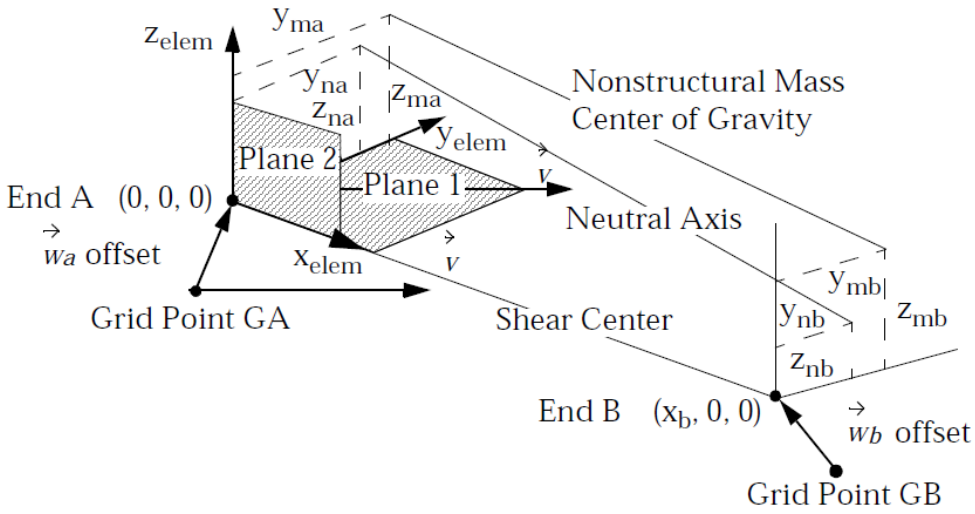

Figure 2.10: CBEAM-type element of NASTRAN, with PBEAM properties. Source: NASTRAN user's reference guide [27].

2.7.2 Static CFD-CSD method

To obtain the static deformations of the blade, a non-linear static analysis is performed with NASTRAN[27] (SOL 106), using the FEM model outlined in Section 2.7.1). The eigenvectors are extracted with the modified GIVens (MGIV) method [32]. This is followed by an iterative process allowing for the large displacements to be taken into account while recomputing the forces due to the aerodynamic loads and the centrifugal forces at each step.

For CFD/CSD exchange, the aerodynamic loads are first extracted from the fluid solution, using a sectional pressure integration, and are then used in NASTRAN (as PLOAD elements) to obtain the blade deflections. The blade is then deformed based on the structural shape using the method described in Section 2.7.4. This process is repeated until the shape of the blade and the aerodynamic loads converge to a final value, as described in Ref.[33]. Figure 2.11 (a) shows a diagram of this process.

2.7.3 Dynamic CFD-CSD method

For unsteady cases, a modal approach is followed. For this, the blade shape (ϕ) is expressed as a sum of eigenvectors (ϕ_i), which represent the blade displacements for each eigen-mode, multiplied by a modal

amplitude α_i,

$$\phi = \phi_0 + \sum_{i=1}^{n_m} \alpha_i \phi_i, \tag{2.42}$$

where ϕ_0 is the undeformed eigenvector. The differential equation for the modal amplitude is solved at each time step, integrated in time along with the time-integration of the N-S equations in the CFD solver.

$$\frac{\partial^2 \alpha_i}{\partial t^2} + 2\zeta_i \omega_i \frac{\partial \alpha_i}{\partial t} + \omega_i^2 \alpha_i = \mathbf{f}\phi_i, \tag{2.43}$$

whose derivatives are discretised as follows:

$$\left[\frac{\partial \alpha_i}{\partial t}\right]_t = \frac{3[\alpha_i]_t - 4[\alpha_i]_{t-1} + [\alpha_i]_{t-2}}{2\Delta t} \tag{2.44}$$

$$\left[\frac{\partial^2 \alpha_i}{\partial t^2}\right]_t = \frac{3[\frac{\partial \alpha_i}{\partial t}]_t - 4[\frac{\alpha_i}{\partial t}]_{t-1} + [\frac{\alpha_i}{\partial t}]_{t-2}}{2\Delta t}, \tag{2.45}$$

with $\mathbf{f}$ representing external forces, ω_i the eigen-frequencies, and ζ_i the damping coefficients. For stability purposes, the analysis is started with strong damping of $\zeta_i = 0.7$ for each mode, to damp the oscillations created by the sudden change in the forcing applied to the system. Once the blade reaches a level of deformation of 80-90%, usually after a half a revolution, the damping is brought back to smaller values (e.g. $\zeta_i = 0.03$) [32]. At each pseudo-time step of the employed dual time-step method, the modal amplitudes are computed by solving the discretised Equation (2.43), which results in Equation (2.46),

$$\begin{bmatrix} 2\zeta_i\omega_i + \frac{3}{2\Delta t} & \omega^2 \\ -1 & \frac{3}{2\Delta t} \end{bmatrix} \begin{pmatrix} [\frac{\partial \alpha_i}{\partial t}]_t \\ (\alpha_i)_t \end{pmatrix} = \begin{pmatrix} [f_i^s]_t + \frac{4[\frac{\partial \alpha_i}{\partial t}]_{t-1} - [\frac{\partial \alpha_i}{\partial t}]_{t-2}}{2\Delta t} \\ \frac{4[\alpha_i]_{t-1} - [\alpha_i]_{t-2}}{2\Delta t} \end{pmatrix}, \tag{2.46}$$

the CFD grid is deformed using the method described in Section 2.7.4 and the flow field updated by solving the N-S equations. At the end of each time step, the blade loads are extracted and re-applied to the system. This process is performed repeatedly until the end of the computation, see Figure 2.11 (b).

2.7.4 Mesh deformation

In both static and dynamic aeroelastic methods, the mesh deformation in HMB2 [34] is performed in three stages. The blade surface is first deformed using the Constant Volume Tetrahedron (CVT) method, which projects each fluid node (**F**) to the nearest structural triangular element (S_1, S_2, S_3), and moves it linearly

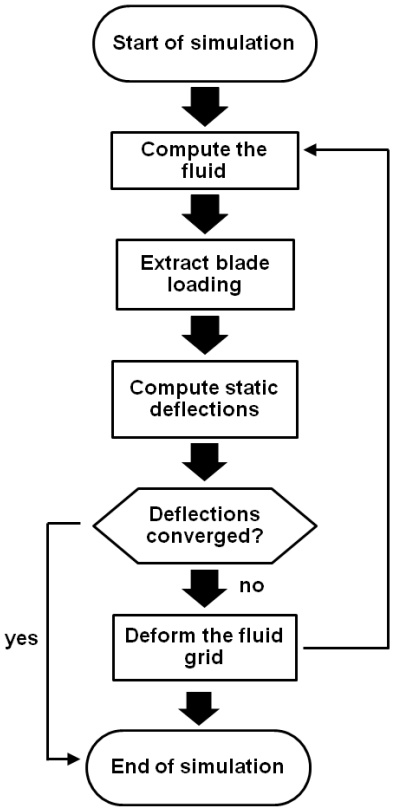

(a) Diagram of static CFD/CSD method.

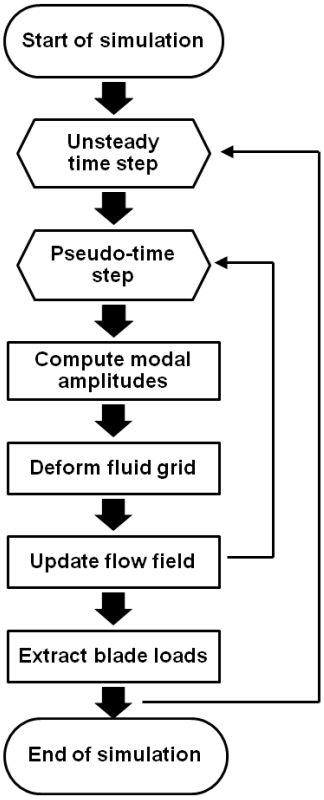

(b) Diagram of dynamic CFD/CSD method.

Figure 2.11: Diagram of the **(a)** static and **(b)** dynamic CFD/CSD coupled methods in HMB2 solver.

with the element, as shown in the shaded region of Figure 2.12. Hence, the initial location of a fluid element **c** is transformed to **c**′,

$$\mathbf{c} = \alpha\mathbf{a} + \beta\mathbf{b} + \gamma\mathbf{d} \rightarrow \mathbf{c}' = \alpha\mathbf{a}' + \beta\mathbf{b}' + \gamma\mathbf{d}', \tag{2.47}$$

where α, β and γ are coefficients that depend on the vectors **a**, **b** and **d** shown in Figure 2.13 (a).

The vertex positions are updated via the spring analogy method (SA). This method consists of adding springs along the sides and the diagonals of each block face of the mesh (dashed lines in Figures 2.12 and 2.13 (a)), which allows to preserve the quality of the mesh, avoiding large compression or dilatation of the block faces and imposing limits on their skewness. In addition, the stiffness of these springs is inversely proportional to their length, except for the ones in contact with the blade, which are stiffer in order to make the blocks close to the blade surface more rigid (first layer of blocks in Figure 2.13 (a)).

Finally, the full mesh is generated via Transfinite Interpolation (TFI). For this, the block faces are

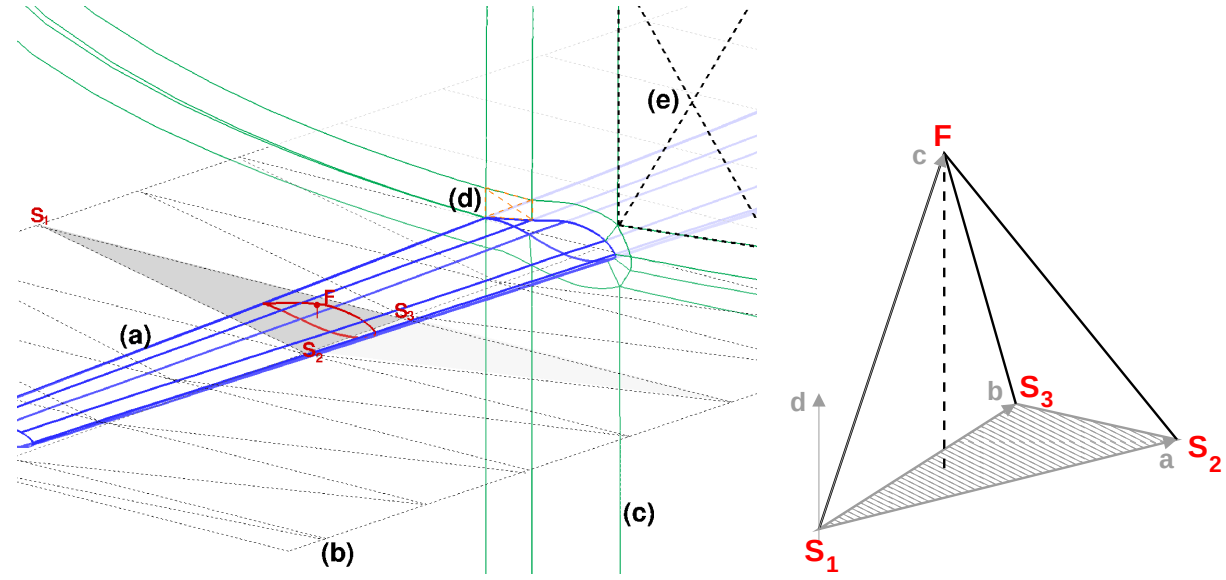

Figure 2.12: Projection of the fluid grid on the structural model through Constant Volume Tetrahedron (CVT). **(a)** Blade shape, **(b)** Blade structural model, **(c)** block boundaries of the fluid grid, **(d)** springs for the Spring Analogy (SA) in contact with the blade, **(e)** springs for the Spring Analogy (SA) not in contact with the blade.

interpolated from the edge deformations, which in turn are used for the interpolation of the full blocks. A weighted approach is employed to interpolate a face/block from the boundary vertices/surfaces, respectively. The weight depends on the curvilinear coordinate divided by the length of the curve, whose notation is shown in Figure 2.13 (b). Following the notation on Figure 2.13 (b), the generation of the mesh on a block face, x_1, x_2, x_3 and x_4, can be expressed as:

$$dx(\xi,\eta) = f_1(\xi,\eta) + \phi_1^0(\eta)\big[dx_1(\xi) - f_1(\xi,0)\big] + \phi_2^0(\eta)\big[dx_3(\xi) - f_1(\xi,1)\big], \tag{2.48}$$

where f_1 is defined as,

$$f_1(\xi,\eta) = \psi_1^0(\xi)dx_4(\eta) + \psi_2^0(\xi)dx_2(\eta) \tag{2.49}$$

with dx_1, dx_2, dx_3 and dx_4, representing the displacements of the four corners of a face and ϕ and ψ the blending functions in the η and ξ directions.

The method is further described in reference [37], and uses the properties of multi-block meshes to maintain its efficiency as the number of blocks increases, particularly in the spanwise blade direction. It provides flexibility and allows for complex multi-block topologies to be used with good control over the distribution of mesh deformation all over the computational domain.

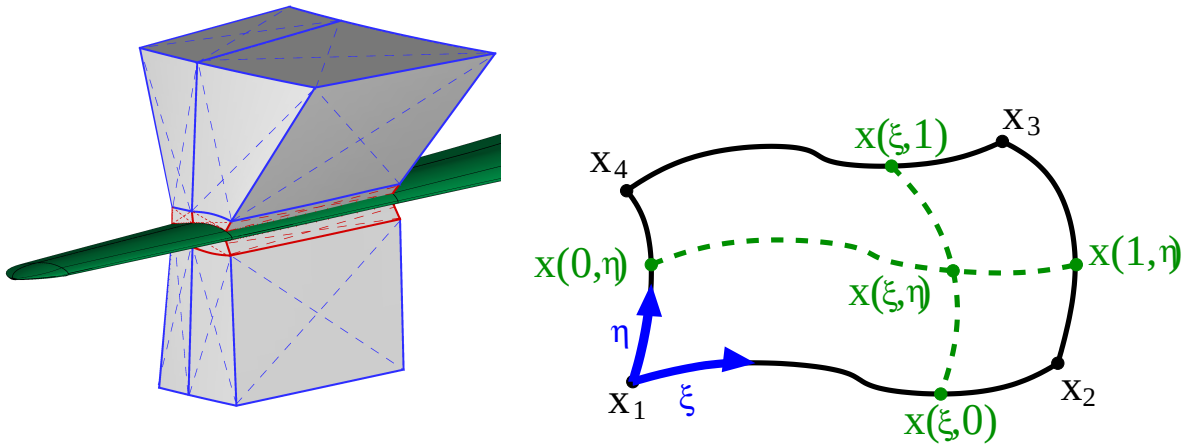

(a) Spring Analogy. **(b)** Notation of a block face for TFI.

Figure 2.13: **(a)** Spring Analogy (SA) to obtain the updated block vertex positions. The springs are on the block sides and the surface diagonals. **(b)** Transfinite Interpolation (TFI) for full mesh generation.

This method preserves the quality of the mesh, avoiding, high cell skewness and drastic change of cell volumes. Figure 2.14 shows the changes on the cell volumes and skewness, as a ratio between the deformed grid and the undeformed one at the tip of the blade ($r_{vol_i} = \frac{vol_{i_{def.}}}{vol_{i_{undef.}}}$ and $r_{Skew_i} = \frac{Skew_{i_{def.}}}{Skew_{i_{undef.}}}$, respectively). For the skewness, the maximum norm of the scalar product of the vectors normal to the surfaces was selected.

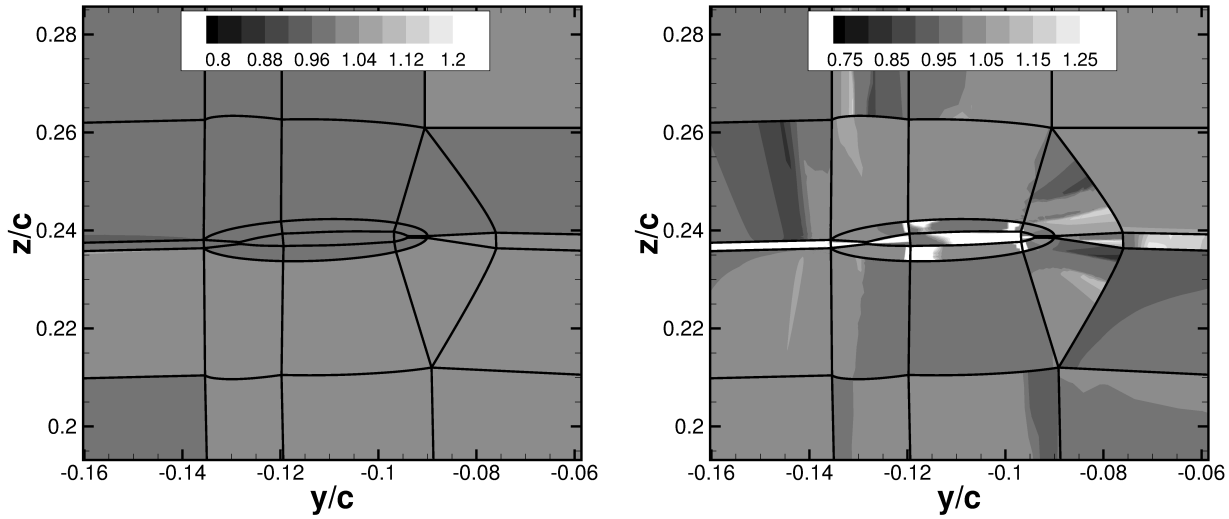

(a) Cell volume ratio. **(b)** Cell skewness ratio.

Figure 2.14: **(a)** Cell volume ratio (r_{vol_i}) and **(b)** cell skewness ratio (r_{Skew_i}) between deformed and undeformed at the tip of the MEXICO blade.

The aeroelastic method described in these paragraphs is employed for computations in Chapter 7.

Chapter 3

All-Mach Roe-type Methods [1]

In this chapter, the low-Mach problem is illustrated with a 2D example. In addition, details of the implementation of all-Mach Roe-type schemes into HMB2 are given, including the explicit implementation (fluxes) and the implicit part (Jacobians).

3.1 Low-Mach problem

Numerical schemes designed for solving the compressible Navier-Stokes equations face a number of problems as the reference Mach number tends to zero. As reported in Refs. [117] and [52], there is a loss of accuracy due to numerical diffusion (artificial viscosity) which is proportional to $O(1/M)$. Likewise, the presence of round-off errors related to the difference of magnitude between the pressure ($O(1)$) and the pressure variations of order $O(M^2)$. The problem of stiffness is due to the disparity between the convective ($|u_n|$) and acoustic ($|u_n + c|$ and $|u_n - c|$) wave speeds at low-speed flows.

Theoretical analysis of the behaviour of upwind schemes in this low-speed flows context was given in Refs. [117] and [52]. This section aims to analyse the problem of stiffness, since it is directly related to the change in magnitude of some of the terms of the Jacobian matrix. As an example, a grid with $1,024$ cells for the NACA 0012 aerofoil at zero incidence angle was computed at two free-stream Mach numbers (0.05

[1] The work presented in this chapter is published in M. Carrión *et al.* , Implementation of All-Mach Roe-type Schemes in Fully Implicit CFD Solvers - Demonstration for Wind Turbine Flows, *International Journal for Numerical Methods in Fluids*, vol. 73, num. 8, p 693-728, 2013.

and 0.005). For this 2D case, the Jacobian matrix for each contribution is simplified, having therefore a total of 16 terms, shown in Equation (3.1). If the Mach number is reduced by one order of magnitude, the terms between $\| \ \|$ decrease one order of magnitude, the ones between $\langle \ \rangle$ increase one order, and the terms in $\{ \ \}$ increase by 2 orders. The rest of the terms stay almost the same. This leads to a less diagonally-dominant Jacobian.

$$\left(\frac{\partial \mathbf{F}}{\partial \mathbf{P}}\right)_{\mathbf{O-Roe}} = \begin{pmatrix} \frac{\partial f_0}{\partial \rho} & \frac{\partial f_0}{\partial u} & \frac{\partial f_0}{\partial v} & \left\| \frac{\partial f_0}{\partial p} \right\| \\ \frac{\partial f_1}{\partial \rho} & \left\langle \frac{\partial f_1}{\partial u} \right\rangle & \left\langle \frac{\partial f_1}{\partial v} \right\rangle & \left\| \frac{\partial f_1}{\partial p} \right\| \\ \frac{\partial f_2}{\partial \rho} & \left\langle \frac{\partial f_2}{\partial u} \right\rangle & \left\langle \frac{\partial f_2}{\partial v} \right\rangle & \frac{\partial f_2}{\partial p} \\ \frac{\partial f_4}{\partial \rho} & \left\{ \frac{\partial f_4}{\partial u} \right\} & \left\{ \frac{\partial f_4}{\partial v} \right\} & \left\langle \frac{\partial f_4}{\partial p} \right\rangle \end{pmatrix} \tag{3.1}$$

The eigenvalues for $M_\infty = 0.05$ and $M_\infty = 0.005$ are shown in the eigenspace of Figure 3.1. Note that these eigenvalues correspond to this 2D case and are obtained before the Jacobian matrix is scaled with the CFL number. The real part determines the speed in which the solution changes, while the imaginary part represents the oscillatory nature of the solution. The effect of decreasing the Mach number by one order of magnitude is seen in the increasing of the order of magnitude of the majority of eigenvalues; however, some of them stay almost the same, being independent of the Mach number. All of them have negative sign in the real part, being the largest real value of -0.125 for both cases.

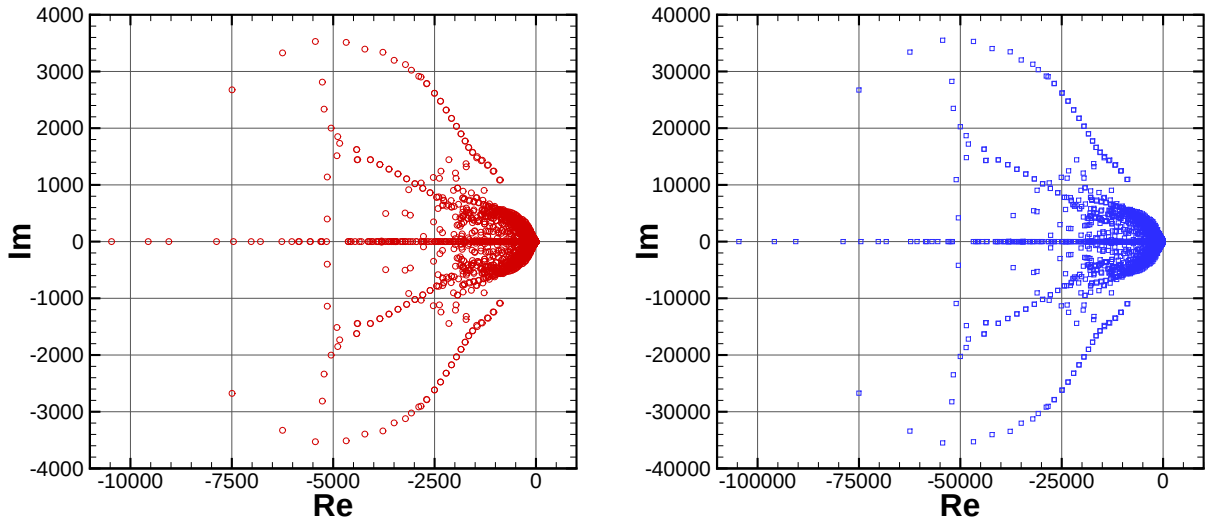

(a) $M_\infty = 0.05$ **(b)** $M_\infty = 0.005$

Figure 3.1: Eigenvalues extracted from the O-Roe Jacobian, before being scaled by the CFL number, for the NACA 0012 aerofoil at zero incidence angle. (a) $M_\infty = 0.05$, (b) $M_\infty = 0.005$.

The condition number of the eigenvalues system is defined as the ratio between the maximum and the minimum eigenvalues.

$$\kappa = \frac{|\lambda_{max}|}{|\lambda_{min}|} \tag{3.2}$$

This leads to an increment of the condition number (κ) of one order of magnitude: for $M_\infty = 0.05$ κ is $1.2 \cdot 10^5$, while for $M_\infty = 0.005$ $\kappa = 1.2 \cdot 10^6$.

3.2 Flux implementation

3.2.1 Original Roe

At present, one of the most widely used approximate Riemann solver in the literature is Roe's [121]. In its definition, the fluxes are calculated by the sum of a convective and a dissipative term,

$$\mathbf{F}^{Roe}_{i+1/2} = \mathbf{F}^{Roe}_{c_{i+1/2}} + \mathbf{F}^{Roe}_{d_{i+1/2}}. \tag{3.3}$$

The central or convective term ($\mathbf{F}^{Roe}_{c_{i+1/2}}$) is usually obtained by averaging the left and right states at each cell of the domain, see Figure 3.2. On the other hand, the dissipation term ($\mathbf{F}^{Roe}_{d_{i+1/2}}$) is evaluated taking into account the matrix of eigenvalues ($|\mathbf{\Lambda}^{Roe}_{i+1/2}|$), right and left eigenvectors at the cell interface ($\mathbf{R}^{Roe}_{i+1/2}$, $(\mathbf{R}^{Roe}_{i+1/2})^{-1}$) , and the difference between right and left conservative variables ($(\mathbf{W}_{i+1} - \mathbf{W}_i)$).

$$\mathbf{F}^{Roe}_{i+1/2} = \frac{1}{2}(\mathbf{F}_i + \mathbf{F}_{i+1}) - \frac{1}{2}\mathbf{R}^{Roe}_{i+1/2}|\mathbf{\Lambda}^{Roe}_{i+1/2}|(\mathbf{R}^{Roe}_{i+1/2})^{-1}(\mathbf{W}_{i+1} - \mathbf{W}_i) \tag{3.4}$$

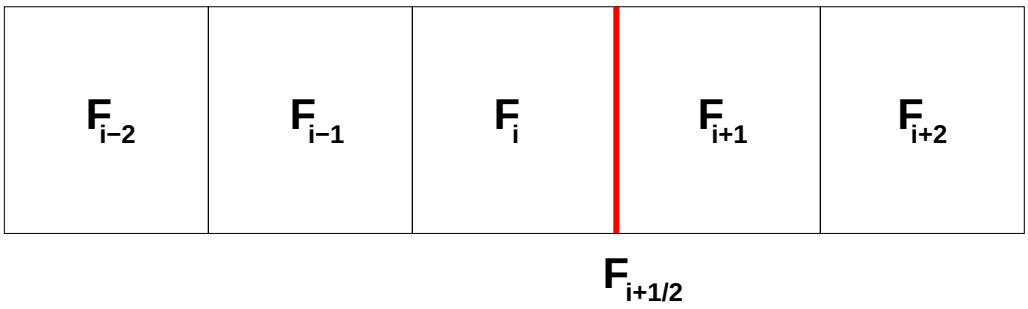

Figure 3.2: Flux in the $i+1/2$ face, considering the left (i) and right ($i+1$) states.

The splitting method employed in HMB2 for Roe's fluxes is the one derived by Liu and Vinokur [89],

$$\mathbf{F}^{Roe} = \frac{1}{2}\Big(\mathbf{F}_R + \mathbf{F}_L\Big) - \frac{1}{2}\Big(|\lambda_2| \cdot \Delta\mathbf{W}^* + \delta_1 \cdot \overline{\mathbf{W}} + \delta_2 \cdot \mathbf{N}\Big) \tag{3.5}$$

The dissipation term is composed by the addition of three vectors ($\Delta\mathbf{W}^*$, $\overline{\mathbf{W}}$, $\mathbf{N}$) and three constants (λ_2, δ_1, δ_2). The constants are defined as,

$$\delta_1 = \lambda^+ \frac{\Delta p}{c^2} + \lambda^- \frac{\overline{\rho}\Delta u_n}{c}, \tag{3.6}$$

$$\delta_2 = \lambda^- \frac{\Delta p}{c} + \lambda^+ \overline{\rho}\Delta u_n. \tag{3.7}$$

Where λ^+ and λ^- are combinations of the eigen values, $\lambda_1 = \overline{u}_n - c$, $\lambda_2 = \overline{u}_n$ and $\lambda_3 = \overline{u}_n + c$.

$$\lambda^+ = -|\lambda_2| + \frac{|\lambda_3| + |\lambda_1|}{2} \tag{3.8}$$

$$\lambda^- = \frac{|\lambda_3| - |\lambda_1|}{2} \tag{3.9}$$

Roe's averaged values are obtained using the ratio of densities in both right and left sides (ρ_r/ρ_l). For a generic fluid property, ϕ, the average is obtained as,

$$\overline{\phi} = \frac{1}{1+\sqrt{\rho_r/\rho_l}}\phi_l + \frac{1}{1+\sqrt{\rho_l/\rho_r}}\phi_r. \tag{3.10}$$

The three vectors $\Delta\mathbf{W}^*$, $\overline{\mathbf{W}}$ and $\mathbf{N}$ denote the difference between right and left states of conservative variables, Roe's averaged values and unitary components, respectively. Hence,

$$\Delta\mathbf{W}^* = \begin{pmatrix} \rho_r - \rho_l \\ (\rho u)_r - (\rho u)_l \\ (\rho v)_r - (\rho v)_l \\ (\rho w)_r - (\rho w)_l \\ (\rho h - p)_r - (\rho h - p)_l \end{pmatrix}, \tag{3.11}$$

$$\overline{\mathbf{W}} = \Big(1, \overline{u}, \overline{v}, \overline{w}, \overline{h}\Big)^T, \tag{3.12}$$

$$\mathbf{N} = \Big(0, n_x, n_y, n_z, \overline{u}_n\Big)^T. \tag{3.13}$$

Note that the last term in Equation (3.11) is the internal energy multiplied by density, written as a function of enthalpy, $\rho e = \rho e + \rho RT - p = \rho h - p$.

Modifications to the original Roe's approximate Riemann solver (O-Roe) were reported in the literature in order to overcome the low-Mach problem. In the following, the implementation of both the fluxes and Jacobian is presented. All of them involve the scaling of the dissipative term of Equation (3.4) by a function $f(M)$, which is dependent on the local Mach number. The main characteristics that this function must have are:

$$0 < f(M) < 1 \text{ when } 0 < M < 1, \tag{3.14}$$

$$f(M) \to 0 \text{ when } M \to 0, \tag{3.15}$$

$$f(M) = 1 \text{ when } M \geq 1. \tag{3.16}$$

In the present study the function employed is the one suggested by Li [82]. However, other types of functions are also used [117, 133, 74]. To avoid problems at the stagnation point, where the Mach number is exactly 0.0, $f(M)$ is truncated to a value of 10^{-5}, see Figure 3.3.

$$f(M) \quad = \quad M\frac{\sqrt{4+(1-M^2)^2}}{1+M^2}. \tag{3.17}$$

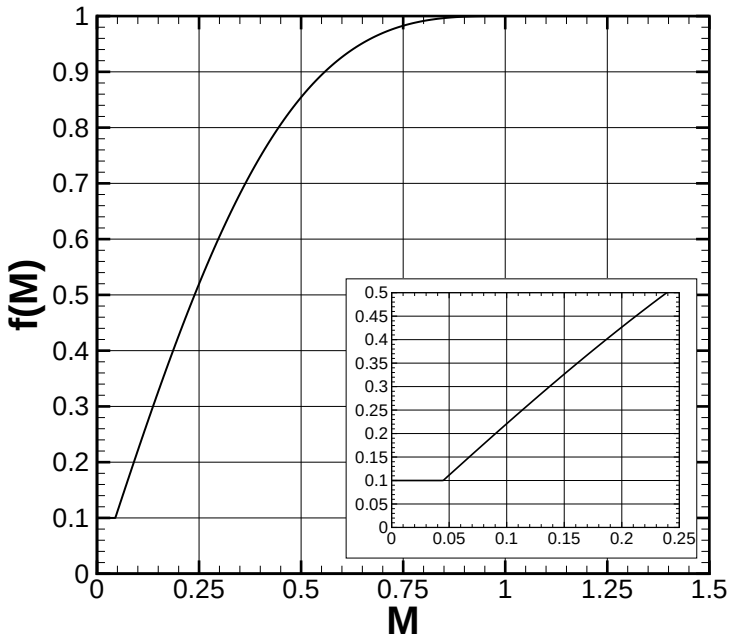

Figure 3.3: Function for scaling the dissipation terms: $f(M) = M\frac{\sqrt{4+(1-M^2)^2}}{1+M^2}$. For the Jacobian evaluation, a minimum value of 0.1 is set.

3.2.2 Low-Mach Roe

The all-Mach scheme known as Low-Mach (LM) was developed by Rieper [117]. This modification of the standard Roe scheme concerns the scaling of the wave strengths, particularly, the velocity jump at the cell interface, denoted as Δu_n. In Ref. [117], it was applied to incompressible cases - moving vortex problem at Mach numbers of 0.1, 0.01 and 0.001, flow around a cylinder at Mach numbers of 0.1 and 0.01 and to a simple acoustic wave; and to the compressible Sod's shock tube problem. It was proved that the scheme's accuracy is independent on the Mach number and avoids "checkerboard" modes.

As reported [117], its explicit implementation is relatively simple. For the implementation in HMB2, the constants δ_1 and δ_2 from the O-Roe scheme in Equation (3.5) are modified to include the scaling function $f(M)$ as:

$$\delta_1^{LM} = \lambda^+ \frac{\Delta p}{c^2} + \lambda^- f(M) \frac{\overline{\rho} \Delta u_n}{c} \tag{3.18}$$

$$\delta_2^{LM} = \lambda^- \frac{\Delta p}{c} + \left(\lambda^+ f(M) - (1 - f(M))|\lambda_2|\right) \overline{\rho} \Delta u_n \tag{3.19}$$

3.2.3 Thornber's Roe

Thornber [150] proposed a modified Roe scheme, in which the sound speed in the right eigenvectors of the system is multiplied by the function $f(M)$. In HMB2, this modification is done in the δ_2 term of the O-Roe scheme, as shown in Equation (3.20).

$$\delta_2^T = \lambda^- f(M) \frac{\Delta p}{c} + \left(\lambda^+ f(M) - (1 - f(M))|\lambda_2|\right) \overline{\rho} \Delta u_n \tag{3.20}$$

3.2.4 All-Speed Roe

This modified scheme, formulated by Li *et al.* [82, 84] is based on the scaling of only the acoustic eigenvalues of the system.

$$\lambda_1^A = \overline{u}_n - f(M)c \tag{3.21}$$

$$\lambda_3^A = \overline{u}_n + f(M)c \tag{3.22}$$

It was employed to solve the flow around a high-loaded T106 turbine blade row, at Mach number of 0.001, obtaining good results, but not not avoiding the checkerboard decoupling.

3.2.5 Preconditioned Roe

This modification of the Roe scheme [84] not only scales both the right and left eigenvectors and eigenvalues with a θ parameter, but it also multiplies the dissipation term by a preconditioning matrix. θ acts as a global cut-off to avoid problems when the local Mach number is 0.0, therefore no extra truncation is needed. For this scheme, the fluxes are written in the following vector-matrix formulation, as reported in Ref. [84].

$$\mathbf{F}_{i+1/2}^{P-Roe} = \frac{1}{2}(\mathbf{F}_i + \mathbf{F}_{i+1}) - \frac{1}{2}\mathbf{\Gamma}_{i+1/2}^{-1}\mathbf{R}_{i+1/2}^{P-Roe}|\mathbf{\Lambda}_{i+1/2}^{P-Roe}|\mathbf{L}_{i+1/2}^{P-Roe}(\mathbf{W}_{i+1} - \mathbf{W}_i) \tag{3.23}$$

θ is a parameter employed to provide a global cut-off in order to avoid instability problems. It is obtained by the following condition,

$$\theta = min[max(KM_{ref}^2, M^2), 1]. \tag{3.24}$$

Here, K is set to 1 and M_{ref} to 0.15. The corresponding normalised velocity and sound speed scaled with this parameter are:

$$\tilde{\overline{u}}_n = \frac{1}{2}(1+\theta)\overline{u}_n \tag{3.25}$$

$$\tilde{c} = \frac{1}{2}\sqrt{4c^2\theta + (1-\theta)^2\overline{u}_n^2} \tag{3.26}$$

The matrix of eigenvalues is a sparse matrix with non-zero terms in the diagonal, see Equation (3.27). The right and left eigenvectors for the preconditioned Roe scheme are detailed in Equations (3.28) and (3.29), respectively.

$$\mathbf{\Lambda^{P-Roe}} = \begin{pmatrix} \tilde{\overline{u}}_n - \tilde{c} & & & & \\ & \overline{u}_n & & & \\ & & \tilde{\overline{u}}_n + \tilde{c} & & \\ & & & \overline{u}_n & \\ & & & & \overline{u}_n \end{pmatrix} \tag{3.27}$$

$$\mathbf{R^{P-Roe}} = \begin{pmatrix} 1 & 1 & 1 & 0 & 0 \\ \overline{u} + \frac{1-\theta}{2\theta}\overline{u}_n n_x - \frac{\tilde{c}}{\theta}n_x & \overline{u} & \overline{u} + \frac{1-\theta}{2\theta}\overline{u}_n n_x + \frac{\tilde{c}}{\theta}n_x & -n_y & -n_x n_z \\ \overline{v} + \frac{1-\theta}{2\theta}\overline{u}_n n_y - \frac{\tilde{c}}{\theta}n_y & \overline{v} & \overline{v} + \frac{1-\theta}{2\theta}\overline{u}_n n_y + \frac{\tilde{c}}{\theta}n_y & n_x & -n_y n_z \\ \overline{w} + \frac{1-\theta}{2\theta}\overline{u}_n n_z - \frac{\tilde{c}}{\theta}n_z & \overline{w} & \overline{w} + \frac{1-\theta}{2\theta}\overline{u}_n n_z + \frac{\tilde{c}}{\theta}n_z & 0 & n_x^2 + n_y^2 \\ \overline{h} + \frac{1-\theta}{2\theta}\overline{u}_n^2 - \frac{\tilde{c}}{\theta}\overline{u}_n & \frac{1}{2}q^2 & \overline{h} + \frac{1-\theta}{2\theta}\overline{u}_n^2 + \frac{\tilde{c}}{\theta}\overline{u}_n & -\overline{u}n_y + \overline{v}n_x & -\overline{u}n_x n_z - \overline{v}n_y n_z + \overline{w}(n_x^2 + n_y^2) \end{pmatrix} \tag{3.28}$$

$$\mathbf{L}^{\mathbf{P-Roe}} = \left(\begin{array}{c|c|c|c|c} (A) & (B) & (C) & (D) & (E) \end{array} \right) \tag{3.29}$$

The matrix of left eigenvectors in Equation (3.29) is composed by the vectors in Equations (3.30) to (3.34).

$$(\mathbf{A}) = \begin{pmatrix} \frac{\gamma-1}{4c^2}q^2 + u_n\frac{\theta}{2\tilde{c}} + \frac{\gamma-1}{8c^2\tilde{c}}(1-\theta)q^2\overline{u}_n \\ 1 - \frac{\gamma-1}{2c^2}q^2 \\ \frac{\gamma-1}{4c^2}q^2 - \overline{u}_n\frac{\theta}{2\tilde{c}} - \frac{\gamma-1}{8c^2\tilde{c}}(1-\theta)q^2\overline{u}_n \\ \overline{u}n_y + \overline{v}n_x \\ \overline{u}n_x n_z + \overline{v}n_y n_z - \overline{w}(n_x^2+n_y^2) \end{pmatrix} \tag{3.30}$$

$$(\mathbf{B}) = \begin{pmatrix} -\left(\frac{\gamma-1}{2c^2}\overline{u} + n_x\frac{\theta}{2\tilde{c}} + \frac{\gamma-1}{4c^2\tilde{c}}(1-\theta)(\overline{u}\overline{u}_n(n_x^2+n_y^2) + \overline{u}n_z^2(-\overline{u}n_x+\overline{v}n_y))\right) \\ \frac{\gamma-1}{c^2}\overline{u} \\ -\left(\frac{\gamma-1}{2c^2}\overline{u} - n_x\frac{\theta}{2\tilde{c}} + \frac{\gamma-1}{4c^2\tilde{c}}(1-\theta)(\overline{u}\overline{u}_n(n_x^2+n_y^2) + \overline{u}n_z^2(-\overline{u}n_x+\overline{v}n_y))\right) \\ -n_y \\ -n_z n_x \end{pmatrix} \tag{3.31}$$

$$(\mathbf{C}) = \begin{pmatrix} -\left(\frac{\gamma-1}{2c^2}\overline{v} + n_y\frac{\theta}{2\tilde{c}} + \frac{\gamma-1}{4c^2\tilde{c}}(1-\theta)(\overline{v}\overline{u}_n(n_x^2+n_y^2) + \overline{v}n_z^2(-\overline{u}n_x+\overline{v}n_y))\right) \\ \frac{\gamma-1}{c^2}\overline{v} \\ -\left(\frac{\gamma-1}{2c^2}\overline{v} - n_y\frac{\theta}{2\tilde{c}} + \frac{\gamma-1}{4c^2\tilde{c}}(1-\theta)(\overline{v}\overline{u}_n(n_x^2+n_y^2) + \overline{v}n_z^2(-\overline{u}n_x+\overline{v}n_y))\right) \\ n_x \\ -n_z n_y \end{pmatrix} \tag{3.32}$$

$$(\mathbf{D}) = \begin{pmatrix} -\left(\frac{\gamma-1}{2c^2}\overline{w} + n_z\frac{\theta}{2\tilde{c}} + \frac{\gamma-1}{4c^2\tilde{c}}(1-\theta)(\overline{w}\overline{u}_n(n_x^2+n_y^2)+\overline{w}n_z^3)\right) \\ \frac{\gamma-1}{c^2}\overline{w} \\ -\left(\frac{\gamma-1}{2c^2}\overline{w} - n_z\frac{\theta}{2\tilde{c}} + \frac{\gamma-1}{4c^2\tilde{c}}(1-\theta)(\overline{w}\overline{u}_n(n_x^2+n_y^2)+\overline{w}n_z^3)\right) \\ 0 \\ n_x^2+n_y^2 \end{pmatrix} \tag{3.33}$$

$$(\mathbf{E}) = \begin{pmatrix} \frac{\gamma-1}{2c^2}\left(1-(1-\theta)\frac{\overline{u}_n}{2\tilde{c}}\right) \\ -\frac{\gamma-1}{c^2} \\ \frac{\gamma-1}{2c^2}\left(1+(1-\theta)\frac{\overline{u}_n}{2\tilde{c}}\right) \\ 0 \\ 0 \end{pmatrix} \tag{3.34}$$

Finally, the preconditioning matrix $\mathbf{\Gamma^{-1}}$ proposed by Guillard *et al.* in [52] is employed in this scheme:

$$\mathbf{\Gamma^{-1}} = \begin{pmatrix} \frac{1}{\theta} & 1 & 0 & 0 & 0 \\ \overline{u}\frac{1-\theta}{\theta} & 1 & 0 & 0 & 0 \\ \overline{v}\frac{1-\theta}{\theta} & 0 & 1 & 0 & 0 \\ \overline{w}\frac{1-\theta}{\theta} & 0 & 0 & 1 & 0 \\ \frac{1-\theta}{2\theta(\gamma-1)}\left(\frac{2c^2}{\gamma}+(\gamma-1)q^2\right) & 0 & 0 & 0 & 1 \end{pmatrix} \tag{3.35}$$

3.3 Jacobian implementation

Unlike Osher's scheme, the exact Roe's Jacobian is difficult to be implemented, since this solver is not continuously differentiable. Applying finite differences to the fluxes, the numerical Jacobian can be obtained. However, for practical problems, this is not an option due to the amount of CPU time required for computations. Hence, an approximate analytical Jacobian needs to be implemented, which provides savings on CPU time of approximately 90%. As can be seen in Figure 3.4, using the numerical and approximate Jacobians the number of iterations is the same, while the latter takes approximately 10% percent of the CPU time. In the following, details of its implementation into HMB2 are provided.

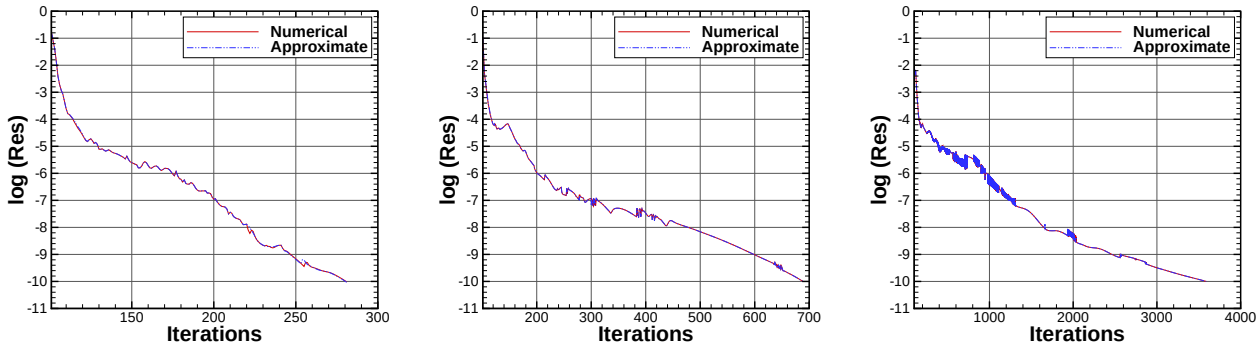

(a) $M_\infty = 0.5$ (10.3%) (b) $M_\infty = 0.1$ (9.9%) (c) $M_\infty = 0.01$ (9.4%)

Figure 3.4: Convergence behaviour of the second order implicit Roe's solver at three free-stream Mach numbers, using numerical and approximate Jacobians. The CFL employed is 100. The test case is the flow over the NACA0012 aerofoil, at zero incidence angle. The CPU times are included in parenthesis, as a percentage based on the time required employing the numerical Jacobian (obtained using Finite Differences).

3.3.1 Original Roe Jacobian

Through derivation of the fluxes with respect to the primitive variables, the approximate Jacobian is obtained, as shown in Equation (3.36).

$$\left(\frac{\partial \mathbf{F}}{\partial \mathbf{P}}\right)_{\mathbf{O-Roe}} = \begin{pmatrix} \frac{\partial f_0}{\partial \rho} & \frac{\partial f_0}{\partial u} & \frac{\partial f_0}{\partial v} & \frac{\partial f_0}{\partial w} & \frac{\partial f_0}{\partial p} \\ \frac{\partial f_1}{\partial \rho} & \frac{\partial f_1}{\partial u} & \frac{\partial f_1}{\partial v} & \frac{\partial f_1}{\partial w} & \frac{\partial f_1}{\partial p} \\ \frac{\partial f_2}{\partial \rho} & \frac{\partial f_2}{\partial u} & \frac{\partial f_2}{\partial v} & \frac{\partial f_2}{\partial w} & \frac{\partial f_2}{\partial p} \\ \frac{\partial f_3}{\partial \rho} & \frac{\partial f_3}{\partial u} & \frac{\partial f_3}{\partial v} & \frac{\partial f_3}{\partial w} & \frac{\partial f_3}{\partial p} \\ \frac{\partial f_4}{\partial \rho} & \frac{\partial f_4}{\partial u} & \frac{\partial f_4}{\partial v} & \frac{\partial f_4}{\partial w} & \frac{\partial f_4}{\partial p} \end{pmatrix} \tag{3.36}$$

Where $\mathbf{F}$ are the fluxes and $\mathbf{P}$ are the primitive variables, $\mathbf{P} = (\rho, u, v, w, p)$. The derivation is therefore done as,

$$\begin{aligned} \frac{\partial \mathbf{F}^{Roe}}{\partial \mathbf{P}} &= \frac{1}{2}\left(\frac{\partial (\mathbf{F}_R + \mathbf{F}_L)}{\partial \mathbf{P}}\right) + \\ &\quad -\frac{1}{2}\left(\frac{\partial |\lambda_2|}{\partial \mathbf{P}}\Delta \mathbf{W}^* + |\lambda_2|\frac{\partial \Delta \mathbf{W}^*}{\partial \mathbf{P}} + \frac{\partial \delta_1}{\partial \mathbf{P}}\overline{\mathbf{W}} + \delta_1 \frac{\partial \overline{\mathbf{W}}}{\partial \mathbf{P}} + \frac{\partial \delta_2}{\partial \mathbf{P}}\mathbf{N} + \delta_2 \frac{\partial \mathbf{N}}{\partial \mathbf{P}}\right) \end{aligned} \tag{3.37}$$

It should be noted that the approximate Jacobian that is actually coded in HMB2 is a simplified version, under the assumption that the differences between the left and right sides are negligible ($\Delta\rho \simeq 0$,

$\Delta p \simeq 0$ and $\Delta u_n \simeq 0$). In the following, the derivatives of the three constants in Equation (3.37) are extended.

$$\frac{\partial|\lambda_2|}{\partial \mathbf{P}} = \frac{\lambda_2}{|\lambda_2|}\frac{\partial\lambda_2}{\partial \mathbf{P}} = \left\{ \frac{\overline{u}_n}{|\overline{u}_n|}\frac{\partial \overline{u}_n}{\partial \mathbf{P}} \right\} \tag{3.38}$$

$$\begin{aligned}\frac{\partial \delta_1}{\partial \mathbf{P}} = {} & \Big(\frac{\partial\lambda^+}{\partial \mathbf{P}}\Big)\frac{\Delta p}{c^2} + \left\{ \Big(\frac{\partial \Delta p}{\partial \mathbf{P}}\Big)\frac{\lambda^+}{c^2} \right\} - \Big(\frac{\partial c^2}{\partial \mathbf{P}}\Big)\frac{\lambda^+\Delta p}{c^4} + \\ & + \Big(\frac{\partial\lambda^-}{\partial \mathbf{P}}\Big)\frac{\overline{\rho}\Delta u_n}{c} + \left\{ \Big(\frac{\partial \Delta u_n}{\partial \mathbf{P}}\Big)\frac{\overline{\rho}\lambda^-}{c} \right\} + \Big(\frac{\partial \overline{\rho}}{\partial \mathbf{P}}\Big)\frac{\lambda^-\Delta u_n}{c} - \Big(\frac{\partial c}{\partial \mathbf{P}}\Big)\frac{\lambda^-\overline{\rho}\Delta u_n}{c^2}\end{aligned} \tag{3.39}$$

$$\begin{aligned}\frac{\partial \delta_2}{\partial \mathbf{P}} = {} & \Big(\frac{\partial\lambda^-}{\partial \mathbf{P}}\Big)\frac{\Delta p}{c} + \left\{ \Big(\frac{\partial \Delta p}{\partial \mathbf{P}}\Big)\frac{\lambda^-}{c} \right\} - \Big(\frac{\partial c}{\partial \mathbf{P}}\Big)\frac{\lambda^-\Delta p}{c^2} + \\ & + \Big(\frac{\partial\lambda^+}{\partial \mathbf{P}}\Big)\overline{\rho}\Delta u_n + \left\{ \Big(\frac{\partial \Delta u_n}{\partial \mathbf{P}}\Big)\overline{\rho}\lambda^+ \right\} + \Big(\frac{\partial \overline{\rho}}{\partial \mathbf{P}}\Big)\lambda^+\Delta u_n\end{aligned} \tag{3.40}$$

Where the intermediate partial derivatives are obtained as,

$$\frac{\partial\lambda^+}{\partial \mathbf{P}} = -\frac{\overline{u}_n}{|\overline{u}_n|}\frac{\partial \overline{u}_n}{\partial \mathbf{P}} + \frac{1}{2}\left[\frac{\overline{u}_n + c}{|\overline{u}_n + c|}\Big(\frac{\partial \overline{u}_n}{\partial \mathbf{P}} + \frac{\partial c}{\partial \mathbf{P}}\Big) + \frac{\overline{u}_n - c}{|\overline{u}_n - c|}\Big(\frac{\partial \overline{u}_n}{\partial \mathbf{P}} - \frac{\partial c}{\partial \mathbf{P}}\Big) \right], \tag{3.41}$$

$$\frac{\partial\lambda^-}{\partial \mathbf{P}} = \frac{1}{2}\left[\frac{\overline{u}_n + c}{|\overline{u}_n + c|}\Big(\frac{\partial \overline{u}_n}{\partial \mathbf{P}} + \frac{\partial c}{\partial \mathbf{P}}\Big) - \frac{\overline{u}_n - c}{|\overline{u}_n - c|}\Big(\frac{\partial \overline{u}_n}{\partial \mathbf{P}} - \frac{\partial c}{\partial \mathbf{P}}\Big) \right]. \tag{3.42}$$

The terms between $\{\}$ in Equations (3.38) to (3.40) are the only ones included in the approximate Jacobian. Hence, they are simplified as,

$$\frac{\partial|\lambda_2|}{\partial \mathbf{P}} \approx \frac{\overline{u}_n}{|\overline{u}_n|}\frac{\partial \overline{u}_n}{\partial \mathbf{P}} \tag{3.43}$$

$$\frac{\partial \delta_1}{\partial \mathbf{P}} \approx \Big(\frac{\partial \Delta p}{\partial \mathbf{P}}\Big)\frac{\lambda^+}{c^2} + \Big(\frac{\partial \Delta u_n}{\partial \mathbf{P}}\Big)\frac{\overline{\rho}\lambda^-}{c} \tag{3.44}$$

$$\frac{\partial \delta_2}{\partial \mathbf{P}} \approx \Big(\frac{\partial \Delta p}{\partial \mathbf{P}}\Big)\frac{\lambda^-}{c} + \Big(\frac{\partial \Delta u_n}{\partial \mathbf{P}}\Big)\overline{\rho}\lambda^+ \tag{3.45}$$

The right and left states non-zero derivatives included in the previous expressions are detailed in the following.

$$\frac{\partial \overline{\rho}}{\partial \rho_l} = \frac{1}{2}\sqrt{\frac{\rho_r}{\rho_l}}; \quad \frac{\partial \overline{\rho}}{\partial \rho_r} = \frac{1}{2}\sqrt{\frac{\rho_l}{\rho_r}} \tag{3.46}$$

$$\frac{\partial \overline{u}_n}{\partial \rho_l} = \frac{-1}{2}\frac{\overline{\rho}}{(\rho_l + \overline{\rho})^2}\Delta u_n; \quad \frac{\partial \overline{u}_n}{\partial \rho_r} = \frac{-1}{2}\frac{\overline{\rho}}{(\rho_r + \overline{\rho})^2}\Delta u_n \tag{3.47}$$

$$\frac{\partial \overline{u}_n}{\partial u_l} = \frac{\sqrt{\rho_l}}{\sqrt{\rho_l}+\sqrt{\rho_r}} n_x; \quad \frac{\partial \overline{u}_n}{\partial u_r} = \frac{\sqrt{\rho_r}}{\sqrt{\rho_l}+\sqrt{\rho_r}} n_x \tag{3.48}$$

$$\frac{\partial \overline{u}_n}{\partial v_l} = \frac{\sqrt{\rho_l}}{\sqrt{\rho_l}+\sqrt{\rho_r}} n_y; \quad \frac{\partial \overline{u}_n}{\partial v_r} = \frac{\sqrt{\rho_r}}{\sqrt{\rho_l}+\sqrt{\rho_r}} n_y \tag{3.49}$$

$$\frac{\partial \overline{u}_n}{\partial w_l} = \frac{\sqrt{\rho_l}}{\sqrt{\rho_l}+\sqrt{\rho_r}} n_z; \quad \frac{\partial \overline{u}_n}{\partial w_r} = \frac{\sqrt{\rho_r}}{\sqrt{\rho_l}+\sqrt{\rho_r}} n_z \tag{3.50}$$

$$\frac{\partial \overline{u}}{\partial u_l} = \frac{\sqrt{\rho_l}}{\sqrt{\rho_l}+\sqrt{\rho_r}}; \quad \frac{\partial \overline{u}}{\partial u_r} = \frac{\sqrt{\rho_r}}{\sqrt{\rho_l}+\sqrt{\rho_r}} \tag{3.51}$$

$$\frac{\partial \overline{v}}{\partial v_l} = \frac{\sqrt{\rho_l}}{\sqrt{\rho_l}+\sqrt{\rho_r}}; \quad \frac{\partial \overline{v}}{\partial v_r} = \frac{\sqrt{\rho_r}}{\sqrt{\rho_l}+\sqrt{\rho_r}} \tag{3.52}$$

$$\frac{\partial \overline{w}}{\partial w_l} = \frac{\sqrt{\rho_l}}{\sqrt{\rho_l}+\sqrt{\rho_r}}; \quad \frac{\partial \overline{w}}{\partial w_r} = \frac{\sqrt{\rho_r}}{\sqrt{\rho_l}+\sqrt{\rho_r}} \tag{3.53}$$

$$\frac{\partial c^2}{\partial u_l} = (\gamma-1)\frac{\sqrt{\rho_l}}{\sqrt{\rho_l}+\sqrt{\rho_r}} u_l(1-\overline{u}); \quad \frac{\partial c^2}{\partial u_r} = (\gamma-1)\frac{\sqrt{\rho_r}}{\sqrt{\rho_l}+\sqrt{\rho_r}} 1+\delta_r u_r(1-\overline{u}) \tag{3.54}$$

$$\frac{\partial c^2}{\partial v_l} = (\gamma-1)\frac{\sqrt{\rho_l}}{\sqrt{\rho_l}+\sqrt{\rho_r}} v_l(1-\overline{v}); \quad \frac{\partial c^2}{\partial v_r} = (\gamma-1)\frac{\sqrt{\rho_r}}{\sqrt{\rho_l}+\sqrt{\rho_r}} v_r(1-\overline{v}) \tag{3.55}$$

$$\frac{\partial c^2}{\partial w_l} = (\gamma-1)\frac{\sqrt{\rho_l}}{\sqrt{\rho_l}+\sqrt{\rho_r}} w_l(1-\overline{w}); \quad \frac{\partial c^2}{\partial w_r} = (\gamma-1)\frac{\sqrt{\rho_r}}{\sqrt{\rho_l}+\sqrt{\rho_r}} w_r(1-\overline{w}) \tag{3.56}$$

$$\frac{\partial c^2}{\partial p_l} = \frac{\gamma}{\rho_l+\overline{\rho}}; \quad \frac{\partial c^2}{\partial p_r} = \frac{\gamma}{\rho_r+\overline{\rho}} \tag{3.57}$$

$$\frac{\partial c}{\partial \rho_l} = \frac{1}{2c}\frac{\partial c^2}{\partial \rho_l}; \quad \frac{\partial c}{\partial \rho_r} = \frac{1}{2c}\frac{\partial c^2}{\partial \rho_r} \tag{3.58}$$

$$\frac{\partial c}{\partial u_l} = \frac{1}{2c}\frac{\partial c^2}{\partial u_l}; \quad \frac{\partial c}{\partial u_r} = \frac{1}{2c}\frac{\partial c^2}{\partial u_r} \tag{3.59}$$

$$\frac{\partial c}{\partial v_l} = \frac{1}{2c}\frac{\partial c^2}{\partial v_l}; \quad \frac{\partial c}{\partial v_r} = \frac{1}{2c}\frac{\partial c^2}{\partial v_r} \tag{3.60}$$

$$\frac{\partial c}{\partial w_l} = \frac{1}{2c}\frac{\partial c^2}{\partial w_l}; \quad \frac{\partial c}{\partial w_r} = \frac{1}{2c}\frac{\partial c^2}{\partial w_r} \tag{3.61}$$

$$\frac{\partial c}{\partial p_l} = \frac{1}{2c}\frac{\partial c^2}{\partial p_l}; \quad \frac{\partial c}{\partial p_r} = \frac{1}{2c}\frac{\partial c^2}{\partial p_r} \tag{3.62}$$

$$\frac{\partial c^2}{\partial \rho_l} = (\gamma-1)\left(\frac{1}{2}\frac{\overline{\rho}}{(\rho_l+\overline{\rho})^2}\left((h_l-h_r)+(\overline{u}\Delta u+\overline{v}\Delta v+\overline{w}\Delta w)\right)\right)-\gamma\frac{\sqrt{\rho_l}}{\sqrt{\rho_l}+\sqrt{\rho_r}}\frac{p_l}{\rho_l^2} \tag{3.63}$$

$$\frac{\partial c^2}{\partial \rho_r} = (\gamma-1)\left(\frac{1}{2}\frac{\overline{\rho}}{(\rho_r+\overline{\rho})^2}\left((h_r-h_l)-(\overline{u}\Delta u+\overline{v}\Delta v+\overline{w}\Delta w)\right)\right)-\gamma\frac{\sqrt{\rho_r}}{\sqrt{\rho_l}+\sqrt{\rho_r}}\frac{p_r}{\rho_r^2} \tag{3.64}$$

3.3.2 Low-Mach Jacobian

The terms of the Jacobian highlighted in bold are the ones that need to be modified with respect to the O-Roe Jacobian in Section 3.3.1, affecting the constants in Equations (3.66) and (3.67).

$$\left(\frac{\partial \mathbf{F}}{\partial \mathbf{P}}\right)_{\mathbf{LM-Roe}} = \begin{pmatrix} \frac{\partial f_0}{\partial \rho} & \frac{\partial \mathbf{f_0}}{\partial \mathbf{u}} & \frac{\partial \mathbf{f_0}}{\partial \mathbf{v}} & \frac{\partial \mathbf{f_0}}{\partial \mathbf{w}} & \frac{\partial f_0}{\partial p} \\ \frac{\partial f_1}{\partial \rho} & \frac{\partial \mathbf{f_1}}{\partial \mathbf{u}} & \frac{\partial \mathbf{f_1}}{\partial \mathbf{v}} & \frac{\partial \mathbf{f_1}}{\partial \mathbf{w}} & \frac{\partial f_1}{\partial p} \\ \frac{\partial f_2}{\partial \rho} & \frac{\partial \mathbf{f_2}}{\partial \mathbf{u}} & \frac{\partial \mathbf{f_2}}{\partial \mathbf{v}} & \frac{\partial \mathbf{f_2}}{\partial \mathbf{w}} & \frac{\partial f_2}{\partial p} \\ \frac{\partial f_3}{\partial \rho} & \frac{\partial \mathbf{f_3}}{\partial \mathbf{u}} & \frac{\partial \mathbf{f_3}}{\partial \mathbf{v}} & \frac{\partial \mathbf{f_3}}{\partial \mathbf{w}} & \frac{\partial f_3}{\partial p} \\ \frac{\partial f_4}{\partial \rho} & \frac{\partial \mathbf{f_4}}{\partial \mathbf{u}} & \frac{\partial \mathbf{f_4}}{\partial \mathbf{v}} & \frac{\partial \mathbf{f_4}}{\partial \mathbf{w}} & \frac{\partial f_4}{\partial p} \end{pmatrix} \tag{3.65}$$

$$\begin{aligned} \frac{\partial \delta_1^{LM}}{\partial \mathbf{P}} &= \left(\frac{\partial \lambda^+}{\partial \mathbf{P}}\right)\frac{\Delta p}{c^2} + \left\{\left(\frac{\partial \Delta p}{\partial \mathbf{P}}\right)\frac{\lambda^+}{c^2}\right\} - \left(\frac{\partial c^2}{\partial \mathbf{P}}\right)\frac{\lambda^+ \Delta p}{c^4} + \left(\frac{\partial \lambda^-}{\partial \mathbf{P}}\right)\frac{\overline{\rho} f(M)\Delta u_n}{c} \\ &+ \left\{\left(\frac{\partial \Delta u_n}{\partial \mathbf{P}}\right)\frac{f(M)\overline{\rho}\lambda^-}{c}\right\} + \left(\frac{\partial \overline{\rho}}{\partial \mathbf{P}}\right)\frac{\lambda^- f(M)\Delta u_n}{c} - \left(\frac{\partial c}{\partial \mathbf{P}}\right)\frac{\lambda^- \overline{\rho} f(M)\Delta u_n}{c^2} + \\ &+ \left(\frac{\partial f(M)}{\partial \mathbf{P}}\right)\frac{\lambda^- \overline{\rho}\Delta \overline{u}_n}{c} \end{aligned} \tag{3.66}$$

$$\begin{aligned} \frac{\partial \delta_2^{LM}}{\partial \mathbf{P}} &= \left(\frac{\partial \lambda^-}{\partial \mathbf{P}}\right)\frac{\Delta p}{c} + \left\{\left(\frac{\partial \Delta p}{\partial \mathbf{P}}\right)\frac{\lambda^-}{c}\right\} - \left(\frac{\partial c}{\partial \mathbf{P}}\right)\frac{\lambda^- \Delta p}{c^2} + \left(\frac{\partial \lambda^+}{\partial \mathbf{P}}\right)\overline{\rho} f(M)\Delta u_n \\ &+ \left\{\left(\frac{\partial \Delta u_n}{\partial \mathbf{P}}\right) f(M)\overline{\rho}\lambda^+\right\} + \left(\frac{\partial \overline{\rho}}{\partial \mathbf{P}}\right)\lambda^+ f(M)\Delta u_n + \\ &+ \left[|\lambda_2|\frac{\partial f(M)}{\partial \mathbf{P}} - (1-f(M))\frac{\partial |\lambda_2|}{\partial P}\right]\overline{\rho}\Delta u_n + \\ &- (1-f(M))|\lambda_2|\left[\left(\frac{\partial \overline{\rho}}{\partial \mathbf{P}}\right)\Delta u_n + \left\{\left(\frac{\partial \Delta u_n}{\partial \mathbf{P}}\right)\overline{\rho}\right\}\right] \end{aligned} \tag{3.67}$$

The terms of the approximate Jacobian for the Low-Mach scheme are ,therefore,

$$\frac{\partial \delta_1^{LM}}{\partial \mathbf{P}} \approx \left(\frac{\partial \Delta p}{\partial \mathbf{P}}\right)\frac{\lambda^+}{c^2} + \left(\frac{\partial \Delta u_n}{\partial \mathbf{P}}\right)\frac{f(M)\overline{\rho}\lambda^-}{c} \tag{3.68}$$

$$\frac{\partial \delta_2^{LM}}{\partial \mathbf{P}} \approx \left(\frac{\partial \Delta p}{\partial \mathbf{P}}\right)\frac{\lambda^-}{c} + \left(\frac{\partial \Delta u_n}{\partial \mathbf{P}}\right)\overline{\rho}\left[f(M)\lambda^+ - (1-f(M))|\lambda_2|\right] \tag{3.69}$$

Figure 3.5 shows, for a range of Mach numbers, that almost quadratic convergence is obtained with the derived Jacobian. In the following, this will be referred to as LM-Roe Jacobian.

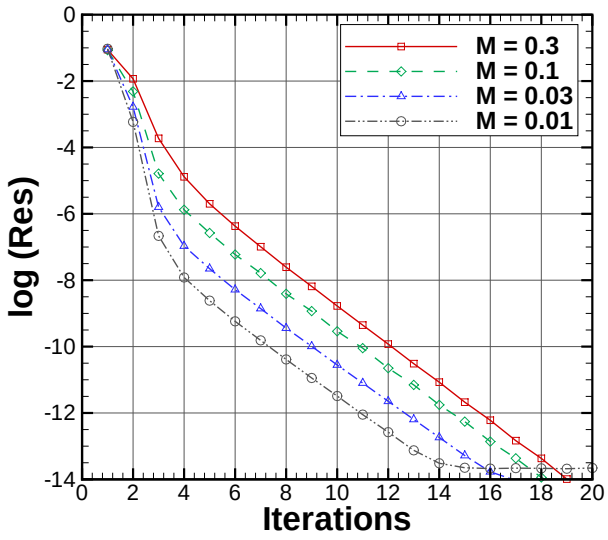

Figure 3.5: Almost quadratic convergence present in the first order LM-Roe scheme. The test case is the flow over the NACA0012 aerofoil, at zero incidence angle. The implicit CFL is 10^8.

3.3.3 Thornber's Roe Jacobian

The only derivative that needs to be modified is the constant δ_2, denoted as δ_2^T in this case (see Equation (3.71)). This affects the terms in bold of the Jacobian matrix of Equation (3.70).

$$\left(\frac{\partial \mathbf{F}}{\partial \mathbf{P}}\right)_{\mathbf{T-Roe}} = \begin{pmatrix} \frac{\partial f_0}{\partial \rho} & \frac{\partial f_0}{\partial u} & \frac{\partial f_0}{\partial v} & \frac{\partial f_0}{\partial w} & \frac{\partial f_0}{\partial p} \\ \frac{\partial f_1}{\partial \rho} & \frac{\partial \mathbf{f_1}}{\partial \mathbf{u}} & \frac{\partial \mathbf{f_1}}{\partial \mathbf{v}} & \frac{\partial \mathbf{f_1}}{\partial \mathbf{w}} & \frac{\partial \mathbf{f_1}}{\partial \mathbf{p}} \\ \frac{\partial f_2}{\partial \rho} & \frac{\partial \mathbf{f_2}}{\partial \mathbf{u}} & \frac{\partial \mathbf{f_2}}{\partial \mathbf{v}} & \frac{\partial \mathbf{f_2}}{\partial \mathbf{w}} & \frac{\partial \mathbf{f_2}}{\partial \mathbf{p}} \\ \frac{\partial f_3}{\partial \rho} & \frac{\partial \mathbf{f_3}}{\partial \mathbf{u}} & \frac{\partial \mathbf{f_3}}{\partial \mathbf{v}} & \frac{\partial \mathbf{f_3}}{\partial \mathbf{w}} & \frac{\partial \mathbf{f_3}}{\partial \mathbf{p}} \\ \frac{\partial f_4}{\partial \rho} & \frac{\partial \mathbf{f_4}}{\partial \mathbf{u}} & \frac{\partial \mathbf{f_4}}{\partial \mathbf{v}} & \frac{\partial \mathbf{f_4}}{\partial \mathbf{w}} & \frac{\partial \mathbf{f_4}}{\partial \mathbf{p}} \end{pmatrix} \tag{3.70}$$

$$\begin{aligned} \frac{\partial \delta_2^T}{\partial \mathbf{P}} &= \left(\frac{\partial \lambda^-}{\partial \mathbf{P}}\right)\frac{f(M)\Delta p}{c} + \left\{\left(\frac{\partial \Delta p}{\partial \mathbf{P}}\right)\frac{f(M)\lambda^-}{c}\right\} - \left(\frac{\partial c}{\partial \mathbf{P}}\right)\frac{f(M)\lambda^-\Delta p}{c^2} + \\ &+ \left(\frac{\partial f(M)}{\partial \mathbf{P}}\right)\lambda^-\frac{\Delta p}{c} + \left(\frac{\partial \lambda^+}{\partial \mathbf{P}}\right)\overline{\rho} f(M)\Delta u_n + \\ &+ \left\{\left(\frac{\partial \Delta u_n}{\partial \mathbf{P}}\right) f(M)\overline{\rho}\lambda^+\right\} + \left(\frac{\partial \overline{\rho}}{\partial \mathbf{P}}\right)\lambda^+ f(M)\Delta u_n + \\ &+ \left[|\lambda_2|\frac{\partial f(M)}{\partial \mathbf{P}} - (1-f(M))\frac{\partial |\lambda_2|}{\partial \mathbf{P}}\right]\overline{\rho}\Delta u_n + \\ &- (1-f(M))|\lambda_2|\left[\left(\frac{\partial \overline{\rho}}{\partial \mathbf{P}}\right)\Delta u_n + \left\{\left(\frac{\partial \Delta u_n}{\partial \mathbf{P}}\right)\overline{\rho}\right\}\right] \end{aligned} \tag{3.71}$$

In the approximate Thornber-Roe Jacobian, Equation (3.71) is simplified,

$$\frac{\partial \delta_2^T}{\partial \mathbf{P}} \approx \Big(\frac{\partial \Delta p}{\partial \mathbf{P}}\Big)\frac{f(M)\lambda^-}{c} + \Big(\frac{\partial \Delta u_n}{\partial \mathbf{P}}\Big)\overline{\rho}\big[f(M)\lambda^+ - (1-f(M))|\lambda_2|\big] \tag{3.72}$$

3.3.4 All-Mach Roe Jacobian

As the eigenvalues are scaled, the terms highlighted in bold are modified with respect to the O-Roe Jacobian. See Equations (3.74) and (3.75) for details.

$$\Big(\frac{\partial \mathbf{F}}{\partial \mathbf{P}}\Big)_{\mathbf{A-Roe}} = \begin{pmatrix} \frac{\partial f_0}{\partial \rho} & \frac{\partial \mathbf{f_0}}{\partial \mathbf{u}} & \frac{\partial \mathbf{f_0}}{\partial \mathbf{v}} & \frac{\partial \mathbf{f_0}}{\partial \mathbf{w}} & \frac{\partial \mathbf{f_0}}{\partial \mathbf{p}} \\ \frac{\partial f_1}{\partial \rho} & \frac{\partial \mathbf{f_1}}{\partial \mathbf{u}} & \frac{\partial \mathbf{f_1}}{\partial \mathbf{v}} & \frac{\partial \mathbf{f_1}}{\partial \mathbf{w}} & \frac{\partial \mathbf{f_1}}{\partial \mathbf{p}} \\ \frac{\partial f_2}{\partial \rho} & \frac{\partial \mathbf{f_2}}{\partial \mathbf{u}} & \frac{\partial \mathbf{f_2}}{\partial \mathbf{v}} & \frac{\partial \mathbf{f_2}}{\partial \mathbf{w}} & \frac{\partial \mathbf{f_2}}{\partial \mathbf{p}} \\ \frac{\partial f_3}{\partial \rho} & \frac{\partial \mathbf{f_3}}{\partial \mathbf{u}} & \frac{\partial \mathbf{f_3}}{\partial \mathbf{v}} & \frac{\partial \mathbf{f_3}}{\partial \mathbf{w}} & \frac{\partial \mathbf{f_3}}{\partial \mathbf{p}} \\ \frac{\partial f_4}{\partial \rho} & \frac{\partial \mathbf{f_4}}{\partial \mathbf{u}} & \frac{\partial \mathbf{f_4}}{\partial \mathbf{v}} & \frac{\partial \mathbf{f_4}}{\partial \mathbf{w}} & \frac{\partial \mathbf{f_4}}{\partial \mathbf{p}} \end{pmatrix} \tag{3.73}$$

$$\begin{aligned} \frac{\partial \lambda^+}{\partial \mathbf{P}} = & -\frac{\overline{u}_n}{|\overline{u}_n|}\frac{\partial \overline{u}_n}{\partial \mathbf{P}} + \frac{1}{2}\Bigg[\frac{\overline{u}_n + f(M)c}{|\overline{u}_n + f(M)c|}\Big(\frac{\partial \overline{u}_n}{\partial \mathbf{P}} + f(M)\frac{\partial c}{\partial \mathbf{P}} + c\frac{\partial f(M)}{\partial \mathbf{P}}\Big) + \\ & + \frac{\overline{u}_n - f(M)c}{|\overline{u}_n - f(M)c|}\Big(\frac{\partial \overline{u}_n}{\partial \mathbf{P}} - f(M)\frac{\partial c}{\partial \mathbf{P}} - c\frac{\partial f(M)}{\partial \mathbf{P}}\Big)\Bigg] \end{aligned} \tag{3.74}$$

$$\begin{aligned} \frac{\partial \lambda^-}{\partial \mathbf{P}} = & \frac{1}{2}\Bigg[\frac{\overline{u}_n + f(M)c}{|\overline{u}_n + f(M)c|}\Big(\frac{\partial \overline{u}_n}{\partial \mathbf{P}} + f(M)\frac{\partial c}{\partial \mathbf{P}} + c\frac{\partial f(M)}{\partial \mathbf{P}}\Big) + \\ & - \frac{\overline{u}_n - f(M)c}{|\overline{u}_n - f(M)c|}\Big(\frac{\partial \overline{u}_n}{\partial \mathbf{P}} - f(M)\frac{\partial c}{\partial \mathbf{P}} - c\frac{\partial f(M)}{\partial \mathbf{P}}\Big)\Bigg] \end{aligned} \tag{3.75}$$

The terms that are kept in the approximate A-Roe Jacobian are the same as in the Original Roe Jacobian, taking into account the scaling in λ^+ and λ^- that affects the derivatives of δ_1 and δ_2.

$$\frac{\partial \delta_1^A}{\partial \mathbf{P}} \approx \Big(\frac{\partial \Delta p}{\partial \mathbf{P}}\Big)\frac{\lambda^{+A}}{c^2} + \Big(\frac{\partial \Delta u_n}{\partial \mathbf{P}}\Big)\frac{\overline{\rho}\lambda^{-A}}{c} \tag{3.76}$$

$$\frac{\partial \delta_2^A}{\partial \mathbf{P}} \approx \Big(\frac{\partial \Delta p}{\partial \mathbf{P}}\Big)\frac{\lambda^{-A}}{c} + \Big(\frac{\partial \Delta u_n}{\partial \mathbf{P}}\Big)\overline{\rho}\lambda^{+A} \tag{3.77}$$

In the next Chapter, the implemented modified all-Mach Roe schemes are assessed.

Chapter 4

All-Mach Methods - Cases [1]

This Chapter presents a series of test cases for validation and accuracy assessment of the different all-Mach schemes presented in Chapter 3. Simple 2D cases, such as the flow around inviscid and viscous aerofoils, were used for an initial validation of these methods, along with more challenging computations consisting of the 3D flow around the MEXICO wind turbine, in parked and rotating conditions.

4.1 Description of cases

For the validation of the all-Mach schemes, the ten test cases listed in Table 4.1 were studied. Note that for the majority of the cases the reference Mach (M_{ref}) is the free-stream Mach number; however for cases **T.VII-T.X** the tip Mach number, M_{tip}, is used. Properties of the employed grids are shown in Table 4.2.

Firstly, 2D flows around the NACA 0012 aerofoil at zero incidence angle were computed for a range of Mach numbers. The same case at two degrees of incidence was also studied, so that some flow asymmetry is present. Additionally, the viscous flow over the S809 aerofoil [136] at 2.1 degrees of incidence was computed and compared with the experimental data reported by Somers [136]. Finally, so as to study the performance of the schemes in an unsteady flow, a pitching NACA0012 aerofoil is used, at a relatively high reduced frequency ($k = 0.1$). Typical multi-block meshes were employed, as described in Ref. [144]. Figure 4.1 shows the the grids employed and the extension of the computational domain.

[1] This work is published in M. Carrión *et al.* , Implementation of All-Mach Roe-type Schemes in Fully Implicit CFD Solvers - Demonstration for Wind Turbine Flows, *International Journal for Numerical Methods in Fluids*, vol. 73, num. 8, p 693-728, 2013.

Table 4.1: Summary of test cases for the validation of all-Mach Roe-type schemes.

Case	Grid	Test	Exp./Imp.	St./Uns.	M_{ref}
T.I	G.I	NACA0012 (α : 0 deg.)	Exp.	St.	[0.001, 0.15]
T.II	G.I	NACA0012 (α : 2 deg.)	Exp.	St.	[0.001, 0.15]
T.III	G.II	3% Bump	Exp.	St.	0.01
T.IV	G.I	NACA0012 (k : 0.1)	Imp.	Uns.	0.01
T.V	G.III	S809 (α : 2.1 deg.)	Imp.	St.	0.01 & 0.1
T.VI	G.IV	Parked MEXICO	Imp.	St.	0.029
T.VII	G.IV	MEXICO WT ($15m/s$)	Imp.	St.	0.2941
T.VIII	G.IV	MEXICO WT ($10m/s$)	Imp.	St.	0.2941
T.IX	G.IV	MEXICO WT ($5m/s$)	Imp.	St.	0.2235
T.X	G.V	MEXICO WT ($15m/s$)	Imp.	St.	0.2941

Exp.: Explicit, Imp.: Implicit, St.: Steady, Uns.: Unsteady., w-t: wind turbine. The explicit study is carried out by means of the four stage Runge-Kutta scheme.

Table 4.2: Summary of employed grids in the validation of all-Mach Roe-type schemes.

Grid ID	Geometry	Size (Blocks)	Chord-(span-) wise cells	Boundaries in radii (R)
G.I	NACA0012	16,384 (8)	257 (-)	FF:15
G.II	Bump	1,680 (3)	-	W:5 H:2.073 BP:2
G.III	S809	29,240 (12)	204 (-)	FF:15
G.IV	MEXICO Blade	2M (94)	144(94)	FF: 10 W: 46.875
G.V	MEXICO Blade & Hub	2M (169)	160 (111)	I:3 O:6 FF:4
G.VI	MEXICO Blade & Hub	10M (270)	224 (176)	I:3 O:6 FF:4

FF: Far-Field, W: Width, H: Height, BP: Bump centroid position with respect to the inflow boundary.

Two 3D cases were also studied. Firstly, the parked MEXICO blade (non-rotating) was computed. Figure 4.3 (a) shows the definition of the blade pitch angle. Note that nose-down is positive angles and at $\phi = 90$ degrees the tip is completely aligned with the free-stream velocity. The blade is therefore computed as a wing, using the computational domain shown in Figure 4.3 (b).

The last test case is the MEXICO wind turbine [135] in axial flight. The blocking employed is based on a C-topology in the stream-wise direction, while an H-topology is selected for the span-wise direction. This optimises the orthogonality of the cells around the blade surface, which leads to good boundary layer resolution (Figure 4.5). Assuming that the domain is periodic in the azimuthal direction, only a third of the rotor is modelled, which allows for faster computations (Figure 4.4), using the hover formulation described in Section 2.4. In order to be able to apply periodicity at the symmetry plane, the hub was approximated as

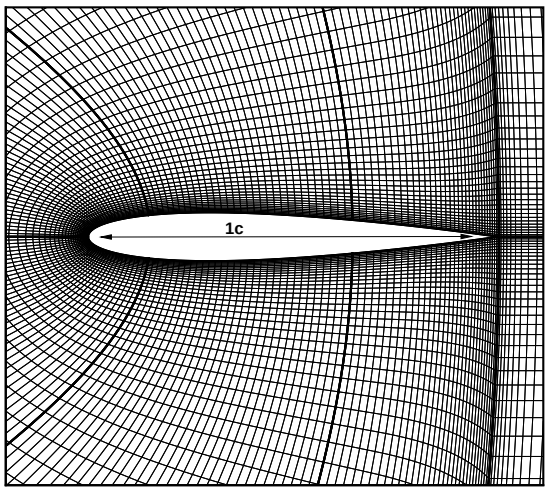

(a) Multi-block inviscid grid around the NACA0012 aerofoil.

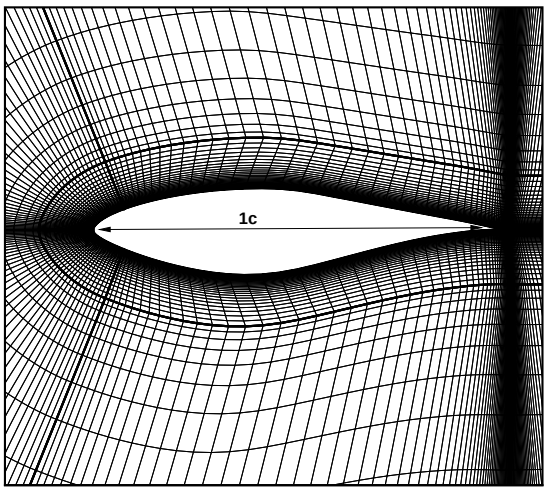

(b) Multi-block viscous grid around the S809 aerofoil

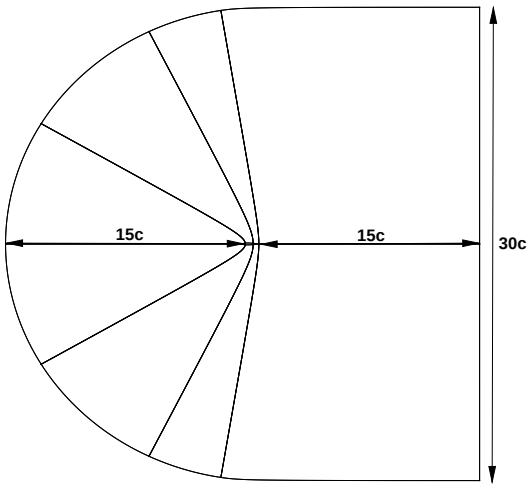

(c) Computational domain used for aerofoil grids.

Figure 4.1: Grids and computational domain employed for the 2D computations, showing the extend of the domain (in chords).

a cylinder extending from inflow to outflow. The results for the MEXICO cases are compared with the wind tunnel experimental data [135], as well as with published results obtained with incompressible flow solvers [16].

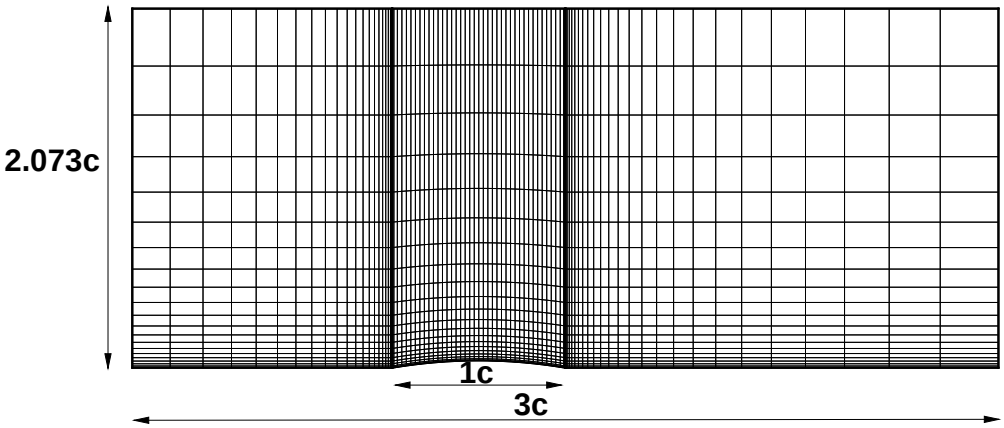

Figure 4.2: 3% bump grid.

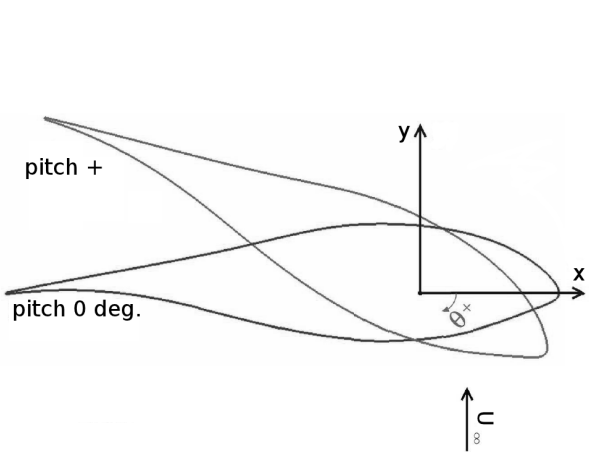

(a) Pitch angle definition of the MEXICO blade.

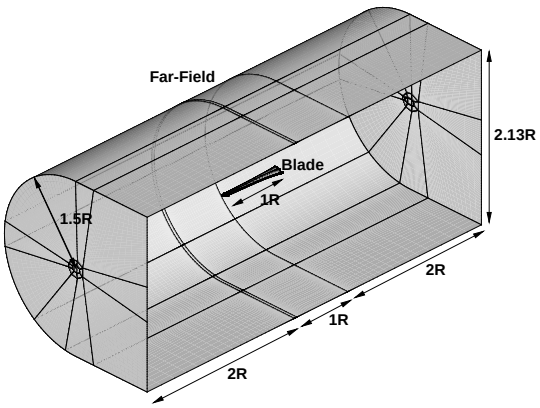

(b) Computational domain for the parked MEXICO blade.

Figure 4.3: **(a)** Pitch angle definition and **(b)** computational domain employed for the MEXICO blade in parked conditions, showing the boundary conditions and the extend of the domain (in blade radii).

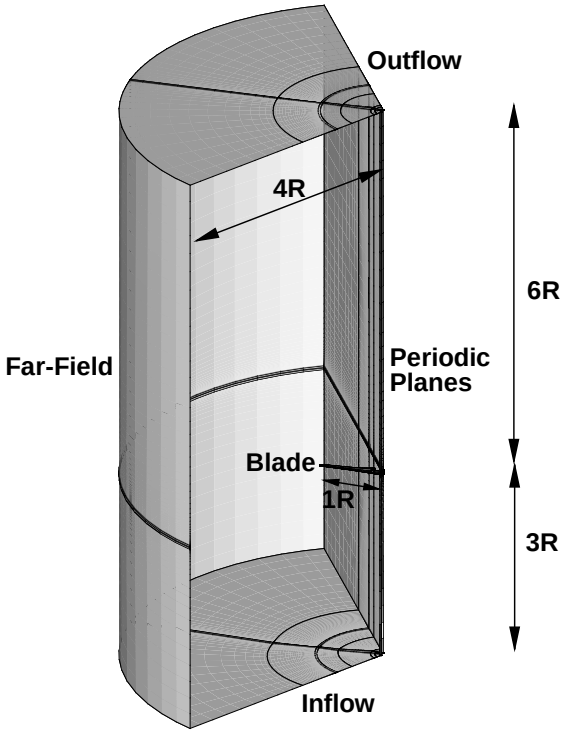

Figure 4.4: Single-blade computational domain employed for the MEXICO computation in axial flight, showing the boundary conditions and the extend of the domain in blade radii (2.25m).

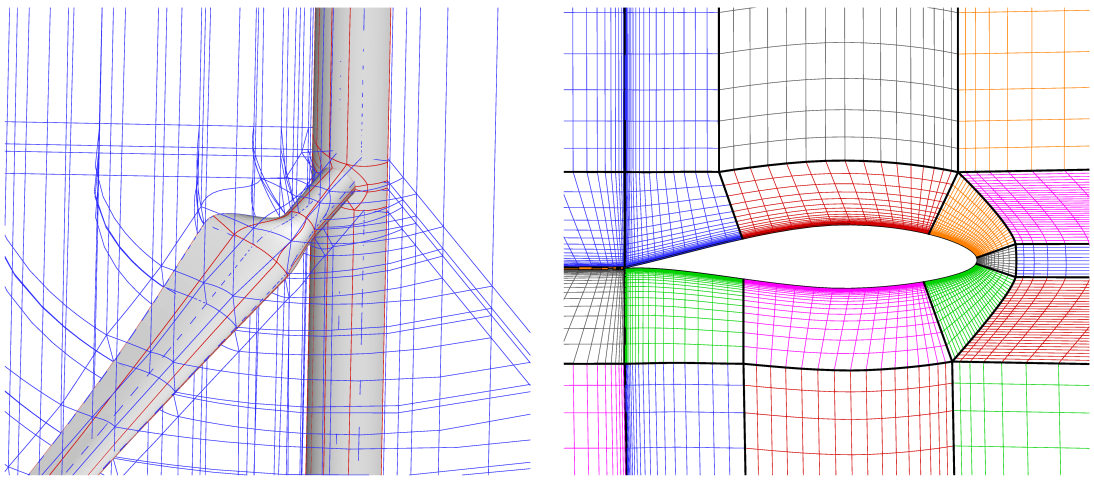

Figure 4.5: **(a)** Multi-block topology around the MEXICO blade and hub; **(b)** C-topology at the leading edge and H-topology at the trailing edge of the aerofoil.

4.2 Study of numerical parameters

4.2.1 Linear solver accuracy investigation

By default, the convergence criterion for the implicit linear solver in HMB2 is set to 4 orders of magnitude. This value was proved to be enough for relatively high Mach numbers. Since the Jacobian employed is an approximation, the linear solver does not need to be fully converged, however, for very low Mach numbers, this seems to be insufficient. As can be seen in Figure 4.6 (a), where the convergence behaviour of the NACA0012 aerofoil is plotted, at $M_\infty = 0.5$ the Osher, O-Roe and LM-Roe schemes have almost identical behaviour. However, when the Mach number is reduced, an oscillatory behaviour on the system's convergence is present in all the schemes, see Figure 4.6 (c). Note that in all cases the first 100 iterations are done explicitly and the plots only show the implicit part. That is the reason why the residuals do not start at 0. The timings in percentage with respect to the Osher's are detailed in Table 4.3.

Table 4.3: Effects of the free-stream Mach number on the convergence timings, on the NACA0012 aerofoil at two degrees incidence angle.

Solver	M_∞		
	0.5	**0.1**	**0.01**
Osher	100	100	100
O-Roe	74.0	87.8	100.4
LM-Roe	68.3	92.6	145.4

The timings are in percentages (%), based on the Osher results.

To avoid these oscillations, an investigation of the tolerance values was carried out for the same test case (see Figure 4.7). It was found that for a free-stream Mach number of 0.01, 6 orders of convergence of the linear solver were needed. Hence, the tolerance can be set as a function of the Mach number, as

$$tol = tol_{ref} M_\infty, \tag{4.1}$$

with $tol_{ref} = 10^{-4}$.

As can be seen from Figure 4.7 and Table 4.4, for all the schemes the number of iterations is highly reduced, while the relation of CPU times is maintained almost constant. Even if the LM-Roe is the slower scheme, one should bear in mind that the solution is much more accurate than using Osher's or Roe's standard solvers, as will be seen in the next sections.

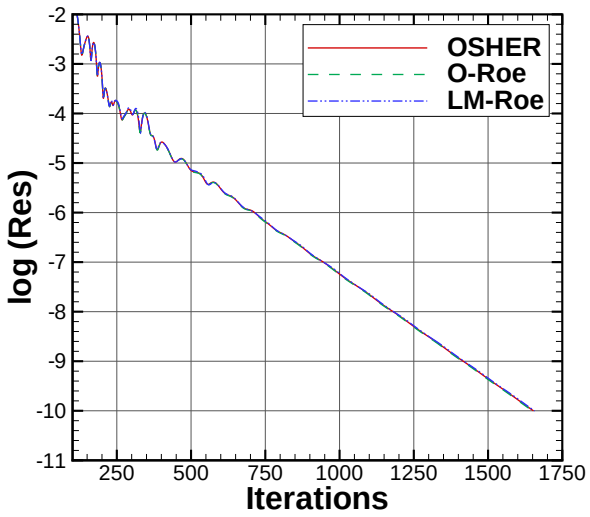

(a) $M_\infty = 0.5$

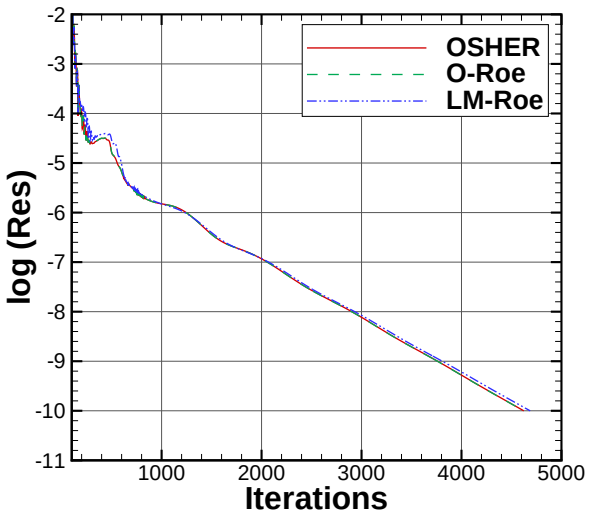

(b) $M_\infty = 0.1$

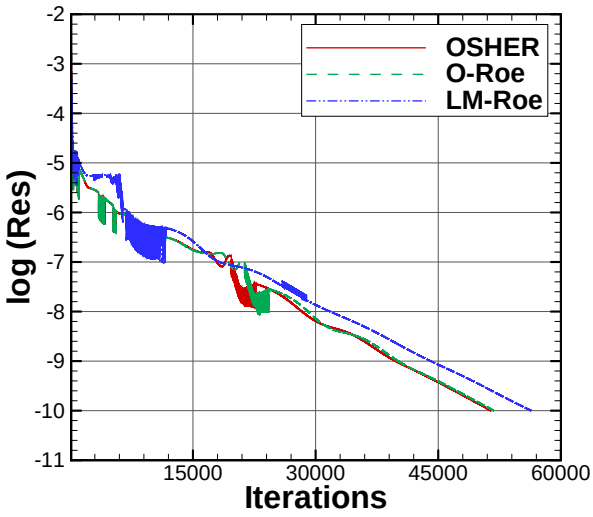

(c) $M_\infty = 0.01$

Figure 4.6: Convergence behaviour of the second order implicit Osher, O-Roe and LM-Roe schemes at three free-stream Mach numbers. The CFL is set to 10 and the linear solver is converged to 4 orders of magnitude. The test case is the flow over the NACA0012 aerofoil, at two degrees of incidence angle.

Table 4.4: Effects of the linear system tolerance on the convergence timings, for the NACA002 aerofoil at two degrees of incidence angle.

Solver	**Linear system tolerance**		
	$\mathbf{10^{-4}}$	$\mathbf{10^{-6}}$	$\mathbf{10^{-8}}$
Osher	100	100	100
O-Roe	100.4	96.6	80.8
LM-Roe	145.4	145.4	142.8

The timings are in percentages (%), based on the results for Osher's scheme.

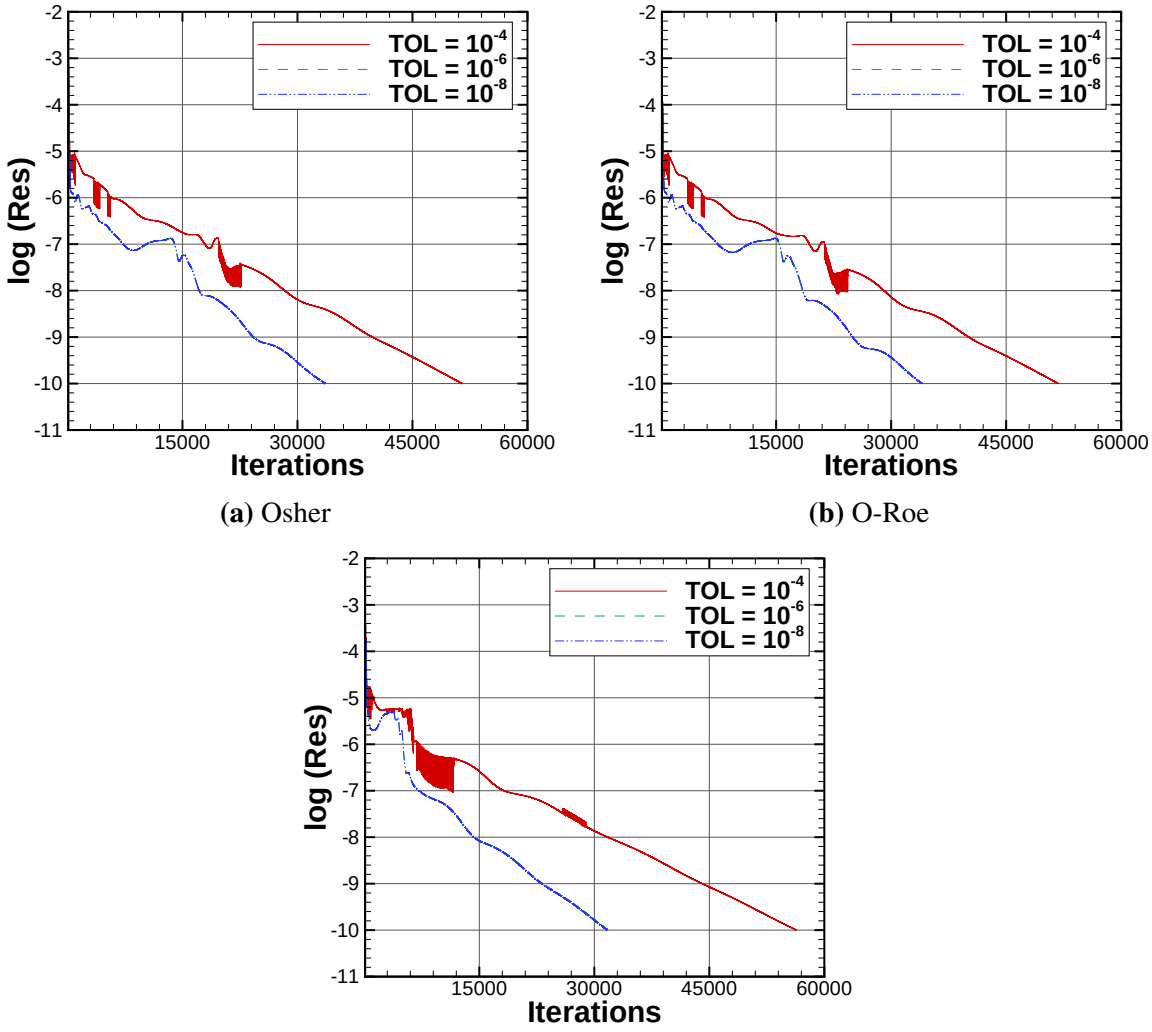

(a) Osher

(b) O-Roe

(c) LM-Roe

Figure 4.7: Convergence behaviour of the second order implicit scheme (a) Osher, (b) O-Roe and (c) LM-Roe, setting three levels of convergence of the linear solver. The CFL was 10. The test case is the flow over the NACA0012 aerofoil, at two degrees of incidence angle at $M_\infty = 0.01$.

4.2.2 CFL investigation

Numerical tests showed that the approximate LM-Roe Jacobian is very restrictive regarding the implicit CFL number that can be employed, for second order fluxes. Figure 4.8 (a) plots the convergence behaviour of this scheme for the flow over the NACA0012 aerofoil at zero incidence angle and $M_\infty = 0.01$. The lack of convergence at CFL of 60 also happens even if the numerical Jacobian (calculated with finite differences) is employed.

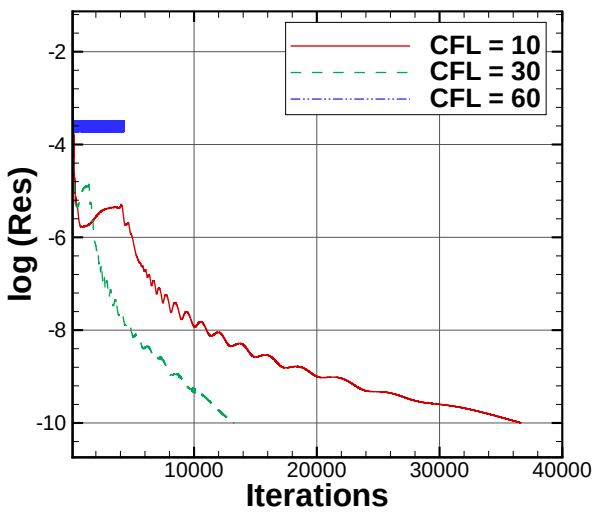

(a) LM-Roe scheme at different CFL numbers.

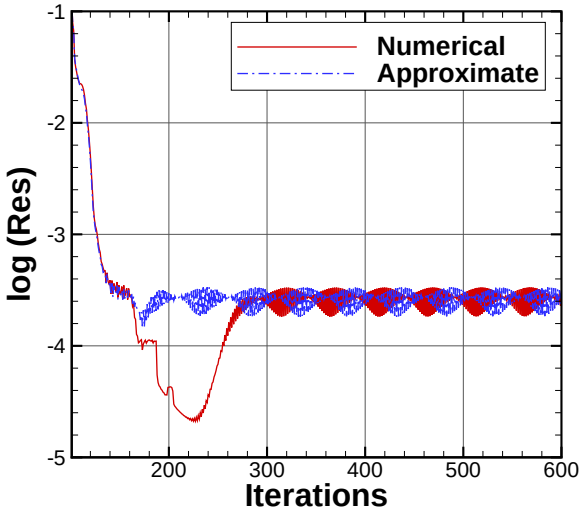

(b) LM-Roe at CFL of 60, using numerical and approximate Jacobian.

Figure 4.8: Convergence behaviour of the LM-Roe scheme at different CFL numbers employing the approximate and numerical Jacobians. The test case is the flow over the NACA0012 aerofoil, at zero incidence angle at $M_\infty = 0.01$

This behaviour is due to the fact that $f(M)$ scales some of the terms of the diagonal, making it less dominant, at very low Mach numbers. This leads to a diagonal-dominance only driven by the terms (inversely proportional to the CFL number) added to the diagonal. Hence, increasing the CFL from 30 to 60, the terms added to the diagonal are reduced by half. The stagnation areas are the ones that suffer from this restriction, where the Mach number tends to zero. Therefore, some extra dissipation is needed. It is proposed that setting a minimum value for the function $f(M)$ in the Jacobian of 0.1 (Figure 3.3) can solve the problem. As an example, for a local Mach number of 0.01 (corresponding to $f(M) \simeq 0.022$), the addition in the diagonal is four times larger. This avoids the restriction mentioned before, as can be seen in Figure 4.9.

Alternatively, the O-Roe's Jacobian (*O-J*) can be employed for this scheme, avoiding these restrictions on the CFL as well. This can be made, since the changes on this scheme are minimal. A combination between the jacobians from the O-Roe and the LM-Roe schemes was also investigated, *COMB-J*. For this, at each cell of the flow domain both O-Roe Jacobian (*O-J*) and LM-Roe (*LM-J*) Jacobians are calculated. In the diagonal terms, the maximum absolute value between them is selected, while for the off-diagonal ones, the minimum absolute value is taken. Hence, for the off-diagonal terms the LM-Jacobian is applied, while in diagonal the O-Jacobian will be applied. This avoids the restriction on the CFL selection too.

A comparison between these three approaches is shown in Figure 4.9 (b) for a CFL of 100. As can be observed, using the LM-Jacobian (with the cut-off value of 0.1) the number of iterations is lower. However, the convergence is more oscillatory and the actual time of computation is much higher than using the O-Jacobian.

Figure 4.10 shows the convergence behaviour of the three different Jacobians for the 3% bump and the S809 aerofoil at 2.1 degrees of incidence. For the former, the tolerance of the linear solver is set to 6 orders, while for the later it is set to 8 orders, since it is a viscous case. The convergence using the LM-Jacobian (floored at 0.1) is faster than with the other two. For the bump case, this difference is much more noticeable.

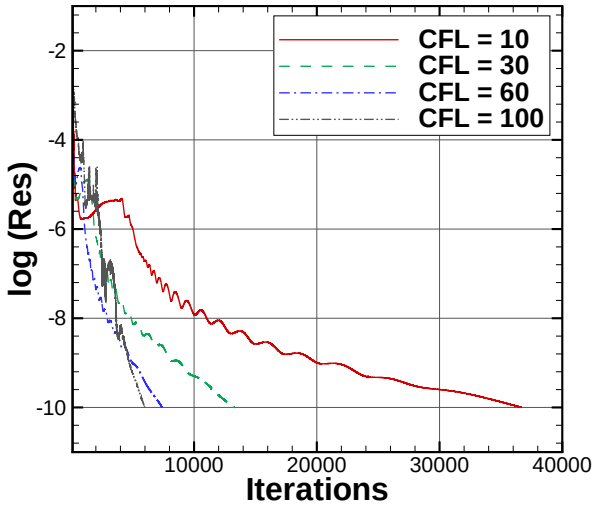

(a) LM-Jacobian at different CFL numbers.

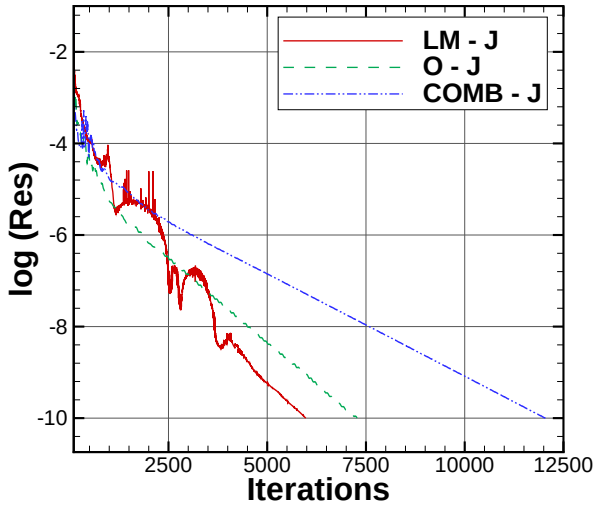

(b) Comparison between LM- and O- and combined Jacobians at a CFL=100.

Figure 4.9: Convergence behaviour of the second order fluxes for the implicit LM-Roe scheme (a) for different CFL numbers and (b) for a CFL=100, comparison with the use of the LM-Jacobian, O-Jacobian and a combination between both (COMB-J). The linear solver convergence is set to 6 orders of magnitude. The test case is the flow over the NACA0012 aerofoil, at zero incidence angle at $M_\infty = 0.01$.

Although at first glance T-Roe and LM-Roe schemes seem very different from each other, when the fluxes equations are expanded (with all the terms developed), the differences are minimal. Therefore, the assumptions that were made for the LM-Roe scheme for the implicit implementation in this scheme can be made as well. Note that the behaviour regarding the CFL number and the three different Jacobian approaches is very similar to the one found in the LM-Roe scheme; see Figures 4.11 and 4.12.

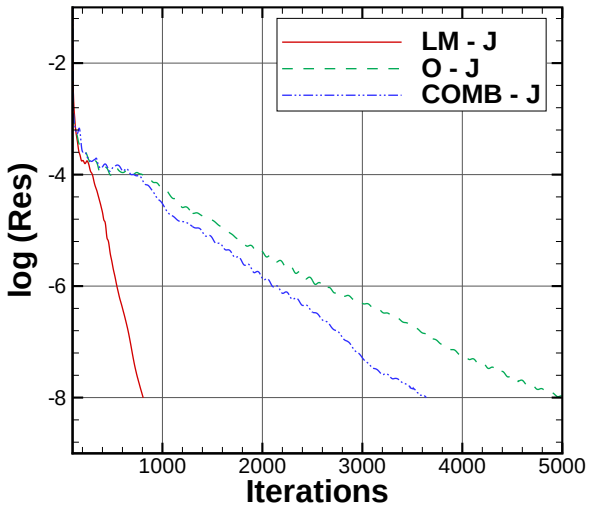

(a) 3% Bump (CFL=100).

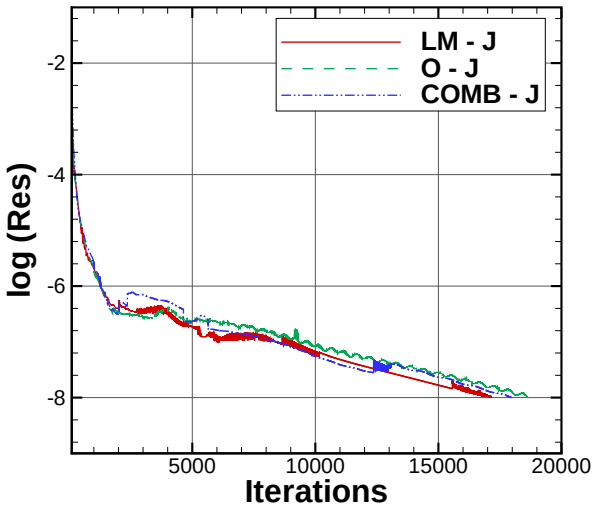

(b) S809 aerofoil at $\alpha = 2.1$ deg. (CFL=50).

Figure 4.10: Convergence behaviour of the second order fluxes for the implicit LM-Roe scheme for (a) the 3% bump at CFL of 100 and (b) the S809 aerofoil at 2.1 degrees of incidence and CFL of 50. A comparison is done between using the LM-Jacobian, O-Jacobian and a combination between both (COMB-J). The linear solver convergence is set to 6 orders of magnitude for the bump case and 8 orders for the aerofoil. The free stream Mach number is $M_\infty = 0.01$ in both cases.

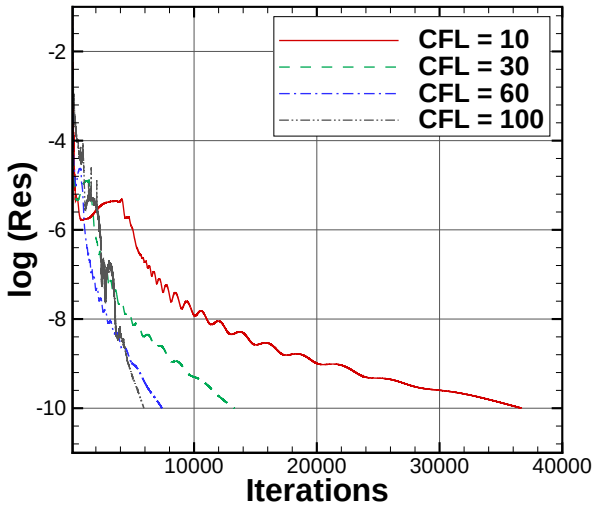

(a) T-Jacobian at different CFL numbers.

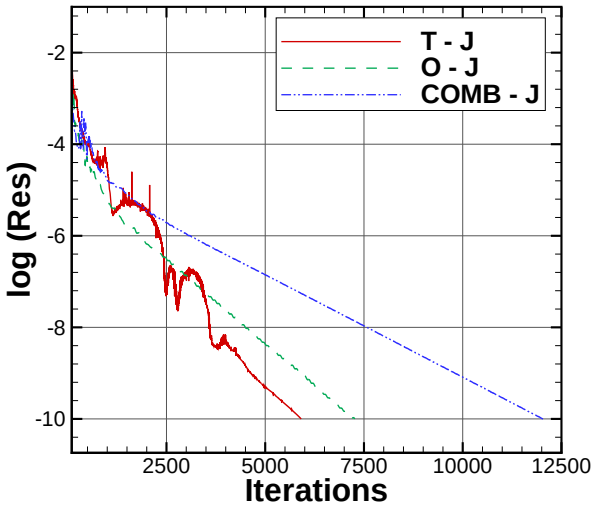

(b) Comparison between T- and O- and combined Jacobians at a CFL=100.

Figure 4.11: Convergence behaviour of the second order fluxes for the implicit T-Roe scheme (a) for different CFL numbers and (b) for a CFL=100, comparison with the use of the T-Jacobian, O-Jacobian and a combination between both (COMB-J). The linear solver convergence is set to 6 orders of magnitude. The test case is the flow over the NACA0012 aerofoil, at zero incidence angle at $M_\infty = 0.01$.

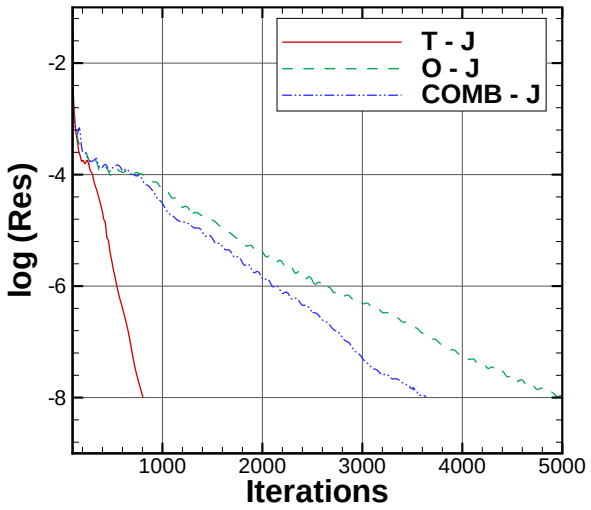

(a) 3% Bump (CFL=100).

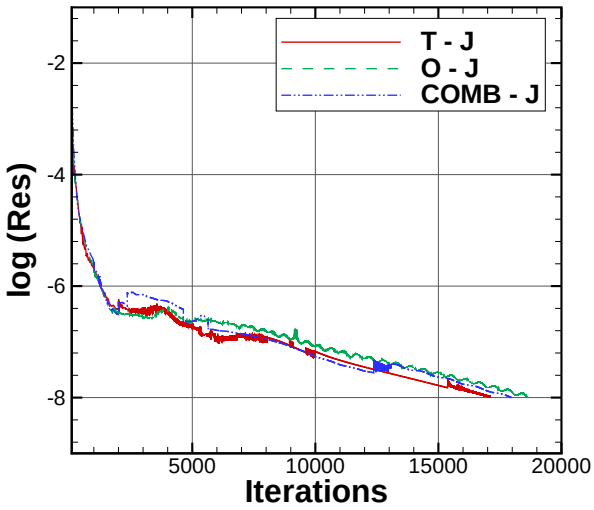

(b) S809 aerofoil at $\alpha = 2.1$ deg. (CFL=50).

Figure 4.12: Convergence behaviour of the second order fluxes for the implicit T-Roe scheme for (a) the 3% bump at CFL of 100 and (b) the S809 aerofoil at 2.1 degrees of incidence and CFL of 50. A comparison is done between using the T-Jacobian, O-Jacobian and a combination between both (COMB-J). The linear solver convergence is set to 6 orders of magnitude for the bump case and 8 orders for the aerofoil. The free stream Mach number is $M_\infty = 0.01$ in both cases.

The same restriction on the CFL number was encountered for the All-Mach Roe (A-Roe) scheme. That is the reason why the three approaches carried out for the previous schemes were also followed here. Figure 4.13 shows a comparison between simulation results obtained using these three Jacobians. Note that for the 3% bump and the S809 aerofoil, the improvement is found using the truncated A-Roe's Jacobian.

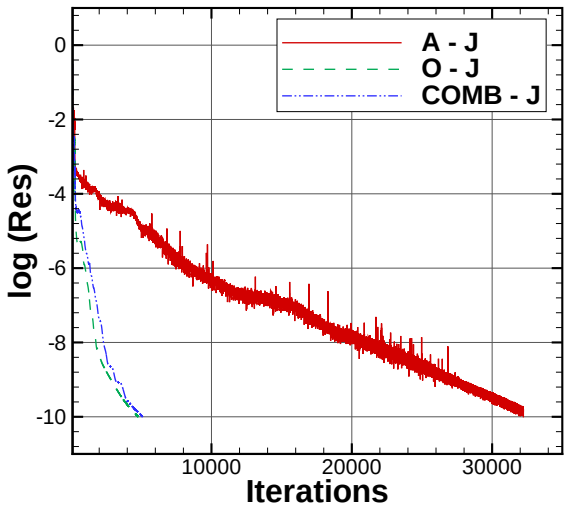

(a) NACA0012 ($\alpha = 0$ degrees).

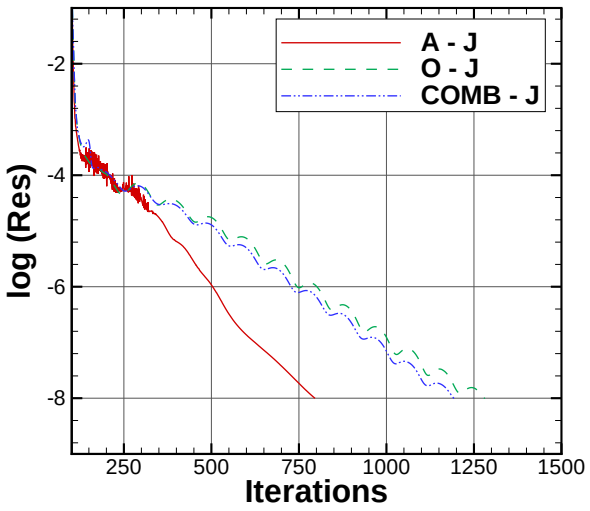

(b) 3% bump.

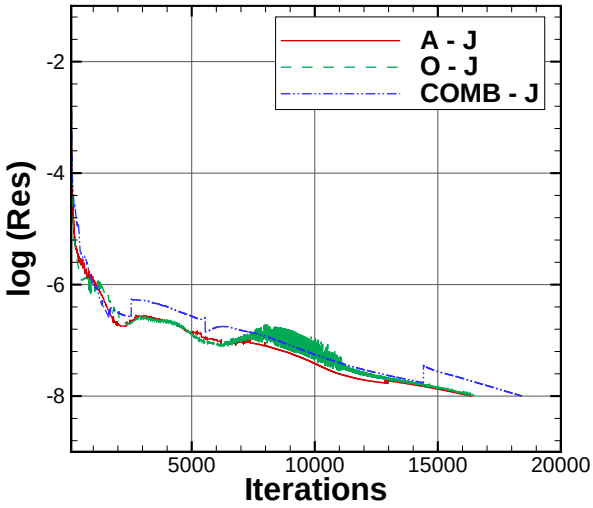

(c) S809 ($\alpha = 2.1$ degrees).

Figure 4.13: Convergence behaviour of the implicit A-Roe scheme, using the A-Roe Jacobian (*A-J*) floored at $f(M) = 0.1$, O-Roe's Jacobian (*O-J*) and a combination of both (*COMB-J*). The CFL for the NACA0012 aerofoil is 60, for the bump is 100.0 and for the viscous S809 aerofoil is 50. The linear solver is converged to 6 orders for the inviscid cases and 8 orders for the viscous one. The free-stream Mach number is $M_\infty = 0.01$.

4.3 Flow around NACA 0012 aerofoil

Case **T.I** detailed in Table 4.1 is firstly analysed employing all modified Roe schemes. For this, the surface pressure coefficient, $C_p = \frac{p-p_\infty}{\frac{1}{2}\rho U_\infty}$, is employed for comparison. Theoretically, for the low Mach numbers employed, the C_p must be identical, regardless of the free-stream Mach number, since the flow is almost incompressible. Taking as a reference the C_p distribution obtained with the incompressible solution of a panel method, the solutions for the modified Roe schemes are plotted in Figure 4.14. These were obtained by means of the explicit four-stage Runge-Kutta method. As it can be noticed, for a Mach number of 0.15 all the modified Roe schemes maintain the same C_p distribution as the benchmark case. At $M_\infty = 0.01$, the best performance is observed in the LM-, T- and P-Roe schemes, while the A-Roe begun to deviate. Finally, in the limit case of $M_\infty = 0.001$ there is a deviation from the incompressible solution in all of them. This is due to the fact that at this low Mach number the solution was not be able to converge further than five orders of magnitude. The LM-Roe and T-Roe, however, are the schemes closer to the correct solution.

In order to quantify the amount of dissipation generated by each of these schemes, the absolute value of the entropy deviation is also plotted, $\Delta S = \frac{p/\rho^\gamma}{p_\infty/\rho_\infty^\gamma} - 1.0$. Note that since these values are very small the logarithm is used. The peaks that are present mainly in the P-Roe scheme are a consequence of this way of expressing the entropy deviation. It can be noticed that, as a general trend, the lower the Mach number the less dissipative are the schemes. The higher dissipative nature of the P-Roe scheme might be due to the fact that an overall scaling of the dissipation term is done, unlike the other schemes, which only scale a small term, as detailed in Chapter 3. Moreover, LM-Roe and T-Roe are the least dissipative, although the ΔS levels are not constant along the streamlines. Conversely, A-Roe shows a constant trend, due to the fact that the reference Mach number M_{ref} acts as a global cut-off, maintaining almost constant scaling function. It is noteworthy the highest levels of dissipation are near the trailing edge of the aerofoil and become sharper as the Mach number is reduced.

Regarding the computed drag, Table 4.5 shows the values obtained with all the schemes. As can be observed, at Mach numbers of 0.15 and 0.05 the values between them were fairly similar, while from 0.01 A- and P-Roe gave the worst results.

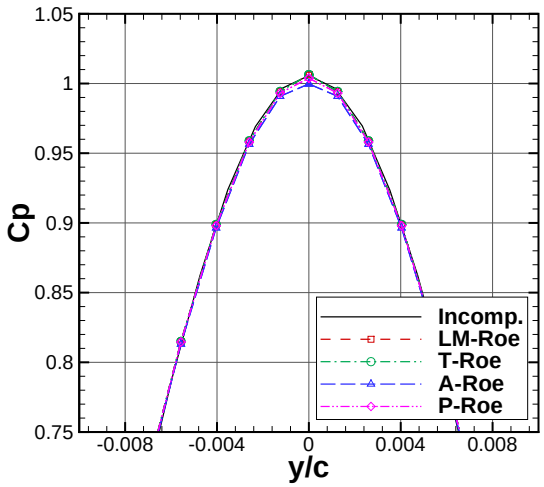

(a) $M_\infty = 0.15$: C_p near stagnation region.

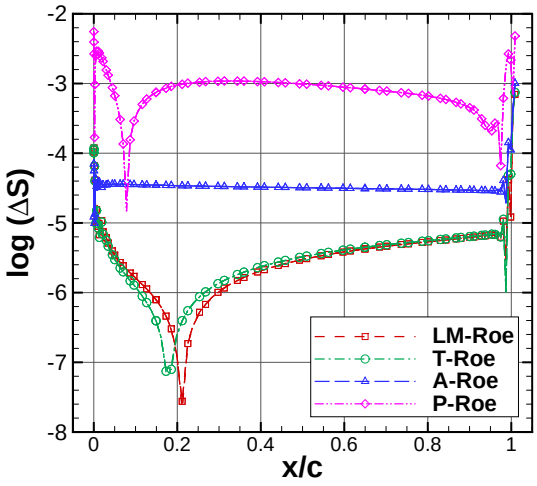

(b) $M_\infty = 0.15$: Entropy deviation.

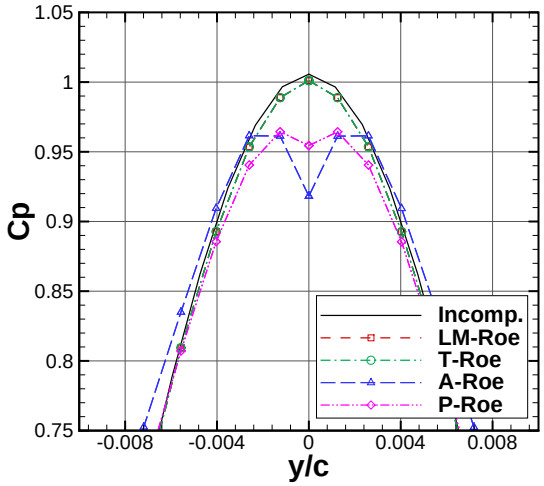

(c) $M_\infty = 0.01$: C_p near stagnation region.

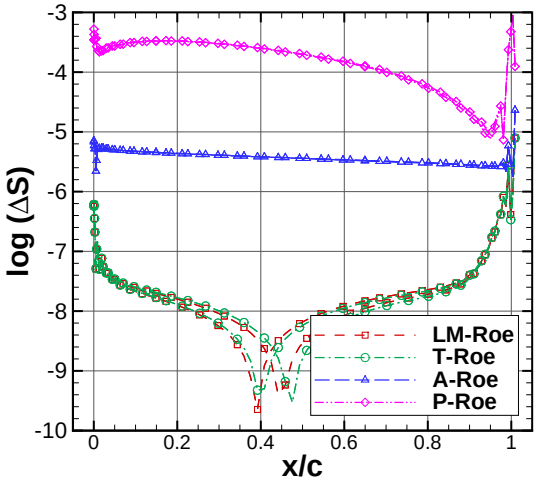

(d) $M_\infty = 0.01$: Entropy deviation.

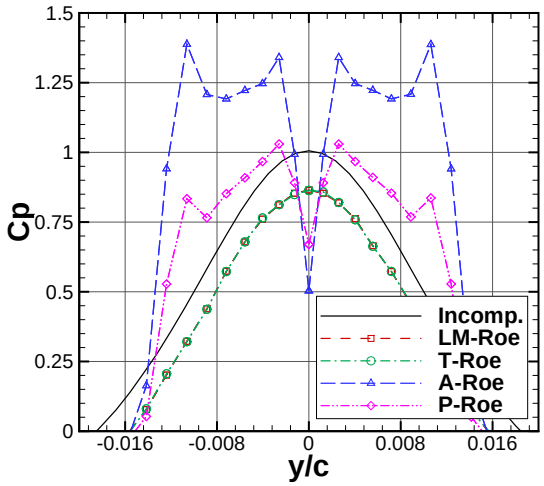

(e) $M_\infty = 0.001$: C_p near stagnation region.

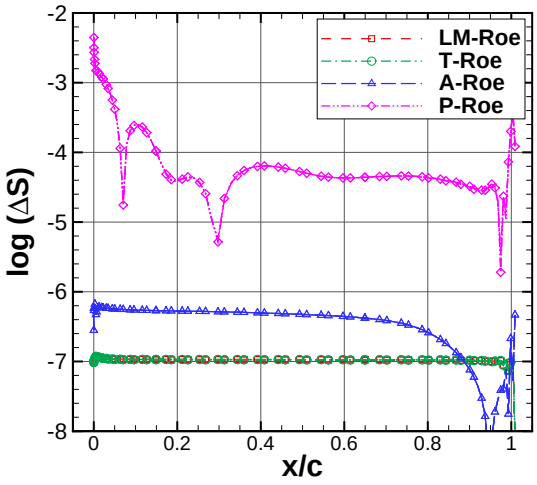

(f) $M_\infty = 0.001$: Entropy deviation.

Figure 4.14: Performance of the modified Roe schemes, compared with the solution obtained with a panel method (250 panels), for the flow over the NACA0012 aerofoil at zero incidence angle. From top to bottom: $M_\infty = 0.15$, $M_\infty = 0.01$ and $M_\infty = 0.001$. Computations run explicitly, with the four stage Runge-Kutta algorithm. (test **T.I** of Table 4.1).

Table 4.5: Obtained drag with the modified Roe schemes, for the NACA002 aerofoil at zero incidence angle.

	M_∞				
	0.15	**0.05**	**0.01**	**0.005**	**0.001**
LM-Roe	$2.57 \cdot 10^{-5}$	$3.10 \cdot 10^{-5}$	$4.03 \cdot 10^{-5}$	$4.56 \cdot 10^{-5}$	$6.08 \cdot 10^{-5}$
T-Roe	$2.64 \cdot 10^{-5}$	$3.15 \cdot 10^{-5}$	$4.06 \cdot 10^{-5}$	$4.59 \cdot 10^{-5}$	$6.08 \cdot 10^{-5}$
A-Roe	$2.58 \cdot 10^{-5}$	$5.15 \cdot 10^{-5}$	$2.48 \cdot 10^{-4}$	$4.57 \cdot 10^{-4}$	$6.43 \cdot 10^{-4}$
P-Roe	$1.70 \cdot 10^{-5}$	$3.56 \cdot 10^{-5}$	$1.17 \cdot 10^{-4}$	$2.38 \cdot 10^{-4}$	$1.08 \cdot 10^{-3}$

(test **T.I** of Table 4.1).

The same study was carried out setting the incidence angle to 2 degrees (test **T.II**). Figures 4.15 to 4.16 and Table 4.6 show the results obtained for a free-stream Mach number of 0.01. The best performance in this case is also observed in the LM- and T-Roe schemes, as the values of the C_p near the stagnation region reveal in Figure 4.15. In addition, the convergence of these two schemes is faster than the A-Roe and P-Roe schemes, as can be observed in Figure 4.16.

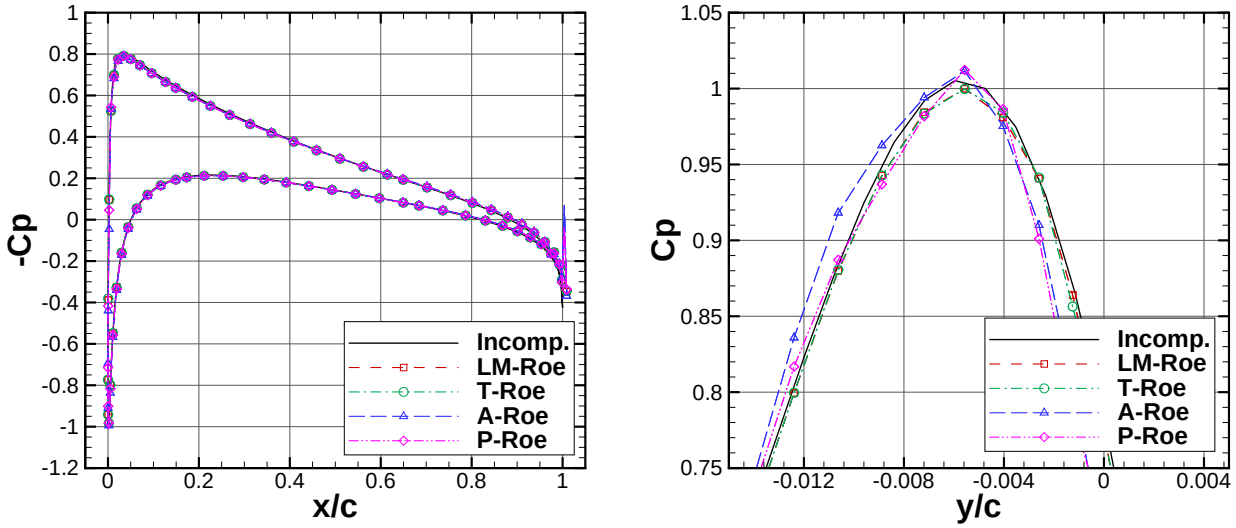

(a) Surface C_p.

(b) C_p near stagnation flow region.

Figure 4.15: Comparison of the C_p of the modified Roe schemes, taking as a benchmark the solution obtained with the panel method (250 panels), for the flow over the NACA0012 aerofoil at 2 degrees of incidence (test **T.II** of Table 4.1).

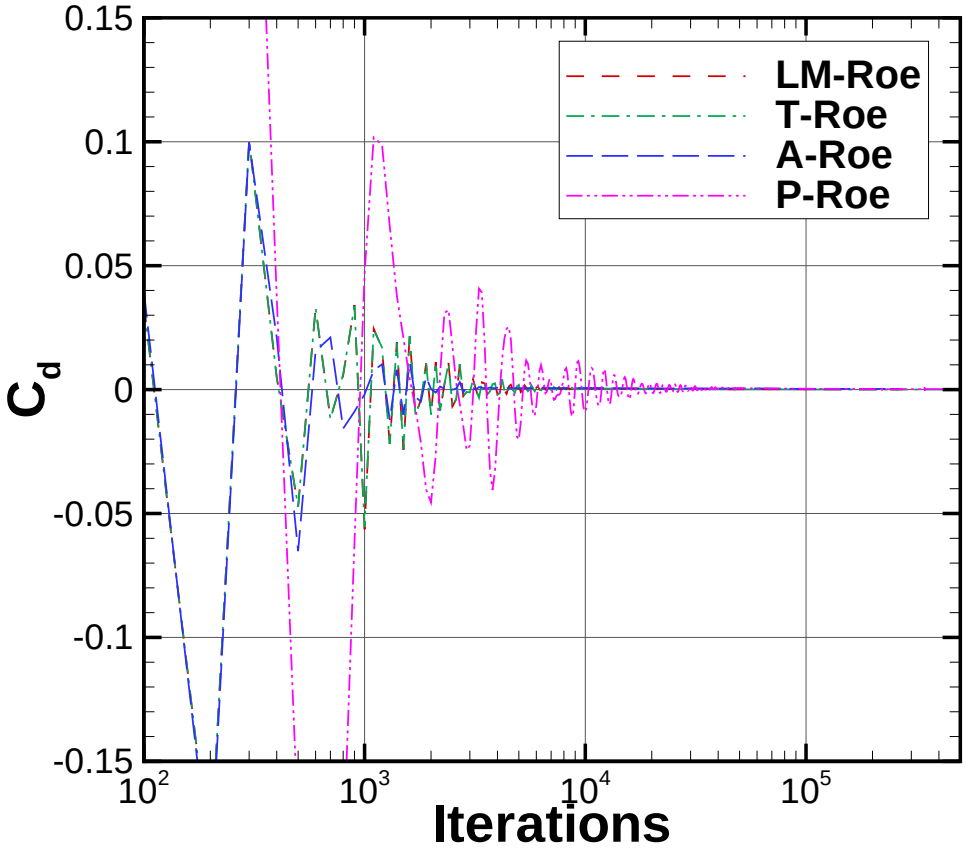

Figure 4.16: Drag convergence history of the modified Roe schemes, taking as a benchmark the solution obtained with the panel method (250 panels), for the flow over the NACA0012 aerofoil at 2 degrees of incidence (test **T.II** of Table 4.1).

Table 4.6: Obtained drag with the modified Roe schemes, for the NACA002 aerofoil at two degrees of incidence.

	$\mathbf{M_\infty = 0.01}$
LM-Roe	$4.64 \cdot 10^{-5}$
T-Roe	$4.68 \cdot 10^{-5}$
A-Roe	$2.82 \cdot 10^{-4}$
P-Roe	$1.42 \cdot 10^{-4}$

(test **T.II** of Table 4.1).

4.4 Flow over a 3% thick bump

The flow over a 3% bump (case **T.III** of Table 4.1) is studied in this section, using the explicit four stage Runge-Kutta method. For this, Figures 4.17 (a) to (d) show the contour lines of the pressure coefficients and a detail in the stagnation flow area at a free-stream Mach number of 0.01. In each plot, one of the modified

Roe schemes is compared with the solution obtained with O-Roe. As can be seen, the solution obtained with the O-Roe's scheme is not smooth. This is more apparent near stagnation regions. Regarding the solution obtained with the modified Roe schemes, the contour lines obtained with A-Roe and P-Roe seem to be smoother when compared with O-Roe; however, an oscillatory behaviour is seen at the stagnation regions too. Conversely, the LM-Roe and T-Roe preserved a smooth solution in the whole domain, therefore improving the solution. The convergence behaviour for all the schemes is plotted in Figure 4.17 (e) and Table 4.7 shows the drag values of the converged solutions. In general, all the modified Roe schemes converge slower than the original Roe, with P-Roe the slowest.

Table 4.7: Drag coefficient obtained with the modified Roe schemes, for the 3% bump at $M_\infty = 0.01$.

	$\mathbf{M_\infty = 0.01}$
O-Roe	$1.43 \cdot 10^{-3}$
LM-Roe	$2.16 \cdot 10^{-3}$
T-Roe	$2.19 \cdot 10^{-3}$
A-Roe	$8.37 \cdot 10^{-3}$
P-Roe	$5.46 \cdot 10^{-3}$

(test **T.III** of Table 4.1).

4.5 Pitching NACA 0012 aerofoil

Figure 4.18 shows the hysteresis loops for the drag and and the pressure coefficient near the stagnation region for all the Roe schemes, for the pitching NACA0012 aerofoil (test **T.IV** of Table 4.1). The free-stream Mach number was set to 0.01 and the reduced frequency was $k = 0.1$. In this case, the implicit schemes were employed with a maximum of 200 iterations in each pseudo-time steps. This leads to a convergence in each unsteady step between 3.5 and 4 orders of magnitude. As can be seen, all the schemes appear to be able to deal with unsteady flows, improving the solution of the original Roe scheme. However, the best performance was observed in LM- and T-Roe, as the C_d is closer to the 0 value (Figure 4.18 (a)). Nevertheless, when compared with the standard Roe (O-Roe), all the schemes show a great improvement, which can also be observed in Figure 4.18 (b), where the C_p at the stagnation flow region obtained with O-Roe is deviated from the correct solution.

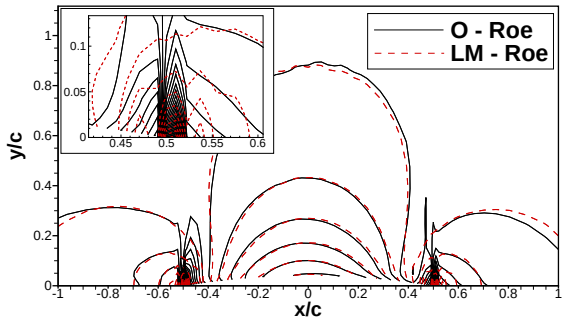

(a) LM-Roe

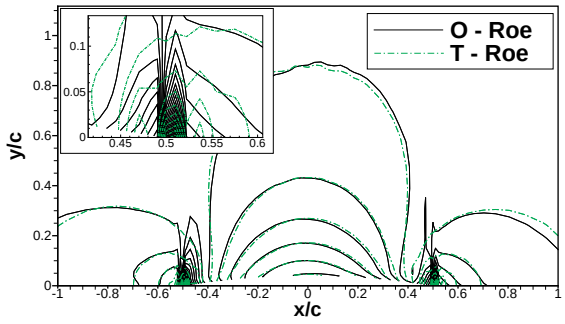

(b) T-Roe

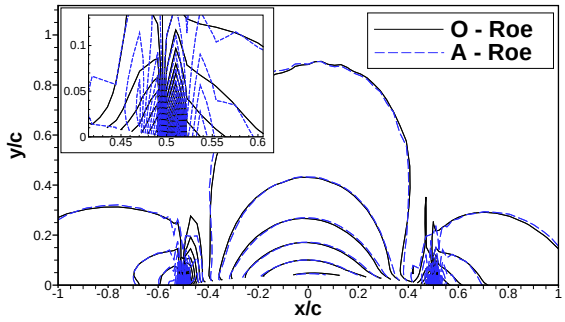

(c) A-Roe

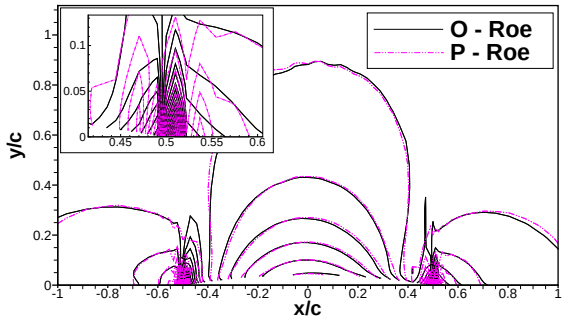

(d) P-Roe

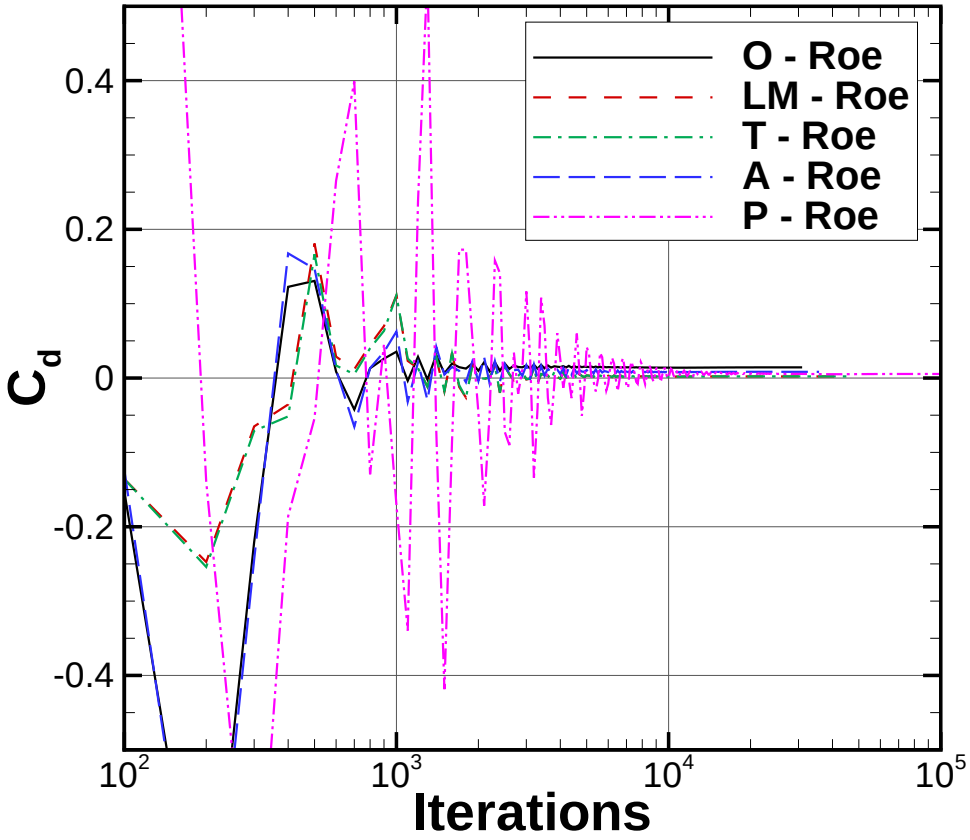

(e) C_d Convergence behaviour

Figure 4.17: Comparison of the C_p contour lines and drag convergence between the original (O-Roe) and modified Roe schemes for the 3% bump case at $M_\infty = 0.01$ (test **T.III** of Table 4.1).

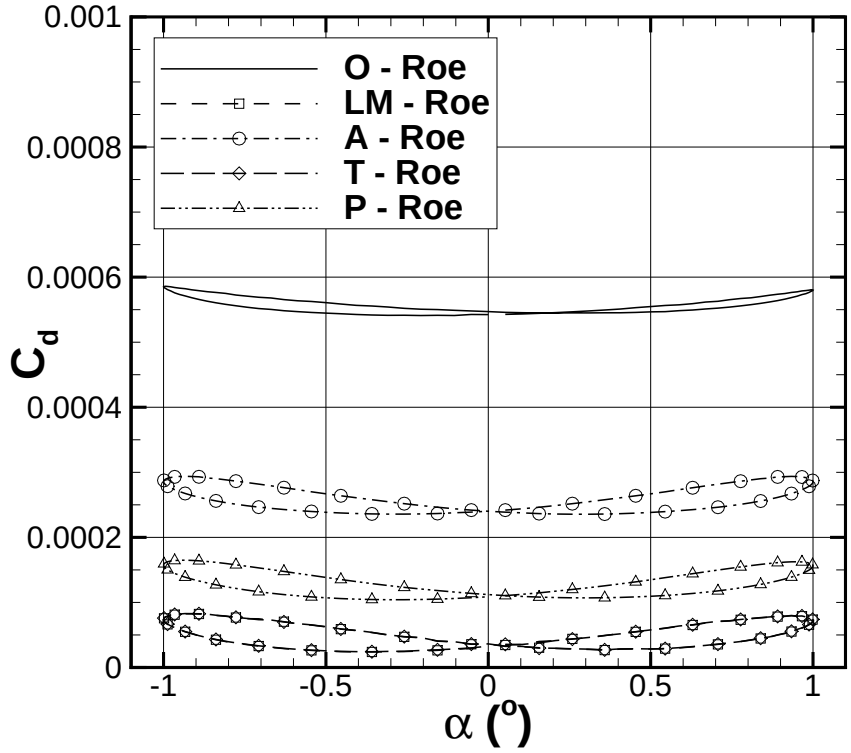

(a) Hysteresis loop of C_d.

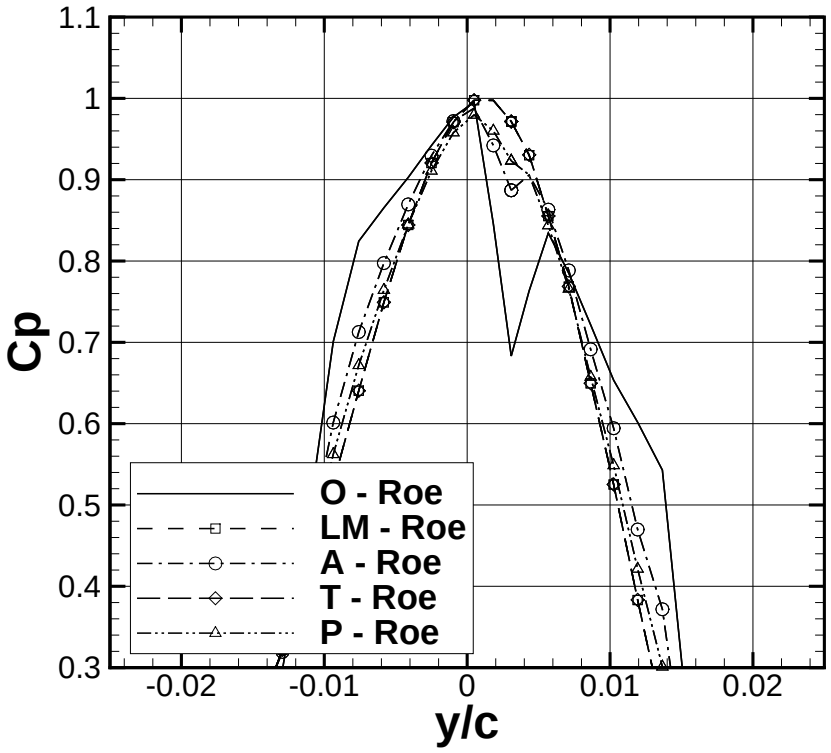

(b) C_p near stagnation flow region at $\alpha = 0.5$ deg.

Figure 4.18: Hysteresis loops for C_d and surface pressure coefficient near the stagnation flow region for the pitching NACA0012 aerofoil at $M_\infty = 0.01$, using implicit scheme (test **T.IV** of Table 4.1). The pitch angle values are obtained according to $\alpha = \alpha_0 + \alpha_1 sin(2kt)$, $\alpha_0 = 0$ deg., $\alpha_1 = 1$ deg, $k = 0.1$.

4.6 Flow around S809 aerofoil

Figure 4.19 plots the surface pressure and drag coefficient for the S809 aerofoil [136] at an incidence angle of 2.1 degrees (test **T.V** of Table 4.1). It was computed with Osher's solver[106] and the LM-Roe[117], using a simple turbulence model (k-ω), without any transition model, where the boundary layer was assumed to be fully turbulent. The results are compared with wind tunnel data published in the work by Somers [136], where the flow was tripped at the leading edge of the aerofoil.

For Mach numbers down to 0.1 the solution obtained with LM-Roe and the Osher's solvers differed by 14%. On the other hand, at lower Mach numbers, the solution obtained with the two schemes differed by 59%, where Osher gave a poor solution, while the LM-Roe scheme maintained good agreement with the experiments. As can be observed, the converged value of the LM-Roe at $M_\infty = 0.01$ is the same as at $M_\infty = 0.1$.

4.7 Parked MEXICO blade

The first 3D case studied is the parked MEXICO rotor (test **T.VI** of Table 4.1). For this, the MEXICO blade has been simulated, imposing a free-stream wind speed of $10m/s$ ($M_\infty = 0.029$) and using the k-ω turbulence model. Note that in the experiments, the parked case was tested at $30m/s$ wind. Since the objective of the present work is the study of low speed flows, a lower wind speed was selected. In fact, there are uncertainties regarding this test case as reported in [43]. The employed mesh had 2 million points and the computational domain shown in Figure 4.3 (b) was used. The pitch angle selected for this calculation was $\phi = 81°$, measured at the tip of the blade (see Figure 4.3 (a) for sign convention). Figure 4.20 shows the C_p distribution at two radial stations, computed with the Osher [106] and the LM-Roe [117] schemes. A detail of the computed stagnation values is included. As can be seen, the solution obtained with the LM-Roe scheme is much better. In the inboard section, the C_p distribution is smoother over all the surface than that obtained with Osher. In addition, the stagnation values obtained with LM-Roe are very close to 1.0, while Osher gives higher values, mainly at the outboard station.

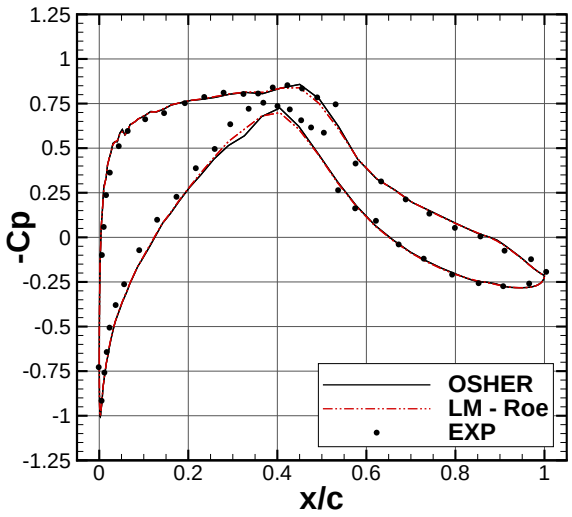

(a) Surface C_p ($M_\infty = 0.1$).

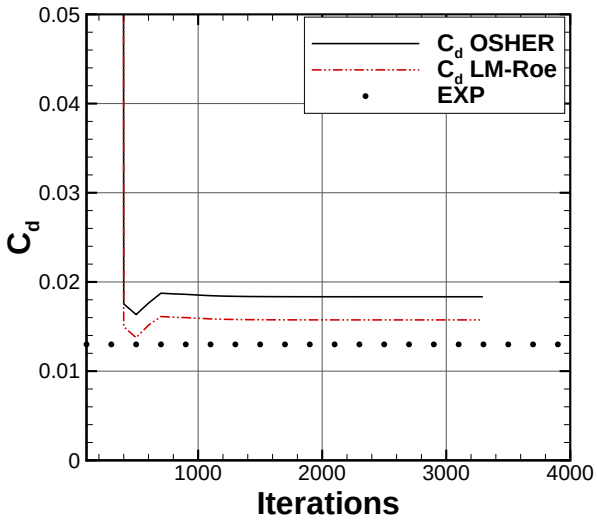

(b) C_d convergence ($M_\infty = 0.1$).

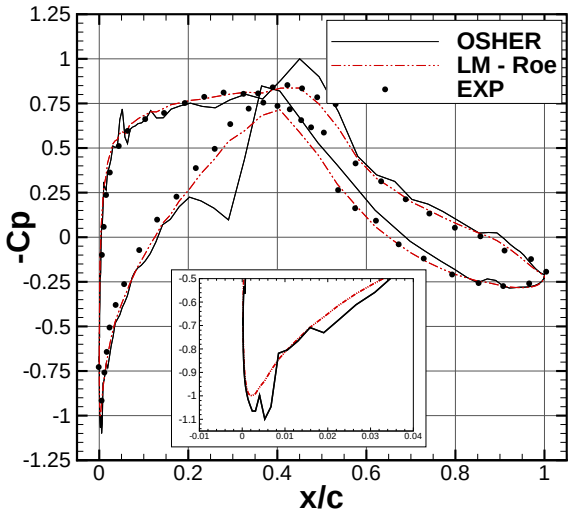

(c) Surface C_p ($M_\infty = 0.01$), with detail of stagnation.

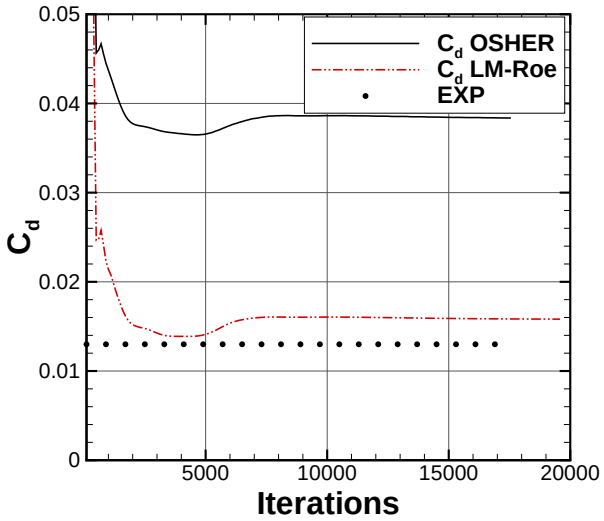

(d) C_d convergence ($M_\infty = 0.01$).

Figure 4.19: Comparison of the performance between Osher's [106] and LM-Roe [117] schemes, for the S809 aerofoil at 2.1 degrees of incidence angle, for surface C_p and the lift coefficient. Top: $M_\infty = 0.1$, Bottom: $M_\infty = 0.01$. The Reynolds number is 10^6 and the turbulence model employed is k-ω. The 2D viscous grid computed has 29,240 cells. (Test **T.V** of Table 4.1).

4.8 Rotating MEXICO wind turbine

The MEXICO blade was run in steady-state periodic formulation using the multi-block topology and computational domain in Figure 4.5, for wind speeds of 15, 10 and $5m/s$ (tests **T.VII** to **T.IX** of Table 4.1). For the first two cases, the rate of rotation was $424.5rpm$ and tip speed $100m/s$ which corresponds to tip speed ratios of $\lambda = 6.7$ and $\lambda = 10.0$, respectively. In the third case, the rotational speed was $343.3rpm$ and the tip speed was $76m/s$, corresponding to a tip speed ratio of $\lambda = 15.2$. For the computations, the reference Mach

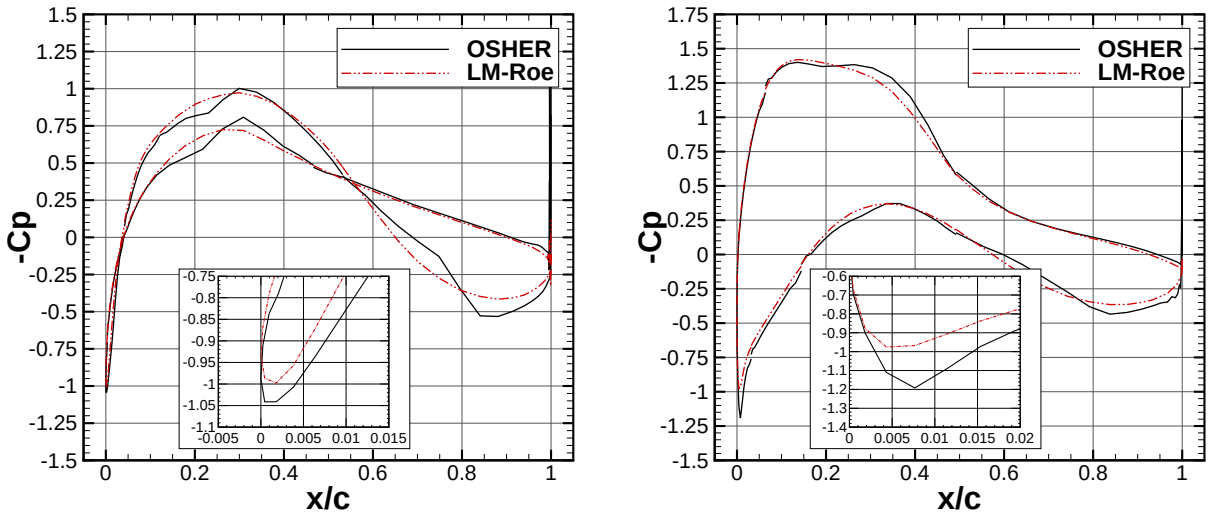

(a) 25% R, $\alpha = -5.25$ deg. **(b)** 60% R, $\alpha = 4.20$ deg.

Figure 4.20: Surface C_p distribution at two MEXICO radial stations, for parked conditions at wind speed of $10m/s$ ($M_\infty = 0.029$), test **T.VI** of Table 4.1. Comparison between Osher [106] and LM-Roe [121] schemes. A detail of the stagnation flow region is included.

number was the one at the tip of the blade: 0.2941 for the two first cases and 0.2235 for the last one. The turbulence model employed was the k-ω and a 2.6 million cells grid was used. Computations were carried out with the Osher [106] and LM-Roe [117] schemes, and compared to each other and to the results obtained by Bechmann *et al.* [16], who employed an incompressible solver (*EllipSys*).

Figure 4.21 shows the convergence behaviour of the integrated thrust and torque coefficients (C_T and C_Q), for the three cases obtained with the Osher [106] and LM-Roe [117] schemes. As can be seen, both schemes take approximately the same number of iterations to reach a converged value. Although the differences between schemes are minimal, LM-Roe converges to slightly lower values than Osher. In fact, the biggest difference is seen in the lowest wind speed case.

Furthermore, Figure 4.22 plots the computed pressure coefficients at two radial stations: one close to the root and the other at the tip of the blade. Regarding the $15m/s$ wind speed, (Figures 4.22 (a) and (b)), the solutions obtained with the different schemes are very similar. LM-Roe gives slightly lower values than Osher in both pressure and suction sides. However, the differences between the two schemes are minimal. This may be due to the fact that, for this test case, the Mach numbers found around the blade are not low enough to highlight differences on the schemes.

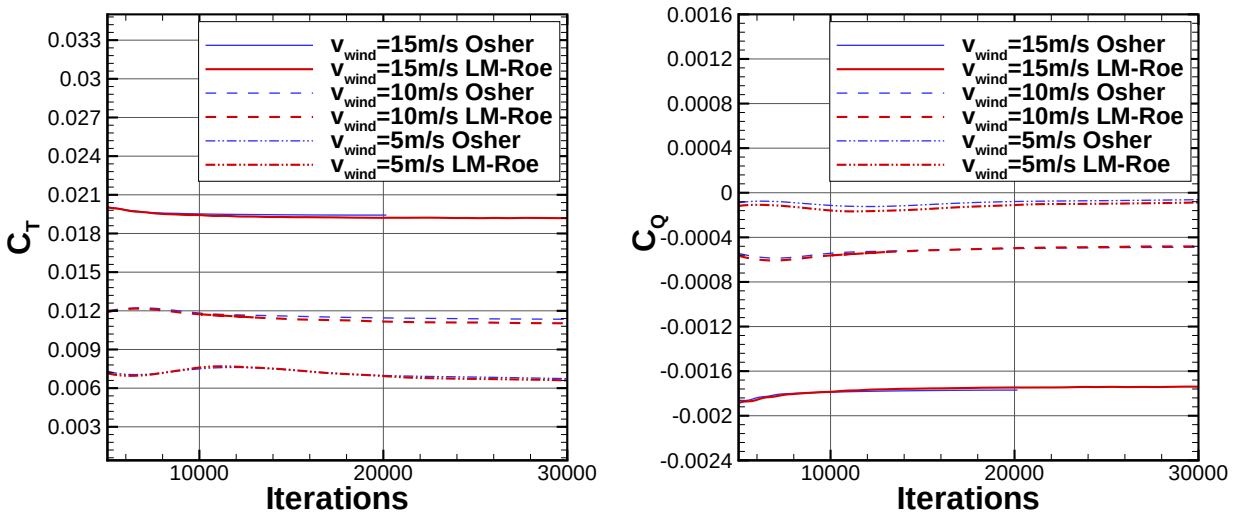

(a) Thrust coefficient.

(b) Torque coefficient.

Figure 4.21: Convergence behaviour of the (a) thrust and (b) torque coefficients for the MEXICO rotor in steady-state axial flight, for wind speeds of $15m/s$, $10m/s$ ($M_{tip} = 0.2941$) and $5m/s$ ($M_{tip} = 0.2235$), tests **T.VII** to **T.IX** of Table 4.1. Comparison between the Osher [106] and LM-Roe [117] schemes.

For the $10m/s$ wind speed (Figure 4.22 (c) and (d)), the pressure distribution is also compared with the incompressible solution obtained with the *EllipSys* solver. As can be observed, the solution obtained with the Osher solver seems to be less smooth than the LM-Roe in the inner station, where the lower speeds are found and therefore the low-Mach effects are present. When compared with the incompressible solution, a small difference in the suction side is found. Although minimal, the biggest difference was observed in the $5m/s$ wind speed case and at the root (Figure 4.22 (e)). There, the C_p obtained with the LM-Roe scheme was much smoother than Osher's and closer to the experiments in the pressure side. As a general trend, it was observed that regarding the loads not much differences between the standard and the low-Mach schemes. This may due to the fact that for all cases the reference Mach number is the same and relatively high, $M_{tip} = 0.2941$.

To capture the near wake, the $15m/s$ wind speed case was computed using a finer grid (10 million cells), refined in the area between 75% and 140% span. In this region, the cells had a size of 5% of the chord length. Hence, a total of 8 cells approximately were defining the vortex core. Figure 4.23 shows contour lines of the axial velocity components, computed with the Osher's and the LM-Roe's solvers and compared with the experimental data. As can be seen, the LM-Roe scheme seems to capture better the vortex positions than the Osher scheme. This is due to the less dissipative nature of this scheme.

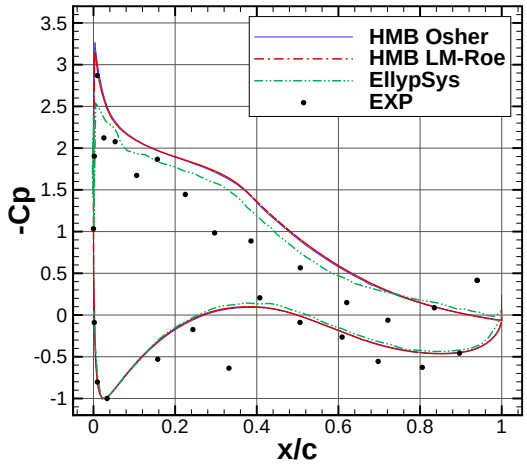

(a) $15m/s$: 25% R

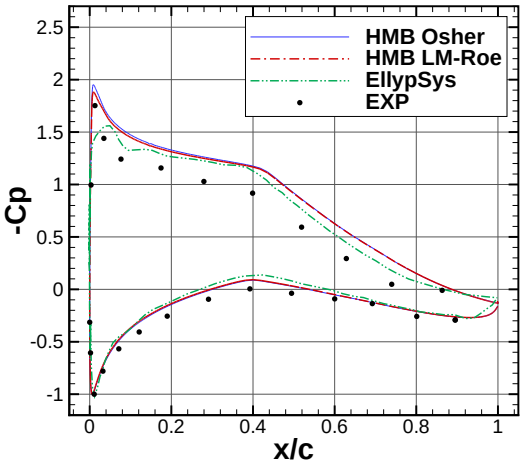

(b) $15m/s$: 92%R

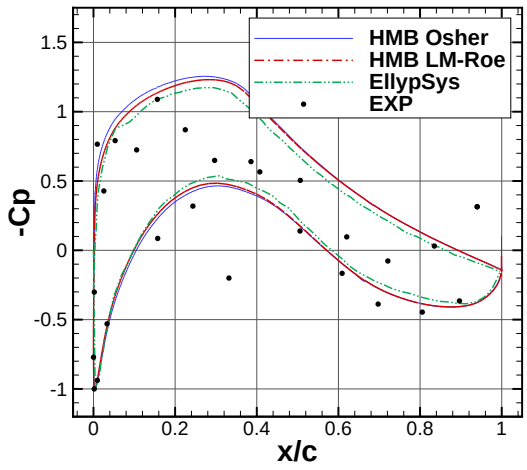

(c) $10m/s$: 25% R

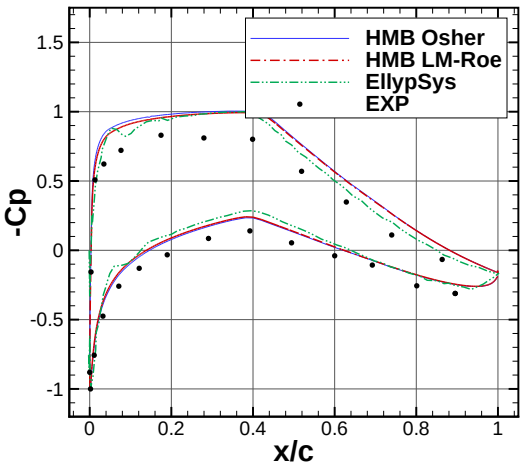

(d) $10m/s$: 92%R

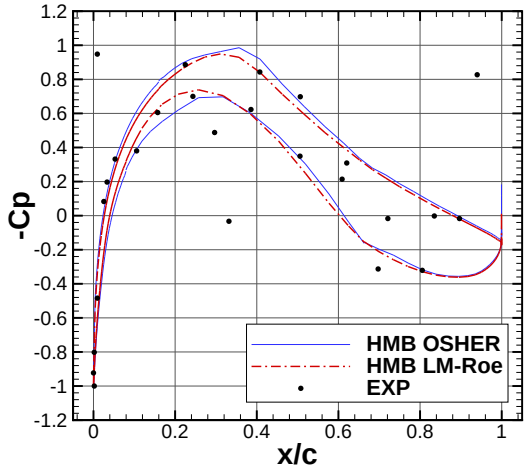

(e) $5m/s$: 25% R

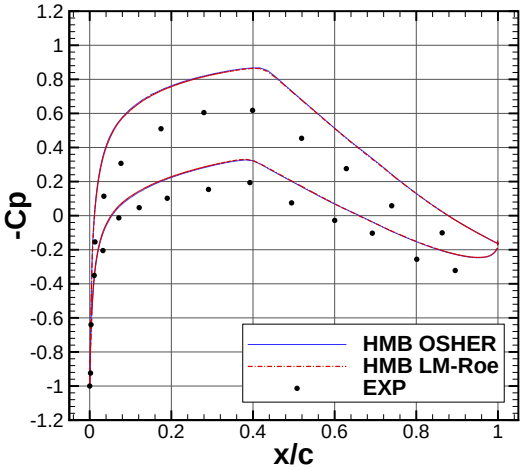

(f) $5m/s$: 92%R

Figure 4.22: Surface C_p at 25% and 92% R of the MEXICO blade, for wind speeds of $15m/s$, $10m/s$ ($M_{tip} = 0.2941$) and $5m/s$ ($M_{tip} = 0.2235$) in steady-state hover formulation, tests **T.VII** to **T.IX** of Table 4.1. Comparison between the compressible solutions obtained with HMB2 (Osher [106], O-Roe [121] and LM-Roe [117] schemes), the results obtained by Bechmann *et al.* [16] with the full incompressible solver *Ellipsys* and the experimental data. Note that the C_p at each station is normalised by $C_{p_{max}}$.

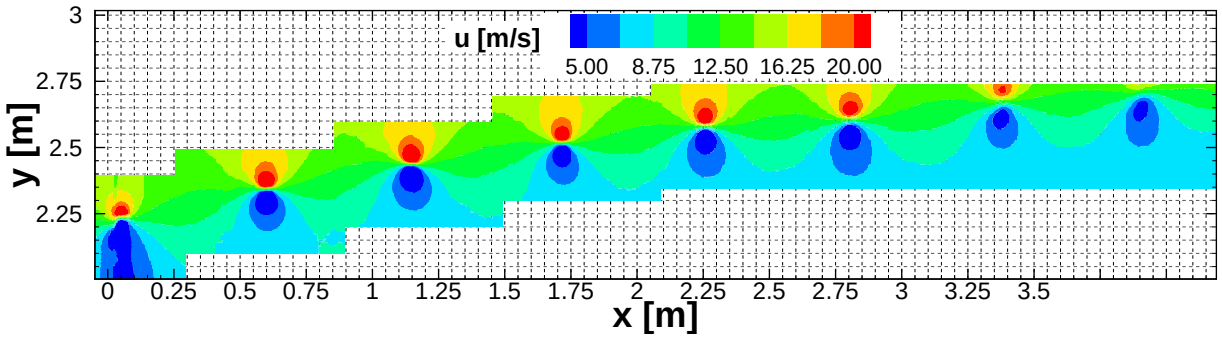

(a) Experiments (PIV)

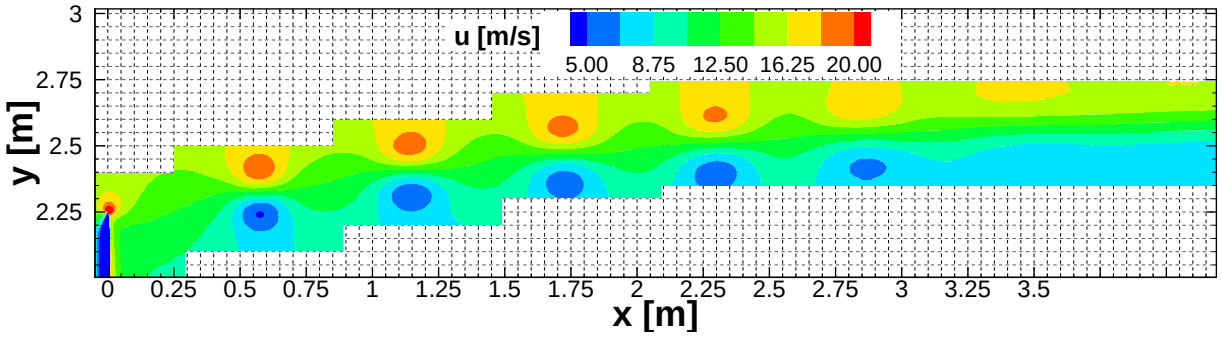

(b) Osher

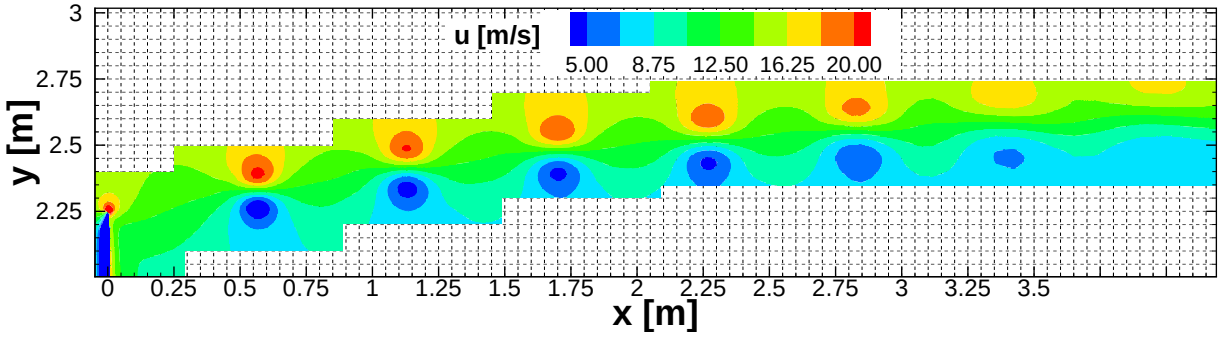

(c) LM-Roe

Figure 4.23: Contour lines of the axial velocity component, for a wind speed of $15m/s$ ($M_{tip} = 0.2941$) in steady-state MEXICO blade hover formulation (tests **T.X** of Table 4.1). The blade is set to an azimuth angle of 270 degrees.

Chapter 5

Wake Study of the MEXICO Rotor [1]

In this Chapter, a study of the velocity field behind the MEXICO rotor is presented, for three wind speeds (10, 15 and 24m/s). Firstly, a preliminary study involving grid convergence regarding the blade loads is performed, along with sensitivity studies on the blade pitch angle and the employed turbulence model. The wake is then visualised with different techniques and the vortex core radii and positions are estimated. The three components of the velocity are compared against experimental data, including the flow at the rotor blade and the near wake up to one and a half rotor diameters downstream. Finally, the capability to resolve the vortex structure between two mesh densities is presented.

5.1 Preliminaries

5.1.1 Description of cases

As MEXICO is a three-bladed rotor, only a third of the domain was meshed, see Figure 5.1 (b), assuming periodicity of the problem in the azimuthal direction. Periodicity is therefore applied as boundary condition in the periodic planes to account for the effect of the other two blades. Table 5.1 lists the employed grids for this study. The blocking employed was based on a C-topology at the leading edge of the blade, while an H-topology was selected at the trailing edge, for good boundary layer resolution (see Figure 5.1 (a)). The first grid space normal to the blade is $2.4 \cdot 10^{-6}$m, which gives y^+ less than 1.0 all over the blade.

[1] This work is published in M. Carrión *et al.* , Computational Fluid Dynamics Analysis of the Wake behind the MEXICO Rotor in Axial Flow Conditions, *Wind Energy*, 2014, DOI: 10.1002/we.1745.

The results are not sensitive to the employed outflow condition, since the wake is not well preserved near the outflow boundary. Due to the coarse grid employed away from the near blade region, the coherency of the wake structure is lost, so free-stream conditions were assumed. The position of the outflow boundary was assessed, with a case with the outflow boundary located twice as far downstream ($12R$). Comparison of the loads showed differences of less than 2%, since the region near the rotor was already well resolved with the shorter computational domain and the induced flow did not change, not affecting therefore the loads. This comparison is presented in Section 5.1.3. The velocity field up to $1R$ downstream was not affected either, as is shown in Section 5.3. Hence, for the study presented in the current paper, the topology with the shorter domain was selected, which enables savings on computational cost. To be able to apply periodicity at the symmetry plane, a hub approximated as an infinite cylinder was considered in the geometry.

For controlling the refinement of the grid in the wake, two techniques were employed: the sliding planes, described in Section 2.6.1, and the overset technique known as chimera (presented in Section 2.6.2). Figure 5.1 (b) shows the configuration of the two sliding planes parallel to the rotor plane at $\pm 0.1R$. Regarding the chimera grid, a total of three levels were employed: *level 0* is the background, *level 1* is a ring for better resolution of the vortices until $1.3R$ downstream and *level 2* is the blade. Figures 5.1 (c) and (d) show its details.

Table 5.1: Summary of mesh properties for the PIV study of the MEXICO rotor.

Grid	Type	Size (Blocks)	Chord-(span-) wise cells	Cell size at wake (%c)	Boundaries in Radii (R)	Cores (Time)
1	Sliding Planes (2)	10M (270)	224 (176)	5%	I:3 O:6 FF:4	30 (48h.)
2	Sliding Planes (2)	64M (757)	340 (326)	2.5%	I:3 O:6 FF:4	64 (120h.)
3	Chimera (3)	120M (1720)	340 (338)	1.5%	I:3 O:6 FF:4	128 (120h.)

I: Inflow, O: Outflow, FF: Far-field, c: maximum aerodynamic chord of the blade.

All the computations presented in this work were performed in the N8 HPC Facility 'Polaris' from Leeds University. Each CPU is composed of 8 cores of Intel@ Xenon E5-2670 type. Table 5.1 includes the number of cores employed for the computation of each grid, along with the computational time.

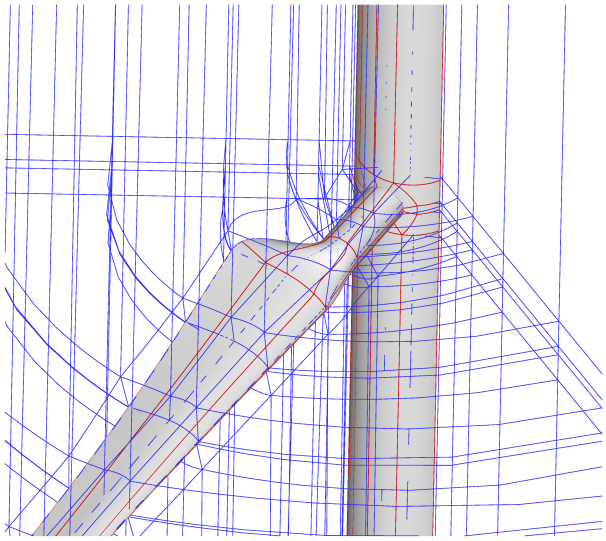

(a) Multi-block topology blocking.

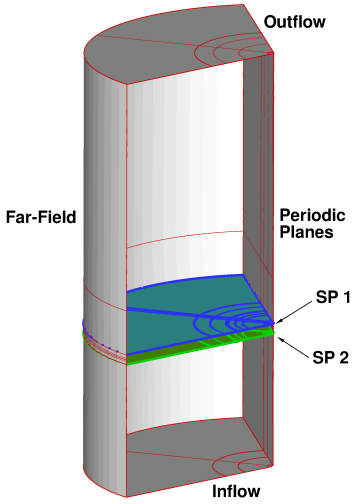

(b) Sliding planes configuration.

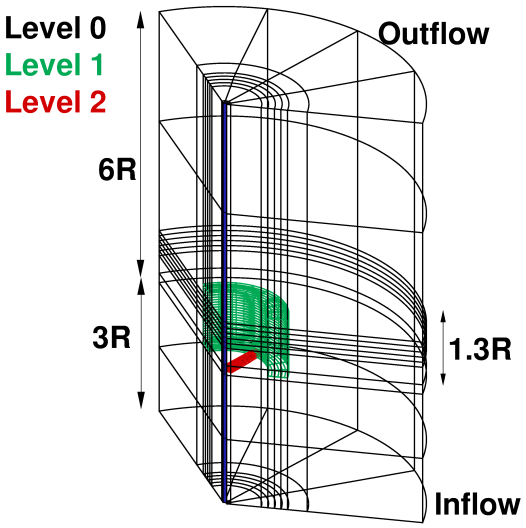

(c) Chimera configuration.

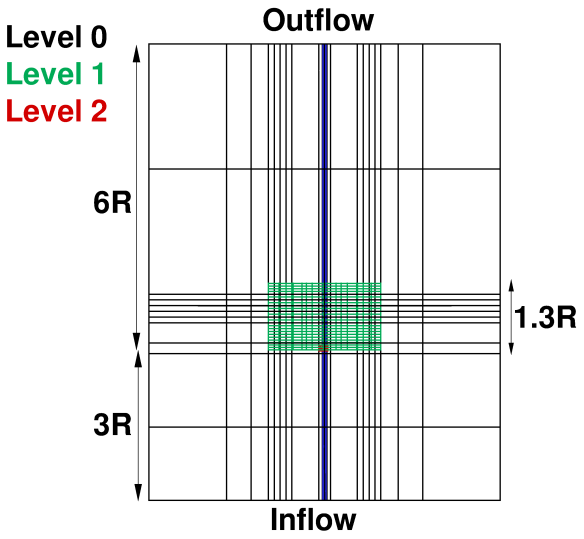

(d) Front view of chimera.

Figure 5.1: Employed multi-block topology grids. **(a)** Topology around the blade and hub; **(b)** Single-blade computational domain, showing the boundary conditions and the extend of the domain. Two sliding planes ($\pm 0.1R$) included for control of wake resolution; **(c)** Overall view of the levels configuration on the chimera grid: *Level 0* is the background, *level 1* is the ring for resolution of the vortices, which is extended from the rotor plane to 1.3 R behind, and *level 2* is the blade; **(d)** Front view of the chimera grid.

In all the cases, axial wind conditions were assumed, the blade pitch angle (at the tip of the blade) was always set to $\phi = -2.3$ degrees (nose up) and the rotational speed was 424.5rpm. The turbulence model employed was the standard k-ω [163]. The Reynolds number is based on the tip speed (100m/s) and the maximum aerodynamic chord (0.24m). Table 5.2 summarises the main features of the computed cases.

Table 5.2: Computed cases for the PIV analysis of the MEXICO rotor.

Test ID	Grid	Re	V_{wind} (m/s)	$M_{tip}(\lambda)$	Low-Mach
1	1	$1.6 \cdot 10^6$	15	0.2941(6.67)	yes/no
2	2	$1.6 \cdot 10^6$	15	0.2941(6.67)	yes/no
3	3	$1.6 \cdot 10^6$	15	0.2941(6.67)	no
4	2	$1.6 \cdot 10^6$	10	0.2941(10)	yes/no
5	2	$1.6 \cdot 10^6$	24	0.2941(4.2)	yes/no

5.1.2 Sensitivity studies

In this section, the effect of the selected pitch angle and the employed turbulence model are studied, for the MEXICO blade and wind speed of 15m/s.

Sensitivity to the blade pitch angle

The pitch angle of the MEXICO blade (based at the tip) has been modified by $+/-$ 0.5 degrees from the baseline value of -2.3 deg. (nose up). Figure 5.2 shows the C_p distribution at two blade sections and the integrated normal force along the blade. As can be observed, increasing the pitch angle leads to higher suction and, hence, higher loads, while decreasing it leads to lower values.

This dependency on the integrated thrust and torque is shown in Figure 5.2 (d). When the pitch angle was increased by half a degree, the thrust and torque increased by 3% and 0.5%, respectively. Likewise, reducing it by half a degree, reduces the thrust by 3% and the torque by 0.7%. This results suggest that the thrust seems to be more sensitive on the pitch angle than the torque.

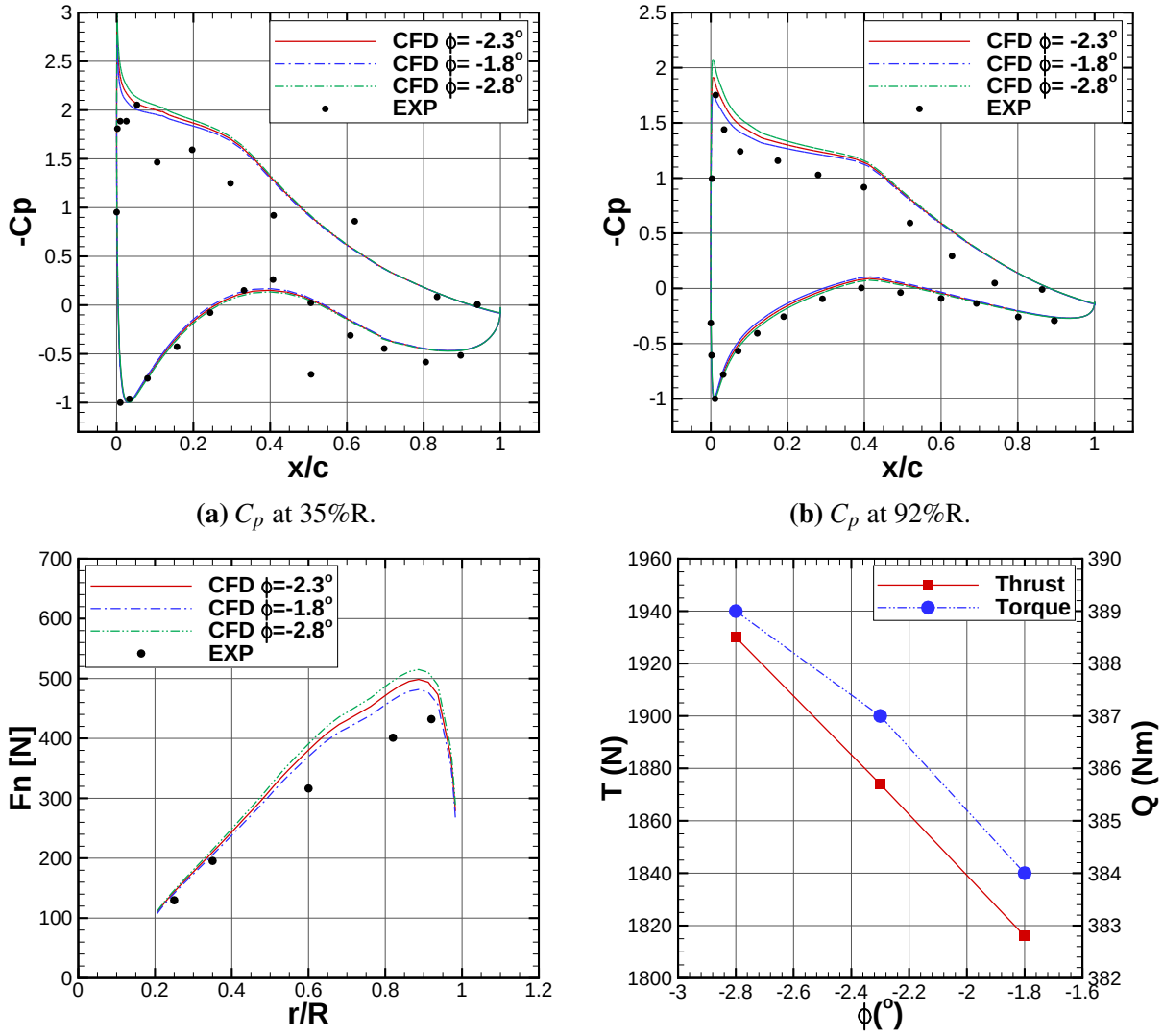

(a) C_p at 35%R.

(b) C_p at 92%R.

(c) Normal force.

(d) Thrust and torque.

Figure 5.2: Effect of the employed pitch angle to the **(a,b)** C_p distribution, **(c)** normal force along the blade span and **(d)** integrated thrust and torque, for wind speed of 15m/s and k-ω turbulence model.

Sensitivity to the turbulence model

The effect of the turbulence model is presented here. Four turbulence models were employed: k-ω [163], k-ω baseline (BSL) [95], k-ω SST [95] and Spalart-Allmaras (S-A) [143]. The C_p distributions presented in Figure 5.3 (a) and (b) show that the effect of the turbulence model is mainly present at the suction side and at the trailing edge of the aerofoil. The k-ω seems to give the highest suction values, the k-ω SST and Spalart-Allmaras solutions are almost identical and the k-ω baseline gives lower values. However, the differences are very small. Regarding the friction coefficient, slightly larger differences can be observed. In the upper

surface of the aerofoil at 92% span (Figure 5.3 (b), all the models (except S-A) predicted an early transition very close to the leading edge. In addition, while for the k-ω and S-A models the flow was attached, the BSL predicted separation at approximately 80% of the aerofoil and k-ω SST predicted a later separation at 90% of the chord. For the integrated normal force along the blade, Figure 5.3 (d), differences can be observed from 70% span to the blade tip. Taking as a reference the values for the k-ω model, the maximum differences are of 3%, 1.8% and 1.2%, for the k-ω baseline, k-ω SST and Spalart-Allmaras models, respectively. Table 5.3 shows the integrated thrust and torque, for all the turbulence models and the three pitch angles.

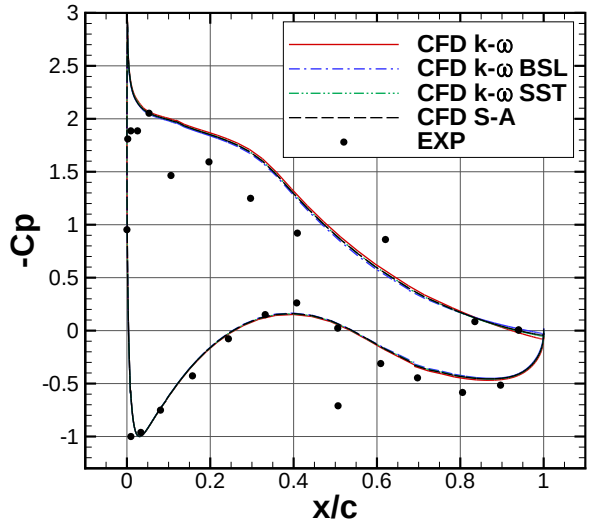

(a) C_p at 35%R.

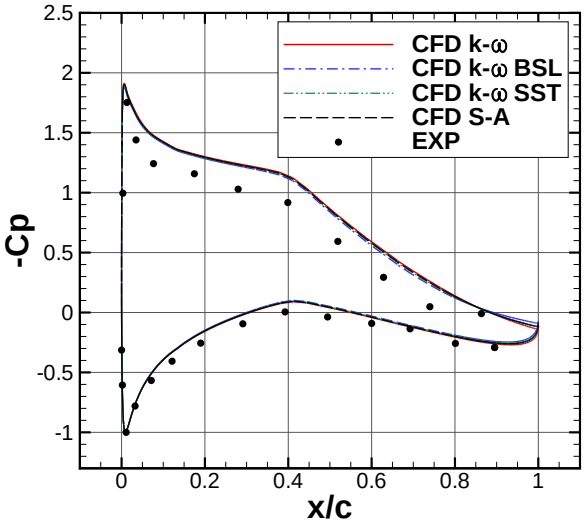

(b) C_p at 92%R.

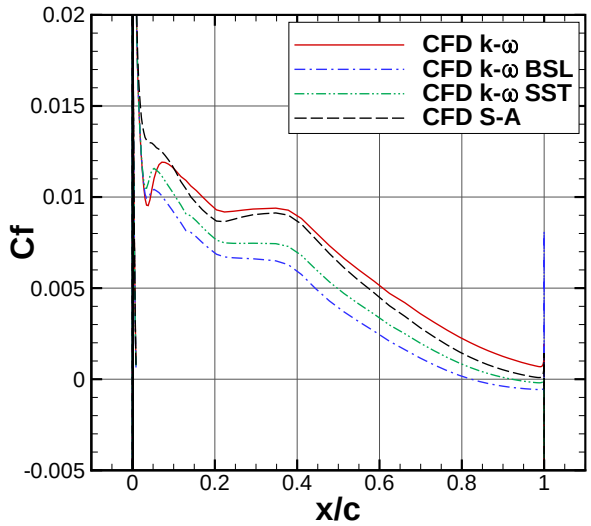

(c) C_f at 92%R (upper surface).

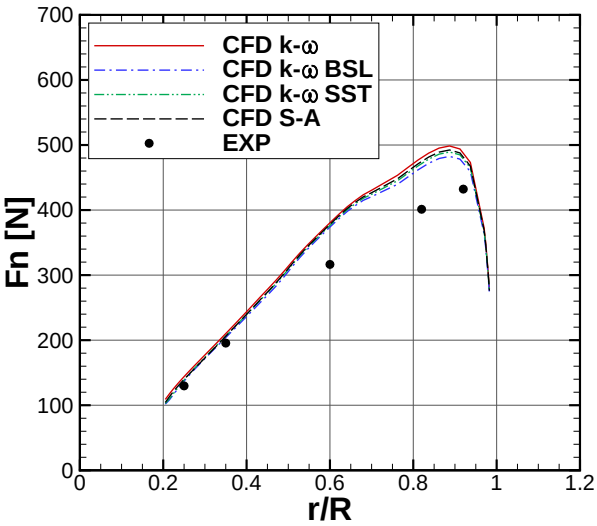

(d) Normal force.

Figure 5.3: Effect of the employed turbulence model (k-ω, k-ω baseline, k-ω SST and Spalart-Allmaras) to the C_p distribution, C_f distribution and the normal force along the blade span, for wind speed of 15m/s and pitch angle of -2.3 deg.

Table 5.3: Sensitivity of the employed turbulence model and pitch angle to the loads on the MEXICO rotor, at 15m/s wind speed.

Pitch Angle ϕ [deg.]	**Thrust [N]**				**Torque [Nm]**			
	k-ω	**k-ω BSL**	**k-ω SST**	**S-A**	**k-ω**	**k-ω BSL**	**k-ω SST**	**S-A**
-2.3	1874	1822	1842	1850	387	377	381	383
-1.8	1816	-	-	-	384	-	-	-
-2.8	1930	-	-	-	389	-	-	-

5.1.3 Loads convergence

The high quality of the employed mesh permitted almost grid independence to be achieved for the loads on the blades. As can be seen in Figure 5.4 (a), the C_p distribution ($C_p = \frac{2(p-p_\infty)}{\rho U_\infty^2}$) is almost identical for all three grids. Likewise, the differences in the torque coefficient ($C_Q = \frac{Q}{1/2\rho U^2 \pi R^3}$) are minimal (less than 2% different) between grids, as seen in Figure 5.4 (b). The almost negligible effect on the loads of the location of the outflow boundary can be also seen in Figure 5.4 (c).

Table 5.4: Comparison of the simulated and measured integrated thrust and torque.

Wind Speed [m/s]	**Thrust [N]**			**Torque [Nm]**		
	Grid 1	**Grid 2**	**Grid 3**	**Grid 1**	**Grid 2**	**Grid 3**
10	-	994 (EXP: 1,000)	-	-	121 (EXP: 60)	-
15	1,855	1,886 (EXP: 1950)	1,928	334	338 (EXP: 290)	343
24	-	3,066 (EXP: 3,200)		-	832 (EXP: 690)	-

In both cases, the integrated values were obtained using the location of the pressure taps. Experimental values published in the report [135] are in parenthesis.

Table 5.4 shows the integrated values for thrust and torque, where the integration of the CFD solution and the experimental values [135] was performed using only the pressure taps locations. Less than 4% difference between the three grids was obtained. The overprediction with respect to the experiments is of the same order as reported in the literature [16, 54, 140]. For example, in reference [16] a thrust of 1757N and torque of 337Nm were predicted for the 15m/s wind speed case.

This shows that the blade loads are not further affected by the mesh size or type or level of wake resolution. In addition, independently of the scheme employed, the method showed excellent stability, with good convergence, as Figure 5.4 (d) shows for the torque coefficient at 10m/s wind speed.

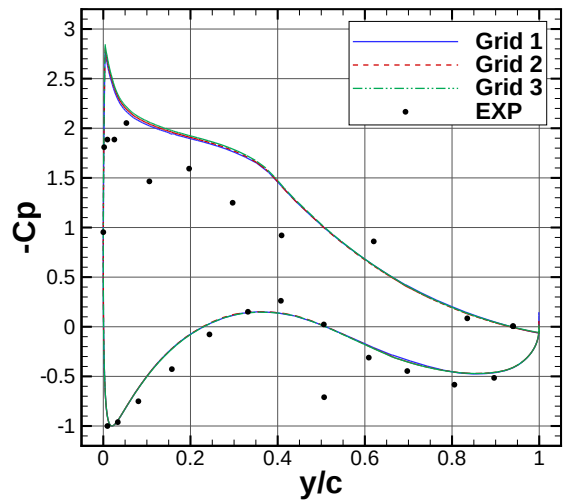

(a) C_p at 35%R for 15m/s wind speed.

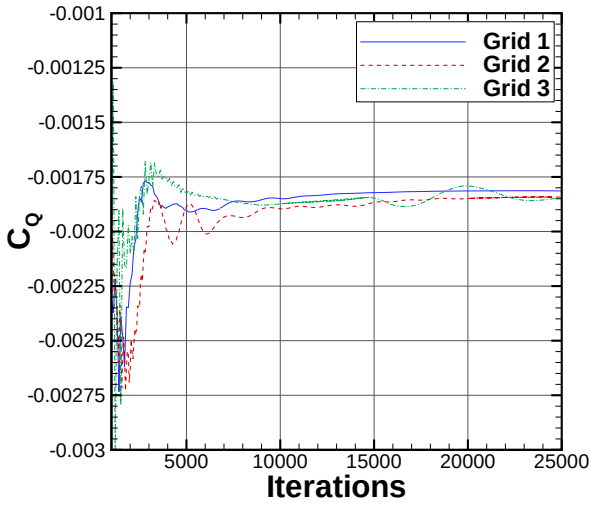

(b) Torque coefficient at 15m/s wind speed.

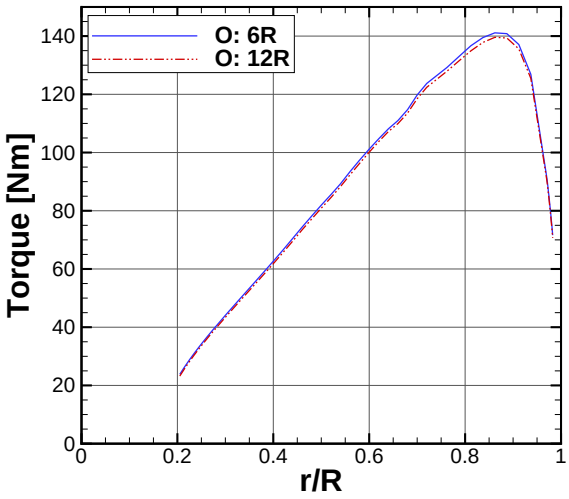

(c) Span-wise torque (15m/s).

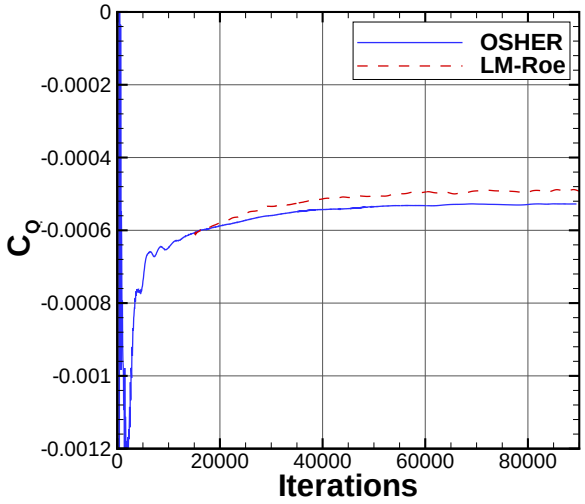

(d) Torque coefficient (10m/s) convergence.

Figure 5.4: Grid convergence for the loads. **(a)** Comparison of the C_p at 35%R for 15m/s wind speed (tests 1 to 3 of table 7.2). **(b)** Comparison of the torque coefficient at 15m/s wind speed (tests 1 to 3 of table 7.2). **(c)** Span-wise torque (15m/s) obtained for cases with outflow boundary at $6R$ and at $12R$. **(d)** Torque coefficient (10m/s) convergence for Osher's and LM-Roe schemes, obtained with grid 2 of Table 6.1.

5.2 Wake visualisation

5.2.1 λ_2 criterion

Q or λ_2 criteria [70] are widely used in the literature for visualisation of vortex cores, shed vorticity and flow direction. The quantity Q is defined as,

$$Q = \frac{1}{2}\left(||\boldsymbol{\Omega}||^2 - ||\boldsymbol{S}||^2\right), \tag{5.1}$$

where the vorticity is defined as

$$\boldsymbol{\Omega} = \frac{1}{2}\left(\nabla \boldsymbol{V} - \nabla \underline{\boldsymbol{V}}^T\right), \tag{5.2}$$

Q is positive when vorticity dominates the flow-field; conversely, negative Q means that the flow is dominated by the shear ($\boldsymbol{S}$). Under the assumption that for the presence of a local pressure minimum two negative eigenvalues of the symmetric matrix ($\boldsymbol{S}^2 + \boldsymbol{\Omega}^2$) are necessary, Jeong *et al.* [70] defined Q as,

$$Q = -\frac{1}{2}\left(\lambda_1 + \lambda_2 + \lambda_3\right). \tag{5.3}$$

Where $\lambda_1 \leq \lambda_2 \leq \lambda_3$. A vortex is defined as long as $\lambda_2 < 0$.

Figure 5.5 shows 3D views of the wake developed behind the rotor for 10, 15 and 24m/s wind speeds, with iso-surfaces of λ_2 criterion, coloured with axial velocity contours. A total of 10 spirals were captured for the 10m/s case (Figure 5.5 (a)), 7 spirals for 15m/s (Figure 5.5 (b)) and 4 spirals for the 24m/s case (Figure 5.5 (c)). As can be observed, the higher the wind speed, the more separated the vortices are, due to the faster convection of the wake. Knowing that the convection ratio is $1/\lambda$, in every third of revolution, the wake travels 10% R (0.225m), 15% R (0.3375m) and 24% R (0.5357m) in the axial direction, for each wind speed case, 10, 15 and 24m/s respectively. Likewise, the lower the wind speed the more expansion of the wake. Taking as a reference the first vortex revolution, at 10m/s the wake expands approximately to $1.25R$ at an axial position of $x = 1.25R$, at 15m/s wind speed the expansion is $1.12R$ for the same axial position and at 24m/s there is almost no expansion. It should be also observed how well the inner vortices created by the root are captured, especially in the lower wind speed case.

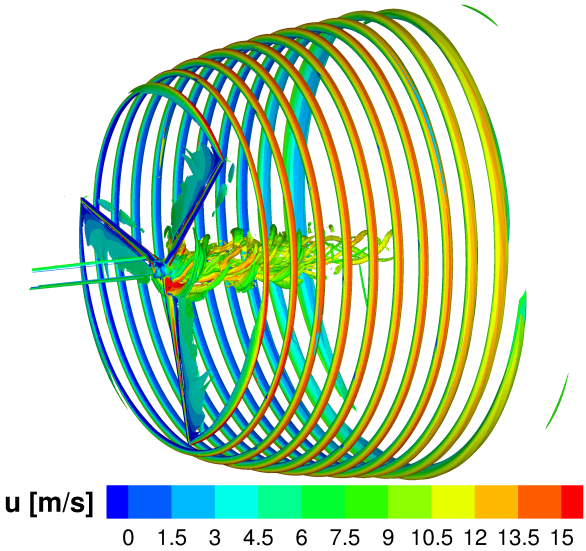

(a) $10m/s$ ($\lambda = 10$)

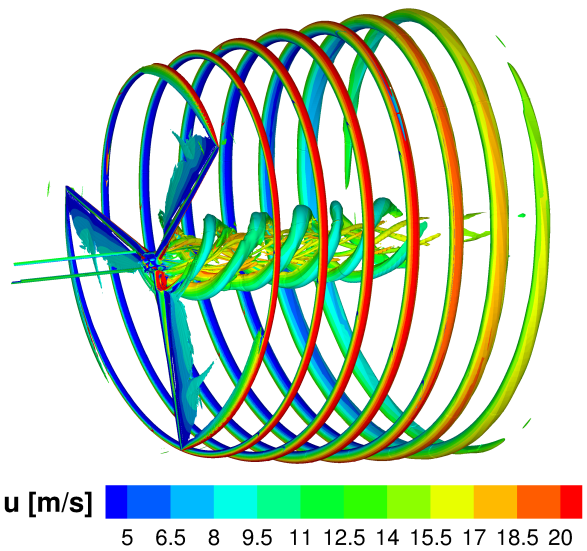

(b) $15m/s$ ($\lambda = 6.7$)

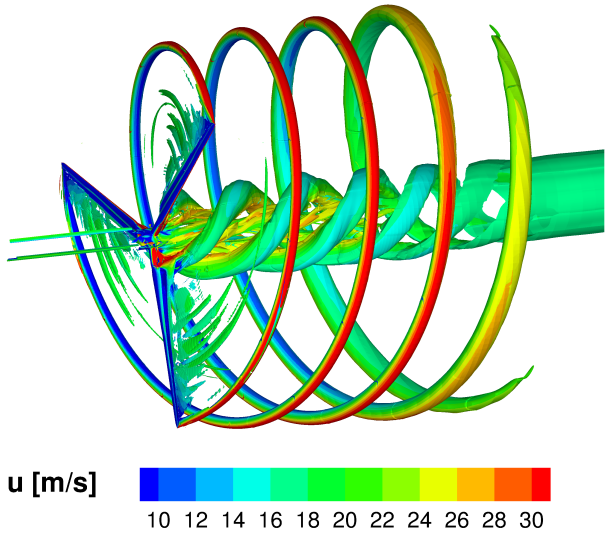

(c) $24m/s$ ($\lambda = 4.2$)

Figure 5.5: Iso-surfaces of λ_2 criterion [70] ($\lambda_2 = -0.01$), shaded with axial velocity contours for wind speeds of **(a)** 10m/s, **(b)** 15m/s and **(c)** 24m/s, corresponding to tip speed ratios of 10, 6.67 and 4.42, respectively. CFD computations obtained with grid 2 of Table 5.1.

5.2.2 Velocity contours

To capture the blade tip vortices, the employed grids were specially refined in the area between 75% and 140% span. In this region, the cells have a size of 5% and 2.5% of the maximum blade chord length (1cm and 0.5cm approximately), for grids 1 and 2 of Table 5.1, respectively. Knowing that in the experiments the vortex diameter was approximately 4cm, with this grid resolution, a total of 4 cells in grid 1 and 8 cells in grid 2 are defining the vortex cores. Figures 5.6 to 5.8 show contours of the three velocity components with the blade at an azimuth angle of 270 degrees and for wind speed of 15m/s (see Figure 1.14 for reference), where the position of the vortices can be observed and compared with the PIV windows averaged over 30 rotor revolutions. CFD results obtained with the standard Osher and the low-Mach scheme (LM-Roe), employing the two levels of grid refinement, are compared with the experiments.

Using the coarser grid (grid 1 in Table 5.1), the agreement with experiments is better with the LM-Roe scheme than with the original Osher scheme. This is due to the less dissipative nature of the low-Mach solution. For grid 2, on the other hand, the agreement improves for the first 5 vortices in both cases and the differences between the schemes become less important. Since the grid is refined, there is less numerical dissipation and therefore the improvements obtained with the low-Mach scheme are not that obvious. In addition, it should be noted that in the tangential velocity (chord-wise component in Figure 5.8) the CFD results successfully captured the deficit of momentum behind the blade's trailing edge. Fairly good qualitative agreement is observed in all three velocity components.

The results for the lower wind speed case (10m/s) are shown in Figures 5.9 to 5.11. Since the wake is convected downstream slowly in this case, more vortices can be seen on the velocity contours. There is good agreement with the experiments, however, the fifth vortex in the PIV frames seems to be not in the correct position. At that stage the distance between vortices should be constant, since no breakdown of the wake is indicated by the CFD computations.

For the high speed case (24m/s), only four vortices are shown, due to the fast convection speed of the wake (see Figures 5.12 to 5.14). Note that there is a loss in quality of the fourth vortex in the computations because that grid region is coarser.

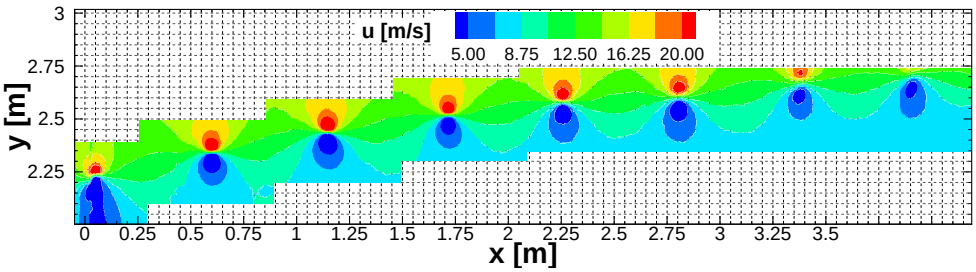

(a) Experiments.

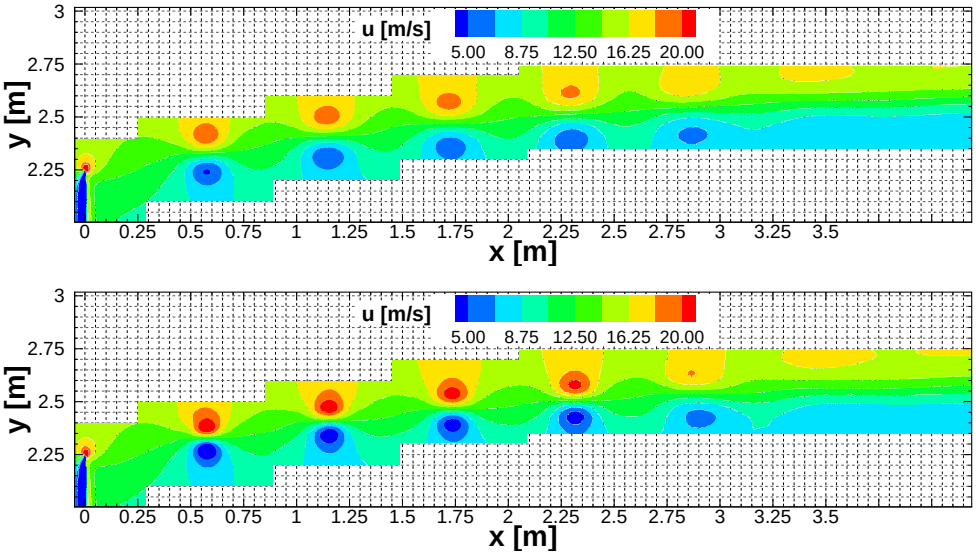

(b) CFD Osher. Top: Grid 1, Bottom: grid 2.

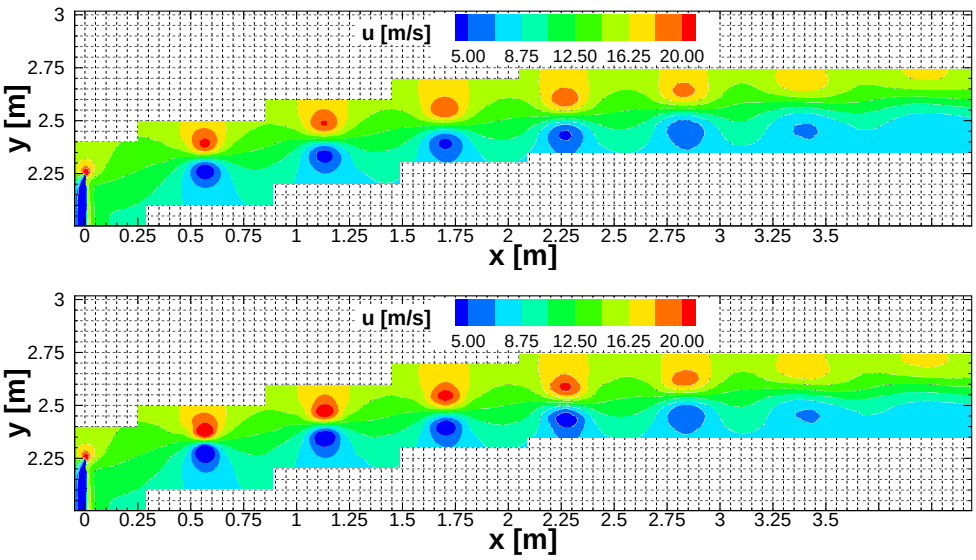

(c) CFD LM-Roe.Top: Grid 1, Bottom: grid 2.

Figure 5.6: Contours of the axial velocity component, for wind speed of 15m/s ($\lambda = 6.67$) and blade at 270 degrees of azimuth angle. The first row shows the values from the experiments, the two rows in the middle show the values obtained with the Osher scheme for two levels of grid refinement (top: grid 1 and bottom: grid 2) and the last two rows show the solution obtained with the LM-Roe scheme.

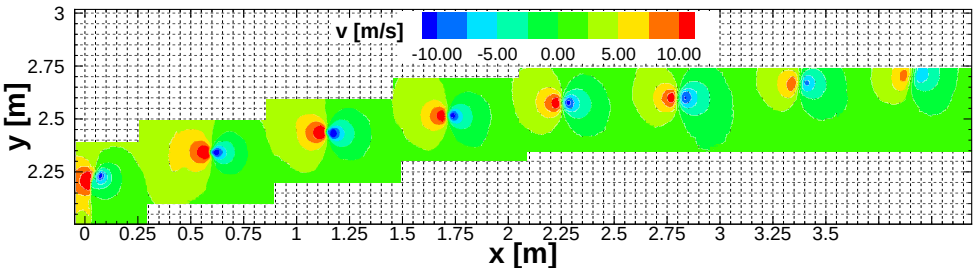

(a) Experiments.

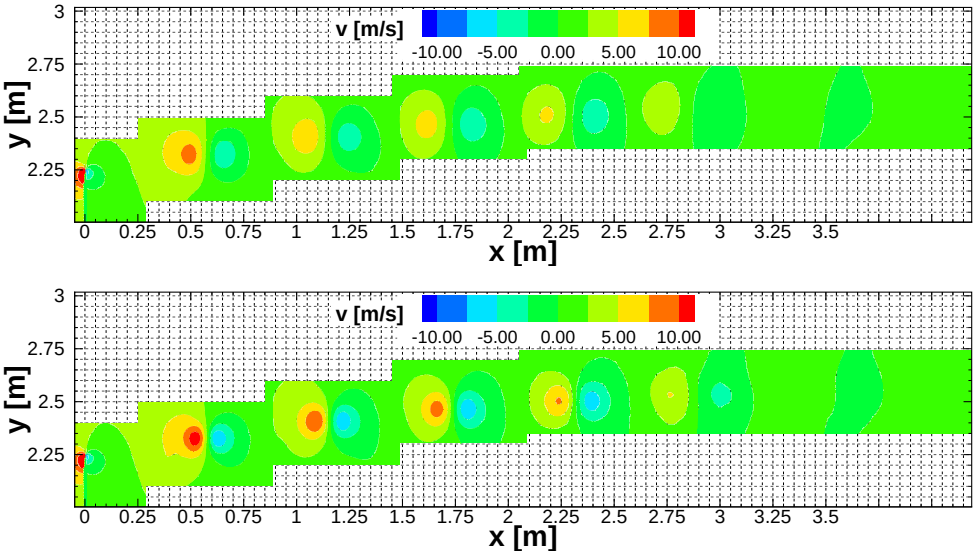

(b) CFD Osher. Top: Grid 1, Bottom: grid 2.

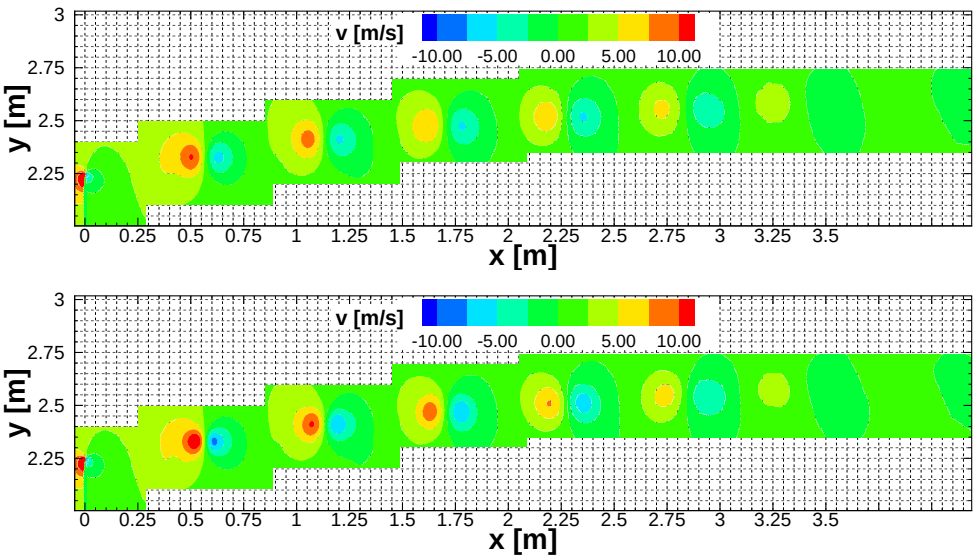

(c) CFD LM-Roe.Top: Grid 1, Bottom: grid 2.

Figure 5.7: Contours of the radial velocity component, for wind speed of 15m/s ($\lambda = 6.67$) and blade at 270 degrees of azimuth angle. The first row shows the values from the experiments, the two rows in the middle show the values obtained with the Osher scheme for two levels of grid refinement (top: grid 1 and bottom: grid 2) and the last two rows show the solution obtained with the LM-Roe scheme.

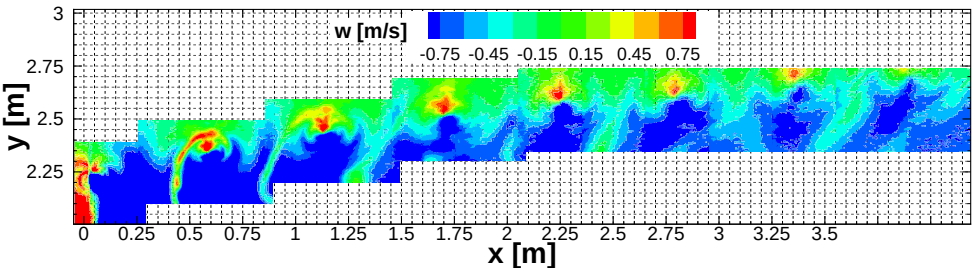

(a) Experiments.

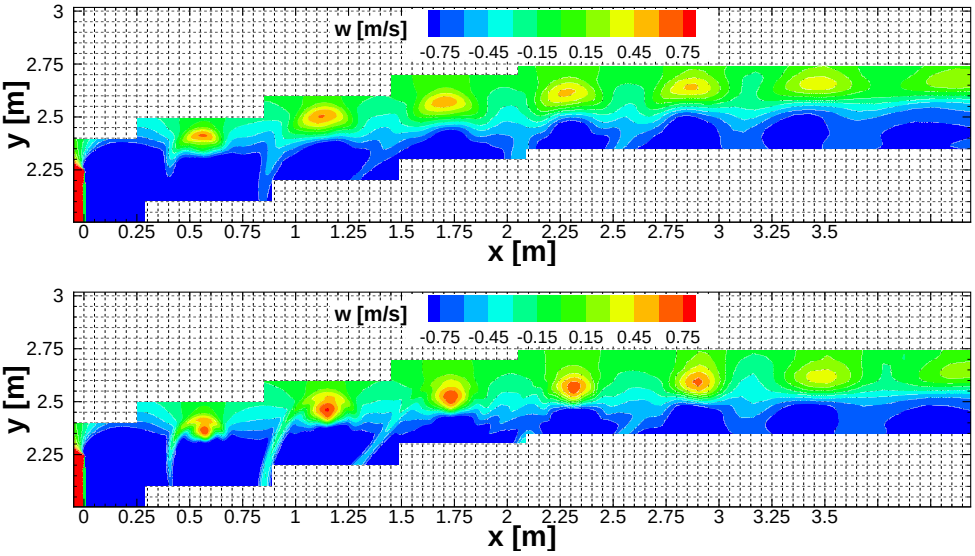

(b) CFD Osher. Top: Grid 1, Bottom: grid 2.

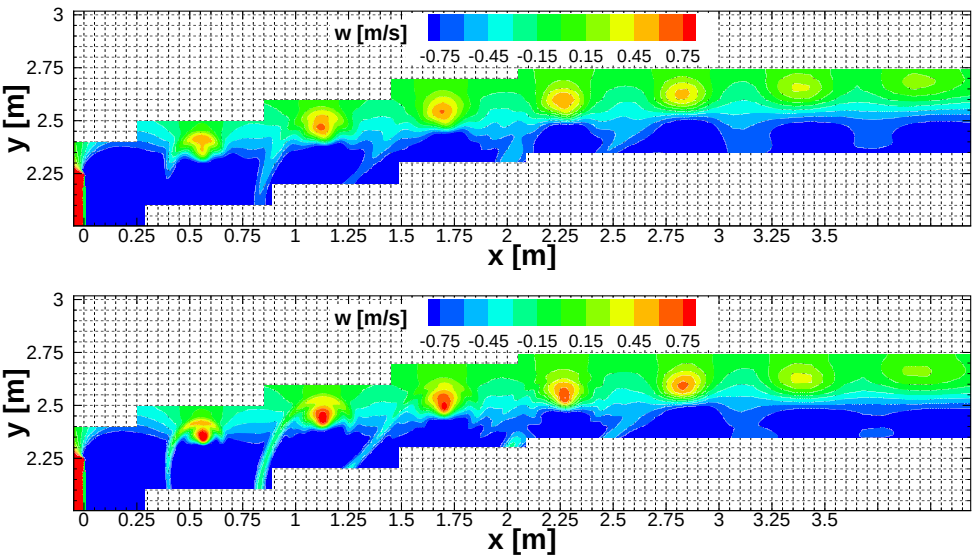

(c) CFD LM-Roe.Top: Grid 1, Bottom: grid 2.

Figure 5.8: Contours of the tangential velocity component, for wind speed of 15m/s ($\lambda = 6.67$) and blade at 270 degrees of azimuth angle. The first row shows the values from the experiments, the two rows in the middle show the values obtained with the Osher scheme for two levels of grid refinement (top: grid 1 and bottom: grid 2) and the last two rows show the solution obtained with the LM-Roe scheme.

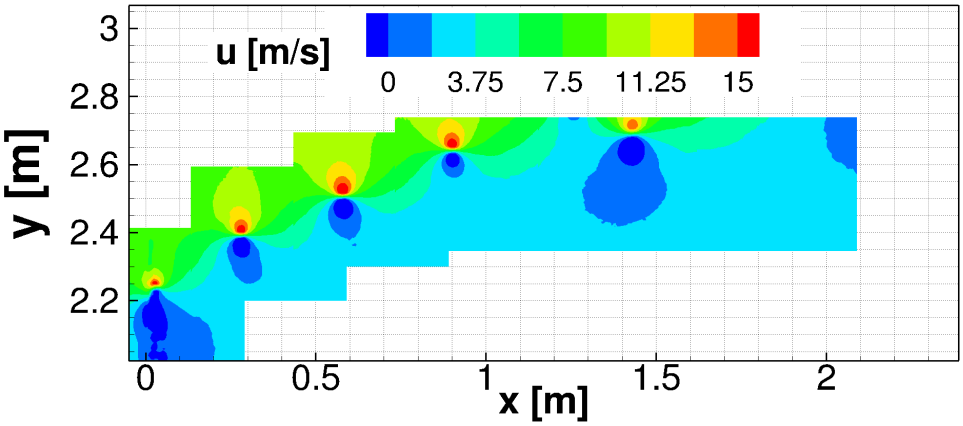

(a) Experiments.

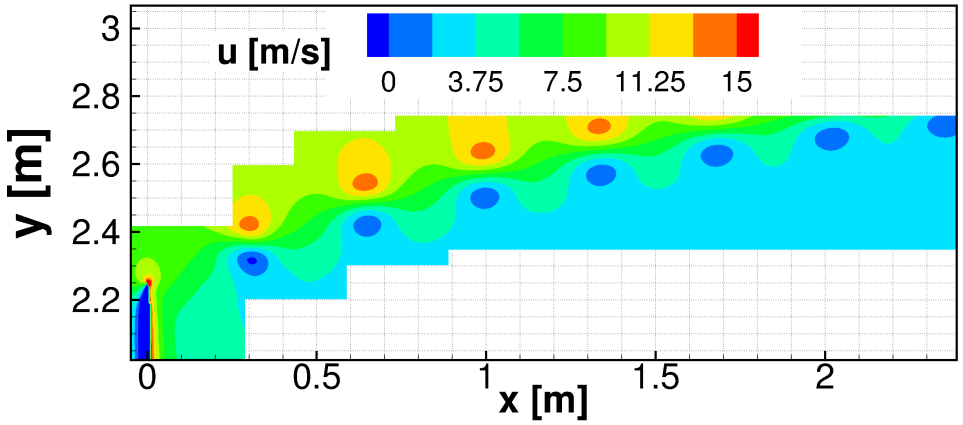

(b) CFD Osher.

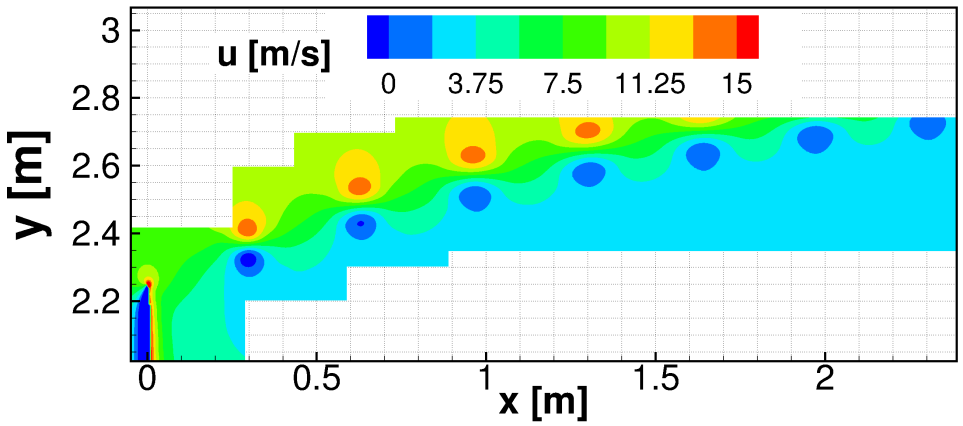

(c) CFD LM-Roe.

Figure 5.9: Contours of the axial velocity component, for wind speed of 10m/s ($\lambda = 10$) and blade at 270 degrees of azimuth angle. Comparison between experiments and CFD results obtained with Osher and LM-Roe schemes, for grid 2 of Table 5.1.

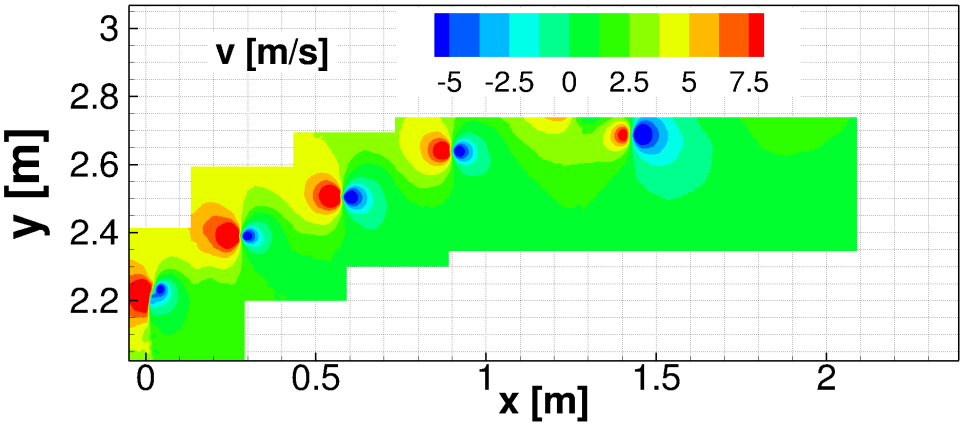

(a) Experiments.

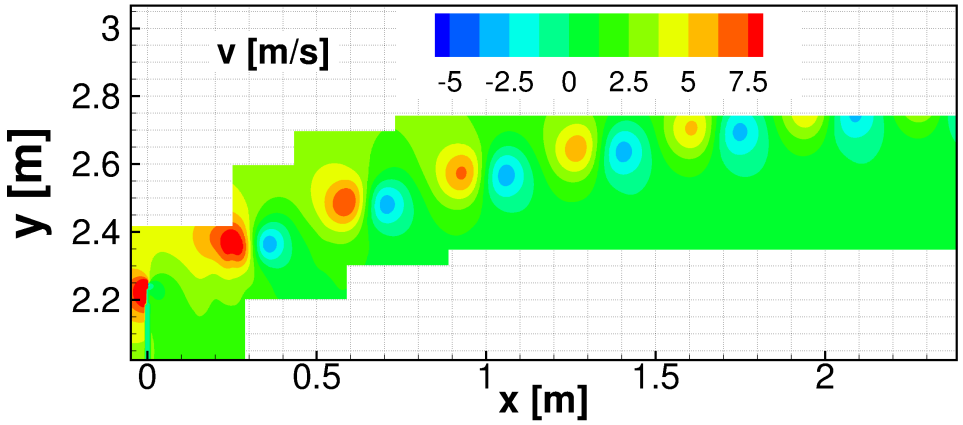

(b) CFD Osher.

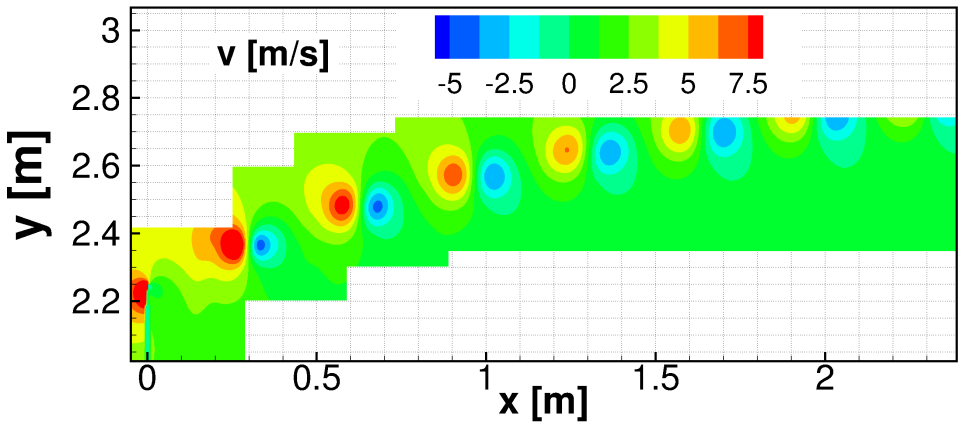

(c) CFD LM-Roe.

Figure 5.10: Contours of the radial velocity component, for wind speed of 10m/s ($\lambda = 10$) and blade at 270 degrees of azimuth angle. Comparison between experiments and CFD results obtained with Osher and LM-Roe schemes, for grid 2 of Table 5.1.

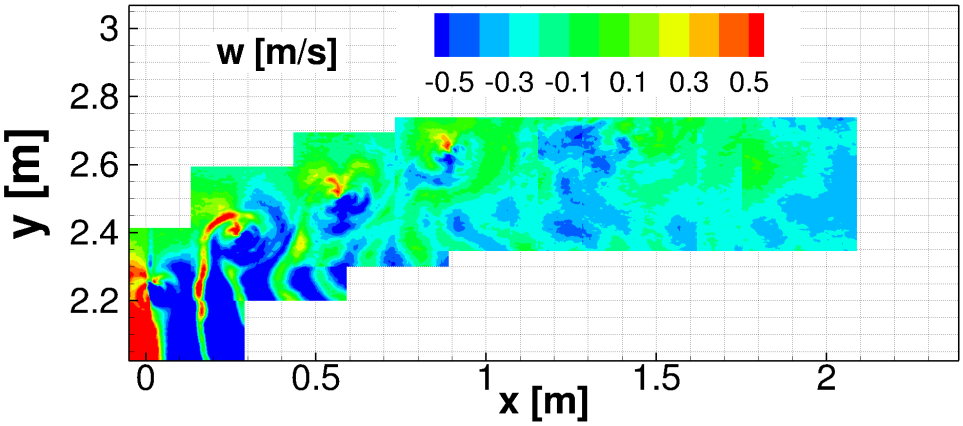

(a) Experiments.

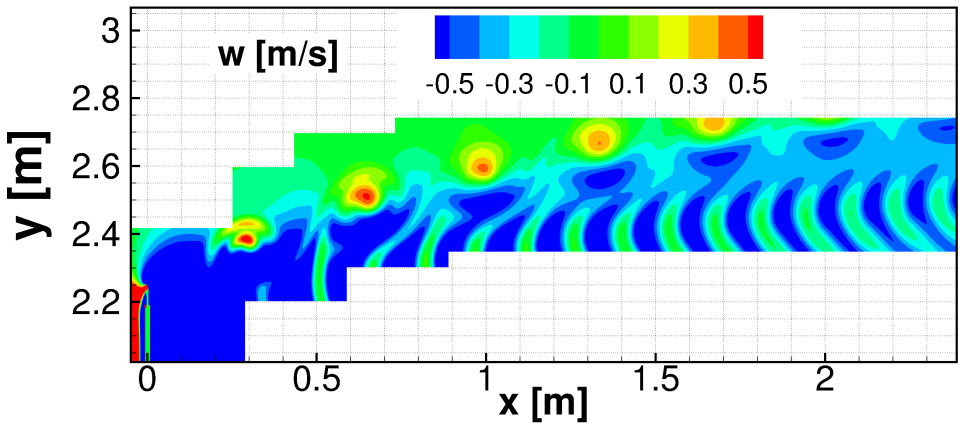

(b) CFD Osher.

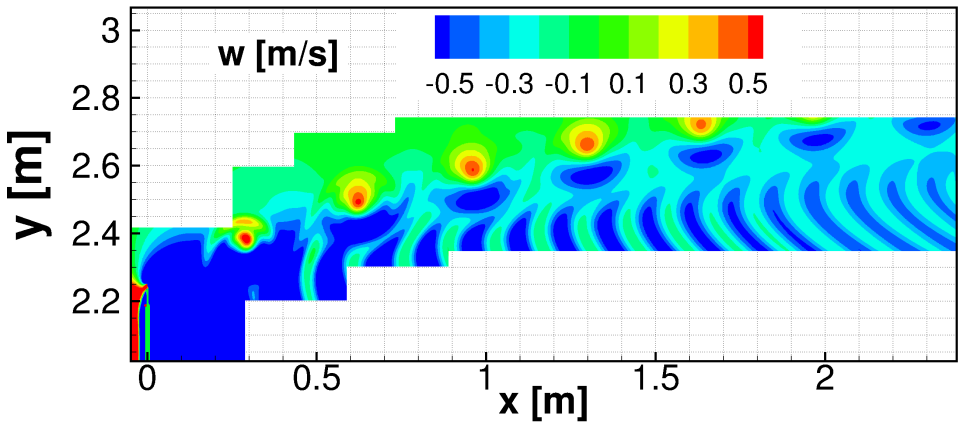

(c) CFD LM-Roe.

Figure 5.11: Contours of the tangential velocity component, for wind speed of 10m/s ($\lambda = 10$) and blade at 270 degrees of azimuth angle. Comparison between experiments and CFD results obtained with Osher and LM-Roe schemes, for grid 2 of Table 5.1.

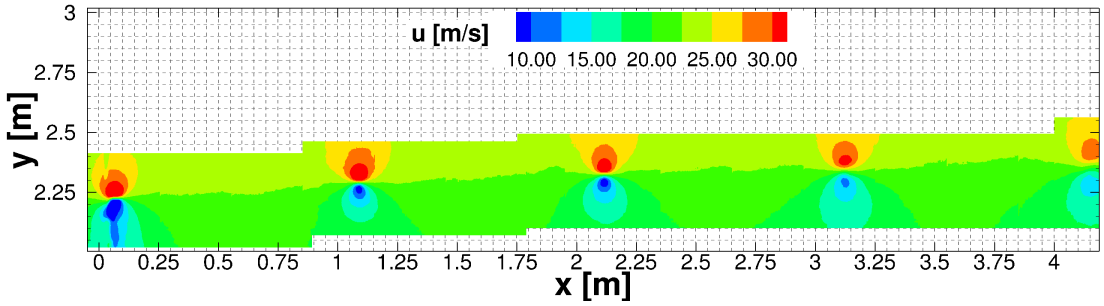

(a) Experiments.

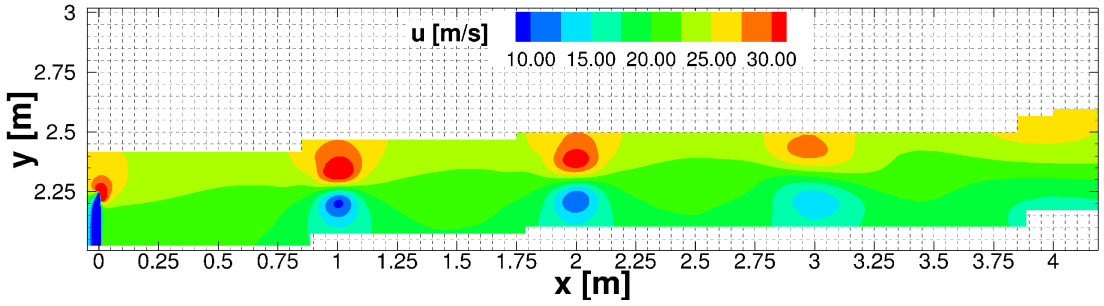

(b) CFD Osher.

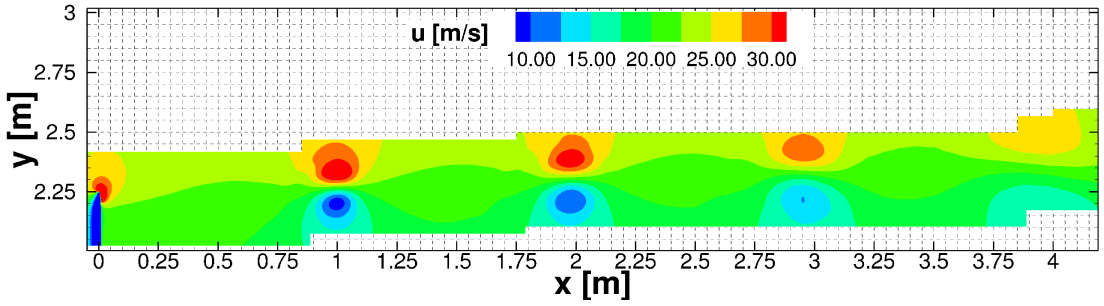

(c) CFD LM-Roe.

Figure 5.12: Contours of the axial velocity component, for wind speed of 24m/s ($\lambda = 4.2$) and blade at 270 degrees of azimuth angle. Comparison between experiments and CFD results obtained with Osher and LM-Roe schemes, for grid 2 of Table 5.1.

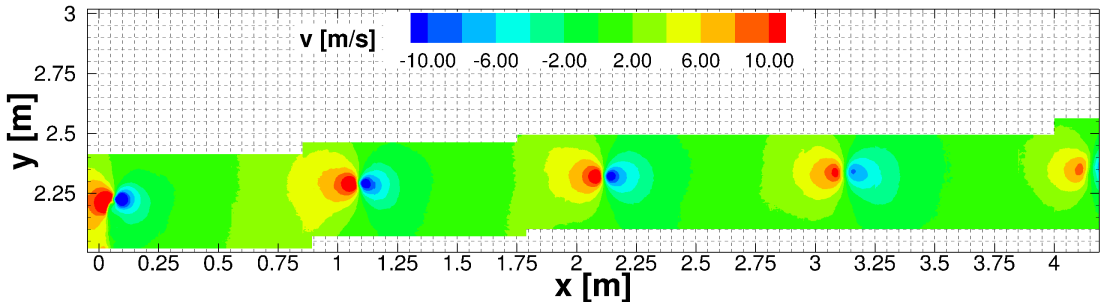

(a) Experiments.

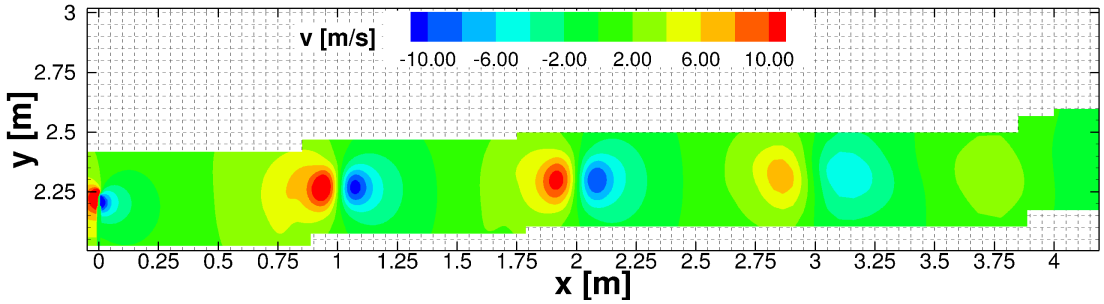

(b) CFD Osher.

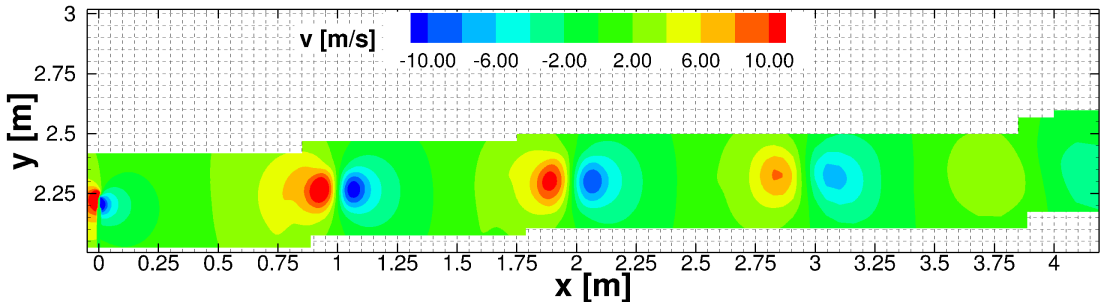

(c) CFD LM-Roe.

Figure 5.13: Contours of the radial velocity component, for wind speed of 24m/s ($\lambda = 4.2$) and blade at 270 degrees of azimuth angle. Comparison between experiments and CFD results obtained with Osher and LM-Roe schemes, for grid 2 of Table 5.1.

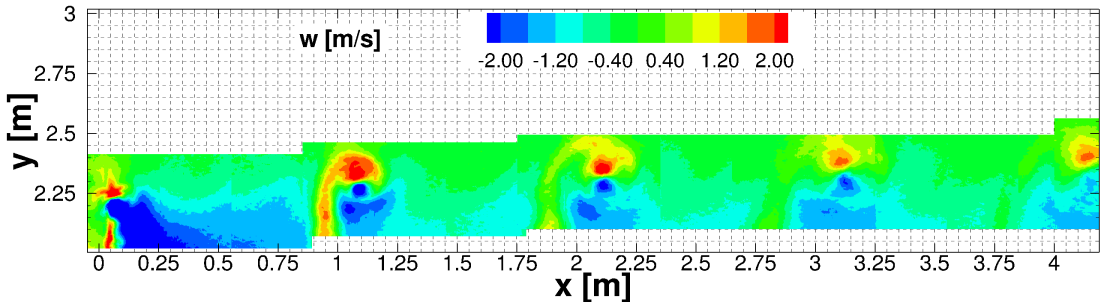

(a) Experiments.

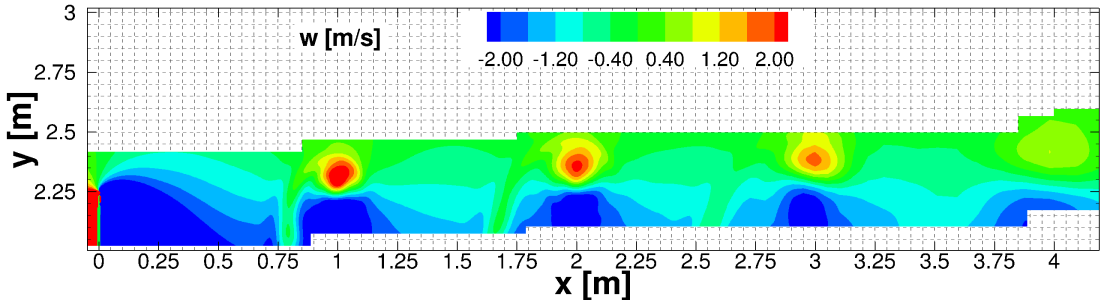

(b) CFD Osher.

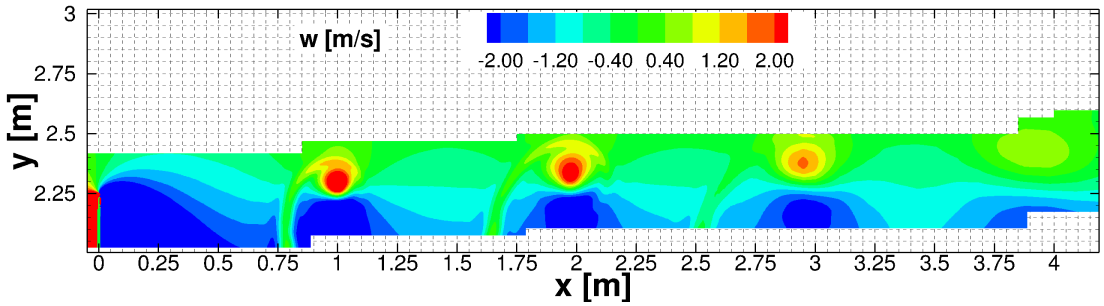

(c) CFD LM-Roe.

Figure 5.14: Contours of the tangential velocity component, for wind speed of 24m/s ($\lambda = 4.2$) and blade at 270 degrees of azimuth angle. Comparison between experiments and CFD results obtained with Osher and LM-Roe schemes, for grid 2 of Table 5.1.

5.2.3 Vorticity contours

For the blade positioned at 270 degrees of azimuth, Figure 5.15 shows contours of vorticity magnitude, whose values are calculated as,

$$|\boldsymbol{\omega}| = |\nabla \times \boldsymbol{V}| \tag{5.4}$$

where $\boldsymbol{V}$ is the velocity vector. Note that in the computations the velocities were normalised by the tip speed (100m/s) and the distances by the maximum aerodynamic chord (0.24m). An interesting feature that can be observed in Figure 5.15 is the discontinuity in the wake at approximately 70% R. At that blade station, two different aerofoils (RISO-A1-21 and NACA-64-418) are blended. The geometric twist along the blade is given by the geometric incidence angle per station and the discontinuity observed might be due to differences of zero-lift angle of the stations with different aerofoil sections. Another blend between the RISO-A1-21 and DU-W2-250 aerofoils is set at 50% R approximately; however, their aerodynamic properties are more similar and that effect on the wake is much milder.

5.2.4 Vortex position and core size

From the axial velocity contours, the vortex core positions were estimated and compared in the left side of Figure 5.16. For the 15m/s wind speed (Figure 5.16 (c)), the axial position of the vortices is well predicted in both cases. However, the wake is more contracted in the CFD computations (by 5cm approx.), as observed from the radial positions. A similar offset is present in the lower and higher wind speed cases, Figures 5.16 (a) and (e), respectively. This was also reported by Breton [21] and Nilsson [105]. The differences between numerical schemes are almost negligible for all the three wind speeds in the predicted vortex positions.

The core radius of the vortices was also estimated, averaging the distance between the maximum and minimum two tangential velocities around the vortex, representing the diameter of the vortex. Figure 5.16 (d) shows a comparison between the values from the PIV windows obtained in the experiments and the CFD obtained using the Osher's and LM-Roe schemes, employing the coarser and finer grids. It should be noticed that the solution obtained with the LM-Roe scheme is closer to the experiments than with the Osher. Additionally, as the grid is refined, the differences between schemes become smaller, see Figure 5.16

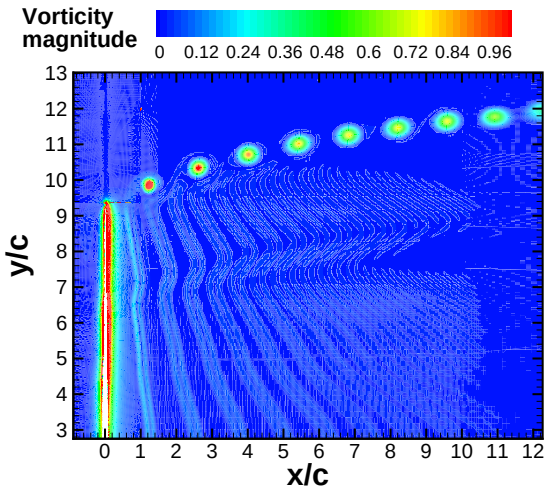

(a) 10m/s ($\lambda = 10$)

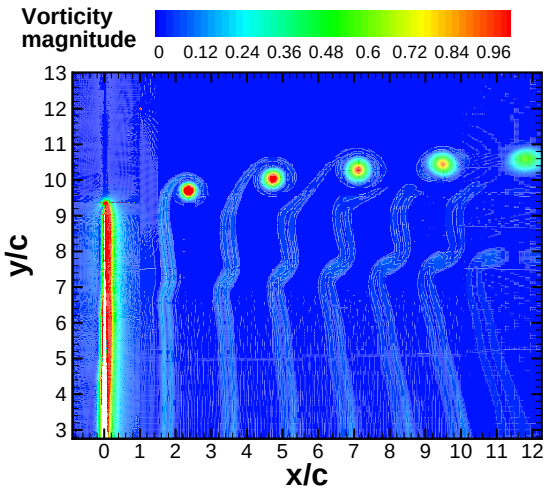

(b) 15m/s ($\lambda = 6.67$)

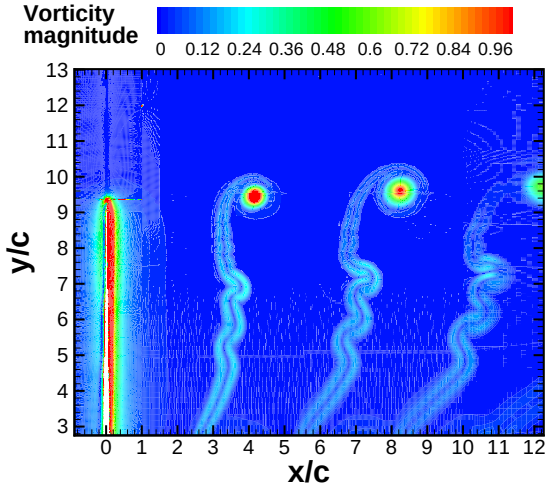

(c) 24m/s ($\lambda = 4.2$)

Figure 5.15: Contours of vorticity magnitude for wind speeds of **(a)** 10m/s **(b)** 15m/s and **(c)** 24m/s. The blade is set at an azimuth angle of 270 degrees. Results obtained with grid 2 of Table 5.1.

(d). Likewise, the solutions of the high wind speed case (24m/s) are practically identical, see Figure 5.16 (f). Conversely, the bigger differences are observed in the lower wind speed case (10m/s), Figure 5.16 (b), where the LM-Roe scheme gives better results.

As can be seen from Figure 5.16, the higher the wind speed, the bigger the size of the vortex core. As an example, Figure 5.17 shows contours of vorticity magnitude for the three wind speed cases and for the second vortex. At 10m/s wind speed, the vortex obtained with the CFD has a radius of 43mm; at 15m/s the radius is 45mm; and at 24m/s it is 65mm. Although these values are over-predicted when compared with the

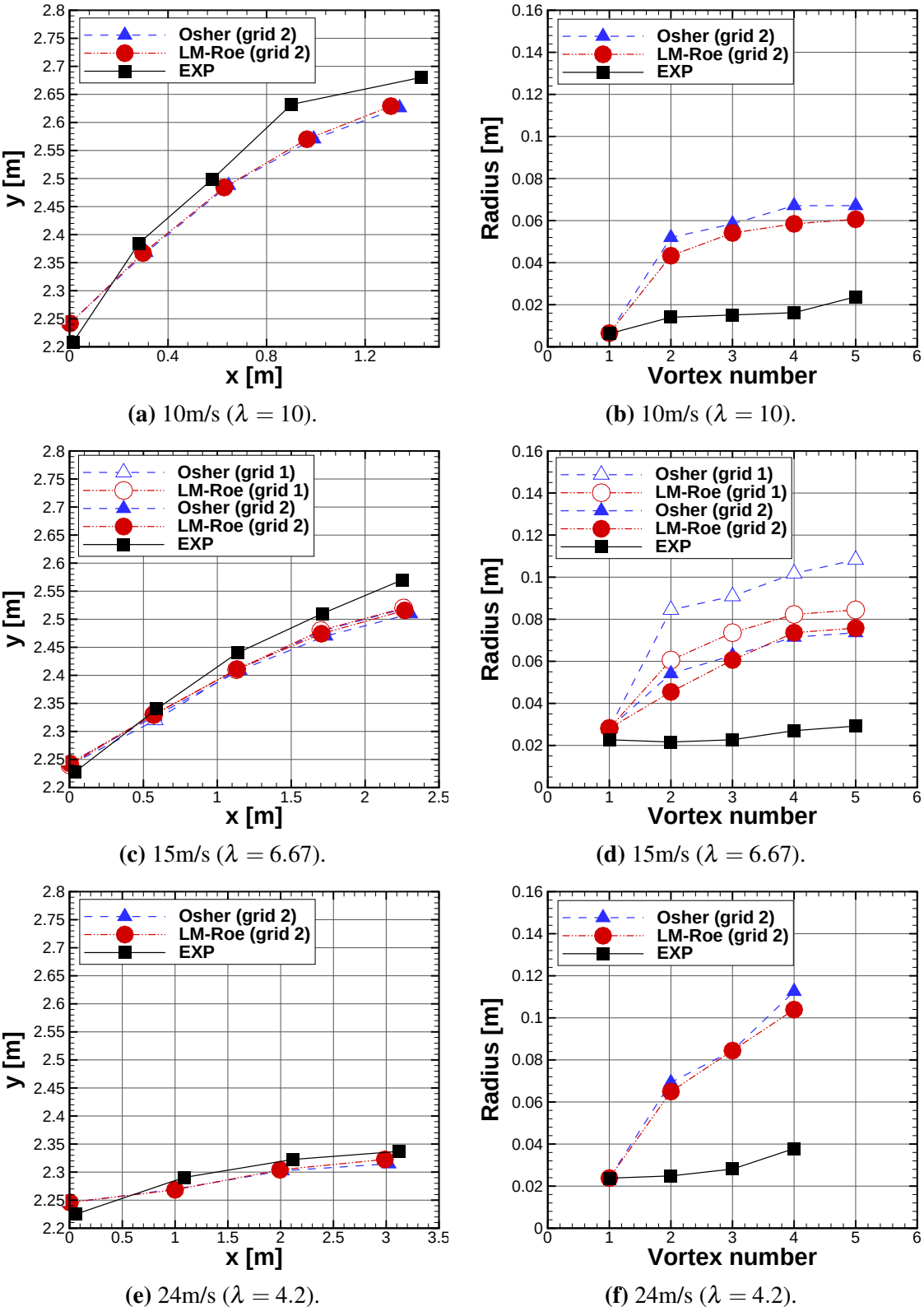

(a) 10m/s ($\lambda = 10$). **(b)** 10m/s ($\lambda = 10$).

(c) 15m/s ($\lambda = 6.67$). **(d)** 15m/s ($\lambda = 6.67$).

(e) 24m/s ($\lambda = 4.2$). **(f)** 24m/s ($\lambda = 4.2$).

Figure 5.16: Position (left) and core radius (right), in meters, of the vortices, for wind speeds of 10, 15 and 24m/s. The blade is set at 270 degrees of azimuth angle. For the 15m/s, a comparison is done between two levels of grid refinement: grid 1 and 2 of Table 5.1 (10 and 64 million cells, respectively), while for wind speeds of 10 and 24m/s grid 2 of Table 5.1 is used.

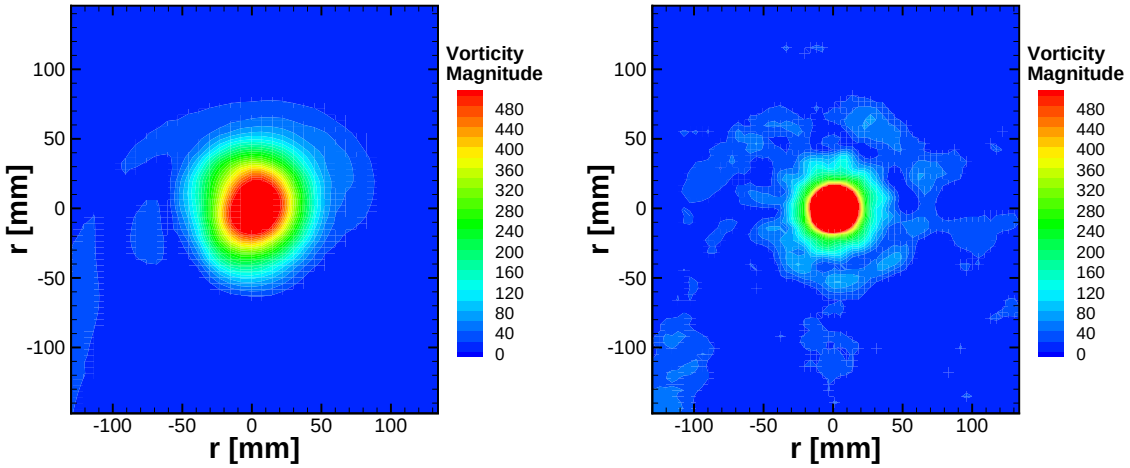

(a) CFD: 10m/s ($\lambda = 10$). **(d)** EXP: 10m/s ($\lambda = 10$).

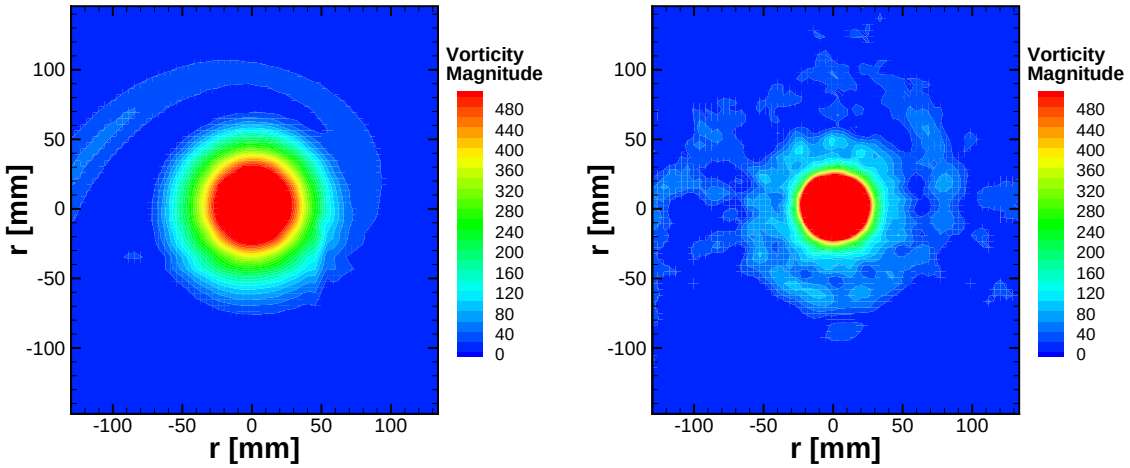

(b) CFD: 15m/s ($\lambda = 6.67$). **(e)** EXP: 15m/s ($\lambda = 6.67$).

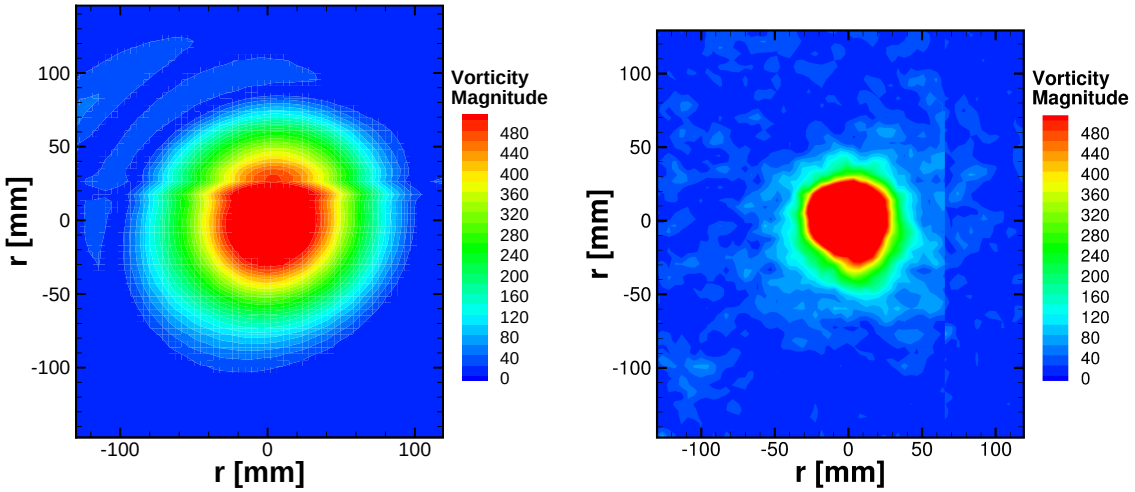

(c) CFD: 24m/s ($\lambda = 4.2$). **(f)** EXP: 24m/s ($\lambda = 4.2$).

Figure 5.17: Contours of vorticity of the second vortex (120 degrees old). Comparison done between CFD results obtained with LM-Roe (left) and experiments (right), for wind speeds of 10m/s (top), 15m/s (middle) and 24m/s (bottom), employing grid 2 of Table 5.1. The vortices were centred at the $r = (0,0)$ position.

experiments (14mm, 22mm and 25mm, respectively), there is consistency between CFD and measurements, and much better predictions are obtained than other works in the literature [21, 105]. To be able to predict the same radius of the experimental vortices, it would be necessary to reduce the cells size by a factor of three, approximately. This would lead to grids 27 (3^3) times larger than the ones employed here and therefore the required computational resources would make the study prohibitive.

5.3 Velocity profiles

5.3.1 Near wake

Figure 5.18 shows the three components of the velocity profiles at two radial stations: 62.2%R and 80%R ($r = 1.4$ and 1.8m, respectively), from one diameter upstream to one and a half diameters downstream the rotor disk, at 15m/s wind speed. Regarding the axial component, Figure 5.18 (a) and (b), a shift of 0.5m/s have been applied to the CFD computations, since the inflow wind speed in the experiments was lower than 15m/s. This shift was also employed by other authors in the literature [16]. As can be seen, there is good agreement with the experiments, especially at 80% R (right side of Figure 5.18). This is due to grid refinement, since the smaller cells were set between 75%R and 140%R. Likewise, little effect is observed between the cases where the outflow boundary was located at 6R and 12R (Figure 5.18 (b)). In addition, the oscillatory pattern behind the rotor plane on the radial component (Figures 5.18 (c) and (d)) was well captured by both schemes. A similar behaviour is observed for the tangential (chord-wise) component (Figures 5.18 (e) and (f)), where both schemes gave similar solutions. However, the coarser regions of the grid are found in that direction. The oscillations observed in the radial and tangential components are due to the maximum and minimum velocities across the vortices and they are repeated with a period of $1/\lambda$.

Good results were also obtained at 24m/s, as shown in the right column of Figure 5.19 for the three velocity components at 80%R. Here, the period of the oscillations is longer than in the previous case, $1/\lambda =$ 42%R, and the differences between schemes are minimal for the three velocity components. The lower wind speed case (10m/s) shows a similar behaviour between both schemes in the axial and radial velocity components (Figures 5.19 (a) and (c)). The oscillatory pattern was well captured and has a lower period than the 15m/s ($1/\lambda_{10m/s} = 10$%R). Regarding the tangential component, however, the differences between the

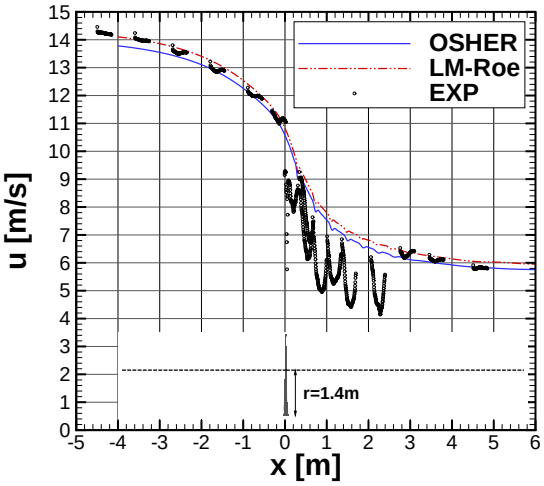

(a) 62.2% R: Axial velocity component.

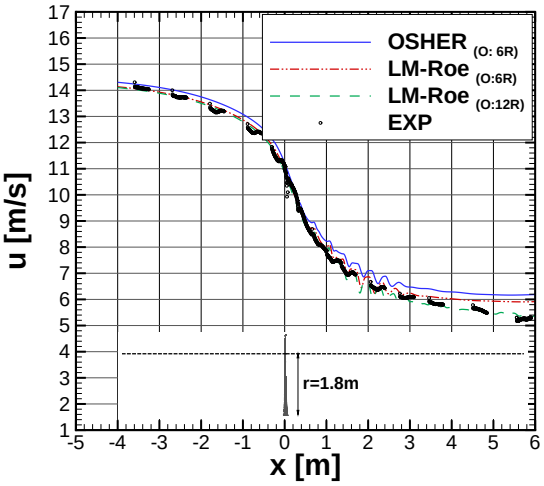

(b) 80% R: Axial velocity component.

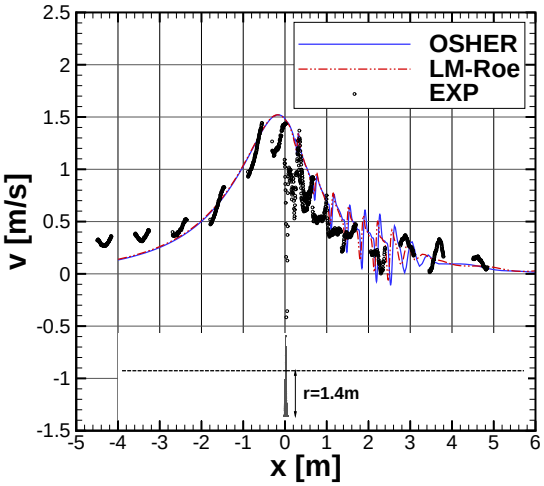

(c) 62.2% R: Radial velocity component.

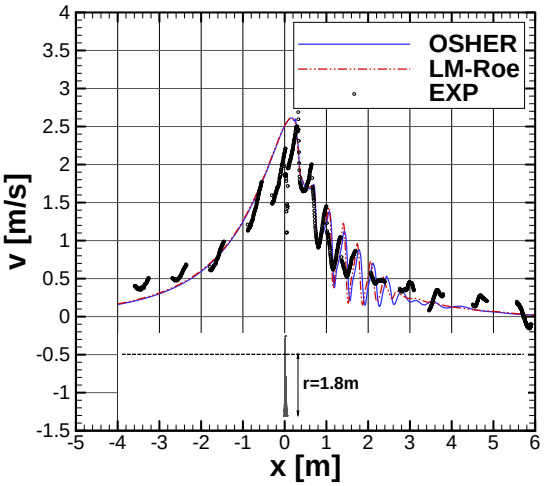

(d) 80% R: Radial velocity component.

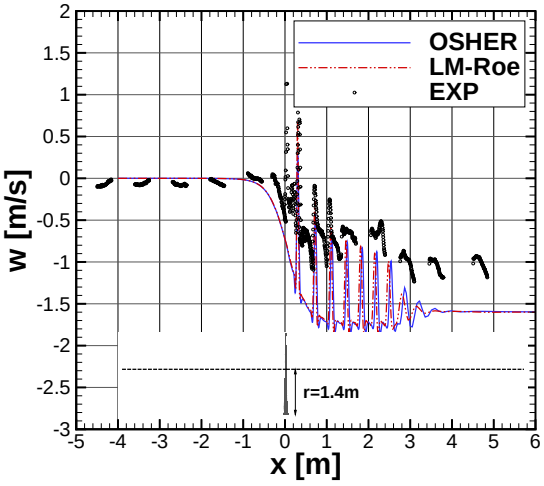

(e) 62.2% R: Tangential velocity component.

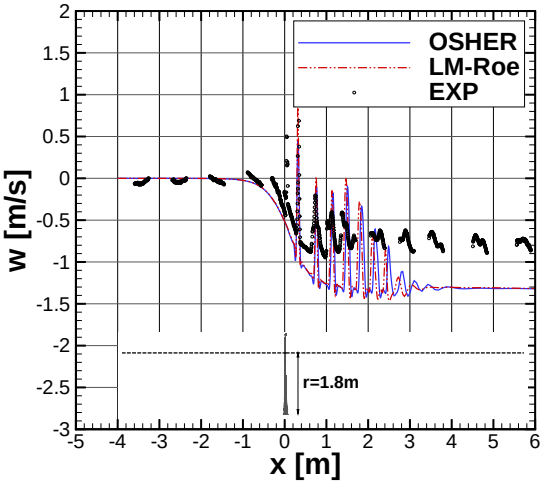

(f) 80% R: Tangential velocity component.

Figure 5.18: Comparison of the axial (top), radial (middle) and tangential (bottom) velocity profiles at 15m/s ($\lambda = 6.67$) at 62.2% R ($r = 1.4$m) and 80% R ($r = 1.8$m). The blade is at 0 degrees of azimuth and grid 2 of Table 5.1 is used.

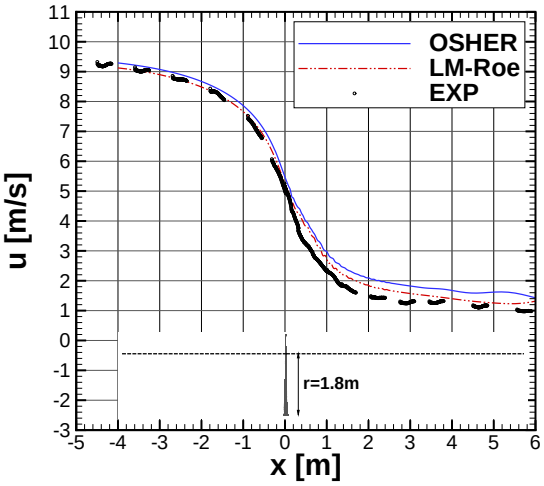

(a) 10m/s: Axial velocity component.

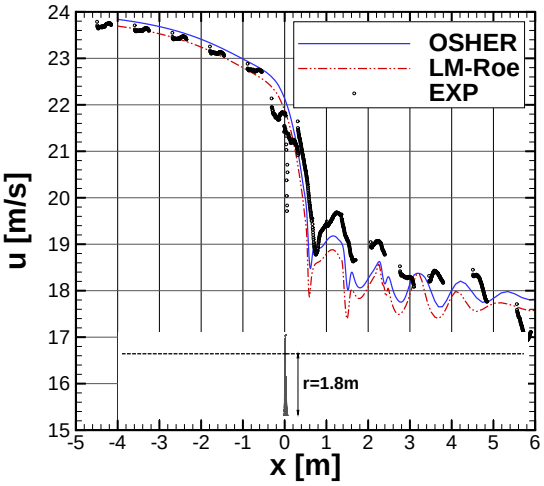

(b) 24m/s: Axial velocity component.

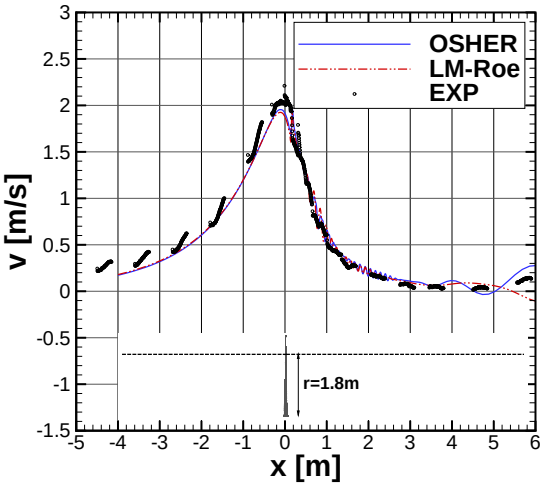

(c) 10m/s: Radial velocity component.

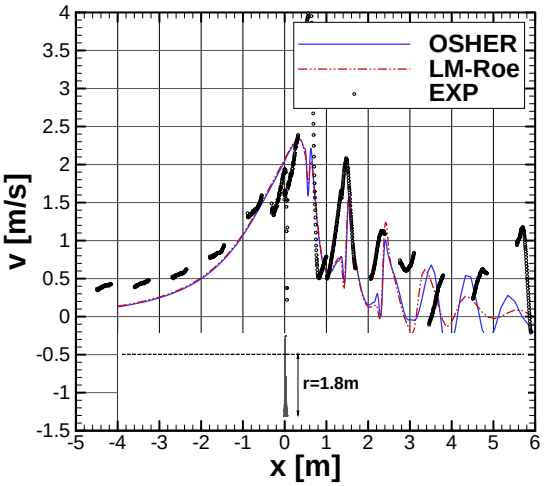

(d) 24m/s: Radial velocity component.

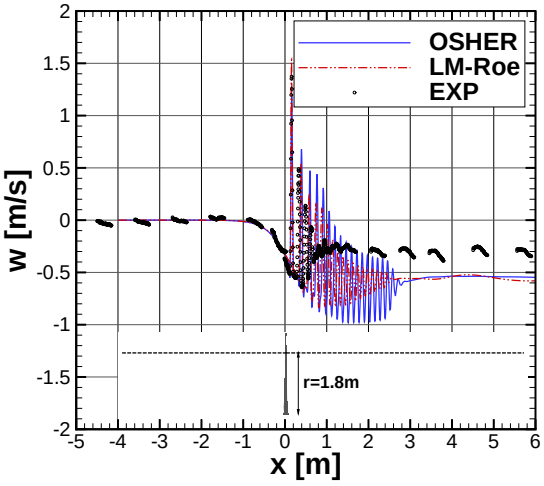

(e) 10m/s: Tangential velocity component.

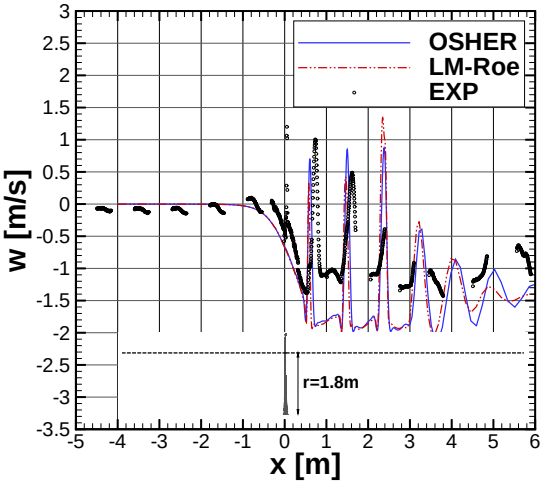

(f) 24m/s: Tangential velocity component.

Figure 5.19: Comparison of the axial (top), radial (middle) and tangential (bottom) velocity profiles at 10 ($\lambda = 10$) and 24m/s ($\lambda = 4.2$) at 80% R ($r = 1.8$m). The blade is at 0 degrees of azimuth and the grid 2 of Table 5.1 is used.

two schemes are more obvious: the absolute magnitude of the oscillations is much higher in the Osher than the LM-Roe solutions, see Figure 5.19 (e). There are two possible reasons for this. Firstly, it might be due to the grid refinement: the cells in the tangential direction are coarser than in the radial and axial directions. As shown in Section 5.2, the low-Mach Roe scheme presented a less dissipative behaviour in coarser grids. Secondly, it might be due to an effect of the low-speed case, since this discrepancy is not observed in the other two higher wind speed cases. At 10m/s, the wake travels downstream more slowly than in the other cases, leading to higher deficits of velocity at 80% span, as can be also observed in the velocity contours of both experiments and CFD in Figure 5.11. These results showed that the differences between schemes become important as the wind speed is reduced.

As presented in Section 5.2, the second vortex core is located at a radial distance of r =2.37m, 2.33m and 2.27m, for wind speeds of 10, 15 and 24m/s, respectively. Radial and tangential velocity components were extracted at these span-wise positions and compared in Figure 5.20. In all wind speed cases, the maximum and minimum peaks observed in these two components correspond to the second vortex. From there, the values start to decay asymptotically. Apart from the loss of vorticity due to numerical dissipation, this behaviour is also due to the fact that the extraction line is missing the vortex cores downstream. The higher the wind speed, the slower the decay of the vortex and the larger the period of the velocity fluctuations.

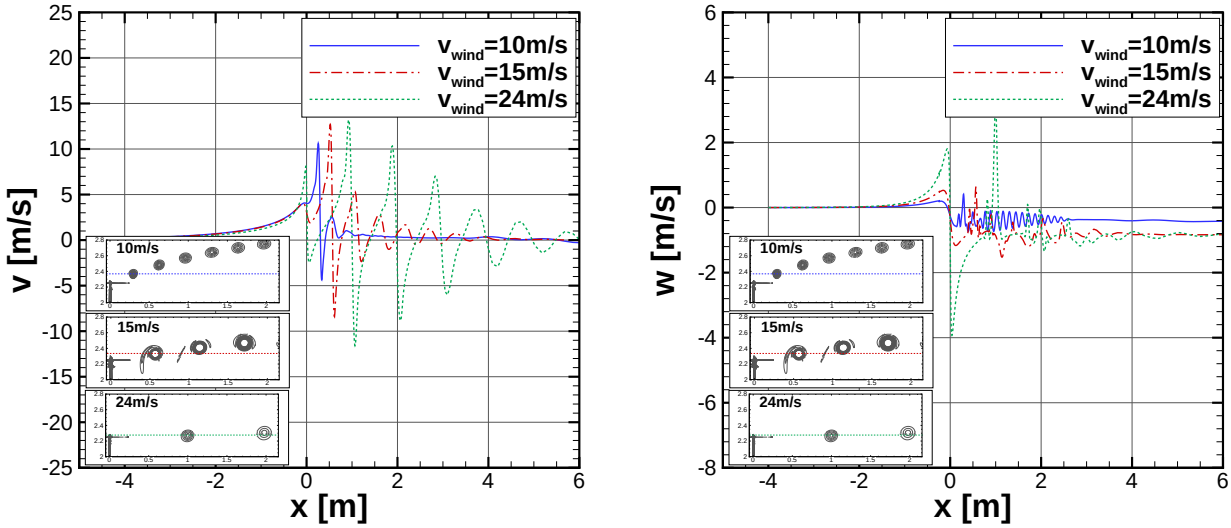

(a) Radial **(b)** Tangential

Figure 5.20: Comparison of the (a) radial and (b) tangential velocity profiles at the line crossing the second vortex core: 10m/s ($r = 2.37$m) 15m/s ($r = 2.33$m) and 24m/s ($r = 2.27$m). The blade is at 270 degrees of azimuth and grid 2 of Table 5.1 was employed.

5.3.2 Flow at the rotor plane

The flow at the rotor plane (from $x = -0.3$m upstream to $x = 0.3$m downstream) is discussed next. Figure 5.21 shows the axial velocity component, at two radial positions: 80%R ($r = 1.8$m) and 120%R ($r = 2.7$m). The studied azimuth angles range from 0 to 60 degrees, in steps of 20 degrees, see Figure 1.12. The results obtained with grid 2 and LM-Roe scheme at $v_{wind} = 15$m/s are compared against the experimental data.

As can be seen, the trend of the CFD computations is very similar to the experiments, with a few discrepancies. Firstly, there is a discontinuity observed in the experiments for azimuth angles of 0 and 20 degrees in the rotor plane (x=0m) at 80%R (Figure 5.21 (a)), which is not captured by the CFD computations. However, these discontinuities are not realistic. For example, at an azimuth angle of 0 degrees (solid line in Figure 5.21 (a)), one of the blades is 30 degrees behind the PIV window, while one of the other blades is at 90 degrees after passage, as seen in Figure 1.12 (a). Hence, the effect of passage should not appear, since one blade has not passed yet and the other is relatively far from the PIV window. Likewise, at an azimuth angle of 20 degrees (dashed lines), one of the blades is 10 degrees before passage, while the other is at 110 degrees after passage (Figure 1.12 (b)), which should not have an effect on the velocity profile either. On the other hand, at azimuth angles of 40 and 60 degrees, the blade is at 10 and 30 degrees after passage, respectively (Figures 1.12 (c) and (d)). This clearly should affect the velocity and that is the reason why in the CFD, like in the experiments, there is a decay on the velocity at $x = 0$m. Hence, the CFD computations seem to be more consistent and the reason of this discontinuity in the experiments might be related to a reflection of the blade or the nacelle on the PIV measurements. Finally, at 120% R, Figure 5.21 (b), the effect of the blade is minimal and the agreement with the experiments is much better.

5.4 Effect of the mesh density

The capability to resolve the vortex structure between two different grid densities is presented here for the 15m/s wind speed case. For this, the solution from a sliding planes grid (grid 2 of Table 5.1) with cell size in the wake of 2.5%c and a chimera grid (grid 3 of Table 5.1), with cell size in the wake of 1.5%c are compared. Figure 5.22 compares vorticity contours of the second vortex, which is 120 degrees old. In the computations, the vortex has a radius of 45mm with the sliding planes (grid 2), while 43mm with

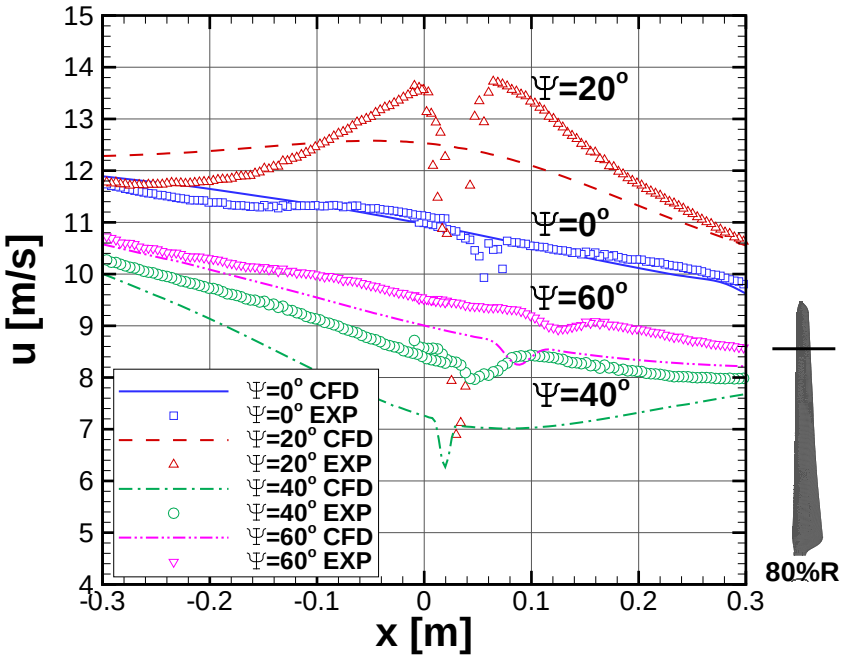

(a) 80% R.

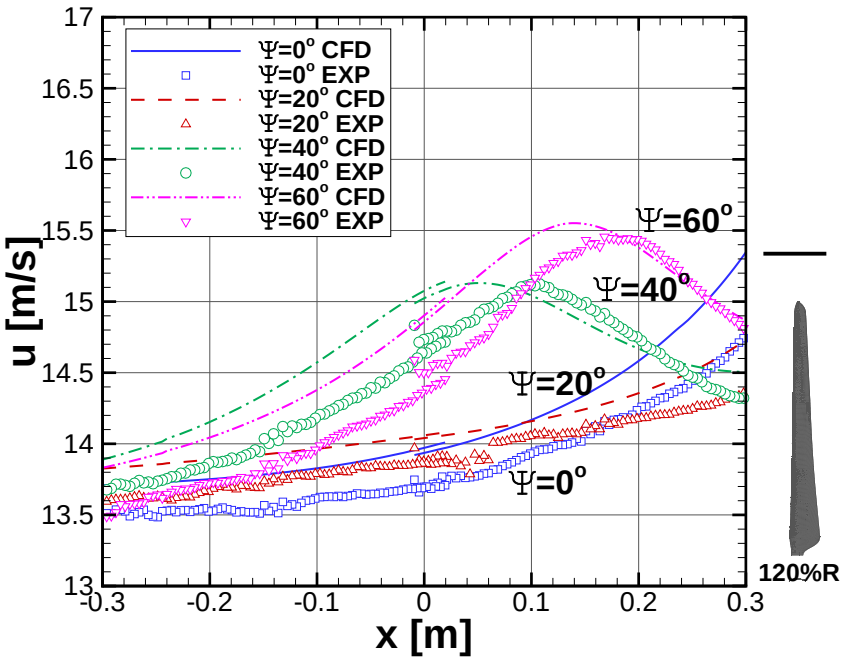

(a) 120% R.

Figure 5.21: Comparison of axial velocity component at 80% R ($r = 1.8$m) and 120% R ($r = 2.7$m) at different azimuth angles and $15m/s$ ($\lambda = 6.67$) wind speed. Results obtained with the LM-Roe scheme and grid 2 of Table 5.1.

the chimera (grid 3). Although the differences are not substantial, as can be observed, the vortex obtained with the latter is tighter than the one using sliding planes. Likewise, in the experiments a spiral around the vortex with lower vorticity levels is present, which is due to the vortex shear as it spins. This effect is more successfully captured with the chimera than with the sliding plane grid, since the former enables better refinement control in localised regions and, therefore, the numerical dissipation is reduced.

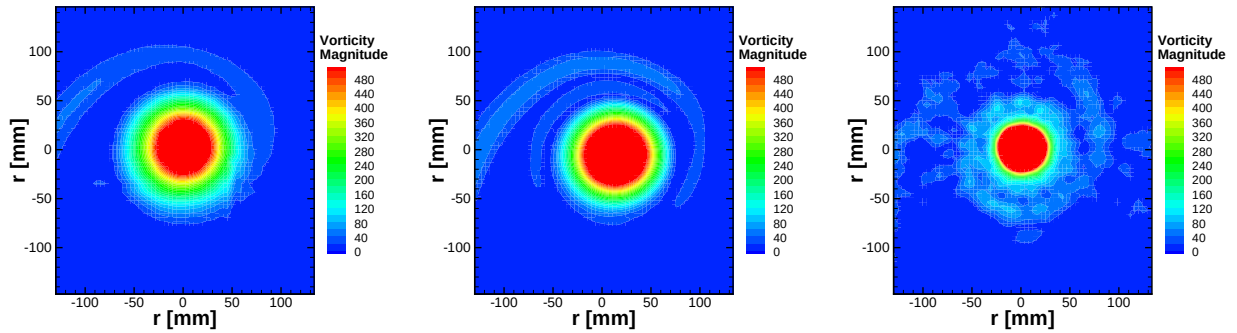

(a) Sliding planes (grid 2). **(b)** Chimera (grid 3). **(c)** Experiments.

Figure 5.22: Contours of vorticity of the second vortex (120 degrees old) for wind speed of 15m/s ($\lambda = 6.67$). Comparison between **(a)** sliding planes **(b)** chimera grids and **(c)** Experiments. The vortices were centred at the $r = (0,0)$ position.

For this particular vortex, the tangential velocity ratio (v/v_{peak}) across the vortex is shown in Figure 5.23. In the comparison with the experimental values, Figure 5.23 (a), similar trend to the measurements is observed: starting with a value of approximately 0.4, reaching a maximum and a minimum (which define the vortex), and finally an asymptotic behaviour downstream. The position where the velocity is zero corresponds to the vortex core. The most significant difference between CFD and experiments is on the curve slope from $v/v_{peak} = +1$ to $v/v_{peak} = -1$, which is an indication of how diffusive is the vortex. As can be seen, the CFD values are very similar and the vortex is more diffused than in the experiments. In order to quantify how diffusive the vortices are, the Vatistas empirical model [160] is employed, where the non-dimensional tangential velocity can be written as,

$$v = \frac{\bar{r}}{(1+\bar{r}^{2n})^{1/n}}, \tag{5.5}$$

Where $\bar{r} = r/r_c$, with r_c the radius core and n a positive integer parameter. The lower the value of n, the more diffusive is the vortex and when $n = \infty$ the perfect Rankine profile is obtained. As can be seen in Figure 5.23 (b), the sliding planes velocity profile follows approximately the Vatistas model with n between

1 and 2, while the chimera solution follows the trend of the Vatistas model between $n = 2$ and $n = 3$. This shows the less diffusive nature of the latter.

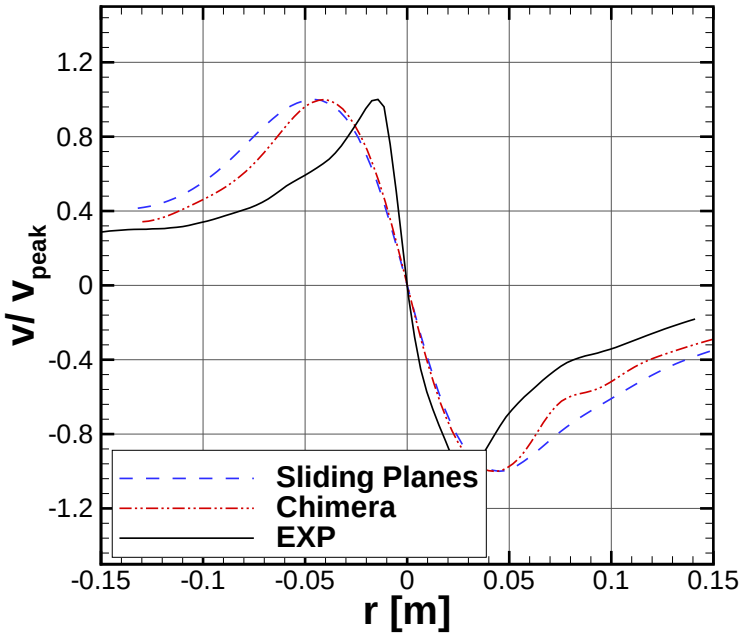

(a) Comparison with experiments.

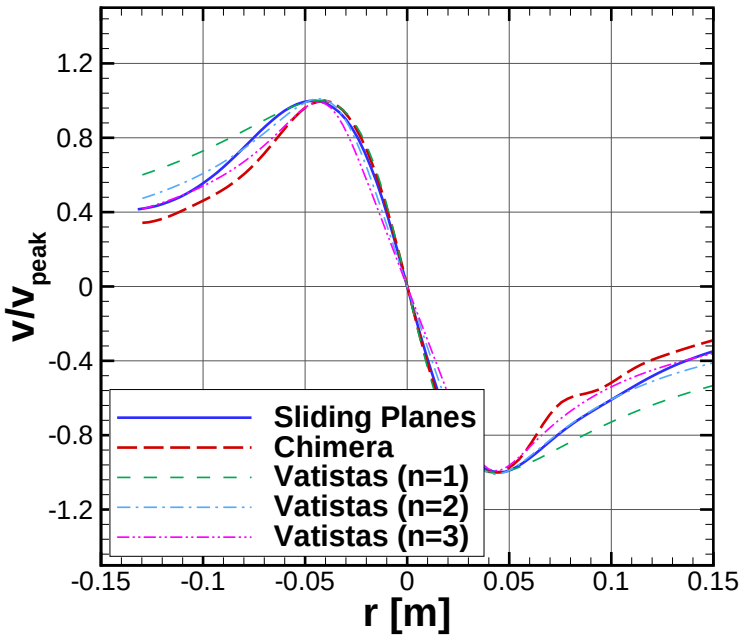

(b) Comparison with Vatistas model.

Figure 5.23: Tangential velocity ratio across the vortex for the second vortex (120 degrees old). Comparison with **(a)** Experiments and **(b)** Vatistas model [160].

The velocity profiles at a radial position of $r = 2.33$m, that is, crossing the second vortex are shown in Figure 5.24. Regarding the radial velocity component (Figure 5.24 (b)) small differences are observed between both grids, apart from 2.8m downstream, where there is a change of refinement in the chimera grid. In fact, there is the interface between the finer grid (ring) and the coarser grid (background). Likewise, larger oscillations in that region are present for this grid in the tangential component, see Figure 5.24 (c). The most significant differences can be observed in the axial velocity component (Figure 5.24 (a)), especially in the peak of velocity where the second vortex is ($x = 0.6$m approximately).

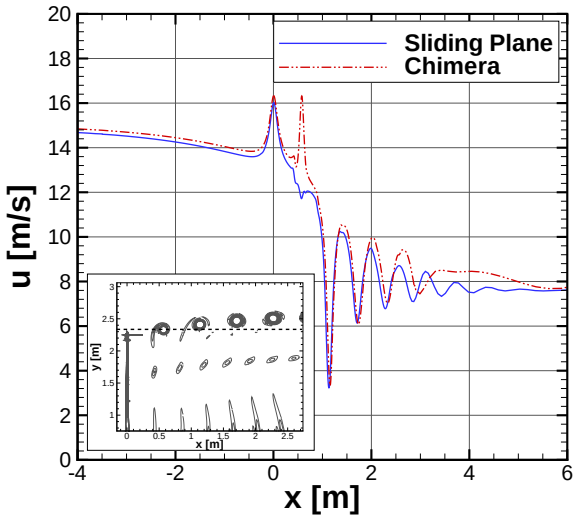

(a) Axial

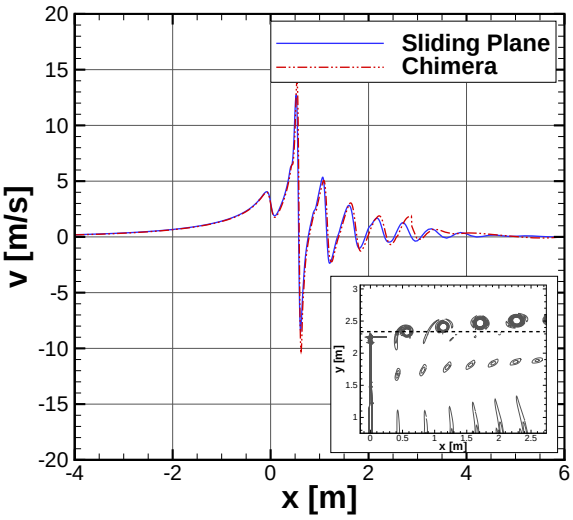

(b) Radial

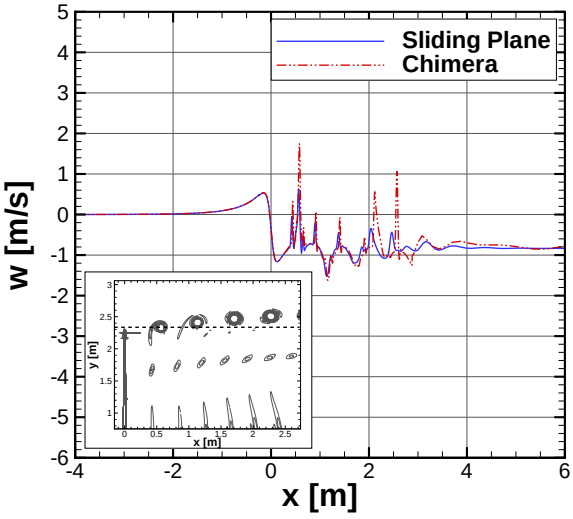

(c) Tangential

Figure 5.24: Comparison of the **(a)** axial, **(b)** radial and **(c)** tangential velocity profiles at 15m/s ($\lambda = 6.67$) wind speed, at $r = 2.33$m. The blade is at 0 degrees of azimuth. Comparison between the sliding plane and chimera, grid 2 and 3 of Table 5.1, respectively.

Chapter 6

Wake Breakdown Study [1]

This Chapter explores the breakdown of the wake downstream of the MEXICO rotor and assesses the capability of CFD in predicting its mechanism. The effect of the wake resolution on the blade loads is firstly studied, using three grids with different vortex resolutions. Different criteria are employed for the identification of the vortex and a stability analysis with Fourier transforms of the axial velocity is presented. The effect of modelling a 120-degree azimuthally periodic domain and a 360-degree three-bladed rotor domain is also studied. Empirical and wake models are also explored, and compared with CFD and a combination of kinematic and field models is proposed.

6.1 Description of cases

In the present work, only the blades of the MEXICO [127] rotor were modelled and no nacelle, spinner or tower were considered in the computations. Two setups were studied: the first one consisted of a 120-degree mesh, where the domain was assumed to be azimuthally periodic and which will be referred to as *single-blade domain* (S.B.). This assumption of periodicity relies on the fact that the rotor has 3 identical blades and since there is no inflow asymmetry, the three blades are expected to behave in the same way. However, the wavelengths of the instabilities are restricted to multiples of the number of blades and therefore a second setup was also considered, which consisted on a 360-degree mesh where all three blades were modelled and

[1] This work is published in M. Carrión *et al.* , Understanding Wind Turbine Wake Breakdown using CFD, *AIAA Journal*, Accepted May 2014.

which will be referred to as *full-rotor domain* (F.R.). In all cases, a chimera grid [68, 69] was employed, which permits localised grid refinement. Table 6.1 shows details of the employed grids and wind speed conditions, as well as the number of cores employed and the total times (in hours) to obtain a converged solution.

Run	Model	V_{wind} (λ)	Comput.	Mesh Size (Blocks)	Boundaries (R)	Cores (Time)
I	S.B.	15 (6.67)	RANS	860M (4,436)	I:3 O:12 FF:4	1,024 (300h.)
II	S.B.	10 (10)	RANS	860M (62,568)	I:3 O:12 FF:4	16,384 (112h.)
III	F.R.	10 (10)	RANS	2,000M (40,224)	I:3 O:12 FF:4	16,384 (180h.)

Table 6.1: Summary of computations (*S.B.: Single blade, F.R.: Full rotor, I: Inflow, O: Outflow, FF: Far-field*).

For computations with an azimuthally periodic domain, a 860 million cell mesh was employed, which consists of 3 chimera levels, as shown in Figure 6.1 (a). Firstly, a coarse background that extends from $3R$ upstream to $12R$ downstream the rotor (*Level 0*) and a blade-fitted grid (*Level 2*) with a C-topolgy for optimally resolving the boundary layer. The mesh region for the wake capture extends from the blade's root up to $1.6R$ in the radial direction and $8R$ behind the rotor plane, denoted as *Level 1* in Figure 6.1 (a). In this region, the cells have a size of 2.5% of the chord at the blade's root and 6.5% of the tip chord (6mm) in the axial and radial directions, covering 0.22 degrees in the azimuthal direction. According to the experiments, the vortex has an approximate diameter of 40mm, hence, with this grid resolution, 7 cells are present across the tip vortex diameter. Figure 6.1 (b) shows a slice at the rotor plane, where *Level 1* and *Level 2* overlap. The first grid space normal to the blade surface (*Level 0*) have a size of $2.4 \cdot 10^{-6}$m, which gives y^+ less than 1.0 all over the blade, and maximum cell sizes of 3mm. A slice near the outflow is shown in Figure 6.1 (c), where *Level 0* and *Level 1* overlap. The smaller cells at the background have a size of 30mm, which increase in size at the inflow and outflow boundaries.

To save computational resources, in the full rotor grid (F.R.) the region for the wake resolution (*Level 1*) extended from the rotor to $6R$ in the streamwise direction, since the low wind speed case was selected for this computation and from the single-blade results it was found that the wake breakdown was much earlier than in the higher wind speed case. That is the reason why the grid has a total of 2 billion cells, instead of being three times bigger than the single-blade one. Also, for those cases run at Hartree HPC Center, a large number of cores was employed and the meshes were cut to an optimal number of blocks to achieve good load balance.

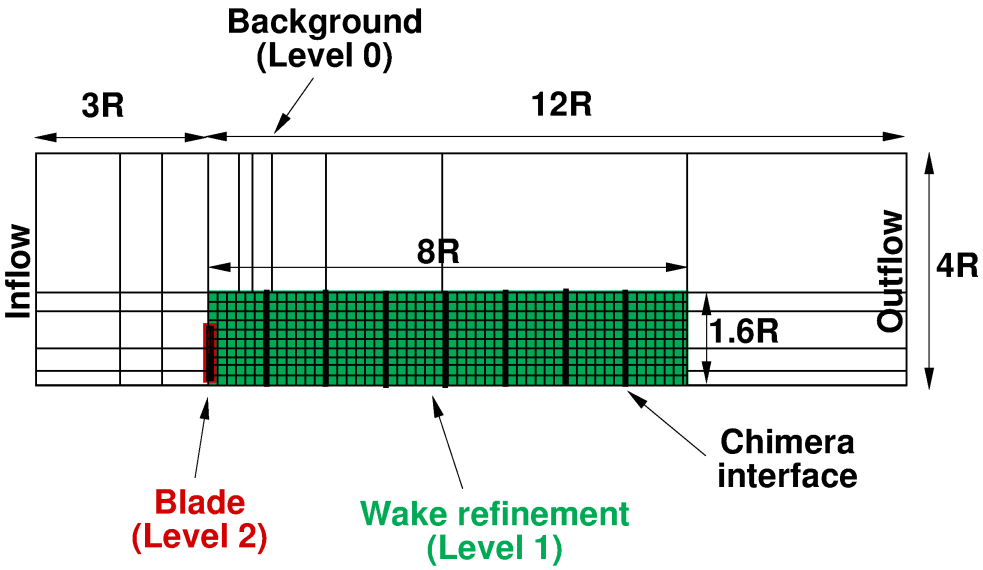

(a) Computational domain and configuration of chimera levels.

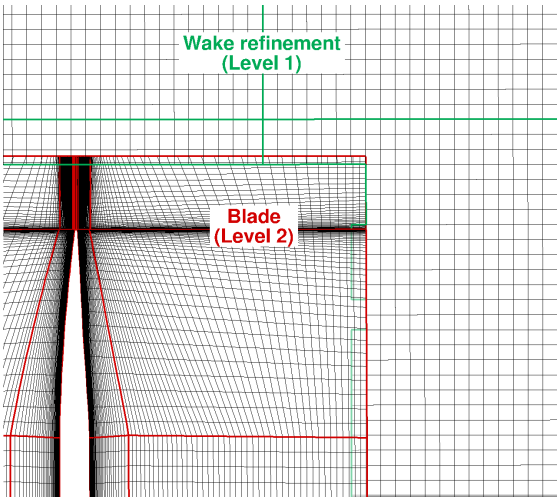

(b) Change of cells around the rotor.

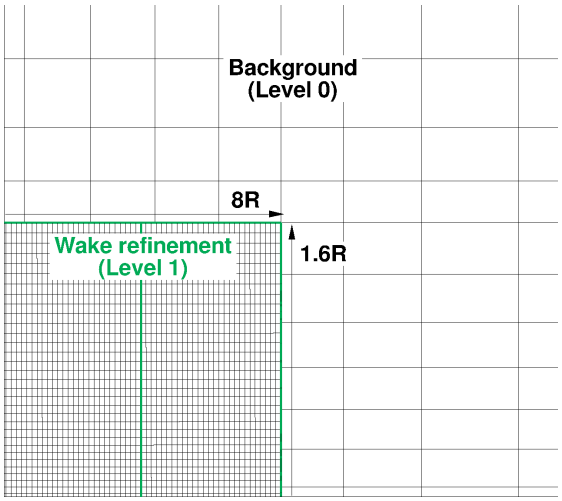

(c) Change of cells density near the outflow.

Figure 6.1: **(a)** Computational domain of the employed grid, including dimensions in radii and three chimera levels. **(b,c)** Cell density for the regions close to the rotor plane and the outflow.

For the present study, RANS computations were performed, since they do not march in real time and therefore results can be obtained faster than with time-accurate simulations. Likewise, the k-ω turbulence model by Wilcox[163] was employed, due to its stability and the presence of attached flow on the blades for the studied wind speeds. In RANS, all the flow scales are modelled and this method has the limitation of being too diffusive if the grid employed is not fine enough. LES is also popular in the literature; it is based on filtering the scales larger than the grid cells and modelling the smaller ones with a sub-grid

model. For a proper use of the LES method, however, both the grid and the time-step sizes should be very small, otherwise all the scales will be modelled instead of being resolved. LES leads to very expensive computations. Although the grids employed for this study may seem very fine, even finer grid cells would be necessary in order to perform an LES computations, which would be prohibitive in terms of time and computational effort. Further, the instability of the core is more essential to the breakdown than the detailed modelling of turbulence.

Two wind speed cases were studied: 15m/s and 10m/s, keeping a constant rotational speed of 424.5rpm, which corresponds to tip speed ratios of $\lambda = 6.67$ and $\lambda = 10$, respectively. Axial wind conditions were assumed and the blade pitch angle was set to -2.3 degrees. A Reynolds number, based on the tip speed (100m/s) and the maximum aerodynamic chord (0.24m), of 1.6 million was selected.

6.2 Effect of the wake on the loads

Three cases with different wake refinement are compared for the 15m/s wind speed case. As shown in Figure 6.2, in the first grid the wake was captured up to $1.25R$ downstream, in the second it was captured up to $4R$ and the third case (presented in Section 6.1) captures the wake up to $8R$. In all of them, the cells at the wake have a size of 2.5% of the chord at the blade root. For the first grid, Figure 6.2 (a) only the first 4 vortices were captured. For the second grid, 16 vortices were captured until they were dissipated due to change of grid density. In the last grid, conversely, there is minimal dissipation and more vortices are captured. It should be mentioned that for the first two cases (Figures 6.2 (a) and (b)), the grids were refined at the location of the tip vortices, being the region of the root vortices coarser. For the last two cases, conversely, the grid was uniform in all the presented region. That is the reason why the root vortices are more dissipated in the first two cases of Figure 6.2.

Figures 6.3 (a) and (b) show sectional thrust and torque versus span-wise position obtained for the three cases. As can be observed, the differences are minimal regardless of the wake resolution. The overall integrated thrust coefficient is also very similar, as shown in Figure 6.3 (c). This indicates that, once the loads have converged, they are not affected anymore by how the wake develops. In terms of classic aerodynamics theory, the $1/r^2$ of the Biot-Savat law also suggests a rapid decay in the influence of the wake on the blades with increasing distance (r).

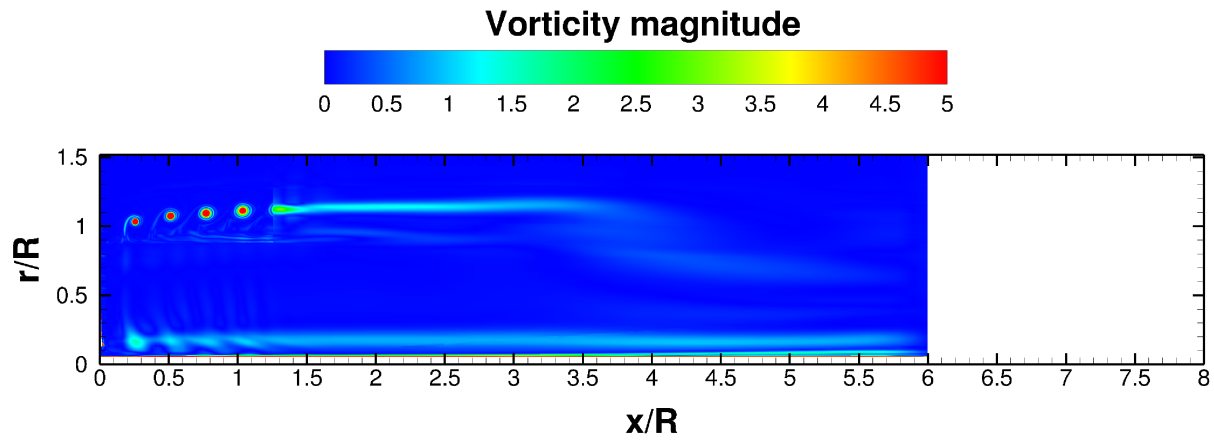

(a) Refinement of the grid to capture the wake up to 1.25R downstream at 15m/s wind speed.

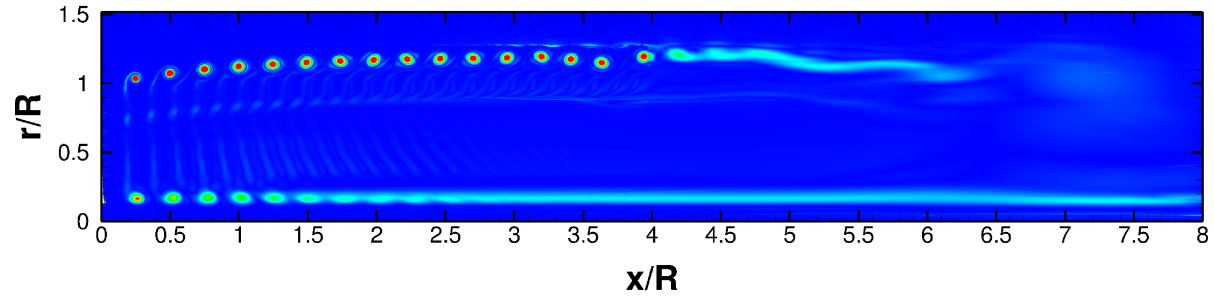

(b) Refinement of the grid to capture the wake up to 4R downstream at 15m/s wind speed.

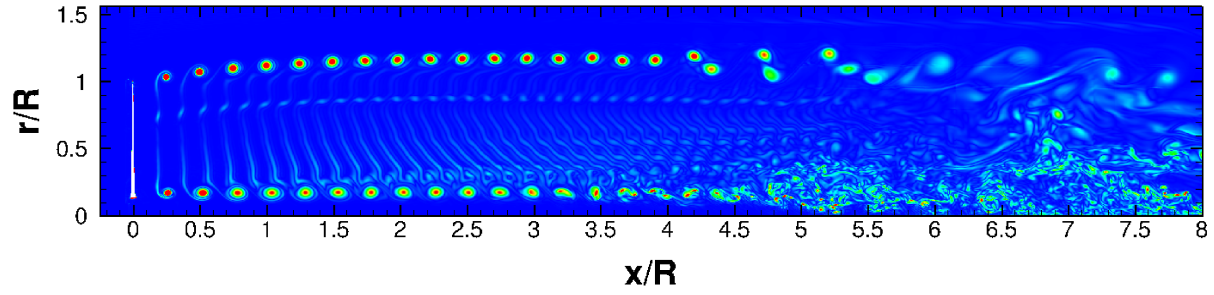

(c) Refinement of the grid to capture the wake up to 8R downstream at 15m/s wind speed.

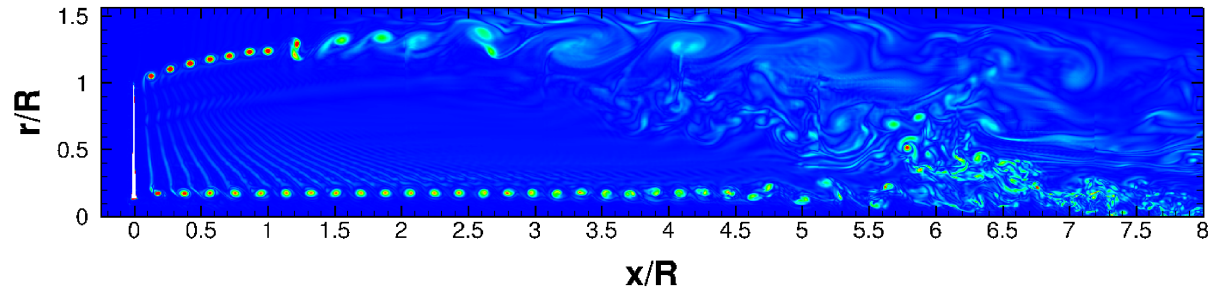

(d) Refinement of the grid to capture the wake up to 8R downstream at 10m/s wind speed.

Figure 6.2: Wake resolution employing different grids. Vorticity contours in planes perpendicular to the rotor through a blade at 12 o'clock. Wake capture up to **(a)** 1.25R, **(b)** 4R and **(c)** 8R downstream at 15m/s ($\lambda = 6.67$) and **(d)** 10m/s ($\lambda = 10$).

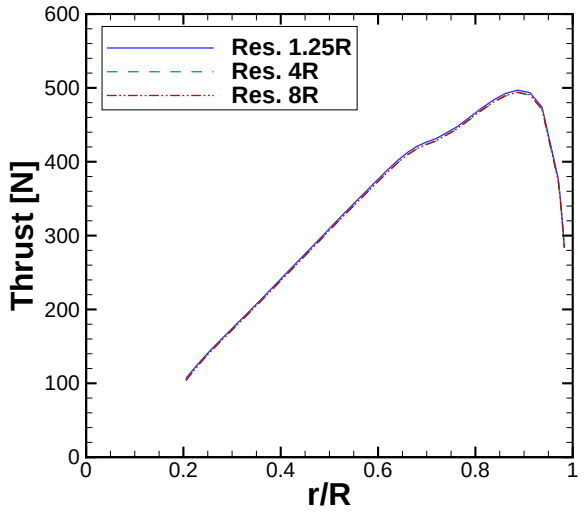

(a) Span-wise thrust.

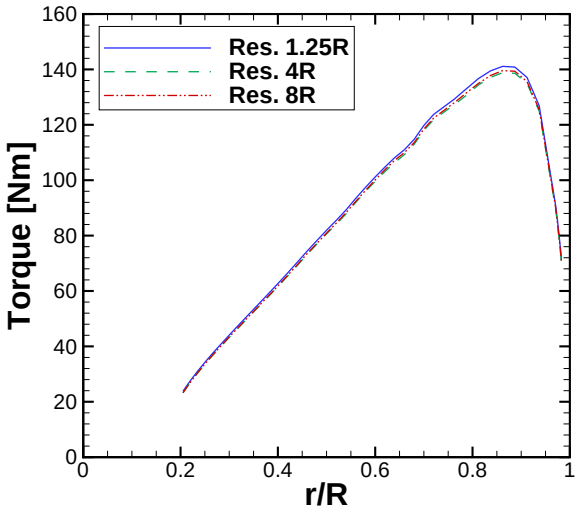

(b) Span-wise torque.

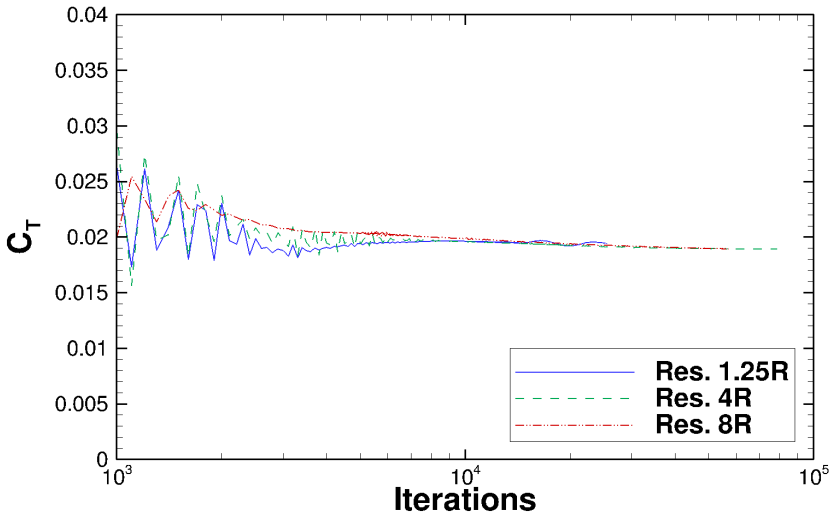

(c) Integrated thrust coefficient convergence.

Figure 6.3: Comparison of the span-wise loads and thrust coefficient obtained with three wake resolutions, at 15m/s wind speed.

6.3 Vortex identification

The vorticity contours presented in Figure 6.2 (c) show that at 15m/s the vortices are equidistant and therefore the wake is stable until 4R downstream, where the tip vortices begin to pair. From that point, the vortices interact and the wake is considered as *unstable*. The first part of the unstable wake (from 4R to 7R) contains coherent structures. From 7R downstream, non-coherent structures are present and a second wind turbine located in that region would not be strongly affected. It is also interesting that the vortices are perfectly round until 2R downstream and, from that point, become elliptical until the pairing begins. Additionally,

in Figures 6.2 (c) and (d) a discontinuity in the wake can be observed at approximately 70% R span-wise position. At that blade station, two different aerofoils (RISO-A1-21 and NACA-64-418) are blended and this discontinuity might be due to differences of their zero-lift angles. At 50% R, there is also a change in aerofoil sections (DU91-W2-250 and RISO-A1-21), but the effect seems to be smaller. For the lower wind speed case shown in Figure 6.2 (d), the vortex pairing starts at 1.25R. This is due to the fact that in this case the vortices are closer to each other and, therefore, the self-induced flow between vortices is higher. In the velocity contours of the experiments presented earlier in Figures 5.9 to 5.11, a discontinuity in the vortex pattern was observed. This could suggest presence of instabilities from 1R. However, the CFD predicts the onset of instabilities slightly later. This could be due to dissipation, that maintains the vortices stable further downstream. With a much finer grid, an earlier onset of instabilities might be predicted. Nevertheless, one should bear in mind that the PIV was averaged and no full information about this mechanism is available for these experiments. It is also noteworthy that the root vortices seem to be stable further downstream than the tip vortices. This should be attributed to the higher blade pitch at the root which, in absence of hub, leads to longer distances between vortices, making therefore the self-induced flow between them lower.

Figure 6.4 shows contours of turbulent Reynolds number (μ_T/μ) for a detailed region of the first tip vortices of the wake, from the rotor to 1.5R downstream. Low levels of turbulence are observed in the vortex cores. However, they are not fully laminar because no limiter to stop the production of eddy viscosity in the vortex was employed.

A comparison between the measured vortices in the experiments and the computed with CFD is presented in Figure 6.5, where good agreement is observed. Although the predicted vortices are slightly bigger than in the experiments due to numerical dissipation, the shear spiral generated as the vortex spins, which can be observed in light colour surrounding the measured vortex core (Figures 6.5 (a) and (c)), is well captured in the CFD, see Figures 6.5 (b) and (d).

Figure 6.6 shows planes parallel to the rotor at different axial locations, for the two wind speed cases. Firstly, Figures 6.6 (a) and (b) show the region where the vortices describe a perfect spiral, denoted as *stable wake*; in Figures 6.6 (c) and (d) the vortices start to oscillate and therefore the instability starts; finally the *unstable wake* is shown in Figures 6.6 (e) and (f). As the instabilities develop, the tip vortices in both wind speed cases start to interact between them and describe an oscillatory pattern as supposed to a perfect circle.

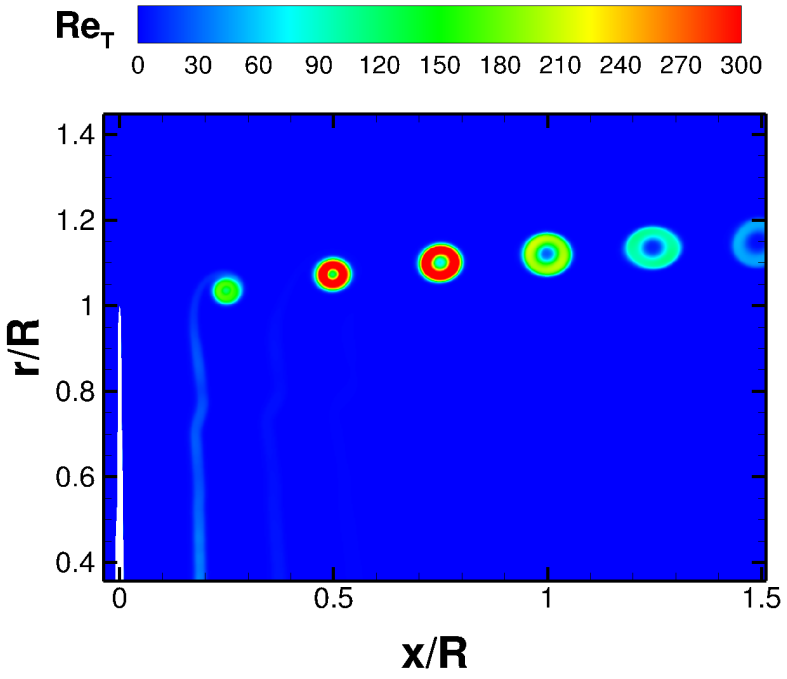

Figure 6.4: Contours of turbulent Reynolds number ($Re_T = \mu_T/\mu$) on a region of the MEXICO wake at 15m/s wind speed.

This can be seen in Figures 6.6 (c) and (f). At higher wind speed, the amplitudes of the oscillations are higher than for the lower speed case.

In Figure 6.7 vortex core lines in the wake are shown, which were generated with the vortex core extractor of *TECPLOT* [149] that examines the vorticity vector. At 15m/s they fall on a perfect spiral until 4R, approximately. Between 4R and 5R the core location has an oscillatory behaviour, which indicates the presence of instabilities. For the lower speed case, Figure 6.7 (b), there is more expansion in the wake and the oscillatory behaviour is observed from 1.25R, approximately.

Iso-surfaces of λ_2-criterion [70] were also generated to visualise the vortical structures and characterise in more detail the wake. Figures 6.8 (a) and (b) show the full wake at 15m/s, along with details of the unstable region between 4R and 6R. For 10m/s, Figures 6.8 (c) and (d), the unstable region starts at 1.25R.

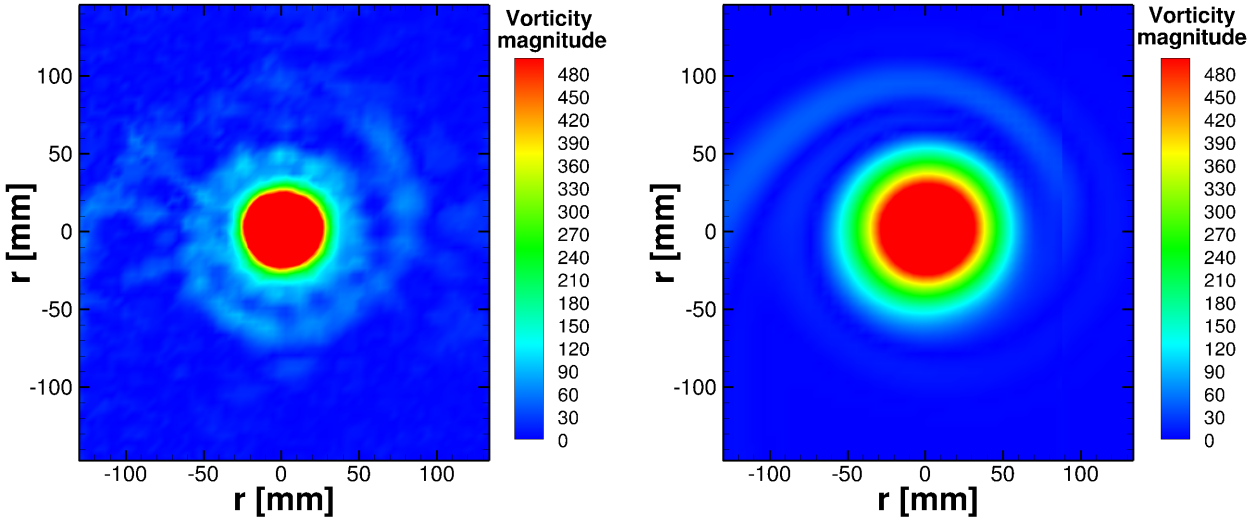

(a) Measured vortex (15m/s).

(b) Computed vortex (15m/s).

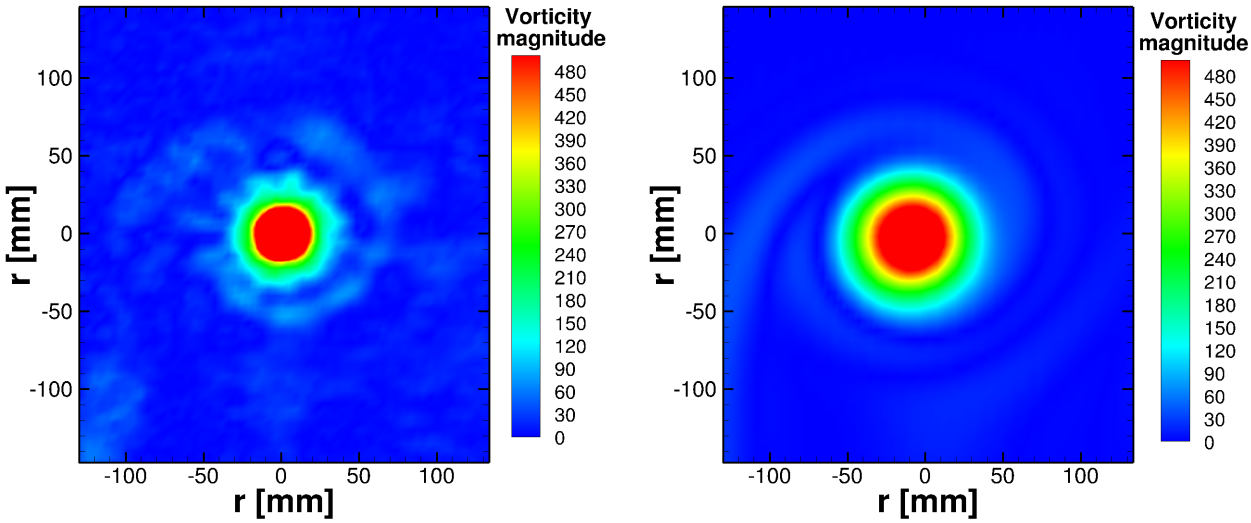

(c) Measured vortex (10m/s).

(d) Computed vortex (10m/s).

Figure 6.5: Comparison between the experimental and computed vortex for wind speeds of 15m/s (Top) and 10m/s (Bottom). Vorticity magnitude is shown (in $1/s$).

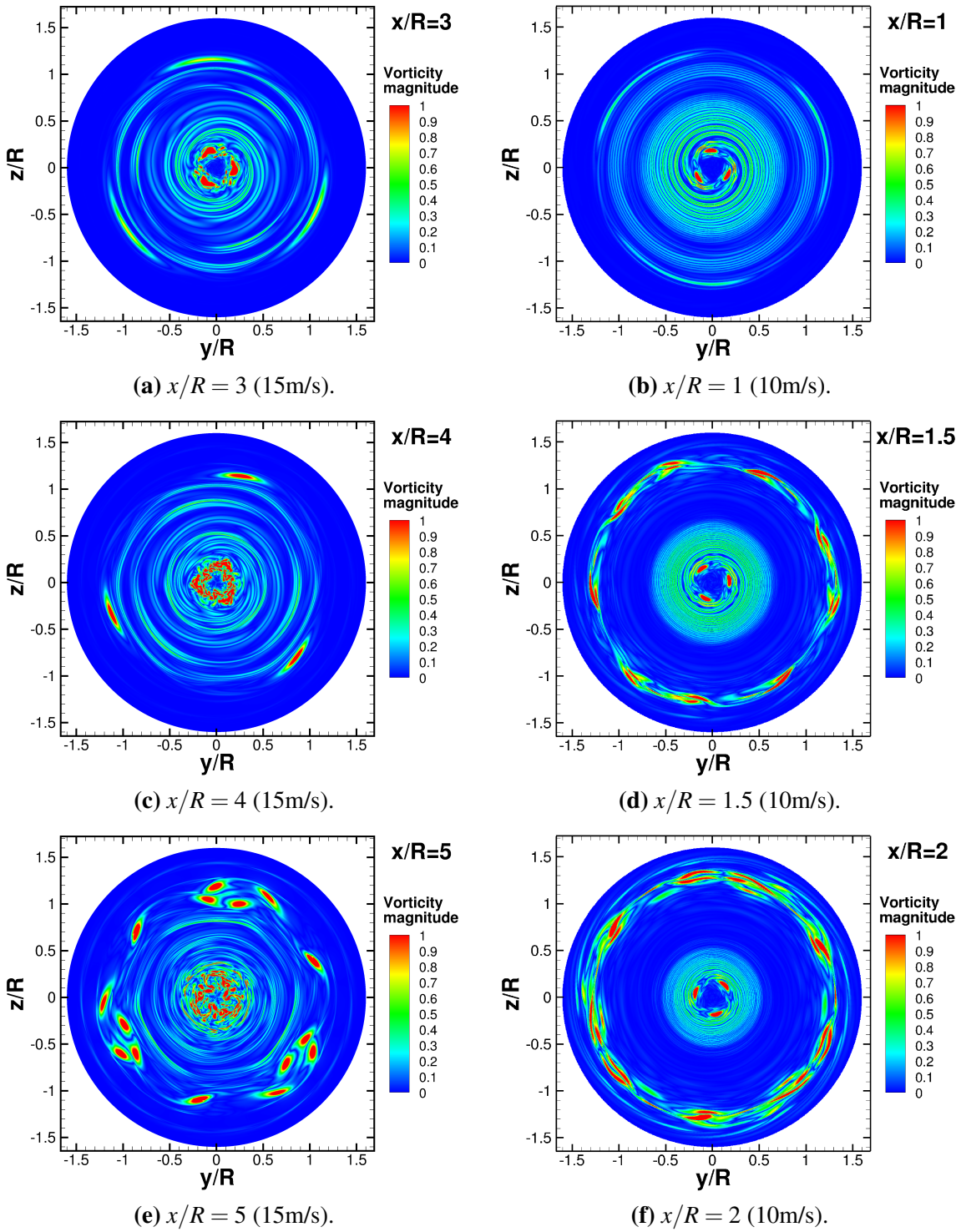

(a) $x/R = 3$ (15m/s). **(b)** $x/R = 1$ (10m/s).

(c) $x/R = 4$ (15m/s). **(d)** $x/R = 1.5$ (10m/s).

(e) $x/R = 5$ (15m/s). **(f)** $x/R = 2$ (10m/s).

Figure 6.6: Wake behind the MEXICO rotor visualised with vorticity contours on planes parallel to the rotor plane at different axial locations. Top: 15m/s ($\lambda = 6.67$) case; Bottom: 10m/s ($\lambda = 10$) case.

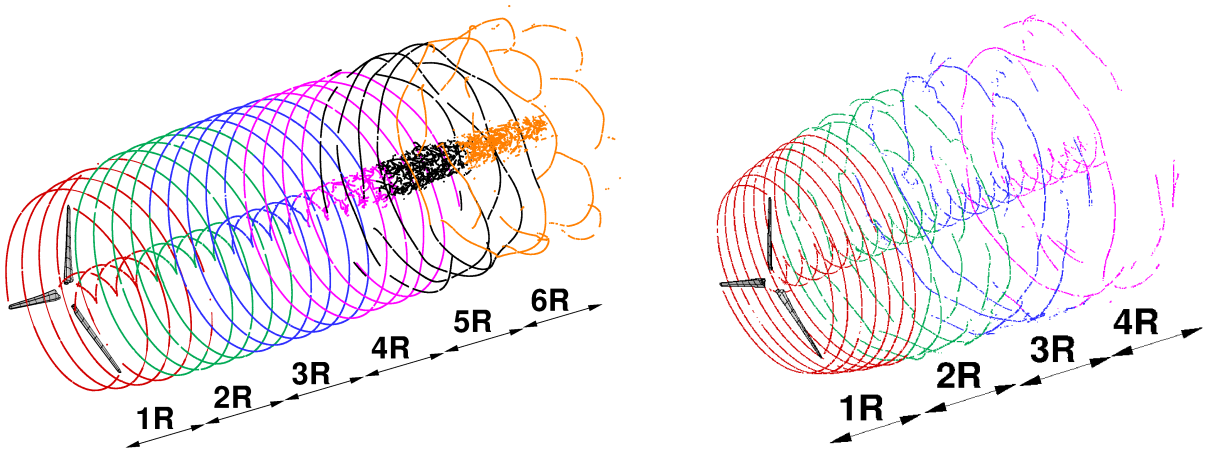

(a) 15m/s ($\lambda = 6.67$). **(b)** 10m/s ($\lambda = 10$).

Figure 6.7: Wake behind the MEXICO rotor with vortex core lines, for **(a)** 15 and **(b)** 10m/s wind speeds.

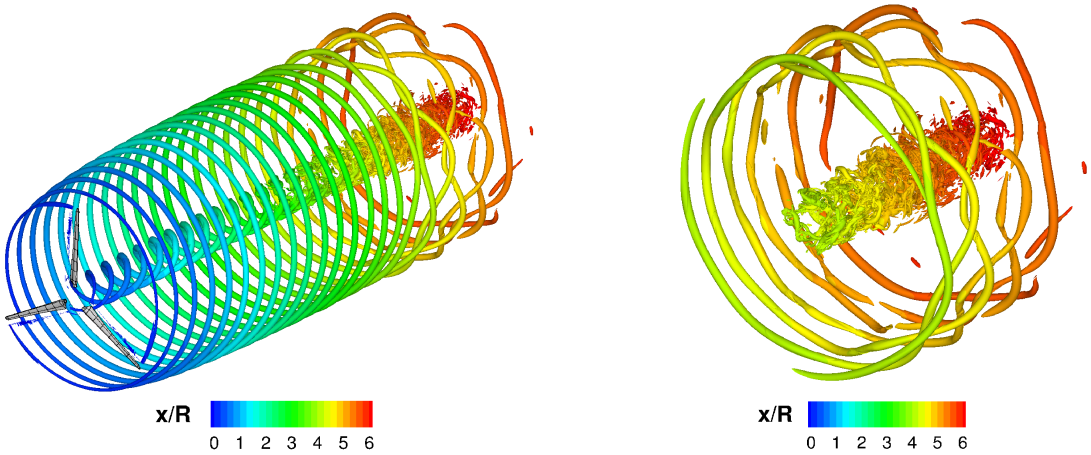

(a) Wake from 0 to 6R (15m/s). **(b)** Unstable region (15m/s).

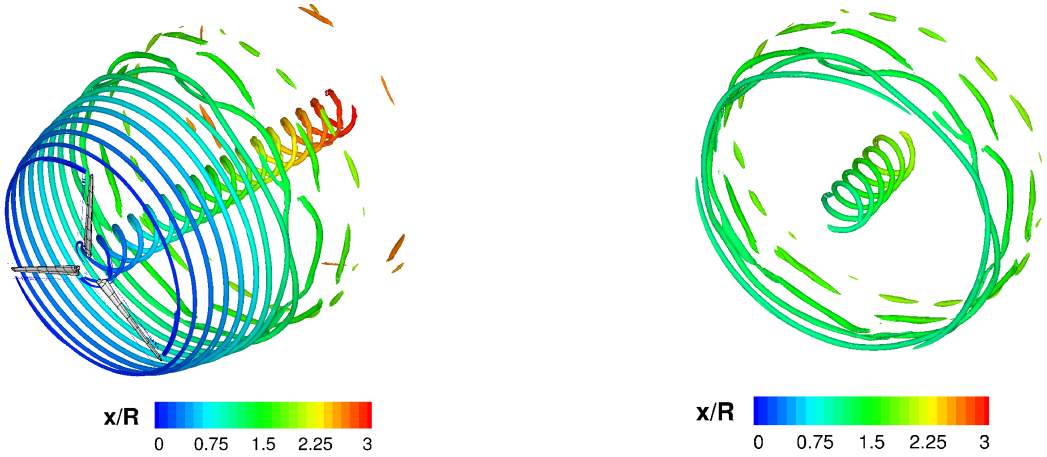

(c) Wake from 0 to 3R (10m/s). **(d)** Unstable region (10m/s).

Figure 6.8: Wake developed behind the MEXICO rotor visualised with iso-surfaces of $\lambda_2 = -0.01$ at wind speed of Top: 15m/s ($\lambda = 6.67$) and Bottom: 10m/s ($\lambda = 10$).

6.4 Stability Analysis

To understand the wake breakdown mechanism, series of sampling data covering different axial and radial positions where extracted in the wake, to obtain the velocity signals and their corresponding FFT. As Figure 6.9 shows, since the wake had very small expansion at 15m/s wind speed, the set of probes for this case were located in a radial station coinciding with the tip of the blade and from the rotor plane to 6R in the streamwise direction. At 10m/s, conversely, the wake had bigger expansion and therefore the probes were located slightly outwards, at 1.1R radial station, and from the rotor plane to 4R in the streamwise direction. Since the CFD was steady-state, the space domain can be converted into time domain, using $t = \frac{\Psi}{\omega}$; where Ψ is the azimuthal position and ω the rotational frequency. 3600 samples of velocity data were extracted, which is equivalent to 1.41s signal (10 rotor revolutions).

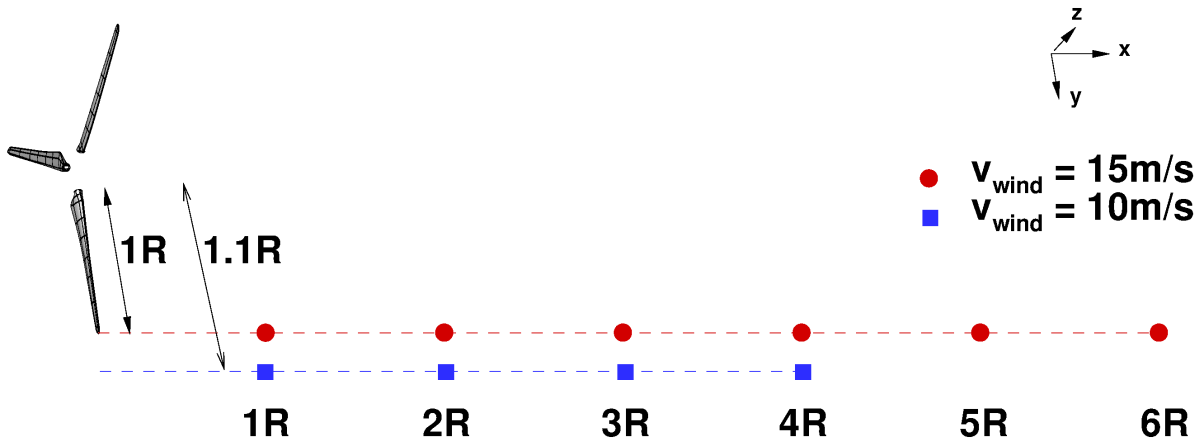

Figure 6.9: Probe setup. For the 15m/s, they were set at 1R radial station and from 1R to 6R downstream; for 10m/s, they were set at radial station of 1.2R and from 1R to 3R downstream.

Since the rotational frequency is 7.075Hz and the rotor has 3 blades, the first harmonic is 21.2Hz, which corresponds to the blade-passing frequency. The results in Figure 6.10 show a frequency of 21.4Hz, and second and third harmonics of 42.8Hz and 64.2Hz, respectively, for both wind speed cases. For the unstable wakes, Figures 6.10 (b) and (d), frequencies up to 300Hz were also captured. This is the result of the interaction between vortical structures that leads to their breakdown into smaller ones. Taking as a reference that each blade covers 7 revolutions every second (7Hz), these high frequency structures cover $1/42$ times that distance or, in other words, a $1/6$ of a circumference. This can be easily visualised in the tip vortices of Figure 6.6 (c).

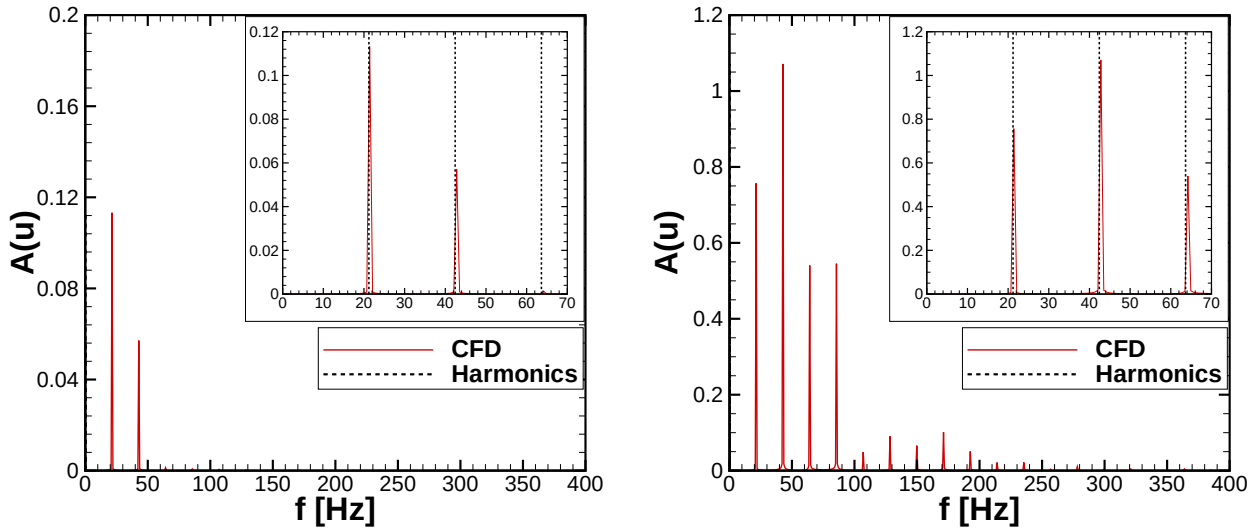

(a) $x/R = 3$ ($v_{wind} = 15$m/s). **(b)** $x/R = 5$ ($v_{wind} = 15$m/s).

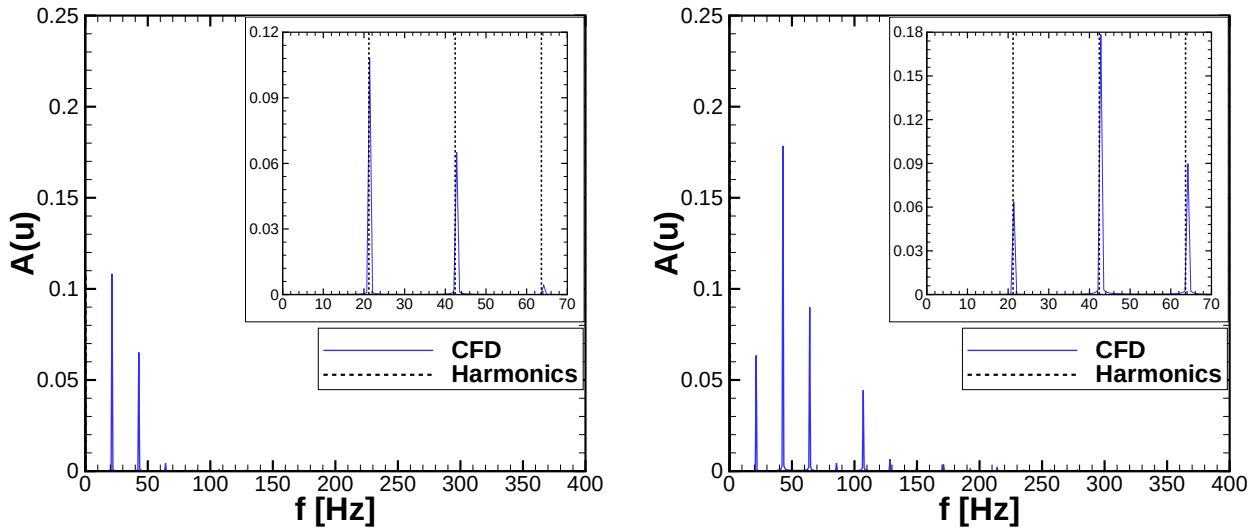

(c) $x/R = 0.75$ ($v_{wind} = 10$m/s). **(d)** $x/R = 2$ ($v_{wind} = 10$m/s).

Figure 6.10: FFT analysis using 3600 sampling data (equivalent to $1.41s$) of the axial velocity component (u) at different axial and radial positions, for the 15m/s (Top) and 10m/s (Bottom) wind speed cases. The blade-passing frequency (f_1) is 21.2Hz and the harmonics are multiples of it ($f_n = n \cdot f_1$).

The amplitudes of the u velocity component at 15m/s wind speed from the rotor plane to $6R$ downstream for these three first harmonics are shown in Figure 6.11 (a). From $1R$ to $3R$ approximately, the amplitudes are almost constant and the main frequency content is the rotational one (21.4Hz). Likewise, from $3R$ to $4.5R$ an approximate exponential growth can be observed, until it reaches a value of $\Delta u = 1.4$m/s. From that point, the second and third harmonics become important, leading to the oscillatory behaviour and vortex pairing discussed in Section 6.3. This is in good agreement with an earlier study presented by Ivanell

et al. [64], where the amplitudes of a prescribed perturbation where tracked in the streamwise direction. In the initial wake evolution, the same exponential growth was obtained and the multiples of the first harmonic were dominant in the vortex pairing region.

Since the onset of the instability is much earlier at 10m/s (at $1.25R$ approximately), Figure 6.11 (b) covers mainly the unstable region, where the higher frequency content is present.

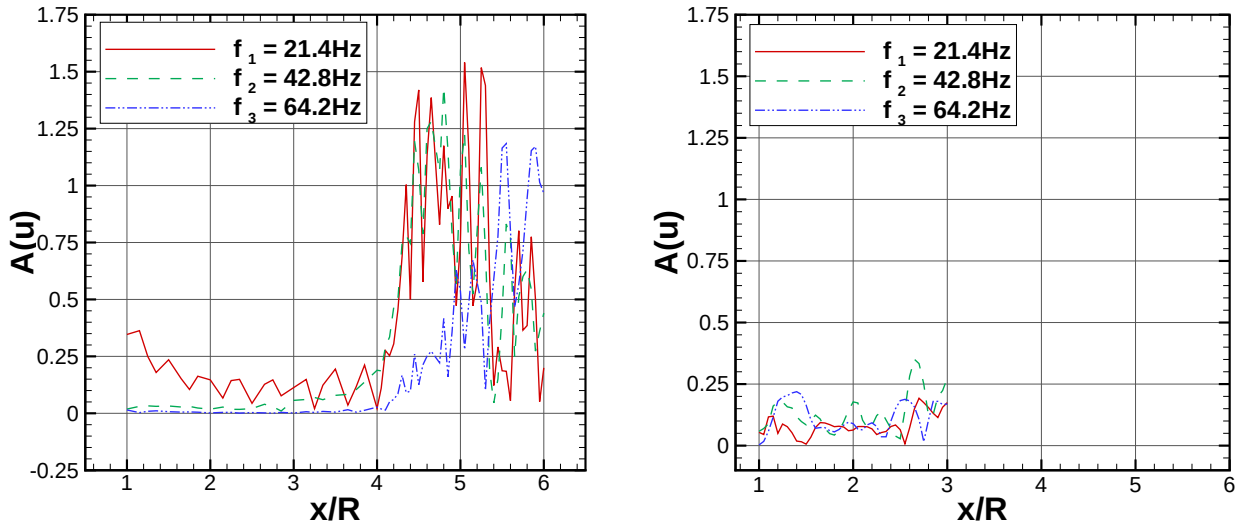

(a) v_{wind}=15m/s. **(b)** v_{wind}=10m/s.

Figure 6.11: Amplitudes of axial velocity for the first three harmonics, as a function of the axial position. In case **(a)** $r/R = 1$ and **(a)** $r/R = 1.1$.

6.5 Sensitivity to spatial periodicity

The effect of the use of spatial periodicity is presented here. For this, the solutions obtained with grids II and III of Table 6.1 are compared, where the former was built for a 120-degree domain, using azimuthally periodic boundaries, and in the latter the full rotor was considered in a 360-degree domain. The onset of instabilities can be seen in the vorticity contours in a plane through one of the blades of Figure 6.12, where the tip vortices start to be unstable and pair between $1R$ and $1.25R$, for both cases. It should be mentioned that the instant where these plots were generated is not exactly the same in both cases and that is the reason why the unstable vortices are not exactly at the same location. Nevertheless, the onset of instability is consistent.

On the other hand, significant differences can be observed at the root vortices. While for the full rotor configuration they begin to pair at $2.5-3R$, for the single-blade case they are stable much further downstream, as a result of enforcing periodicity. Since the one-third-circle covering the domain at the root is much shorter than at the tip, the root vortices are confined in a much smaller azimuthal region and do not have as much freedom to oscillate as the tip ones, and therefore are restricted to fall in an almost perfect spiral. In fact, for the same streamwise location of $2.5R$, the main frequency of the root vortices pairing is 7Hz, while at the tip is 42.8Hz, which means that instabilities with much longer wavelength may be dominant in the root region. This is, however, secondary to the fact that the hub and nacelle are not modelled here.

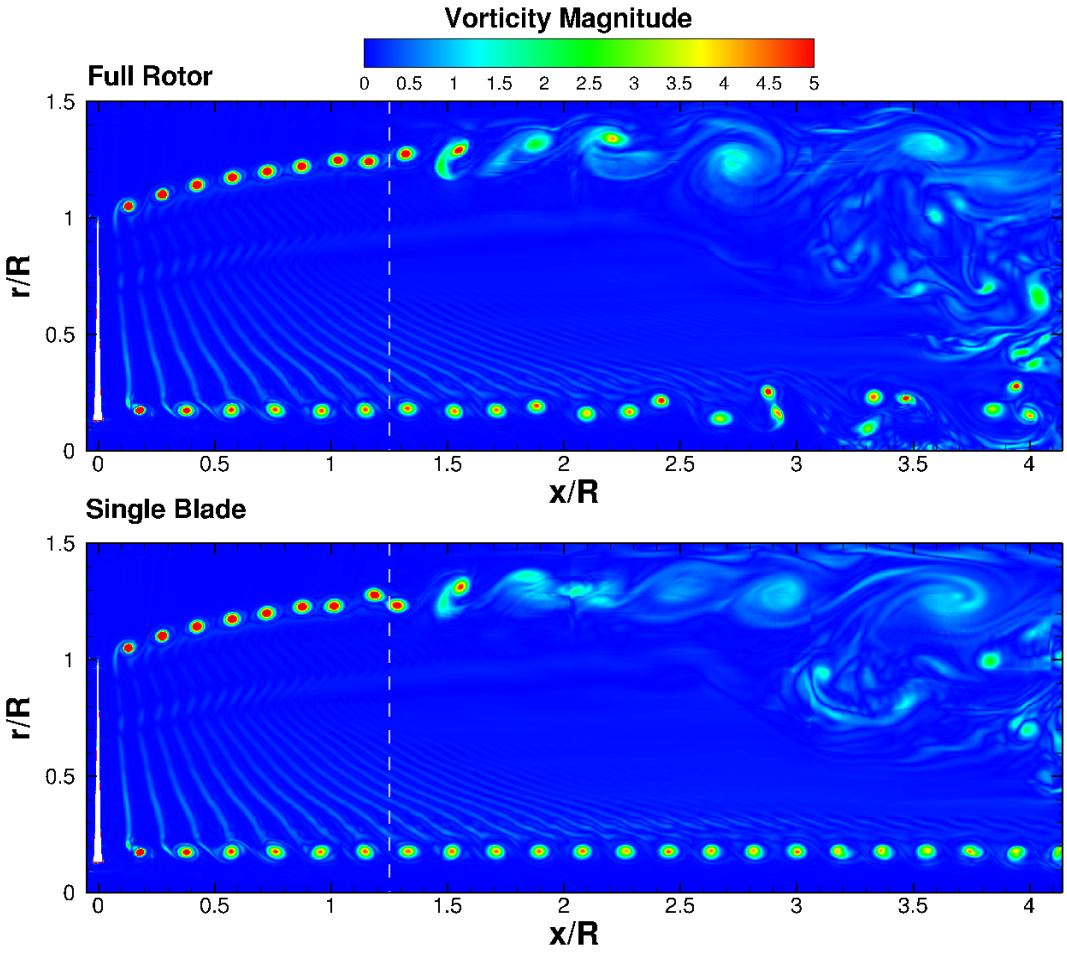

Figure 6.12: Wake developed behind the MEXICO rotor visualised with vorticity contours in a plane perpendicular to the rotor through a blade at 12 o'clock, for wind speed of 10m/s ($\lambda = 10$). Top: full rotor configuration; Bottom: Single-blade configuration.

Figure 6.13 shows the main harmonics of the wake, extracted from the axial velocity signals. When periodicity was assumed, the captured harmonics were multiples of the blade passing frequency ($21.2Hz$). Conversely, when the full rotor is modelled, much frequency content is captured, as multiples of the rotational frequency ($f = 7.07Hz$). As can be seen in Figure 6.13 (a) for the stable wake, in both cases the main frequency content is the blade passing ratio. For the unstable wake shown in Figure 6.13 (b), however, higher harmonics become important and clear differences are observed between the single-blade and full rotor cases, where the latter captures much more harmonics.

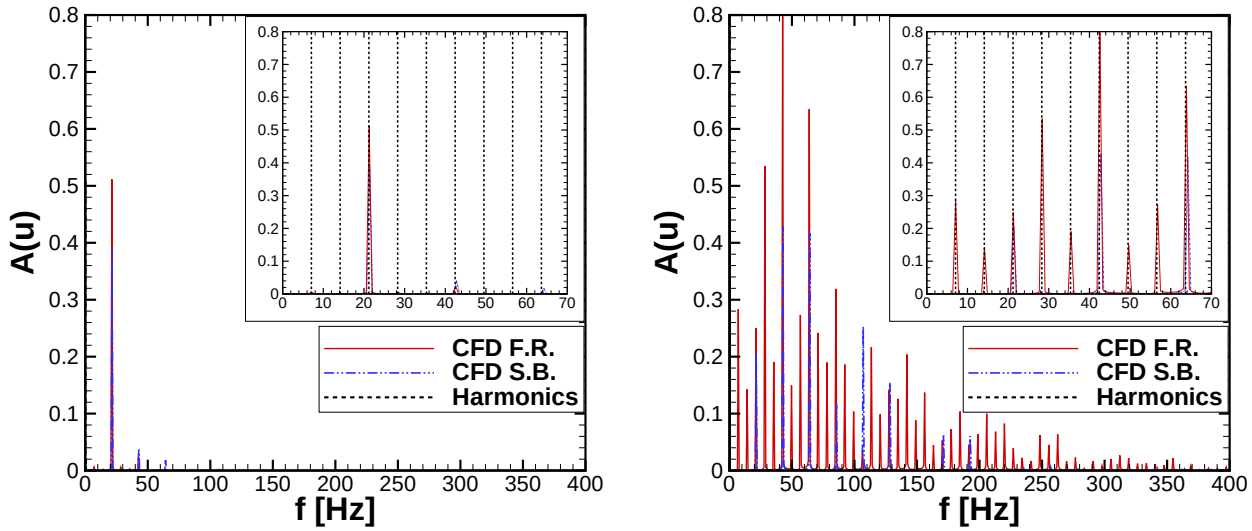

(a) Stable wake ($x/R = 0.5$, $r/R = 1.1$). **(b)** Unstable wake ($x/R = 1.5$, $r/R = 1.2$).

Figure 6.13: FFT analysis using 3600 sampling data (equivalent to $1.41s$) of the axial velocity component (u) at **(a)** $x/R = 0.5$, $r/R = 1.1$ and **(b)** $x/R = 1.5$, $r/R = 1.2$, for the 10m/s wind speed single-blade (S.B.) and full rotor (F.R.) computations. The rotational frequency (f_1) is 7.07Hz and the harmonics are multiples of it ($f_n = n \cdot f_1$).

These results show that the stable wake and the onset of instabilities can be successfully captured using periodicity. On the other hand, for a more detailed study of the breakdown mechanism, the full rotor provides more information about the frequency content in the wake.

6.6 Velocity profiles

In this section, a comparison with the MEXICO experimental data [127] is presented. For the single-blade case at 15m/s wind speed, Figures 6.14 (a) and (b) show axial and radial velocity profiles extracted at a straight line crossing the first vortex. For the lower wind speed case, Figures 6.14 (c) and (d), a comparison between the single-blade and full rotor configurations is done.

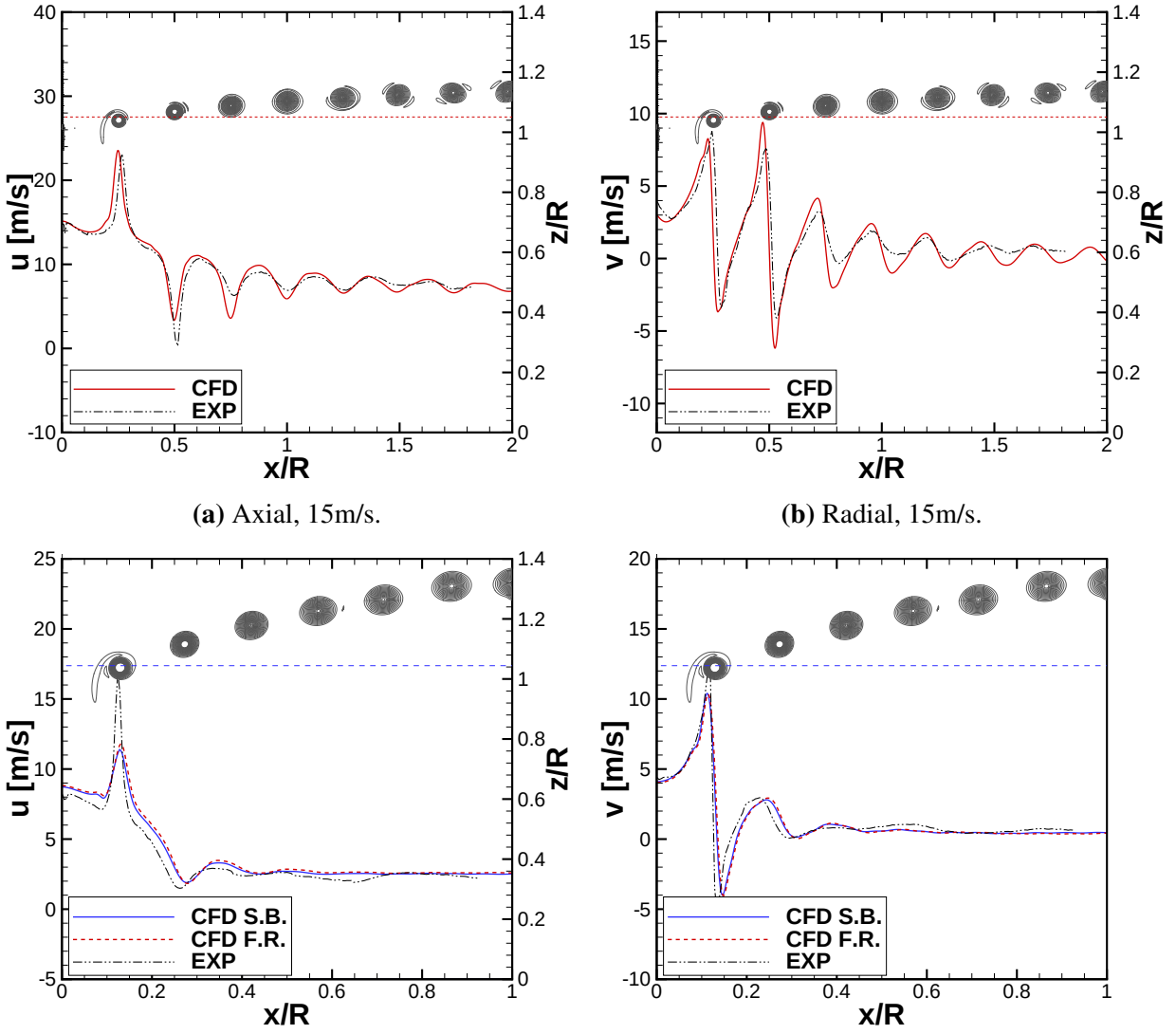

(a) Axial, 15m/s.

(b) Radial, 15m/s.

(c) Axial, 10m/s.

(d) Radial, 10m/s.

Figure 6.14: Axial and radial velocity profiles extracted at a straight line crossing the first vortex. Top: single-blade at 15m/s ($\lambda = 6.67$); Bottom: single-blade and full rotor configuration at 10m/s ($\lambda = 10$). Comparison with experimental values. Details of the position of the extracted lines with respect to the vortices are included.

Overall, there is good agreement with the experiments. Strong oscillations are observed in the region crossing the first vortex, which decay with distance. The small shift between experiments and CFD could be because in the CFD computation baseline geometry of the blades was employed and the measured blade from where the vortices were extracted had a deflection of 3mm approximately towards the upper surface which can lead to a difference of 0.6% with respect to R.

6.7 Turbulence Intensity

Since no experimental data is available to validate the CFD predictions of the MEXICO wind turbine wake breakdown, a comparison with a semi-empirical model is presented here to compare the averaged turbulence generated in the computations. The radial average was performed from the root of the blade (at $r = 0.25$) to $r = 2R$. In this model, whose description is presented in Ref[102] an exponential law is employed for the calculation of the turbulence intensity levels, whose expression is presented in Equations (6.1) and (6.2).

$$Tu = \sqrt{I_o^2 + I_+^2} \tag{6.1}$$

$$I_+ = 5.7 C_T^{0.7} I_o^{0.68} \left(\frac{x}{x_n}\right)^{-0.96} \tag{6.2}$$

Here, I_o is the inflow turbulence intensity one radius upstream ($I_o = 0.005\%$) and I_+ follows the exponential decay law of Equation (6.2), which depends on the thrust coefficient of the rotor ($C_T = 0.845$). The downstream distance behind the wind turbine is x and the length of the near wake x_n, which depends on the tip speed ratio ($\lambda = 6.67$), the rotor radius ($R = 2.25$m), the number of blades ($B = 3$) and the inflow turbulence intensity ($I_o = 0.005\%$).

As can be seen in Figure 6.15, the overall behaviour of the CFD is similar to the semi-empirical model, with some discrepancies. For the 15m/s wind speed case, in the CFD result, a maximum value of turbulence of approximately 3.2% is observed at the rotor plane, which is in good agreement with the model. A decay to a value of 0.9% is then observed. In the near wake (at 1R), it increases again as a result of the vortices generated at the tip. However, this change is not present in the model, since it sees the blade as something with no thickness and the conversion of eddies into turbulence is not accounted for in the model. These discrepancies were also observed by Mo *et al.* [102], for the NREL Phase VI wind turbine at 7m/s. For

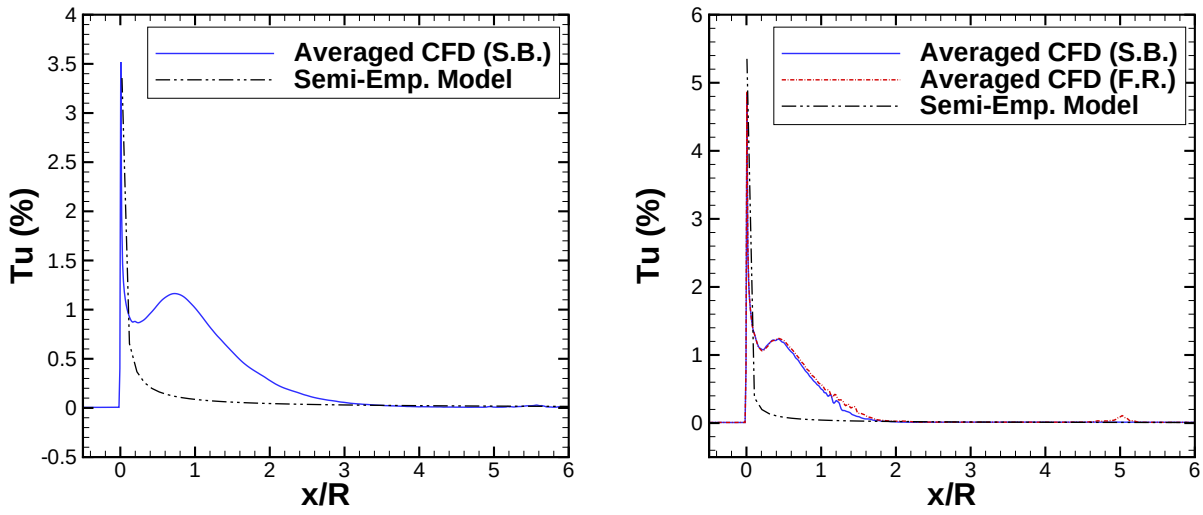

(a) 15m/s. **(b)** 10m/s.

Figure 6.15: Averaged turbulence intensity (from $r = 0.25$ to $r = 2R$) extending from the rotor plane to $6R$ downstream for wind speed cases of **(a)** 15m/s and **(b)** 10m/s. Comparison between the averaged CFD solution and a semi-empirical model [102].

the lower wind speed case shown in Figure 6.15 (b), the CFD result compared to the semi-empirical model in the same manner as in the previous case and both single-blade and full rotor configurations gave almost identical averaged turbulence values.

6.8 Comparison with Wake Models

In this section, a comparison between the averaged CFD solution for the 15m/s wind speed case and two wake models is presented. Firstly, the kinematic model by Katic *et al.* [72] is used, as shown in Equation (6.3).

$$u = U_\infty \left[1 - \frac{1-\sqrt{1-C_T}}{1+(2(WDC)\frac{x}{R})^2}\right] \tag{6.3}$$

It should be noted that this model includes a wake decay constant (WDC), which is problem-dependent. For this comparison, a value of 0.04 was selected to match the maximum wake expansion obtained with CFD (at 1.5D downstream, approximately). On the other hand, the field model employed is the one developed by Ainslie [6]. In this case, the near wake is modelled with an empirical wake profile,

$$1 - \frac{u}{U_\infty} = (U_\infty - u_c)\, exp\left(-3.56\left(\frac{r}{b}\right)^2\right), \tag{6.4}$$

where the initial velocity deficit at the centerline of the wake depends on the thrust coefficient ($C_T = 0.845$) and the inflow turbulence intensity ($I_0 = 0.005\%$), as indicated in Equation (6.5).

$$(U_\infty - u_c) = C_T - 0.05 - (16C_T - 0.5)\frac{I}{10}. \tag{6.5}$$

For the wake width b (Equation (6.6)), the constant σ used in the model [6] is 3.56. The value of this constant dictates the deficit of velocity at the rotor plane and to match the CFD results, a value of 2.2 was selected.

$$b = \sqrt{\frac{\sigma C_T}{4(u_\infty - u_c)(2 - (u_\infty - u_c))}} \tag{6.6}$$

Likewise, the eddy viscosity term for closure of the N-S equations (see Equation (6.7)) also requires a constant (κ), which was selected as 0.015 as suggested by Ainslie [6].

$$\varepsilon = \varepsilon_0 + \kappa b\left(U_\infty - u_c\right) \tag{6.7}$$

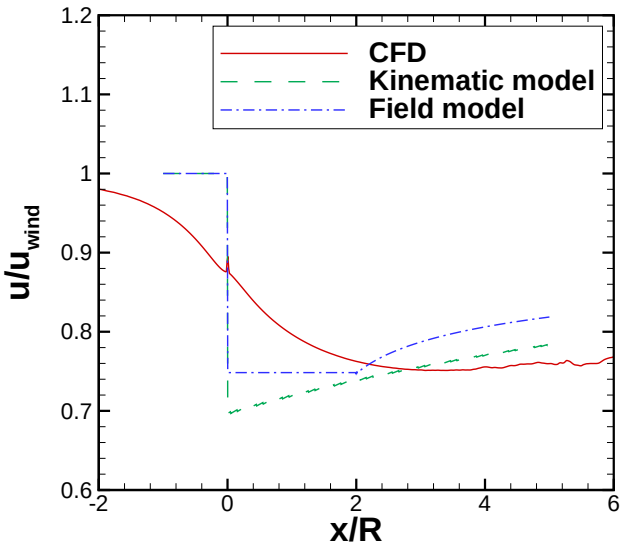

Figure 6.16: Averaged axial velocity for a third of the wake, at 15m/s wind speed. Comparison between a kinematic model [72], field model [6] and averaged CFD.

Figure 6.16 shows a comparison between the three solutions for the averaged axial velocity. The deficit of velocity at the rotor plane ($x/R = 0$) is assumed to have zero streamwise extent (it jumps from free-stream to a minimum value) in the wake models, whereas in reality it is progressive as the CFD shows. Once the velocity reached a minimum value, in the kinematic model it starts to increase asymptotically;

while in the field model the deficit stays constant up to 4R and then increases. The field model has a more similar behaviour to the CFD than the kinematic model. In the latter, the initial deficit of velocity is higher than in the the CFD and with the field model (30% instead of 25%). At 8R, the field model gives a slightly higher velocity (80%) while in the CFD and the kinematic model it is 75% of the free-stream velocity. However, one should bear in mind that, as presented in the previous sections, from 4R downstream vortex pairing due to instabilities was observed in the CFD and these models do not take this into account.

The shape of the predicted wakes (for a single blade) can be observed in Figure 6.17. Qualitatively, the kinematic model predicts better the expansion of the near wake than the field model ("top-hat" shape). For the far wake, on the other hand, the prediction of the field model is more accurate. A combination of both models is also presented (denoted as *Combined models* in Figure 6.17), where the expansion of the near wake (up to 2D downstream) is modelled using the analytical expression of the kinematic model (Equation (6.3)) and this serves as boundary conditions to model the far wake with the field model of Ainslie [6]. With this combined model, a much better agreement with the CFD is obtained.

The results show that, using the correct set of constants, these simplified models can be used as a rough approximation of the wind turbine wakes, with minimal computational cost.

6.9 Acoustic tones generated by the W.T.

This section provides an analysis of the acoustics on the MEXICO rotor, where case III from Table 6.1 is employed (2-billion cells grid and 10m/s wind speed). A set of probes were located in a spherical region as shown in Figure 6.18. Blue dots highlight the ones selected for the present study. Three spherical configurations were approached, as shown in Figure 6.19. The first one had a radius of $r = 1.1$R, the second 1.25R and the third 1.5R.

Figure 6.20 shows the sound pressure levels (SPL) at probes located downstream and upstream the rotor plane (see Figure 6.18 for reference). SPL (in decibels) is obtained using Equation 6.8,

$$SPL(dB) = 20log_{10}\left(\frac{p_{rms}}{p_{ref}}\right), \tag{6.8}$$

where p_{rms} is the root mean square (*rms*) of the sound pressure and the reference pressure in air is $p_{ref} =$

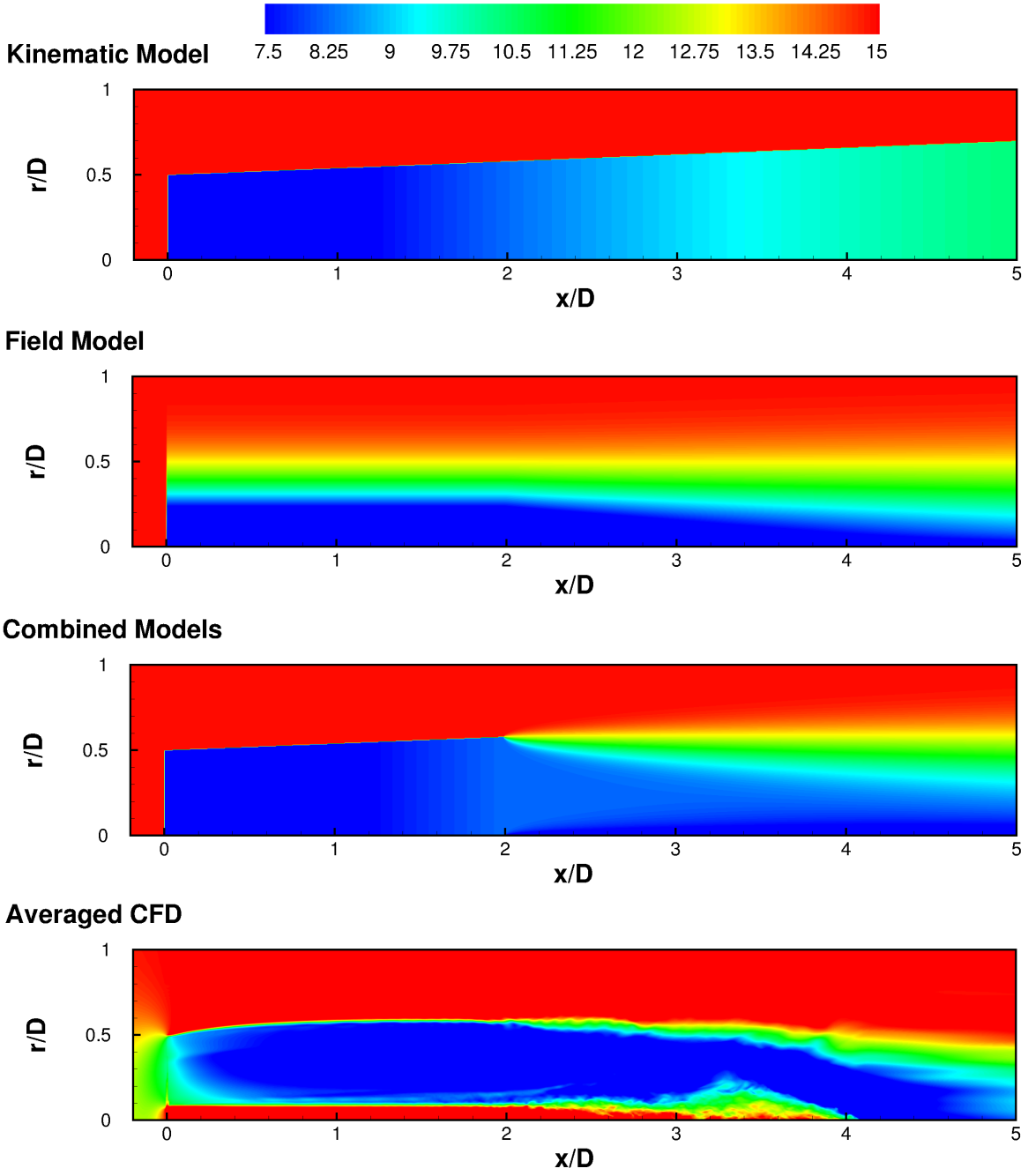

Figure 6.17: Contours of averaged axial velocity for a third of the wake, at 15m/s wind speed. Comparison between a kinematic model [72], field model [6], a combination of both and averaged CFD.

$2 \cdot 10^{-5}$Pa, which is normally considered the human threshold of hearing. It should be mentioned that in this study a total of 1,440 samples were taken, with a size of 0.25deg., or based on the rotational speed, at sampling frequency of 10.1kHz.

A first peak corresponding to the blade-passing frequency (f=21.2Hz) is observed in Figure 6.20 (a).

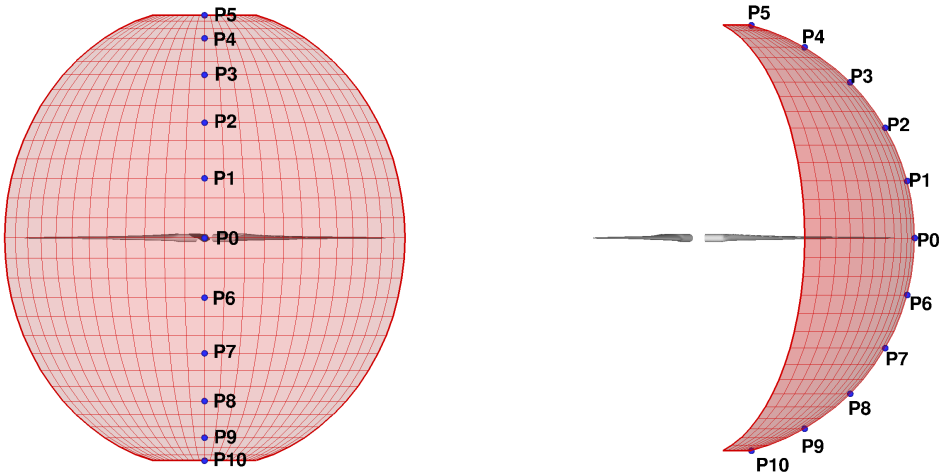

Figure 6.18: Configuration of probes into a spherical region.

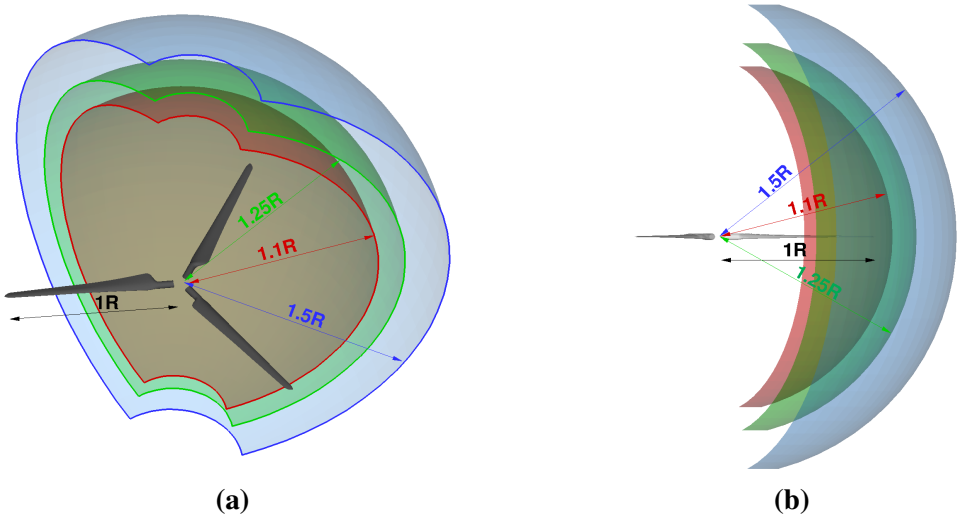

Figure 6.19: Three spherical acoustic region configurations: $r = 1.1$R, $r = 1.25$R and $r = 1.5$R.

This low frequency noise, known as tonal noise, is the result of the blade passage (thickness noise) and the pressure field (loading noise). Likewise, if the length scale of the turbulence is on the order of or larger than the blade length, the blade acts as a dipole source and radiates very low frequency noise. The highest SPL is 70dB approximately and for probe P1, which is located at 0.34R downstream the rotor plane, instead of being the one coinciding with the blade tip (P0). This means that the tip noise due to the interaction between the blade and the generated tip vortex is less important than the noise due to the blade loading. In addition, the noise levels at the suction side of the blade are higher than at the pressure side, as seen in Figures 6.20 (a) and (b).

The high frequency noise ($f > 500$Hz), known as broadband noise, is due to the turbulent flow scales, which are much smaller than the blades. Although a fine grid was employed for this analysis, RANS computations were performed, which make the capture of the broadband noise almost impossible. To properly capture this type of noise, LES or DES computations would be more suitable. Nevertheless, the tonal predictions follow the line of other works in the literature [148].

As can be observed in Figure 6.21, the tonal noise levels decrease when the radius of the sphere increases, while the broadband noise is practically not affected.

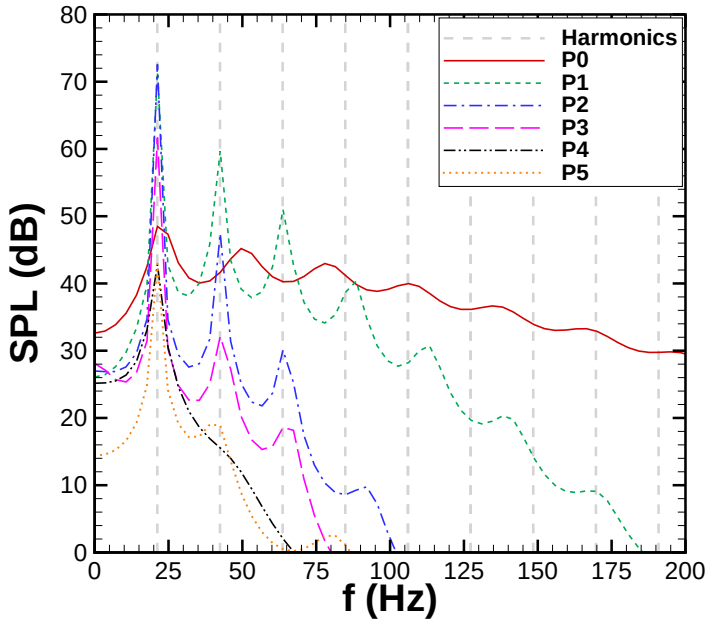

(a) Probes downstream the rotor.

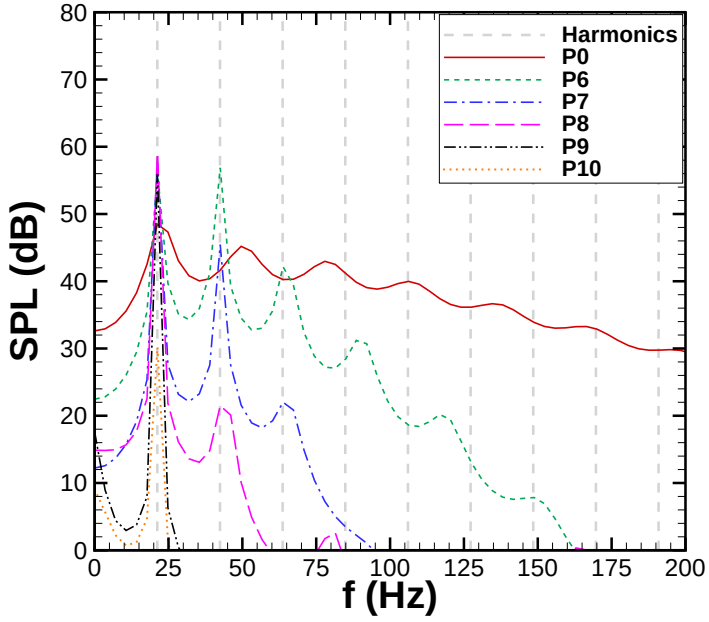

(b) Probes upstream the rotor.

Figure 6.20: Sound pressure level (SPL) in decibels (dB) at the probes located **(a)** downstream and **(b)** upstream the rotor, in a sphere of radius $r = 1.1$R. The harmonics are multiples of the blade-passing frequency (f_1=21.2Hz, f_2=42.4Hz f_3=63.6Hz f_4=84.8Hz).

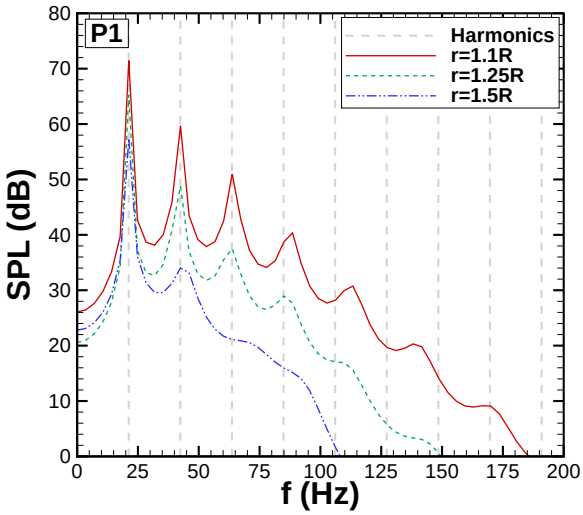

(a) Probe P1.

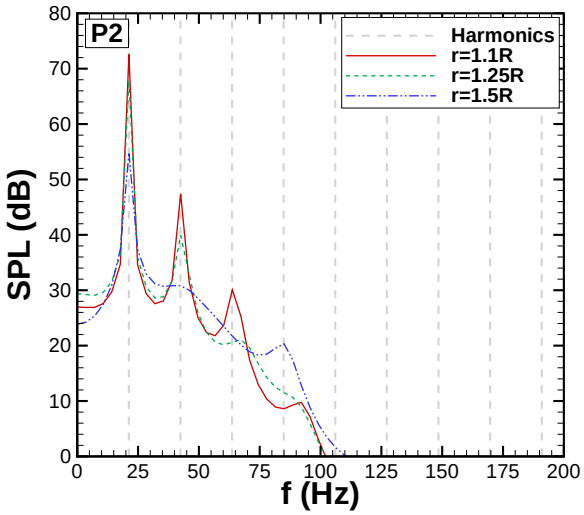

(b) Probe P2.

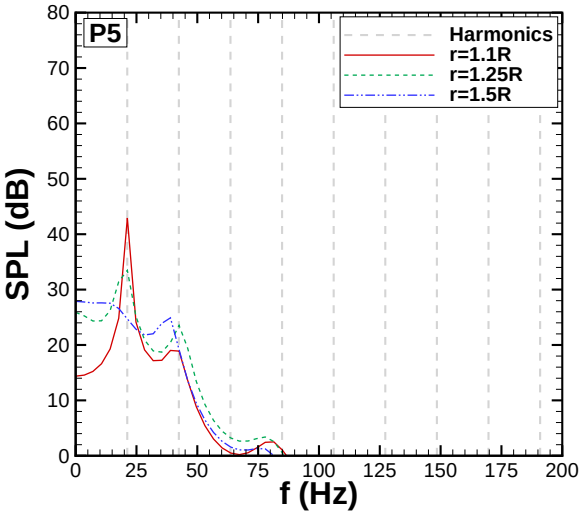

(c) Probe P5.

Figure 6.21: Sound pressure level (SPL) in decibels (dB) at probes **(a)** P1, **(b)** P2 and **(c)** P5 at three radial locations: $r = 1.1$R, $r = 1.25$R and $r = 1.5$R. The harmonics are multiples of the blade-passing frequency (f_1=21.2Hz, f_2=42.4Hz f_3=63.6Hz f_4=84.8Hz).

Chapter 7

Aeroelastic Analysis [1]

This chapter presents aeroelastic analysis for two wind turbine cases. Firstly, a static analysis on the MEXICO blade was performed, for three wind speed conditions (10, 15 and 24m/s). The analysis includes a sensitivity study on the blade torsional stiffness and the pre-coning angle. A dynamic aeroelastic method was applied to the NREL Annex XX full wind turbine (including the rotor, hub, nacelle and tower), for wind speeds of 7 and 20m/s. The aim is in this case to quantify the effect of the tower in the rotor blades deformations.

7.1 Description of cases

A multi-block topology was employed for the generation of both wind turbine meshes. Around the blades, a C-topology was employed, which leads to good boundary layer resolution. For the MEXICO blade, a total of 8 blocks around the blade were employed since it has a blunt trailing edge, see Figure 7.1 (a). For the NREL blade, 6 blocks were employed as Figure 7.1 (b) shows. Note that in this case the blade had a sharp trailing edge (Figure 7.1 (b)).

Regarding the computational domains, only one blade was modelled in the MEXICO case, as the tower was far from the rotor plane (2.13m $\sim$ 1R) and its influence was negligible. Likewise, a third of the domain was meshed since MEXICO is a three-bladed rotor, see Figure 7.1 (c), assuming periodicity of

[1] This work is published in M. Carrión *et al.* , Aeroelastic Analysis of Wind Turbines using a Tightly Coupled CFD-CSD Method, *Journal of Fluids and Structures*, Accepted July 2014.

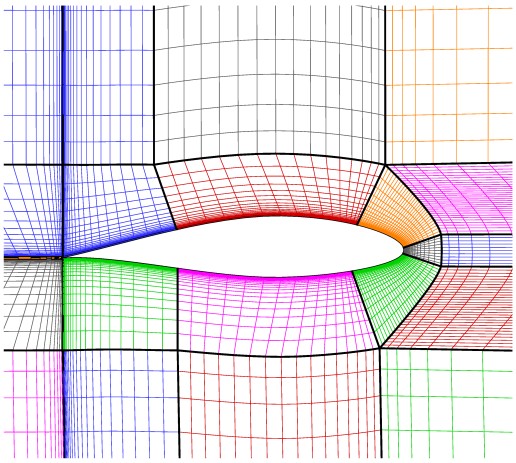

(a) Multi-block grid around a MEXICO blade section.

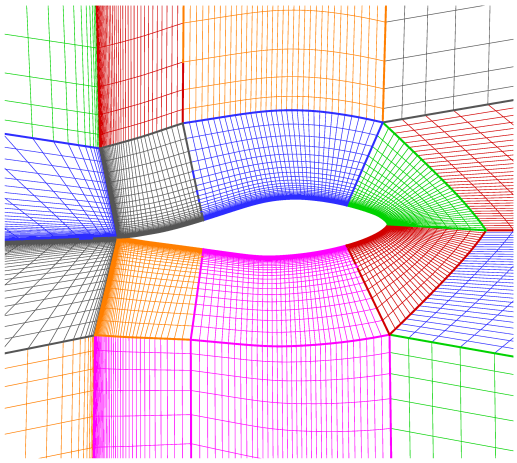

(b) Multi-block grid around a NREL blade section.

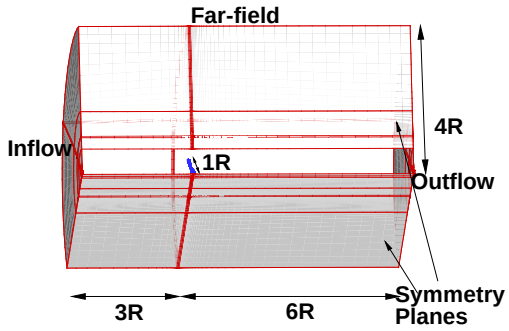

(c) Single-blade computational domain for MEXICO blade.

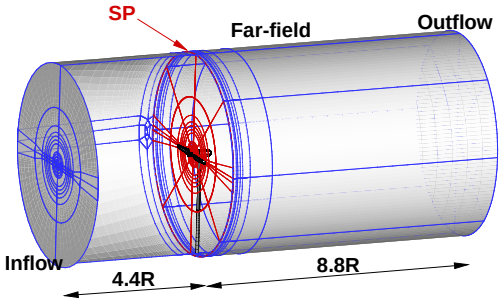

(d) Full rotor computational domain for NREL wind turbine, with 1 sliding plane.

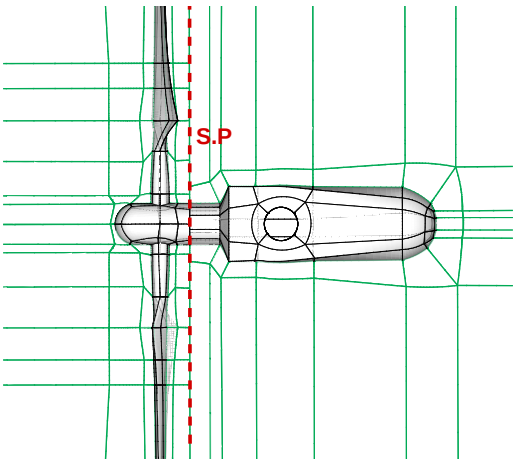

(e) Bottom view of the blocking around the NREL rotor, nacelle and tower.

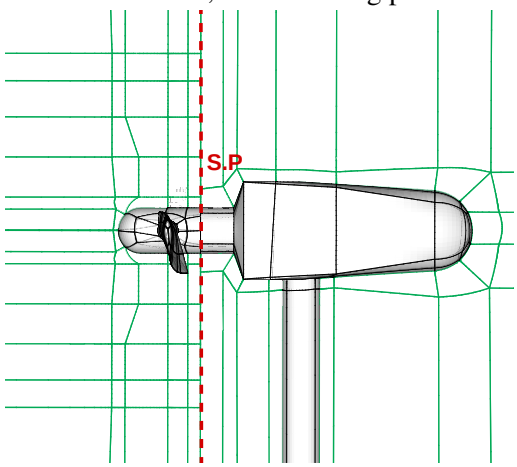

(f) Side view of the blocking around the NREL rotor, nacelle and tower.

Figure 7.1: Employed blocking topology and grids for the MEXICO isolated blade and the NREL Annex XX wind turbine (including rotor, nacelle and tower). The boundary conditions and the extend of the domain in radii are included.

the problem in both time and space. In order to be able to apply periodicity at the symmetry plane, a hub approximated as an infinite cylinder was considered in the geometry. For the NREL Annex XX cases, the isolated blade, as well as the full wind turbine (including the nacelle and the tower) were considered. For the second case, and to account for rotor rotation, while the nacelle and the tower are fixed, a sliding plane was employed, as shown in Figures 7.1 (d) to (f). For further details about the employed sliding plane algorithm the reader might refer to Section 2.6.1. Table 7.1 lists the employed grids for the present study.

Table 7.1: Summary of mesh properties for the aeroelastic analysis.

Grid ID	Wind Turbine	Geometry	Size (Blocks)	Chord-(span-) wise cells	Boundaries in Radii (R)	CPUs
1	MEXICO	Isolated blade & hub	2.6M(169)	160(111)	I:3 O:6 FF:4	12
2	NREL	Isolated blade & hub	5M(1298)	210(108)	I:4.4 O:8.8 FF:3	20
3	NREL	Rotor, nacelle & tower	18M(2916)	222(124)	I:4.4 O:8.8 FF:3	128

I: Inflow, O: Outflow, FF: Far-field.

In the following sections, different computed cases are analysed, and are listed in Table 7.2. For the MEXICO blade, static aeroelasticity was employed, for three wind speeds (cases **M.1** to **M.3** of Table 7.2). For the NREL case, a static analysis was also employed (case **N.1**) and two tests employing the dynamic aeroelastic method were computed (cases**N.2** and **N.3**). In all cases, axial wind conditions were considered. It should be noted that the reference Mach number employed for the steady computations was the tip Mach number, while for the unsteady cases the reference is the free-stream value. Likewise, the Reynolds number was obtained using the reference velocity and the maximum blade aerodynamic chord. The turbulence model employed was the standard k-ω [163] for MEXICO and the k-ω SST [95] for the NREL Annex XX case.

Table 7.2: Summary of computed cases for aeroelastic analysis.

Test ID	Grid	Comput.	Re	V_{wind} (m/s)	$M_{tip}(\lambda)$	ϕ *(deg.)*
M.1	1	RANS	$1.6 \cdot 10^6$	15	0.2941 (6.67)	-2.3
M.2	1	RANS	$1.6 \cdot 10^6$	10	0.2941 (10)	-2.3
M.3	1	RANS	$1.6 \cdot 10^6$	24	0.2941 (4.2)	-2.3
N.1	2	RANS	$1.9 \cdot 10^6$	7	0.11 (5.4)	3.0
N.2	3	URANS	$3.7 \cdot 10^5$	7	0.11 (5.4)	3.0
N.3	3	URANS	$1 \cdot 10^6$	20	0.11 (1.88)	3.0

M: MEXICO case; N: NREL Annex XX case.

7.2 Static analysis on the MEXICO blade

7.2.1 Structural model

A structural model of the MEXICO blade was put together using data from the MEXICO project reports documenting the manufacturing of the blade [122, 123]. The stiffness of the blade was based on assumed data for 7075 aluminium series ($E = 71.7$ MPa). It should be noted that the torsional stiffness J of each blade section was not defined. Hence, two different approaches were adopted: taking the minimum between the flapwise and edgewise inertias $min(I_{i,j})$, and the average $avg(I_{i,j})$. Figure 7.2 shows the employed model that includes 20 elements of the CBEAM type of NASTRAN [27], which contain structural properties, and several rigid bar elements (RBAR) used to allow for better mapping between the CFD and FEM grids.

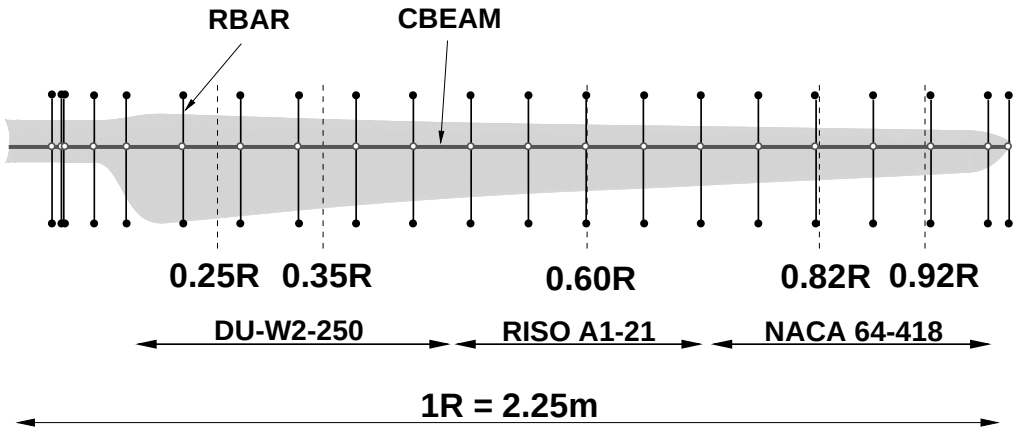

Figure 7.2: Structural model for the MEXICO blade, including 20 CBEAM elements with structural properties and RBAR rigid elements type of NASTRAN [27]. The maximum aerodynamic chord is 0.24m. Dashed lines denote the location of the pressure transducers.

The natural frequencies were obtained using modal analysis in NASTRAN, in non-rotating and rotating configurations ($f = 7.07$Hz) and for $J = min(I_{i,j})$ case, see Table 7.3. As can be observed, for the MEXICO blade, the first four modes are in flap and in edge-wise directions, and the rest are torsional modes. Likewise, there is a significant difference on the natural frequencies between rotating and non-rotating cases, due to the high rate of rotation of this case. Figure 7.3 shows a comparison of the flapping and edge-wise modes between the two blades.

Table 7.3: Ten first natural frequencies in Hz for the MEXICO blade in rotating and non-rotating configurations, using $J = min(I_{i,j})$

Mode		f = 7.07Hz	f = 0
1st	Flap	10.37	4.59
2nd	Flap	18.29	14.38
3rd	Edge	24.16	18.80
4th	Flap	42.67	33.99
5th	Torsion	63.10	59.56
6th	Torsion	71.38	63.9
7th	Torsion	105.98	96.71
8th	Torsion	146.29	13.59
9th	Torsion	156.53	153.86
10th	Torsion	195.62	186.25

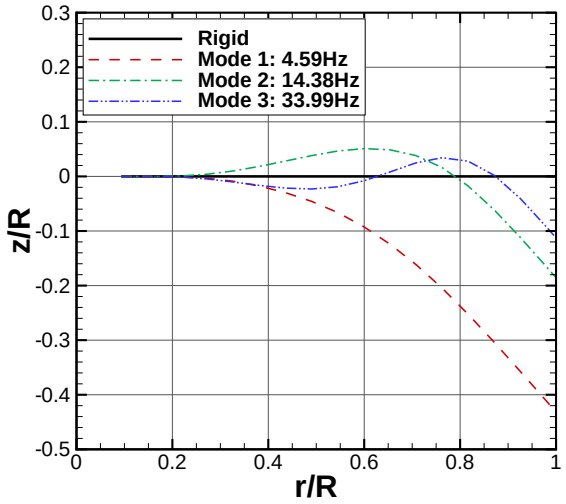

(a) Flapping modes.

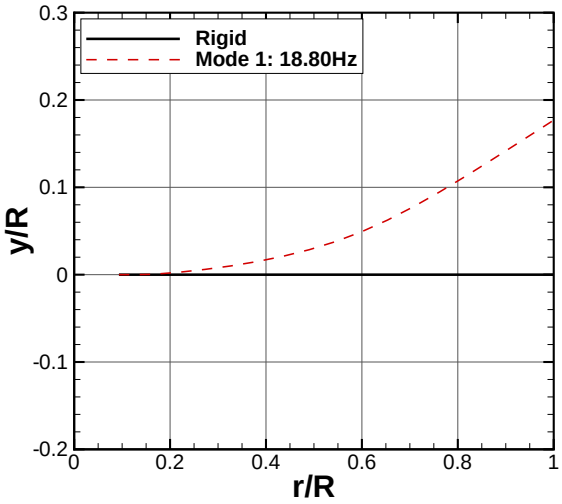

(b) Edgewise modes.

Figure 7.3: Mode shapes in flap and edgewise vibration for the non-rotating MEXICO blade, normalised with the blade radius.

This model was used for the static analysis of the blade, with aerodynamic loads generated using CFD. The exchange of loads between NASTRAN and the CFD solver was taking place several times during the computations until the shape of the blade and the aerodynamic loads converged to a final value, as described in Section 2.7.2. Three wind speeds were selected (10, 15 and 24m/s) and the rotational speed was 424.5rpm, as employed in the wind tunnel experiments. The initial pitch angle was $\phi = -2.3$ degrees (measured at the blade tip, towards the wind), the k-ω turbulence model was employed and a Reynolds number of 1.6 million (using the tip speed and the aerodynamic chord at the blade's root). Full convergence of the deformations was achieved after 3 aeroelastic iterations.

7.2.2 Sensitivity to the torsional stiffness

Figure 7.4 shows the sensitivity to the torsional stiffness of the predicted blade deformation in bending and torsion, for the two approaches previously mentioned, $min(I_{i,j})$ and $avg(I_{i,j})$, and including variations of $\pm$10%, at 15m/s wind speed. As can be seen, the bending is slightly dependent on the stiffness modulus (variation of less than 1cm from one approach to the other), while the torsional deflection is highly influenced. This leads to large deflections when the minimum value is taken and small deflections when the inertias are averaged. The values were 3.50° and 0.23° of torsion at the tip, respectively. The resulting effective geometric angle of attack is shown in Figure 7.5, and varies significantly from one approach to the other: with J_{avg} the incidence angle at the tip is negative (towards the wind), while it is positive (against the wind) using J_{min}. This leads to a completely different type of flow that will affect the surface pressure and, therefore, the blade loads.

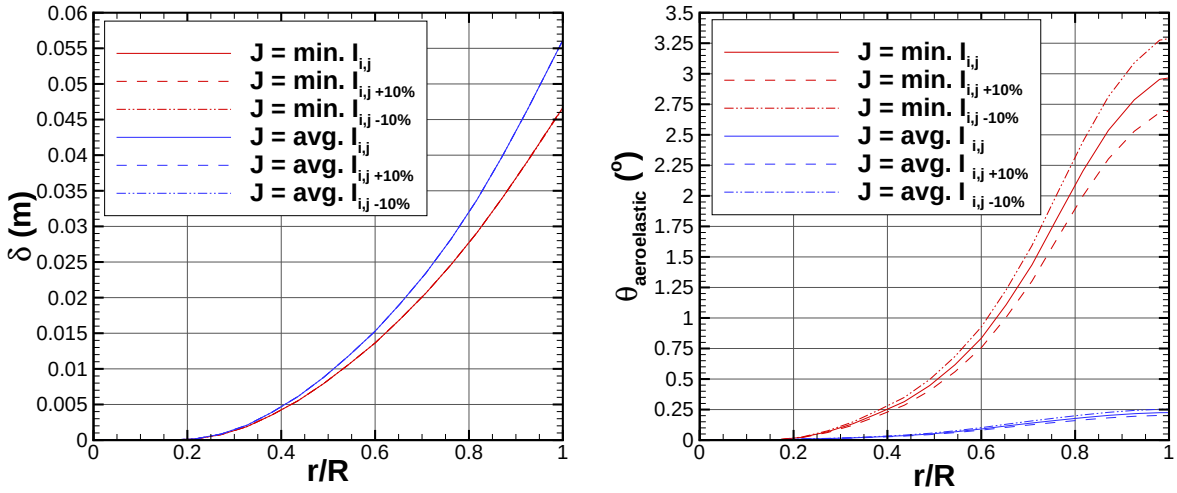

(a) Bending deflection. **(b)** Torsional deflection.

Figure 7.4: Influence of the torsional stiffness magnitude on the **(a)** bending and **(b)** torsional deflection. Two definitions of J employed: minimum value of inertias ($J = I_2$) and average between inertias ($J = \frac{I_1+I_2}{2}$); sensitivities of $\pm$10% are included. Test case **M.1** of Table 7.2.

Such strong dependency was also observed at the lower and higher speed cases (10 and 24m/s, respectively), see Figure 7.6. At 10m/s wind speed, the obtained tip torsional deflection was 2.2 and 0.17 degrees with J_{min} and J_{avg}, respectively. Likewise, for the 24m/s case, the maximum deflections observed are of 4.2 and 0.32 degrees. Since the MEXICO model blade is much shorter than full-size blades, the

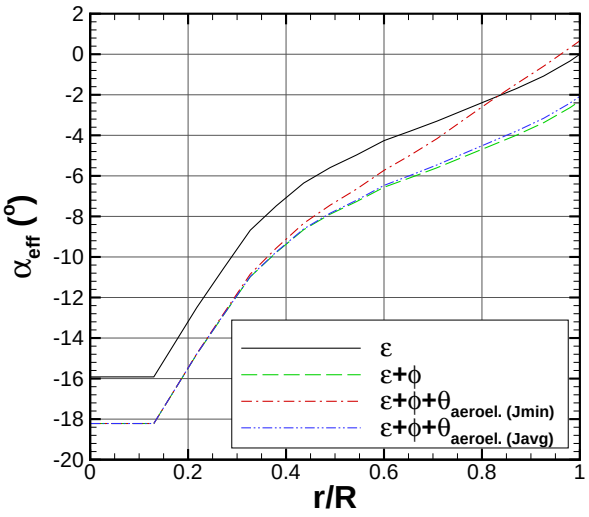

Figure 7.5: Influence of the torsional stiffness magnitude on the effective geometric angle of attack along the blade, due to aeroelastic effects. Two definitions of J employed: minimum value of inertias ($J = I_2$) and average between inertias ($J = \frac{I_1+I_2}{2}$). *(ε: twist angle, ϕ: pitch angle, $\theta_{aeroel.}$: torsional deflection due to aeroelastic effects)* Test case **M.1** of Table 7.2.

expected deformations should be small. Therefore the second approach appears to be more realistic for this wind turbine.

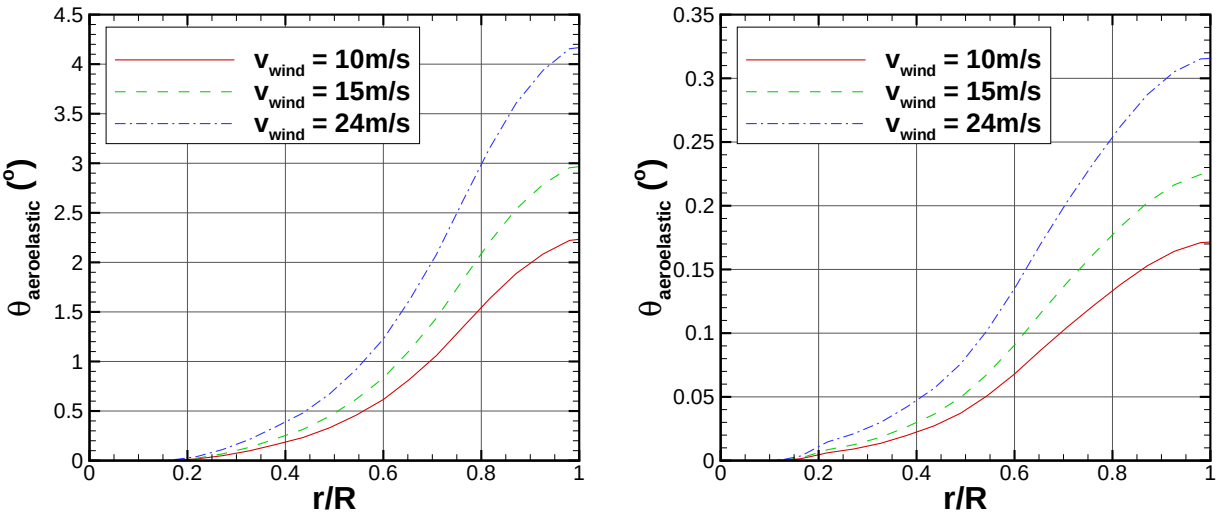

(a) $J = I_2$. **(b)** $J = \frac{I_1+I_2}{2}$.

Figure 7.6: Influence of the torsional stiffness magnitude of the MEXICO blade defined as **(a)** $J = I_2$ and **(b)** $J = \frac{I_1+I_2}{2}$ on the torsional deflection, for wind speeds of 10 ($\lambda = 10$), 15 ($\lambda = 6.67$) and 24m/s ($\lambda = 4.2$).

The effect on the sectional pressure coefficient is shown in Figure 7.7, where a comparison between the rigid and deformed blades at three blade stations is presented. For all wind speeds, the approach of using

the minimum inertia as the value of the torsional stiffness (dash-dotted lines) reduces the overprediction on the suction side, while the agreement of the pressure side worsens. On the other hand, using the averaged value of inertias (dash-double dotted lines) the difference in C_p between rigid and deformed blades are minimal, as should be expected from a short blade with the stiffness of the MEXICO design. For all wind speeds, the aeroelastic effects are present from mid-span to the outboard stations.

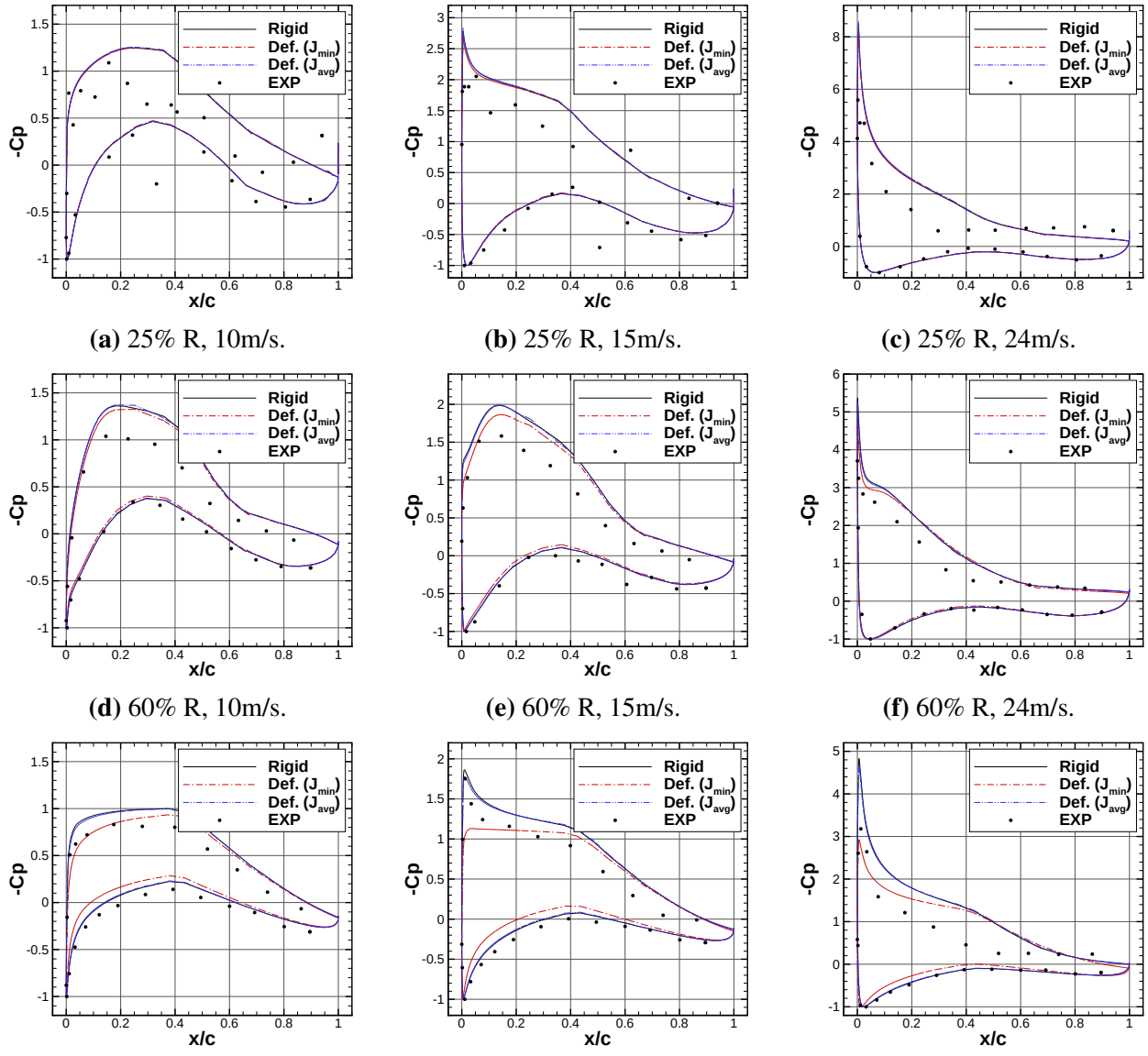

(a) 25% R, 10m/s. **(b)** 25% R, 15m/s. **(c)** 25% R, 24m/s.

(d) 60% R, 10m/s. **(e)** 60% R, 15m/s. **(f)** 60% R, 24m/s.

(g) 92% R, 10m/s. **(h)** 92% R, 15m/s. **(i)** 92% R, 24m/s.

Figure 7.7: Comparison of the C_p distribution between the rigid and the deformed MEXICO blade ($J_{min} = I_2$ and $J_{avg} = \frac{I_1+I_2}{2}$) for wind speeds of 10 ($\lambda = 10$), 15 ($\lambda = 6.67$) and 24m/s ($\lambda = 4.2$).

7.2.3 Visualisation of the blade deformation

The most realistic approach was the one defining the torsional stiffness as the averaged inertias (J_{avg}), since lower deformations were obtained, as expected from a short blade made of aluminium like MEXICO. Figure 7.8 shows the details of the deformations at the tip region for this approach and at three wind speeds. As can be observed, the higher the wind speed the larger the deformation.

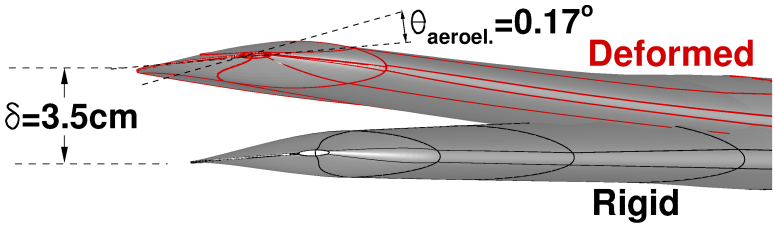

(a) v_{wind} =10m/s.

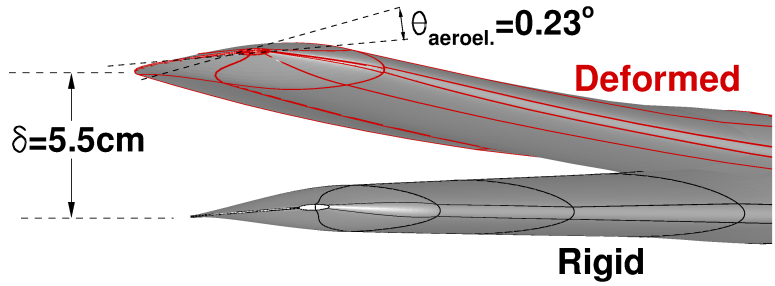

(b) v_{wind} =15m/s.

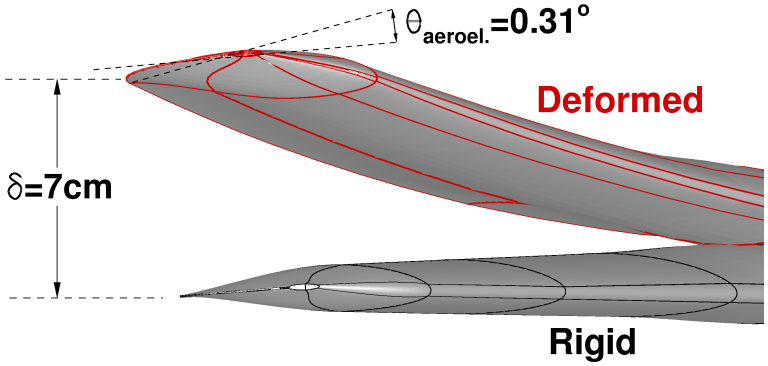

(c) v_{wind} =24m/s.

Figure 7.8: Comparison between rigid and elastic MEXICO blades, at the tip region, for **(a)** 10, **(b)** 15 and **(c)** 24m/s wind speeds. Torsional deflection values given in degrees (nose up) and bending deflections are given in cm. Test cases **M.1**, **M.2** and **M.3** of Table 7.2.

These results show the strong dependency of the aerodynamic results on the stiffness. Further work is, however, needed to characterise the structural behaviour of the MEXICO blade so that the exact effect of the blade aeroelasticity is quantified.

7.2.4 Effect of the blade coning

The aeroelastic deformations with the blade cone angle set at 3.0 degrees are studied here, for the 15m/s wind speed case and the torsional stiffness parameter set to J_{avg}. The employed structural model is the more conservative one, which showed more realistic deformations in the previous sections. Figure 7.9 shows a comparison for the deflections in bending and torsion. As can be seen, pre-coning the blade leads to lower deformations, as was pointed out in Ref. [119]. However, the effect in the MEXICO blade is not significant, due to its large stiffness.

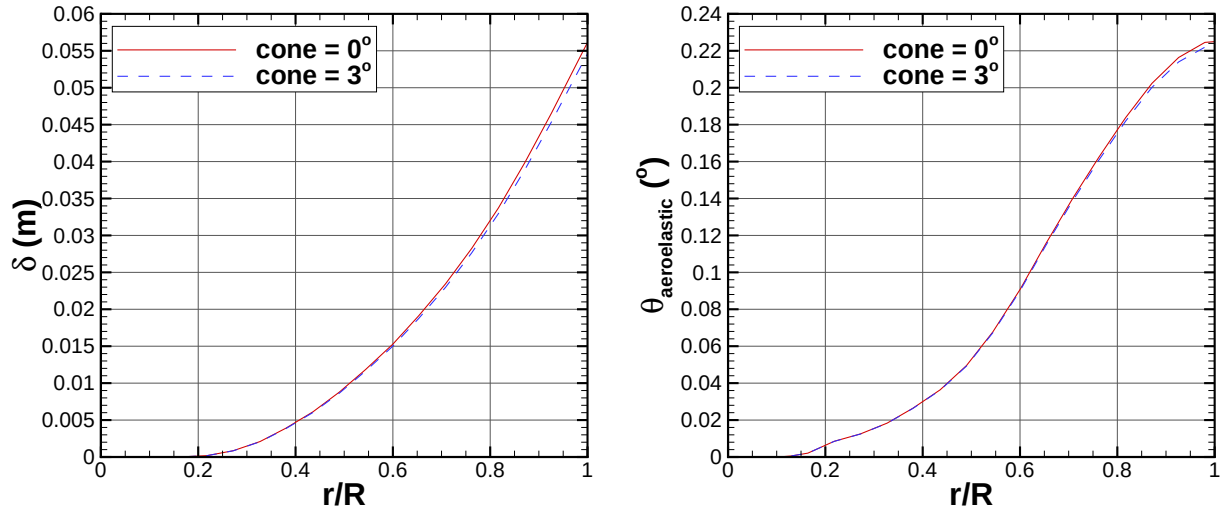

(a) Bending deflection.

(b) Torsional deflection.

Figure 7.9: Effect of pre-coning the MEXICO blade on bending and torsion deflections, for wind speed of 15m/s ($\lambda = 6.67$).

7.3 Static analysis on the NREL blade

For the NREL Annex XX blade, the structural model detailed in Ref. [56] was employed. The elastic (E) and shear modulus (G) were modified using the SOL 200 optimisation routine of NASTRAN [27], in order to match the first flapwise and edgewise experimental natural frequencies. Then, the centrifugal forces were applied, employing the aforementioned non-linear static analysis. As shown in Figure 7.10, this blade was modelled using 22 CBEAM elements, with prescribed structural properties, and rigid RBAR elements for better CSD/CFD mapping.

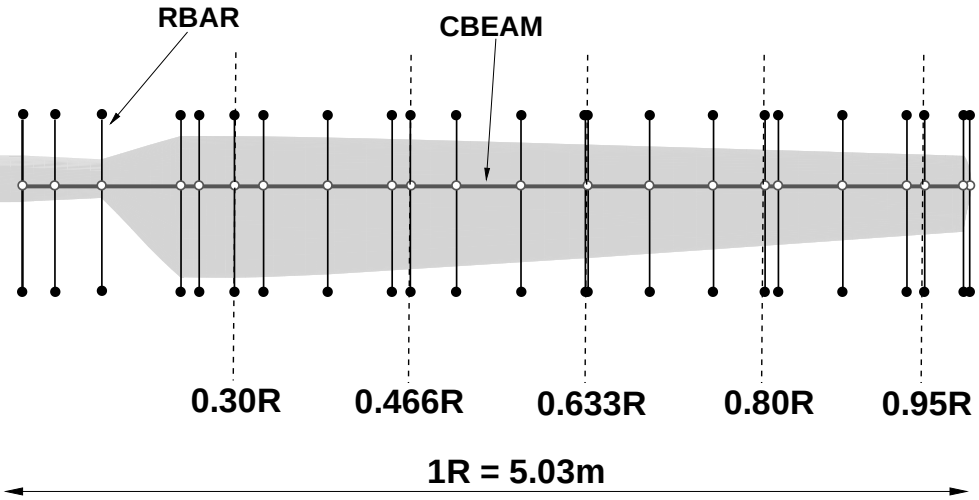

Figure 7.10: Structural model for the NREL Annex XX blade, including 22 CBEAM elements with structural properties and RBAR rigid elements type of NASTRAN [27]. The chord at the root is 0.737m.

Table 7.4 shows the first ten natural frequencies for a non-rotating and a rotating case. As can be seen, flapping and edgewise motions are present and no torsion is observed. This is due to the modifications applied to the structural model to match the flapping and edgewise modes measured in the wind tunnel experiment. Likewise, knowing that the rotational frequency is 1.2Hz, the lower frequency is approximately six times higher. In the experiments [56], the three first frequencies were 7.25-7.313Hz, 8.90-9.062Hz and 29.438-30.062Hz, for the fixed rotor, which are in good agreement with the modal predictions. Figure 7.11 shows a comparison of the flapping and edgewise modes between the two blades.

To characterise the deformations of the NREL blade, a static aeroelastic analysis was first performed, using the structural model presented in Figure 7.10. A wind speed of 7m/s was selected and a rotational

Table 7.4: Ten first natural frequencies for the NREL blade in rotating and non-rotating configurations.

Mode		$\omega = 72rpm$	$\omega = 0$
1st	Flap	7.34Hz	7.23Hz
2nd	Edge	8.79Hz	8.79Hz
3rd	Flap	20.13Hz	19.23Hz
4th	Edge	26.03Hz	25.87Hz
5th	Flap	39.65	39.37
6th	Edge	47.47	47.22
7th	Flap	59.34	58.95
8th	Edge	64.39	63.99
9th	Flap	76.73	76.21
10th	Edge	81.91	81.41

speed of 72rpm, corresponding to a tip speed ratio of 5.4. Two aeroelastic iterations were only required to obtain convergence on the deformations. Figure 7.12 shows the deflections in flapping (as a percentage of the blade radius) and torsion. A maximum flapping deflection of 0.26%R at the blade's tip (1.3 cm) is observed, which is in good agreement with earlier results presented by McTavish *et al.* [93]. As shown in Table 7.5, there is less than 8% difference in the integrated thrust and torque between the CFD solution and the experiments. Likewise, the differences in the loads between the rigid and the elastic blades are almost negligible.

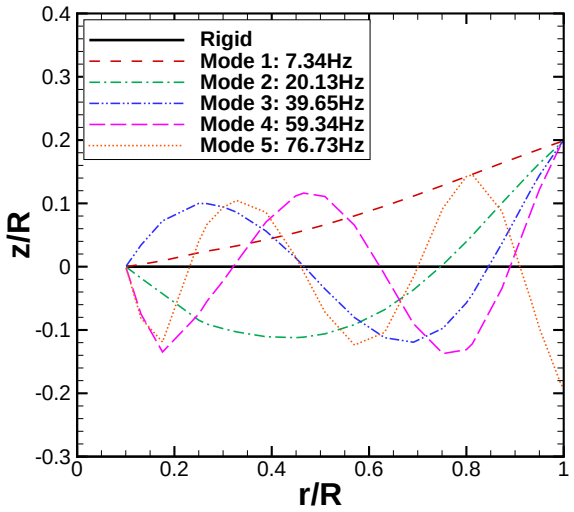

(c) Flapping modes.

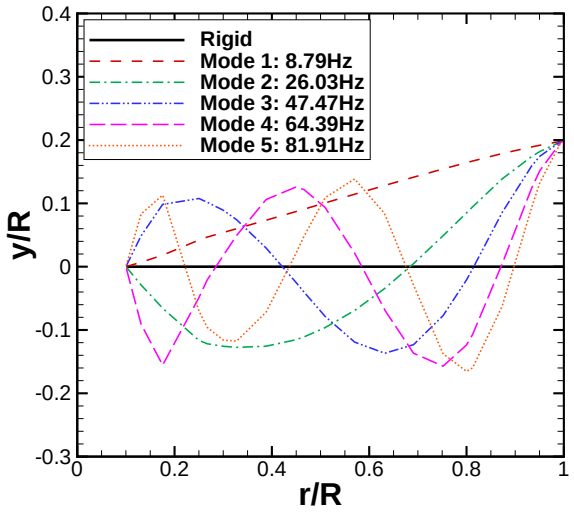

(d) Edgewise modes.

Figure 7.11: Mode shapes in flap and edgewise vibration for the NREL blade in non-rotating configuration, normalised with the blade radius.

Table 7.5: Integrated thrust and torque for the rigid and elastic NREL blade and comparison with the averaged value in the experiments. Test case **N.1** of Table 7.2.

	CFD Rigid	**CFD Elastic**	**Experiment**
Thrust	1112N	1113N	1157N
Torque	741Nm	741Nm	804Nm

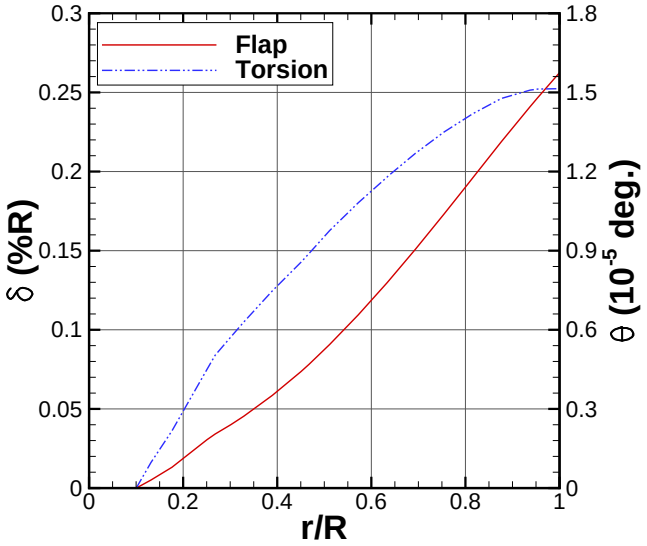

Figure 7.12: Deflection in flap and torsion obtained from a static aeroelastic analysis on the NREL blade, at 7m/s wind speed. Test case **N.1** of Table 7.2.

In aeroelastic static analysis, where the tower is not accounted for, deformations in torsion can affect the local incidence angle and, therefore, change the blade loads. Since the main deflections obtained for the NREL blade are in flapping modes, an unsteady, dynamic analysis is required, since the bending motion can effectively change the angle too.

7.4 Dynamic analysis on the NREL full W.T.

The dynamic aeroelastic coupling method described in Section 2.7.3 was employed for the study of the full wind turbine case, where the blades were allowed to deform, while keeping the hub, nacelle and tower rigid. The structural model for the blades presented in Figure 7.10 was used and the first four natural frequencies of Table 7.4 were included, which correspond to the first and second flapping and edgewise motions.

For this study, a number of rotor revolutions with rigid blades was performed and the aeroelastic method was activated once a quasi-periodic behaviour was achieved. Unsteady steps of 0.25 degrees were

selected and both wind speed cases of 7m/s and 20m/s were studied, corresponding to tip speed ratios of $\lambda = 5.4$ and $\lambda = 1.88$, respectively. The following sections provide first an analysis of the type of flow generated by the turbine for the two wind speed cases. Further analysis of the effect of aeroelasticity is then presented, including the blade deformations, their effect on the loads, as well as the effect in the tower.

7.4.1 Effect of the wind speed on the type of flow

The effect of the wind speed on the aeroelastic response is studied here. For this, wind speeds of 7m/s and 20m/s, cases **N.2** and **N.3** of Table 7.2, are studied and compared. Since the higher wind speed case was reported in the literature to suffer from stall over the blade, the Scale-Adaptative Simulation (SAS) method was employed, to allow for the stall flow [96].

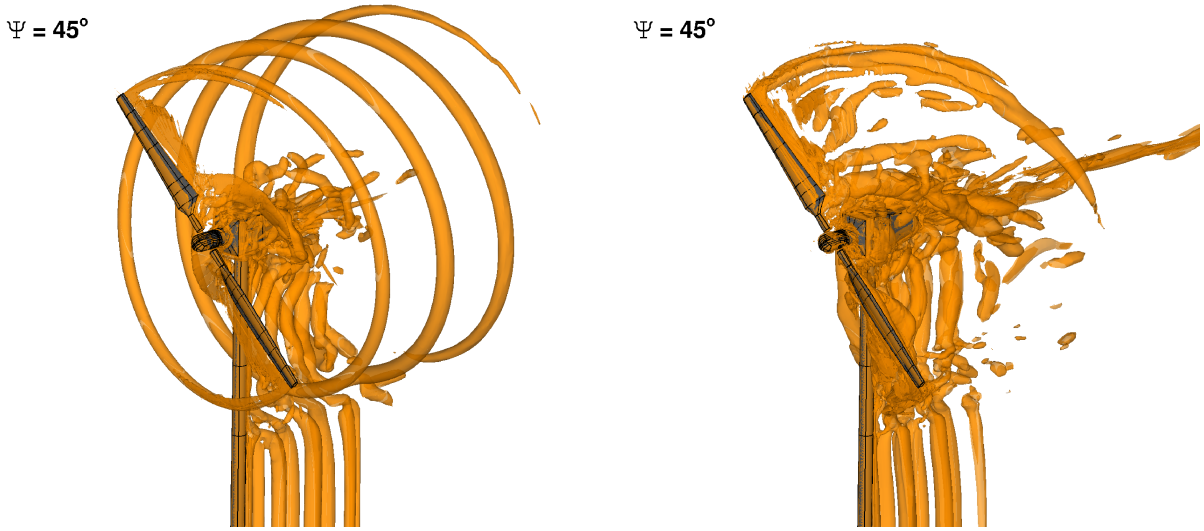

(a) 7m/s ($\lambda = 5.04$). **(b)** 20m/s ($\lambda = 1.88$).

Figure 7.13: Visualisation of the rotor and tower wakes with iso-surfaces of λ_2-criterion ($\lambda_2 = -0.25$) for wind speeds of **(a)** 7m/s and **(b)** 20m/s (test cases **N.2** and **N.3**, respectively). The reference blade is positioned at 45 deg. of azimuth.

The difference between the two cases can be seen in Figure 7.13, that shows iso-surfaces of the λ_2-criterion, at an instance when the reference blade is positioned at 45 degrees of azimuth. The interaction of the wake generated by the rotor and the Kárman vortex street generated by the cylindrical tower can be clearly identified. An interesting feature is that at 7m/s the flow is attached and the tip vortex is captured and preserved up to 2 radii downstream the rotor plane, where the grid starts to be coarser. This can be observed

in the contours of vorticity magnitude of Figure 7.14 (a). On the other hand, at 20m/s the vortical structures suggest separated flow on the blade, which can also be observed in Figure 7.14 (b). Due to the large step of the wake spiral at the 20m/s case, the wake reaches the coarse part of the mesh relatively early, and begins to dissipate prematurely. This is similar to the situation reported in Ref. [85].

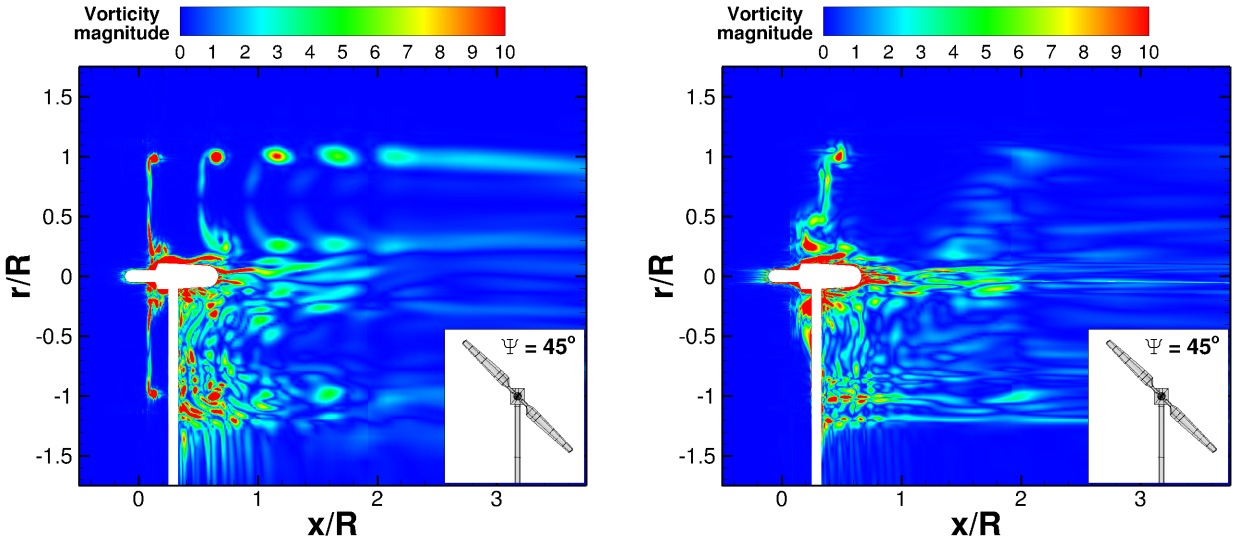

(a) 7m/s ($\lambda = 5.04$). **(b)** 20m/s ($\lambda = 1.88$).

Figure 7.14: Visualisation of the rotor and tower wakes with contours of vorticity magnitude (cases **N.2** and **N.3**, respectively). The reference blade is positioned at 45 deg. of azimuth.

Figure 7.15 shows FFTs of the sectional thrust at three blade stations. More frequency content is observed in the 20m/s wind speed case than at 7m/s. This is due to the presence of stall almost everywhere on the blade for this high wind case. In addition, there is a peak very close to the first flapping mode, which could trigger flutter.

Comparison between k-ω SST and SAS-SST turbulence models

A comparison between the performance of the k-ω SST [95] and SAS-SST [38] model for the 20m/s wind speed case is presented here. Figure 7.16 shows contours of radial velocity, vorticity magnitude and Re_T on a slice through one of the blades' section (at Ψ =45 deg.) and the tower. Small differences are observed in the velocity and the vorticity magnitude. However, the overall Re_T (turbulence Reynolds number, $Re_T = \mu_t/\mu$) levels shown in Figure 7.16 (c) have different order of magnitude.

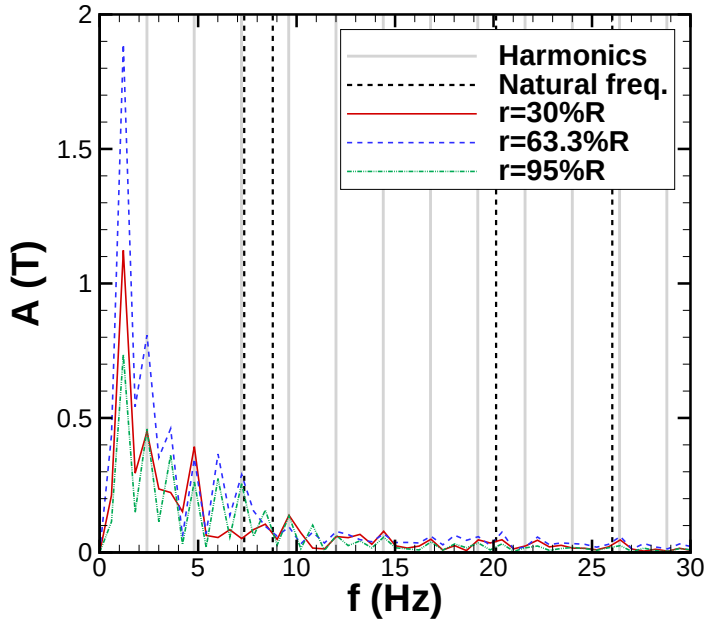

(a) 7m/s.

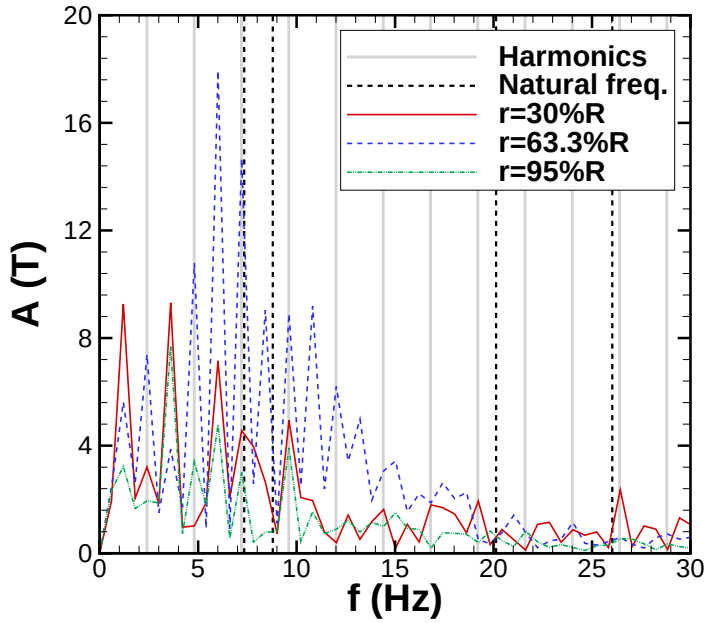

(b) 20m/s.

Figure 7.15: FFTs of sectional thrust at different blade stations, for wind speeds of **(a)** 7m/s and **(b)** 20m/s. (test cases **N.2** and **N.3**). The harmonics correspond to multiples of the blade passing frequency $f_n = nf_1$ (f_1 =2.4Hz). The natural frequencies are: $f_{n_1} = 7.34$, $f_{n_2} = 8.79$, $f_{n_3} = 20.13$, $f_{n_4} = 26.03$.

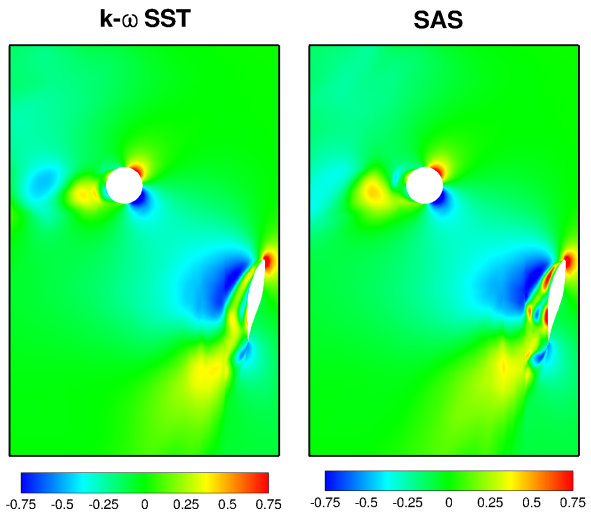

(a) Contours of radial velocity.

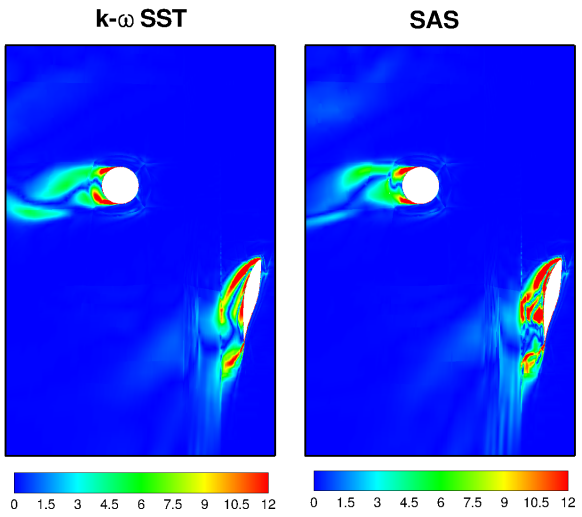

(b) Contours of vorticity magnitude.

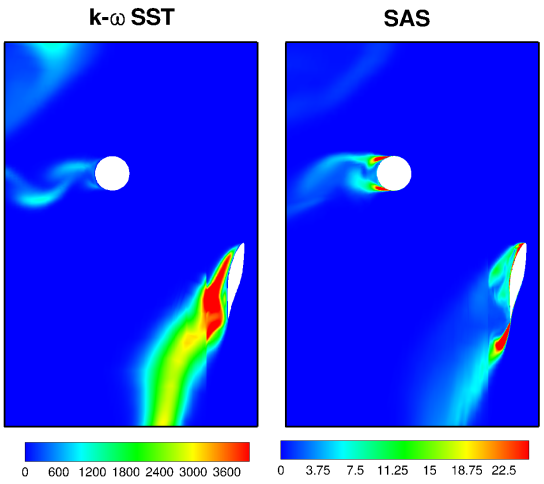

(c) Contours of Re_T.

Figure 7.16: Comparison between k-ω SST and SAS-SST turbulence models on a slice through the tower and the blade, visualised with contours of **(a)** radial velocity, **(b)** vorticity magnitude and **(c)** Re_T, at 20m/s.

The Re_T along the blade and downstream is shown in Figure 7.17. Although the overall Re_T levels are much lower for the SAS model, very close to the solid surface both models produce the same Re_T. This is due to the fact that the SST-SAS model acts as URANS in the boundary layer region, while far from it acts as LES, capturing more frequency content by producing less turbulent viscosity. The overall integrated thrust and the sectional thrust coefficient in Figure 7.18 show the same mean values for the two cases, however, the SAS model captures more frequencies. Likewise, the C_p distributions of Figure 7.19 show small difference at the sections from mid-span to the tip of the blade and higher differences are present at the root.

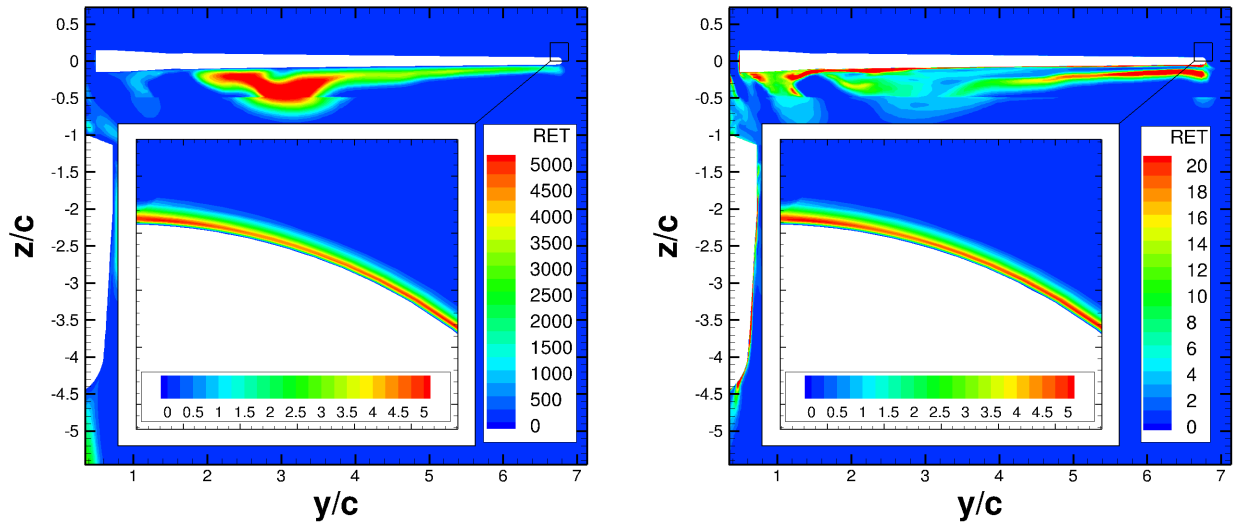

(a) k-ω SST model. **(b)** SAS model.

Figure 7.17: Comparison between k-ω SST and SAS-SST turbulence models on the Re_T values on the flow and at the solid surfaces, at 20m/s wind speed.

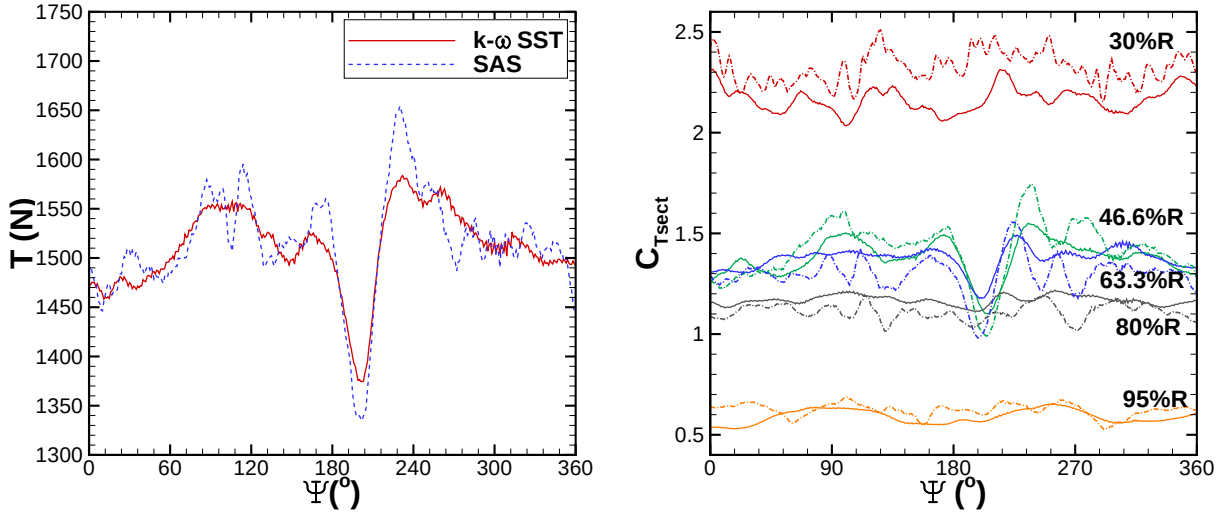

(a) Integrated thrust. **(b)** Sectional thrust coefficient.

Figure 7.18: Comparison between k-ω SST and SAS-SST turbulence models on the **(a)** overall integrated thrust and the **(b)** sectional thrust coefficient, at 20m/s wind speed.

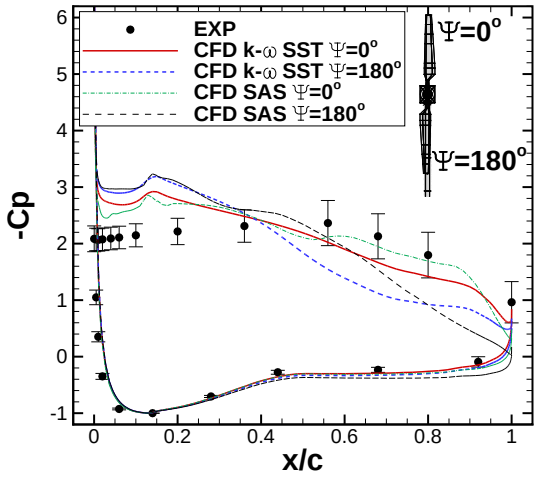

(a) 30% R.

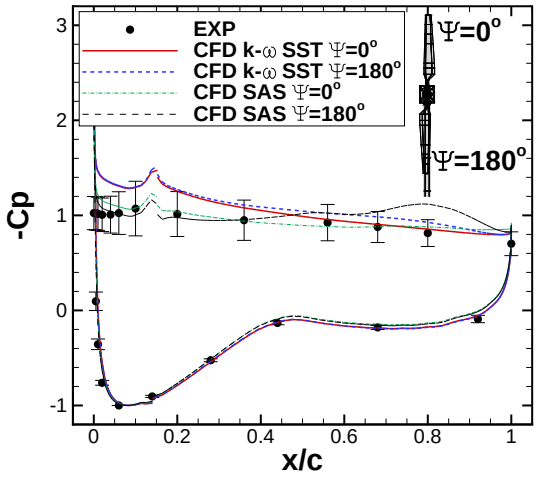

(b) 63.3% R.

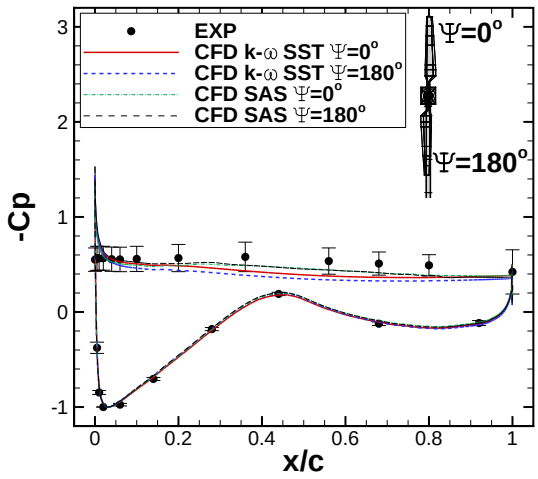

(c) 95% R.

Figure 7.19: Comparison between k-ω SST and SAS-SST turbulence models for the surface C_p distribution along three blade stations and at azimuthal positions of $\Psi = 0$ deg. and $\Psi = 180$ deg., at 20m/s wind speed.

7.4.2 Study of the blade deformations

Five rotor revolutions were performed with the aeroelastic method, until the deflections were almost constant from one revolution to the next. For stability reasons, during the first aeroelastic revolution, the structural damping (ζ) was reduced from an initial value of 0.7 to a final value of 0.03. Figure 7.20 shows the logarithmic decrement of the amplitudes from the second revolution, computed as

$$d = ln\left(\frac{A_i}{A_{i+1}}\right), \tag{7.1}$$

which tends to zero at 7m/s and 0.02 at 20m/s from the fourth to the fifth revolution. As presented in Section 7.4.1, the flow around the blade at 20m/s is more complex than at 7m/s due to the presence of stall, hence, reaching a value of $d = 0$ is more difficult in this case.

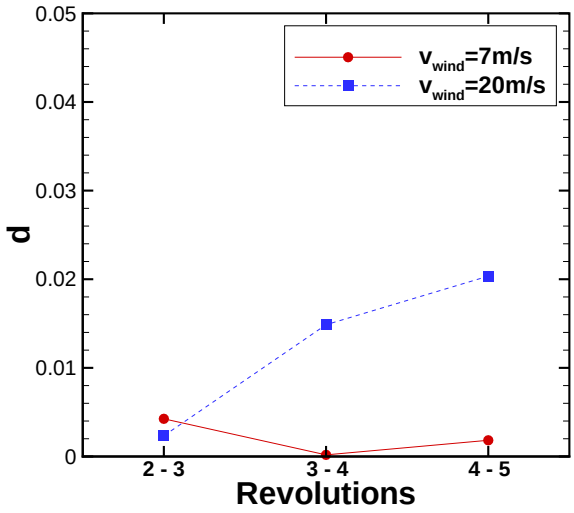

Figure 7.20: Logarithmic decrement of the flap amplitudes over five revolutions for wind speeds of 7m/s and 20m/s. Test cases **N.2** and **N.3**.

Figures 7.21 (a) and (b) show the flapping motion of the leading edge of the blade tip during the fifth aeroelastic revolution for both wind speed cases. With the employed sign convention, negative δ values indicate that the blade deflects towards the tower and blade 2 has been plotted with an azimuthal shift of 180 degrees, for easier comparison. As observed in Figure 7.21 (a), the mean deflection at 7m/s is 1.73% of the blade's maximum aerodynamic chord (or 0.25%R) towards the tower, which is in good agreement with the static aeroelastic analysis presented in Section 7.3. Maximum oscillations of approximately $+/-$ 5.2% with respect to the mean value are observed. A mean deflection of 4%c (0.59%R) is observed in the

20m/s case (Figure 7.21 (b)) and oscillates around that mean value with maximum amplitudes of $+/-37\%$. The maximum amplitudes are present after the blades have passed in front of the tower ($\Psi = 0$deg. and $\Psi = 180$deg. for blades 2 and 1, respectively), with a delay of 70 degrees at 7m/s wind speed and 80 degrees at 20m/s. The plots show an almost symmetric behaviour between blades, with 180 degrees of off-set applied.

The induced speeds due to the flapping motion are shown in Figures 7.21 (c) and (d), in chords per second (c/s). With the employed sign convention, negative values add extra velocity to the axial component, while positive values reduce the axial velocity. The maximum increase/decrease of velocities is of $+/-$ 0.02c/s and $+/-$ 0.40c/s, for wind speeds of 7 and 20m/s, respectively, whose equivalent values in SI units are 0.015m/s and 0.30m/s. Therefore, the blade flapping adds $+/-$ 0.2% and $+/-$ 1.5% instantaneously to the axial component, respectively. This means that there is a change in the effective angle of attack of approximately $\Delta\alpha = 0.02$deg. and $\Delta\alpha = 0.36$deg. at 7m/s and 20m/s, respectively. The FFTs of the flapping signal obtained from the last two rotor revolutions are presented in Figures 7.21 (e) and (f). The frequency multiples of the blade-passing (2.4Hz) are included, as well as the first four natural frequencies as presented in Table 7.4. The highest peak corresponds to the second harmonic (4.8Hz).

For the edgewise motion, Figure 7.22 shows the obtained amplitudes and their derivatives. Note that, for better visualisation, the amplitudes of blade 2, although negative, are shown with positive sign and the 180 degrees off-set is also applied. Compared to the flapping motion, the amplitudes of the edgewise motion are one order of magnitude smaller and the same delay observed in the flapping motion is presented here. The maximum addition to the tangential tip velocity component (37.7m/s) when the blades have passed in front of the tower is 0.005% and 0.008% for wind speeds of 7 and 20m/s, respectively, as shown in the derivatives in Figures 7.22 (c) and (d). From the FFTs presented in Figures 7.22 (e) and (f), a highest peak at 6Hz is observed, corresponding to five times the rotational frequency.

A 3D view of the region closed the the blade tip is presented in Figure 7.23, for the reference blade (blade 1), where the differences between the rigid and elastic blades can be observed, as well as the difference in deformation between the two wind speed cases.

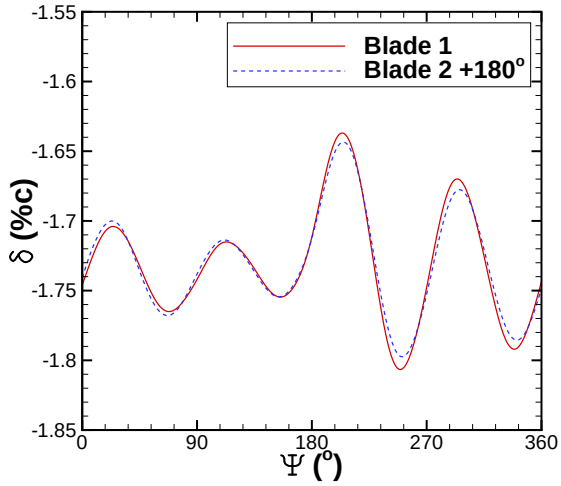

(a) Flapping amplitudes (7m/s).

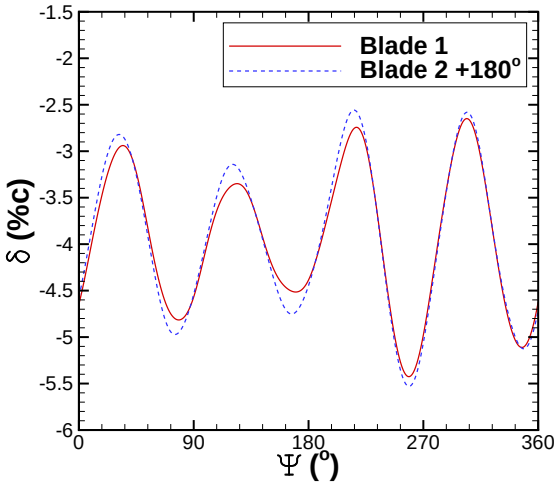

(b) Flapping amplitudes (20m/s).

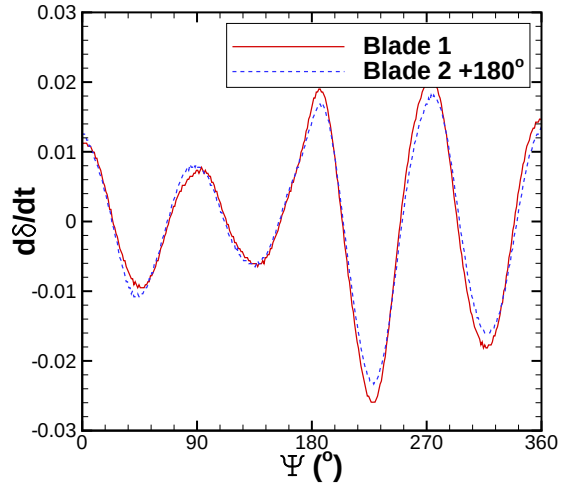

(c) Flapping derivatives (7m/s).

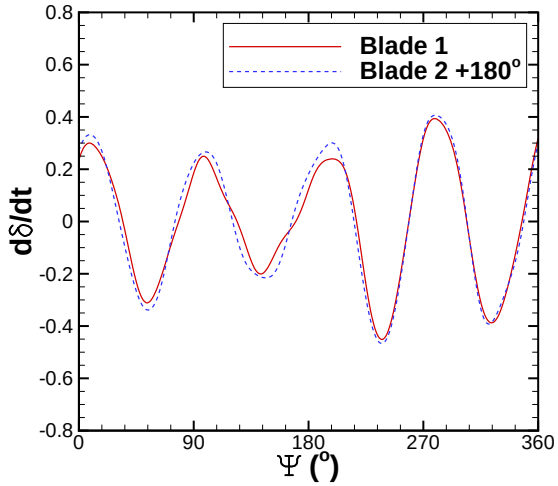

(d) Flapping derivatives (20m/s).

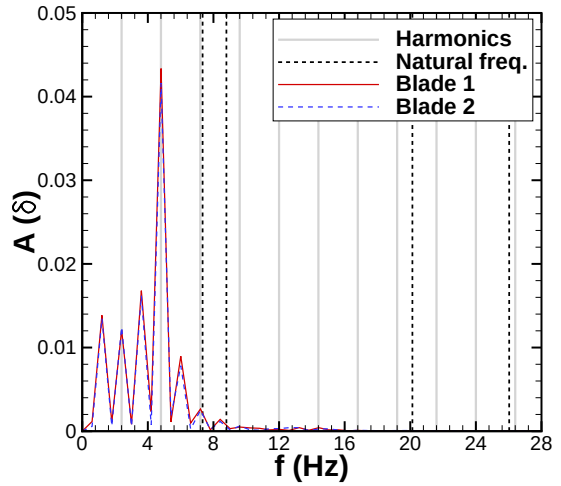

(e) Flapping FFTs (7m/s).

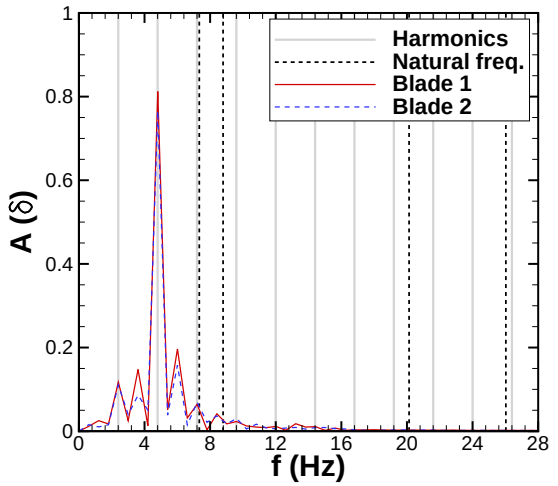

(f) Flapping FFTs (20m/s).

Figure 7.21: Flapping motion of the tip leading edge of the NREL Annex XX blades, including amplitudes (%c), derivatives and FFTs, at wind speeds of 7m/s (left) and 20m/s (right). Ψ =0 deg. indicates that blade 1 is at the top and blade 2 is aligned with the tower. The harmonics correspond to multiples of the blade passing frequency $f_n = nf_1$ (f_1 =2.4Hz). The natural frequencies are: $f_{n_1} = 7.34$, $f_{n_2} = 8.79$, $f_{n_3} = 20.13$, $f_{n_4} = 26.03$. Test cases **N.2** and **N.3** of Table 7.2.

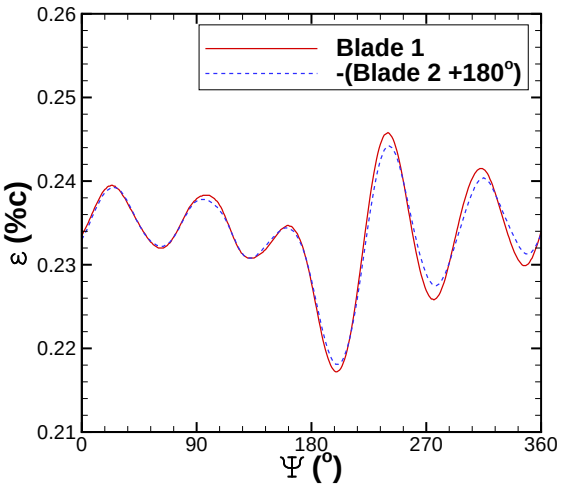

(a) Edgewise amplitudes (7m/s).

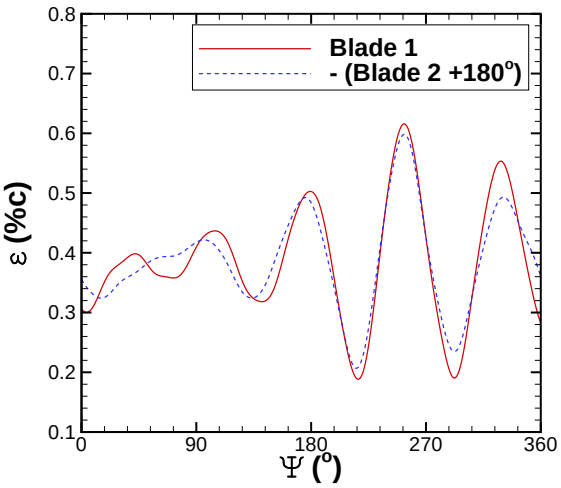

(b) Edgewise amplitudes (20m/s).

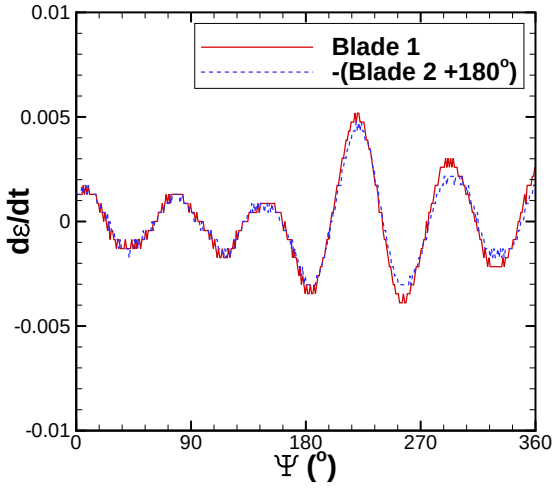

(c) Edgewise derivatives (7m/s).

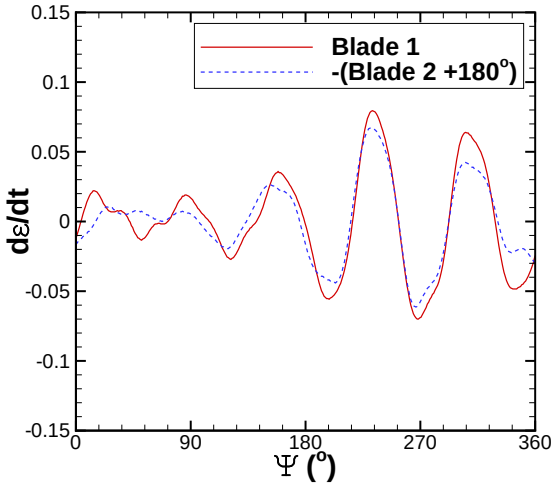

(d) Edgewise derivatives (20m/s).

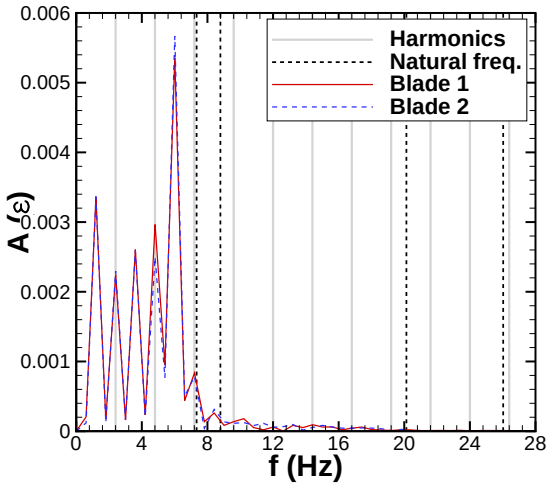

(e) Edgewise FFTs (7m/s).

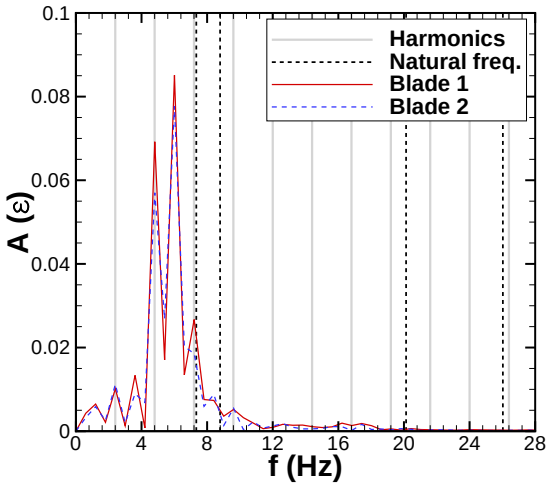

(f) Edgewise FFTs (20m/s).

Figure 7.22: Edgewise motion of the tip leading edge of the NREL Annex XX blades, including amplitudes (%c), derivatives and FFTs, at wind speeds of 7m/s (left) and 20m/s (right). Ψ =0 deg. indicates that blade 1 is at the top and blade 2 is aligned with the tower. The harmonics correspond to multiples of the blade passing frequency $f_n = nf_1$ (f_1 =2.4Hz). The natural frequencies are: $f_{n_1} = 7.34$, $f_{n_2} = 8.79$, $f_{n_3} = 20.13$, $f_{n_4} = 26.03$. Test cases **N.2** and **N.3** of Table 7.2.

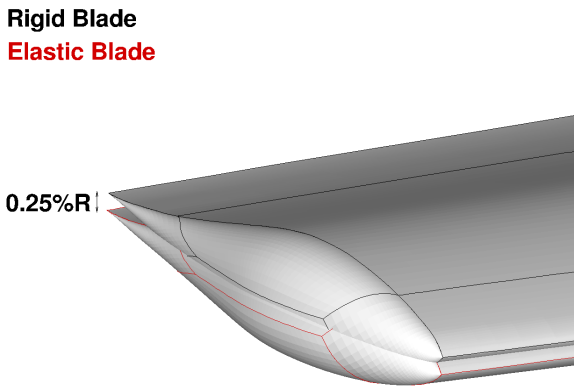

(a) Rigid and elastic blades at 7m/s.

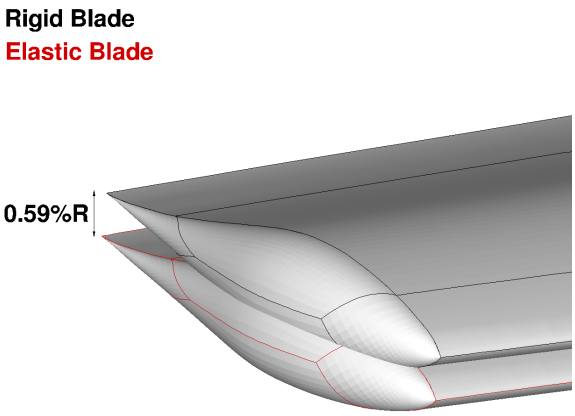

(b) Rigid and elastic blades at 20m/s.

Figure 7.23: Comparison between the rigid and elastic blades at the blade tip region. At $\Psi = 0$deg. the blade is at 12 o'clock and at $\Psi = 180$ degrees it is front of the tower. Results corresponding to cases **N.2** and **N.3** of Table 7.2.

7.4.3 Study of the blade loads

The effect of aeroelasticity on the integrated thrust, torque and aerodynamic power for the reference blade (blade 1) is presented in Figure 7.24, during a full revolution. The CFD results were averaged over the last two rotor revolutions, and error bars with standard deviation are included in the plots. Note that the integration of the loads for both CFD and experiments was performed using only the locations of the measurement pressure taps at five blade stations and summing them up according to the area they cover and the dynamic pressure, using Equations (7.2) and (7.3),

$$T = \sum_{i=1}^{5} C_{T_i} q_i A_i, \tag{7.2}$$

$$Q = \sum_{i=1}^{5} C_{Q_i} q_i A_i r_i, \tag{7.3}$$

where, the thrust and torque coefficients (C_{T_i} and C_{Q_i}) were obtained by integration of the C_p normalised with the maximum sectional value and the sectional dynamic pressure was defined as $q_i = \frac{1}{2}\rho(U_\infty^2 + \frac{r_i}{R}\omega^2)$. To compute the aerodynamic power, Equation (7.4) was used.

$$P(kW) = Q \cdot \omega(rpm) \cdot \frac{\pi}{30,000} \tag{7.4}$$

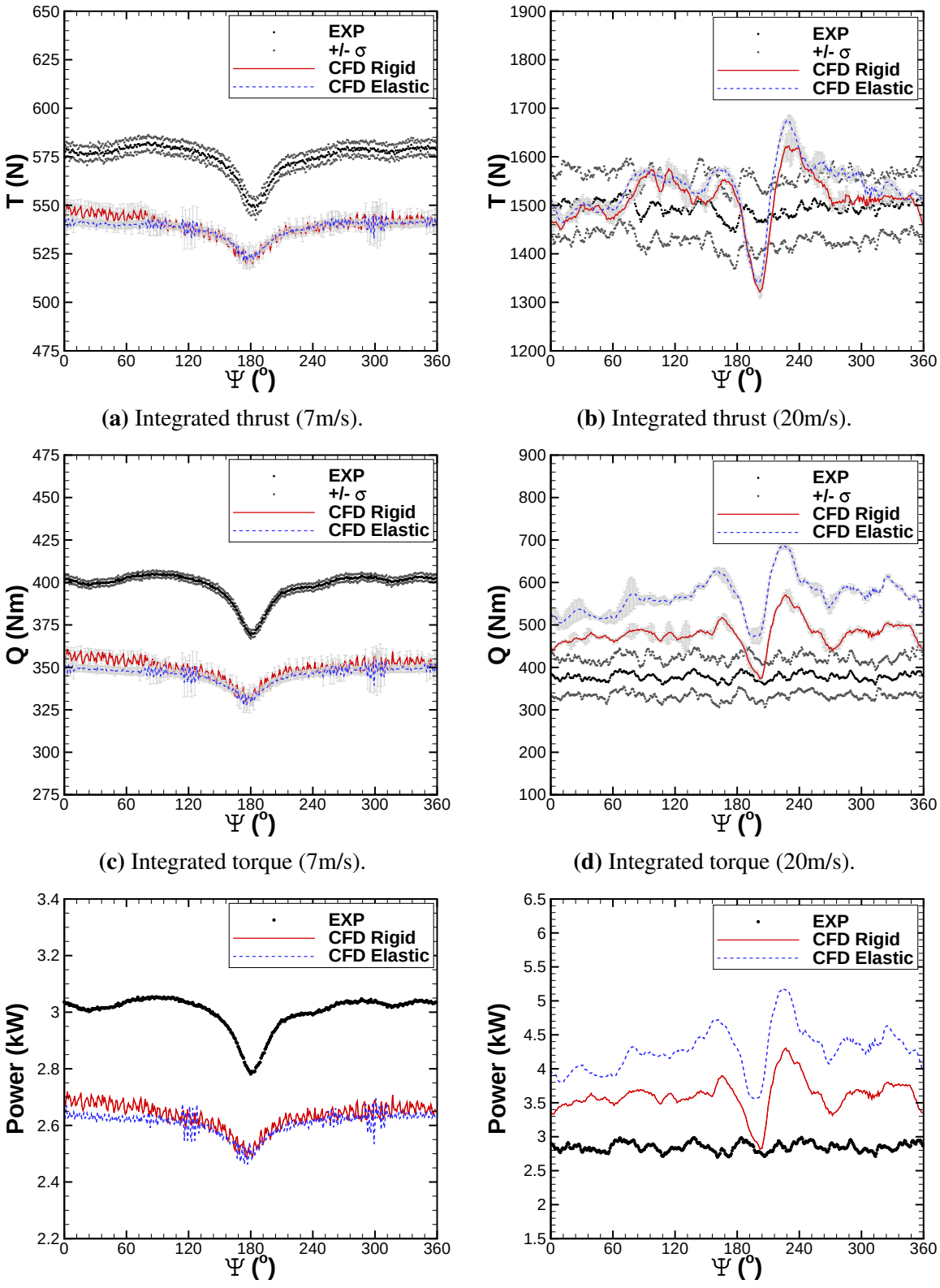

(a) Integrated thrust (7m/s).

(b) Integrated thrust (20m/s).

(c) Integrated torque (7m/s).

(d) Integrated torque (20m/s).

(e) Aerodynamic power (7m/s).

(f) Aerodynamic power (20m/s).

Figure 7.24: Comparison with the experiments of the integrated thrust (top), torque (middle) and aerodynamic power (bottom), including averaged values and standard deviation, for the rigid and elastic reference blades and wind speed of 7m/s (left) and 20m/s (right) (test cases **N.2** and **N.3**). At $\Psi = 0$ deg. the blade is at 12 o'clock and at $\Psi = 180$ deg. is in front of the tower.

At 7m/s wind speed, shown in the left column of Figure 7.24, for both rigid and elastic blades, a deficit of approximately 5% in the integrated quantities is observed as a result of the blade passing in front of the tower at an azimuth angle of 180 degrees (when the reference blade is at 6 o'clock), which is in good agreement with the experiments. This is due to a change in pressure between the blade and the tower and a change in the angle of attack as a consequence of the air being deflected when it hits the tower. Overall, there is good agreement with the experiments, with under-predictions of approximately 4% thrust and 10% in the torque and aerodynamic power, which are consistent all over the blade, as can be seen in Figure 7.25 (a), where the contribution of each section to the overall loads is shown. This differences are similar to the IEA NREL report [91]. The high frequency oscillatory pattern present in the integrated loads is attributed to the presence of stalled flow in the section close to the root (30%R), as can be observed in the sectional thrust coefficients over a revolution of Figure 7.26. The thrust coefficients were obtained by integrating the sectional C_p values, which where scaled with the maximum local value, as shown in Equation (7.5).

$$C_p = 2\left(\frac{p - p_\infty}{\gamma p_\infty M_\infty^2}\right)\frac{1}{C_{p_{max}}} \tag{7.5}$$

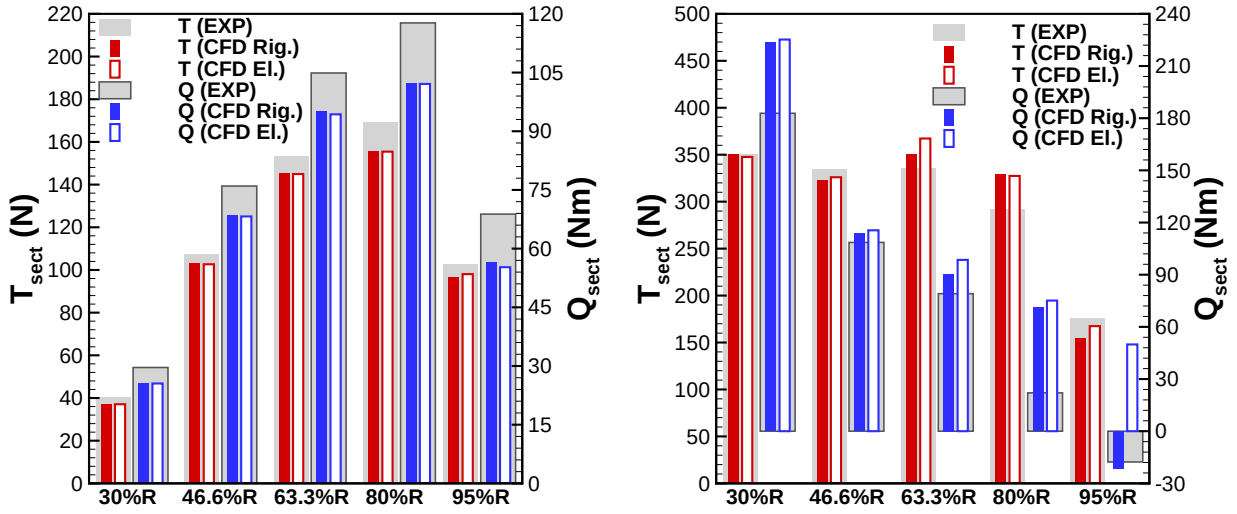

(a) 7m/s. **(b)** 20m/s.

Figure 7.25: Sectional integrated thrust and torque at five blade sections for rigid (Rig.) and elastic (El.) cases and wind speeds of **(a)** 7m/s and **(b)** 20m/s (test cases **N.2** and **N.3**).

At 20m/s, the experiments are more oscillatory and do not reveal a clear deficit at the region of the blade-tower interaction, Figures 7.24 (b) and (d), while in the CFD the effect is much clearer. In fact, the sections from the root to midspan are the ones that include this dip on the loads, as Figure 7.26 shows. Likewise, the standard deviation of the measured quantities is much higher than at 7m/s. In this case, the dip in the integrated quantities is delayed by 20 degrees approximately from the 180 degrees azimuthal position. The averaged values of thrust are in very good agreement with the experiments, falling inside the range of error of the experiments, while the torque is overpredicted by 10% approximately from the measured mean value. Similar issues were reported in the literature [46, 85], good agreements with thrust and differences in torque predictions. The contribution of each section to the integrated loads, plotted in Figure 7.25 (b), shows that the source of disagreement on the integrated torque is the section close to the root at 30%R and the section at 80%. At this wind conditions, the predicted deformations were higher and oscillated more rapidly than at the lower wind speed case, which resulted in an increase of the integrated torque and therefore aerodynamic power of 13% approximately from the rigid case, as shown in Figures 7.24 (d) and (f). The section that contributes the most to this change is at the tip of the blade (95%R), where there is a change of sign of the integrated torque (from -21Nm in the rigid case to 50Nm in the elastic case), see Figure 7.25. This is the result of the fast oscillation that the tip suffered, which led to an addition of 1.5% to the free-stream velocity component, as discussed in Section 7.4.2, leading to changes in angle of attack.

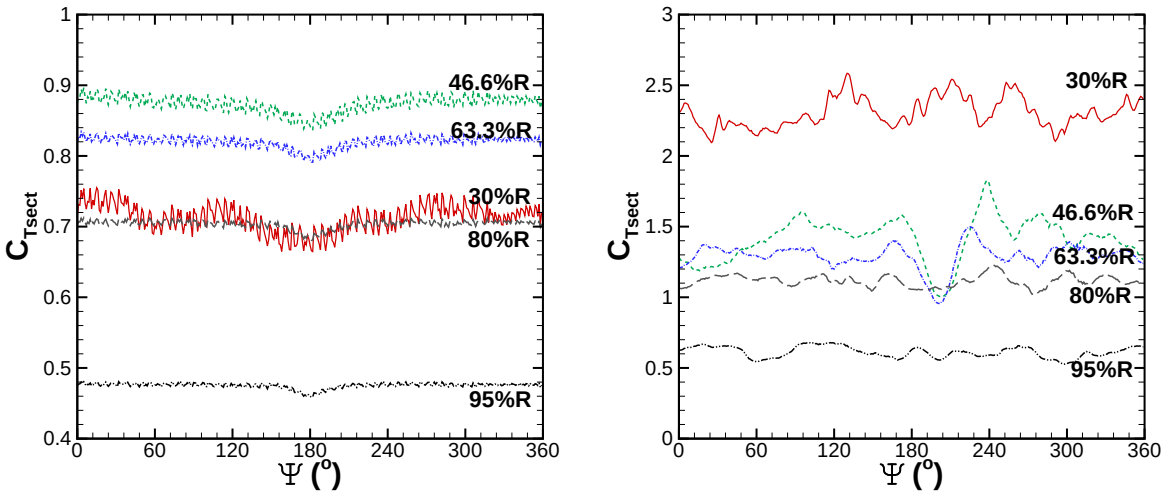

(a) 7m/s. **(b)** 20m/s.

Figure 7.26: Integrated thrust coefficient over a full revolution at five blade sections for **(a)** 7m/s and **(b)** 20m/s wind speeds (test cases **N.2** and **N.3**).

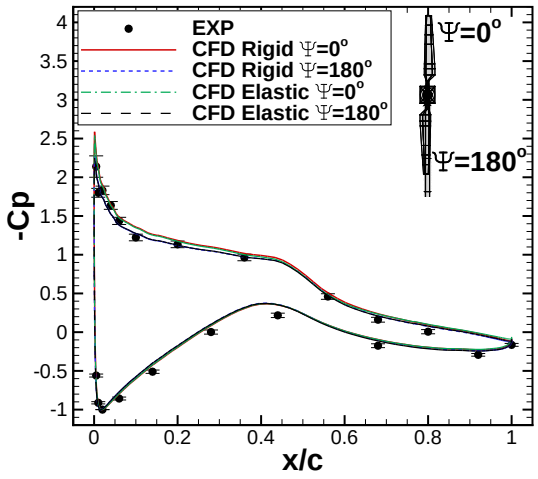

(a) 30%R (7m/s).

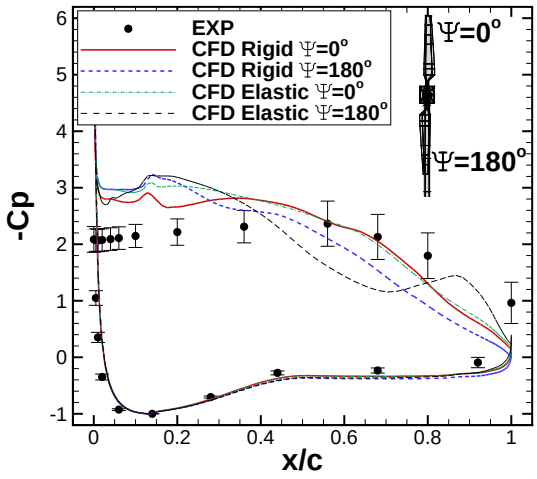

(b) 30%R (20m/s).

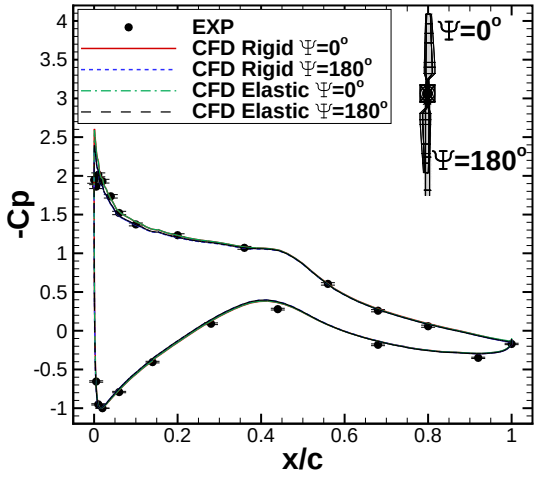

(c) 63.3%R (7m/s).

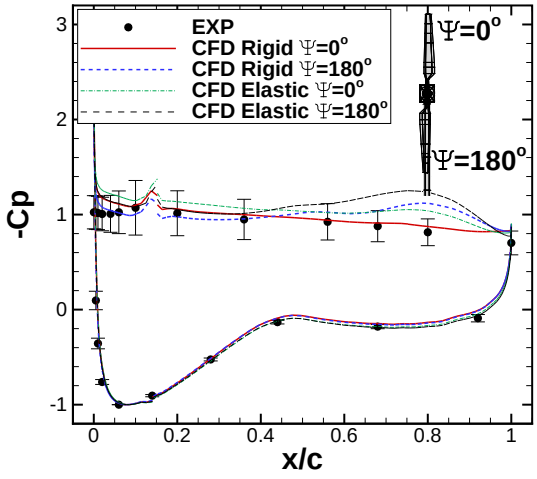

(d) 63.3%R (20m/s).

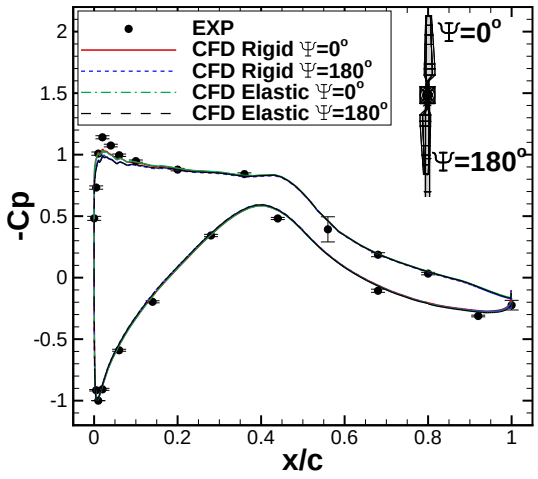

(e) 95%R (7m/s).

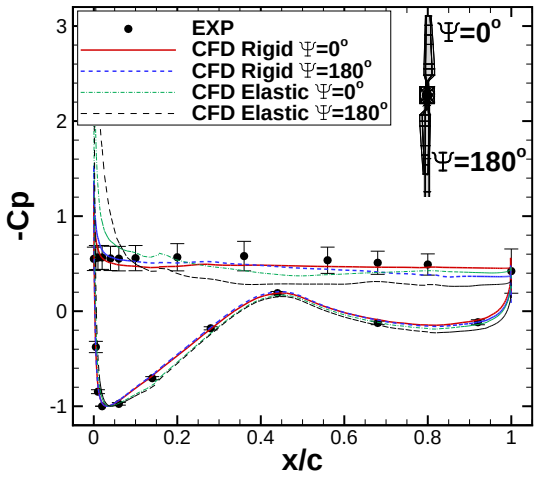

(f) 95%R (20m/s).

Figure 7.27: C_p distribution ($C_p = C_p/C_{p_{max}}$) at three blade stations when the reference blade is positioned at 0 and 180 degrees of azimuth (12 o'clock and 6'clock, respectively). Comparison between rigid and elastic blades, at wind speeds of 7m/s (left) and 20m/s (right) (test cases **N.2** and **N.3**, respectively).

For a more detailed analysis, pressure coefficient distributions at three blade sections along the blade are presented in Figure 7.27, for the reference blade positioned at 0 and 180 degrees of azimuth (12 o'clock and 6'clock, respectively), and for both rigid and elastic cases. For this comparison, the C_p has been scaled with the maximum value ($C_p/C_{p_{max}}$). A reduction of the suction is observed when the blade is in front of the tower, which is more significant close to the root due to the fact that the aerodynamic chord at the root is larger and therefore closer to the tower than the tip region. For the low wind speed case shown at the top of Figure 7.27, very small differences can be appreciated between the rigid and elastic blades, since the blade suffered very small deformations. At 20m/s, the relative position of the blade with respect to the tower shows to affect more the local C_p distribution, with the 30%R section (Figure 7.27 (b)) the most affected one. Likewise, the effect of the blade deformations shows significant changes in this case, which are mainly observed at the tip of the blade. At that station, although there is a reduction in suction as a result of the blade being affected by the tower, there is an additional increase close to the leading edge, as a result of the change in the effective angle of attack, which contributes to an overall increase of the loads. This resulted in the change of sign of the torque presented in Figure 7.25.

7.4.4 Effects on the tower

The effect of the blades passage in front of the tower is studied here, for the rigid and elastic cases. Five probes were located along the tower (Figure 7.28 (a)), and the pressure fluctuations over time were tracked. Note that the rotational speed is 72rpm (1.2Hz) and a full revolution is therefore covered in 0.83s. Since the flow takes time to settle into a periodic solution, the first three revolutions were disregarded in this analysis.

For the rigid cases, Figures 7.28 (b) and (d) show C_p signals over two rotor revolutions, where two peaks at every period are observed, as a result of the blade passing in front of the tower. A mean C_p value of 1 should be expected, since the flow stagnates on the tower, which can be seen in the signals of the probes from the blade tip outwards (P04 and P05). High C_p peaks are observed in the probe coinciding with the tip (P04), as a result of a pressure pulse created by the blade disturbance. On the other hand, those probes covering the inner part of the blade passage present a mean value of C_p =0.5, which is attributed to the fact that the rotor takes momentum out of the free-stream flow and therefore there is reduced stagnation.

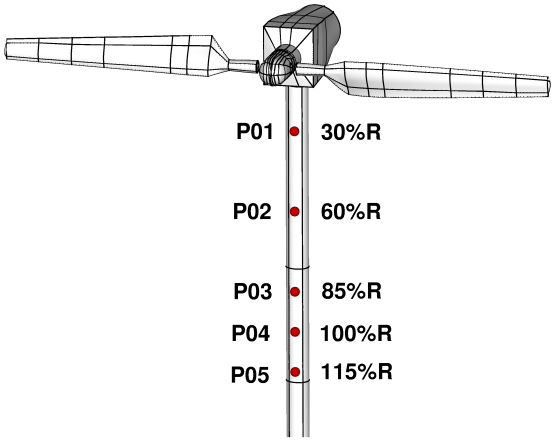

(a) Probes on the tower.

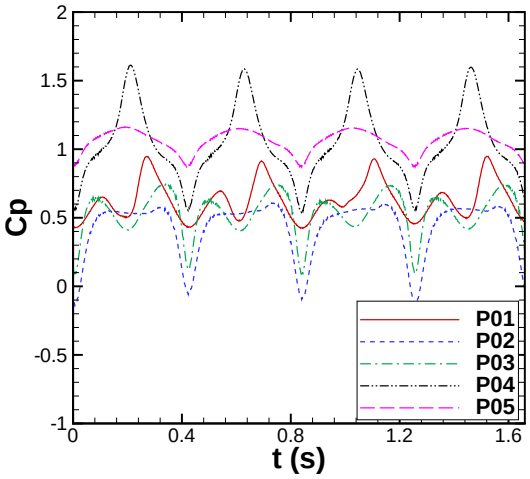

(b) C_p signal (7m/s).

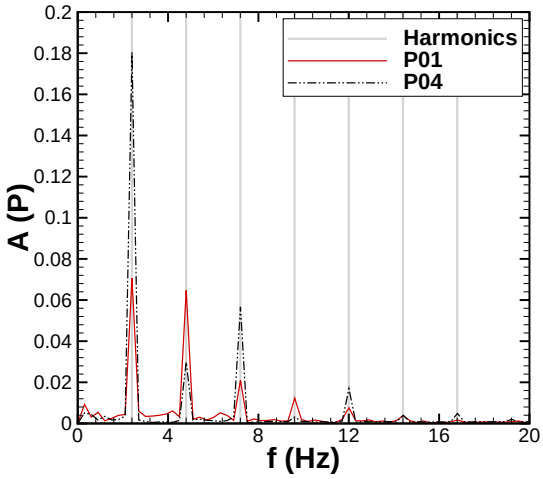

(c) FFTs of probes P01 and P04 (7m/s).

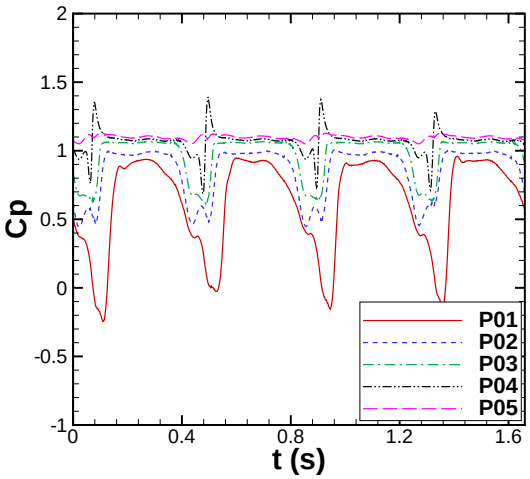

(d) C_p signal (20m/s).

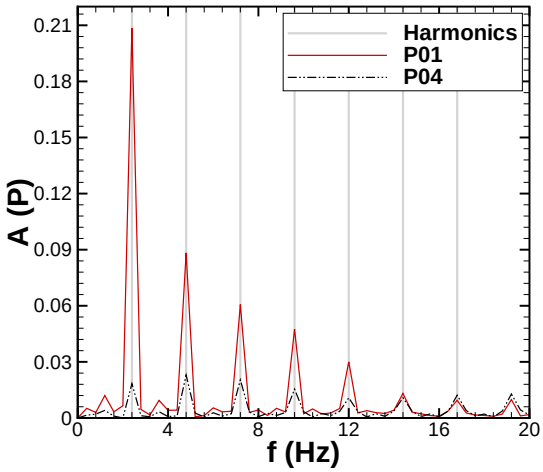

(e) FFTs of probes P01 and P04 (20m/s).

Figure 7.28: **(a)** Probe setup along the tower. **(b),(d)** C_p signals (based on the free-stream Mach number) on the tower surface over two rotor revolution ($T = 0.83$s). **(c),(d)** FFTs of the pressure signals of probes P01 and P04, using 1,440 data samples. The harmonics correspond to multiples of the blade-passing frequency $f_n = nf_1$ (f_1 =2.4Hz). Cases **N.2** and **N.3**.

Similar behaviour is observed for the higher wind speed case in Figure 7.28 (d). As expected, the main frequency corresponds to the blade-passing frequency (2.4Hz), as shown in the pressure FFTs of Figures 7.28 (c) and (e). However, at 7m/s wind speed, the higher peak was present for the probe located at the tip of the blade passage (P04) and at 20m/s it corresponded to the probe located at the root passage (P01). This is consistent with the sectional loads presented in Figure 7.25, where at 20m/s the root of the blade was more loaded than the tip and at 7m/s there was an opposite effect.

A more detailed comparison of the C_p signals between the rigid and elastic cases is presented in Figure 7.29, for a probe close to the root (P01), one towards the tip (P04) and another one outside the blade range (P05). As can be observed, the signals from probes P04 and P05 are almost identical between rigid and elastic cases and for both wind speeds. The signal on the probe close to the root shows, although small, slightly higher differences differences.

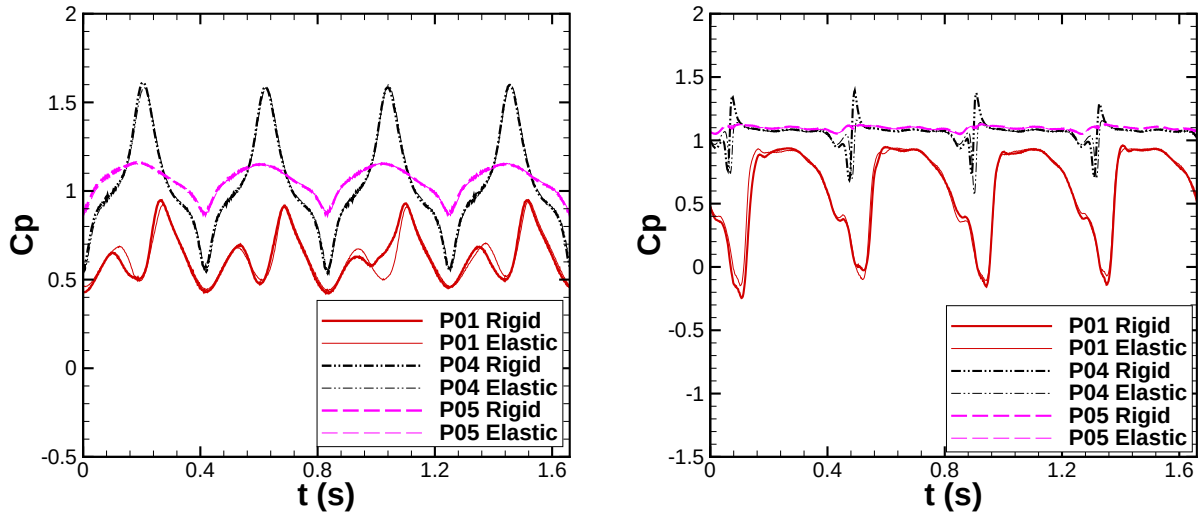

(a) 7m/s. **(b)** 20m/s.

Figure 7.29: C_p signals on the tower surface for a rigid and elastic passing blades, for wind speeds of **(a)** 7m/s and **(b)** 20m/s.

7.4.5 Sensitivity to the structural damping

The effect of reducing the structural damping (ζ) from 0.03 to 0.01 is presented in Figure 7.30. As can be observed, the mean blade deflections are not affected, however, the oscillations around the mean value are larger. The change in the flapping deflections at 7m/s (Figure 7.30 (a)) is of 0.90%, while the edgewise is

affected by 2.35% (Figure 7.30 (b)). At 20m/s, reducing the structural damping by 66.67% increases the maximum flapping and edgewise deflections by 6.91% and 7.46%, respectively, as shown in Figures 7.30 (c) and (d).

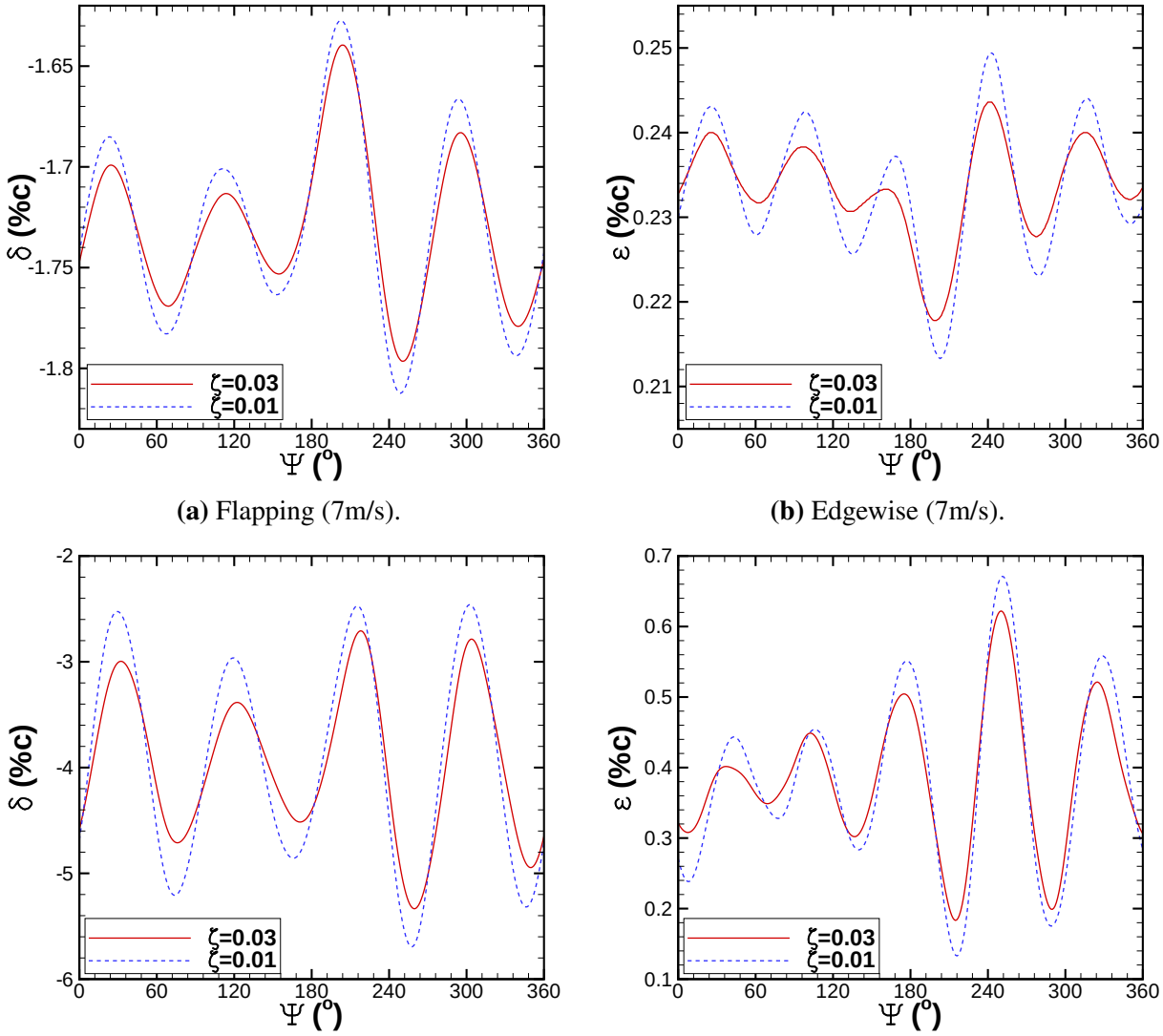

(a) Flapping (7m/s). **(b)** Edgewise (7m/s).

(c) Flapping (20m/s). **(d)** Edgewise (20m/s).

Figure 7.30: Flapping and edgewise amplitudes (%c) of the tip leading edge of the NREL Annex XX blade, at wind speeds of 7m/s (Top) and 20m/s (Bottom). Ψ =0 deg. indicates that blade 1 is at the top and blade 2 is aligned with the tower.

The induced speeds produced by the flapping and edgewise motions are directly affected by the larger oscillations, as shown in Figure 7.31. The maximum increase/decrease to the axial velocity component increases by 19.20% at 7m/s and 18.1% at 20m/s when ζ is reduced from 0.03 to 0.01. At 7m/s the change

in the effective angle of attack goes from $\Delta\alpha = 0.02$deg. to $\Delta\alpha = 0.03$deg.; at 20m/s it goes from $\Delta\alpha = 0.36$deg. to $\Delta\alpha = 0.59$deg. In the edgewise direction, this increase/decrease to the tangential velocity component is of 31.7% and 25.5% at wind speeds of 7 and 20m/s, respectively.

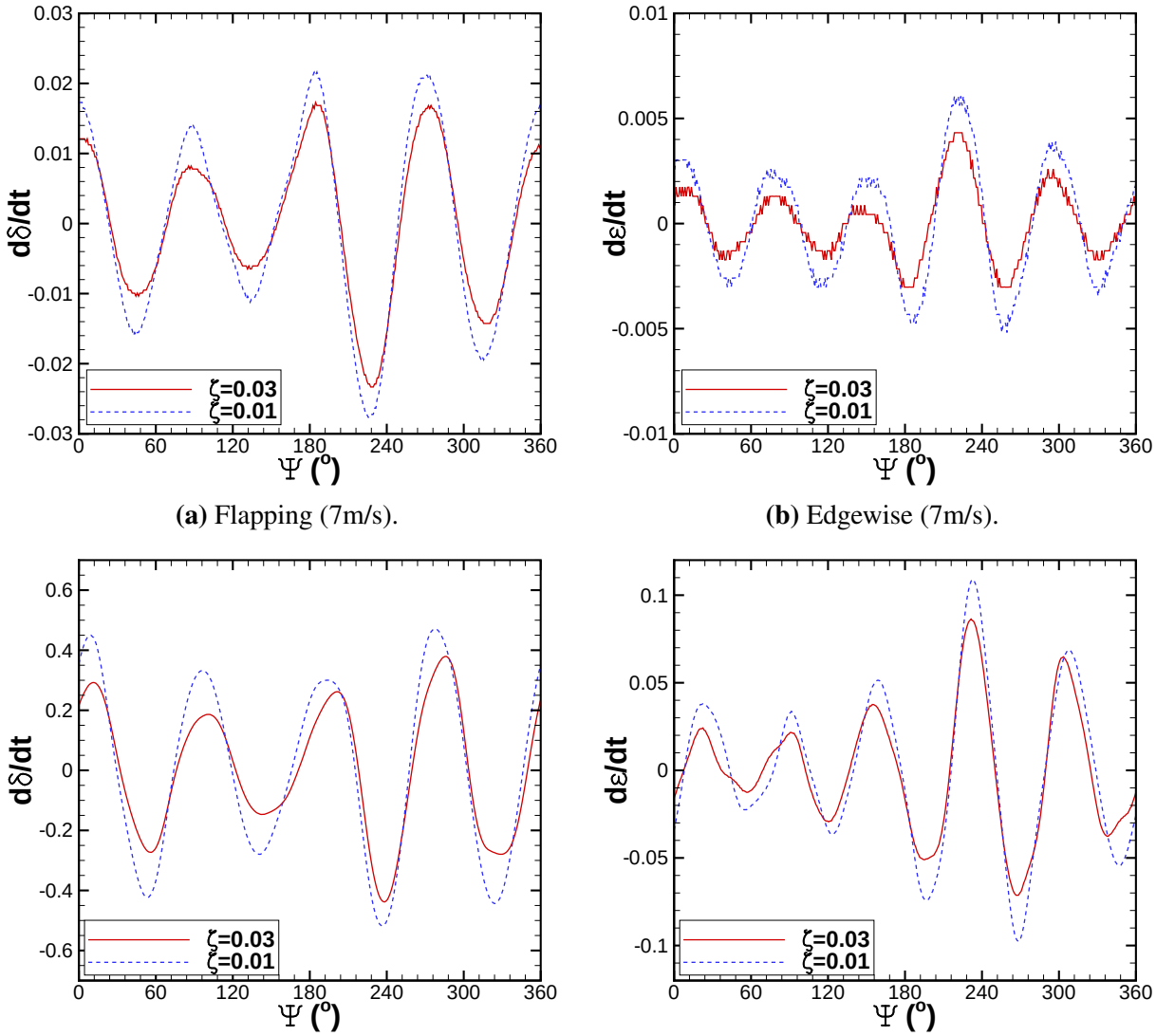

(a) Flapping (7m/s). **(b)** Edgewise (7m/s).

(c) Flapping (20m/s). **(d)** Edgewise (20m/s).

Figure 7.31: Flapping and edgewise derivatives (c/s) of the tip leading edge of the NREL Annex XX blade, at wind speeds of 7m/s (Top) and 20m/s (Bottom). Ψ =0 deg. indicates that blade 1 is at the top and blade 2 is aligned with the tower.

This shows that the structural damping is an important parameter. Too high values would remove blade oscillations and too low values would lead to very large oscillations that would persist much longer over time, as presented in Ref. [104].

Chapter 8

Conclusions and Future Work

The present thesis covered some aspects of wind turbine Computational Fluid Dynamics. Firstly, low-Mach schemes were studied and implemented, to improve the performance of the compressible HMB2 solver of Liverpool University for low-speed flows. Using the most promising scheme, studies were performed, employing the reference MEXICO and NREL Annex XX wind turbines to show the potential of compressible CFD solvers for wind turbine analysis as opposed to incompressible methods. Analysis of the velocity field at the wake of the MEXICO blade was performed and comparisons with experiments were presented. In addition, the wake breakdown mechanism was simulated. Finally, structural analysis methods coupled with CFD were applied to both wind turbines.

In the following, the main conclusions of the different parts of this thesis are detailed, as well as recommendations for future work.

8.1 All-Mach methods

The implementation and evaluation of modified Roe schemes for application to low-Mach flows were presented. For the assessment of their performance, different test cases were employed, including 2D/3D, inviscid/viscous and steady/unsteady flows. The ultimate objective was to apply the schemes to wind turbine flows.

In the implicit formulation of the modified Roe schemes, a restriction on the CFL number was observed relative to the original Roe, at very low Mach numbers. This is due to the scaling of the diagonal terms of the modified Jacobian, that is less diagonal-dominant. To overcome this and therefore accelerate the convergence, three different options were assessed. Firstly, extra dissipation was added, by means of limiting the scaling function ($f(M)$) in the Jacobian to a minimum value. It was found that a value of 0.1 was appropriate. Since the Jacobian of the original Roe scheme (O-Roe) lacked this restriction, it was used as second approach to drive the solution. Finally, a combination of the modified Roe Jacobian with the original one (COMB-J) was tested. For this, the maximum absolute value between them was selected for the diagonal terms, while for the off-diagonal ones the minimum absolute value was taken; which lead to a more diagonal-dominant Jacobian. Among the three approaches, the first one proved to be the most efficient.

For 2D cases, the modified Roe schemes showed great improvement in the convergence and the quality of the solution, when compared to the Original Roe and Osher schemes. For all computed cases, the Low-Mach Roe scheme showed good convergence and no CFL reduction was necessary. This scheme was therefore selected for application to wind turbines.

The results showed an improvement for the parked case of the MEXICO blade, mainly at radial stations close to the root of the blade and at stagnation regions. Regarding rotating wind turbine cases, the pressure distributions of the high-speed case (15m/s) obtained with the different schemes were almost identical. However, the vortices were captured much better with the Low-Mach Roe scheme, as it was found to be less dissipative. For 10 and 5m/s wind, a slight improvement was present in the inner stations of the blade, mainly observed in the slowest case.

In the future, nonetheless, further low speed wind turbine cases with velocity data near the blade are necessary for a complete assessment of the method.

8.2 Wake study of the MEXICO rotor

Assuming periodicity in time and space, CFD computations were performed for the MEXICO rotor at different wind speed conditions and grid sizes. The Osher's scheme and low-Mach schemes implemented into HMB2 were employed.

Firstly, a grid convergence study regarding the blade loads was presented. The pressure distribution and integrated thrust and torque were of the same level of agreement as published works in the literature. Likewise, small differences were observed between different grid sizes and therefore grid convergence for the loads was assessed.

A detailed analysis of the velocity field behind the MEXICO rotor was then pursued. Velocity contours showed fairly good agreement with the experiments and from the tangential (chord-wise) component the deficit of momentum behind the blade trailing edge could be observed. Vorticity contours showed a discontinuity in the developed wake due to a change of aerofoil section with different zero-lift angle. The position and radius of the vortices were estimated. The former showed fair agreement with the experiments, while the latter were over-predicted. Likewise, the low-Mach scheme (LM-Roe) showed less sensitivity on the grid size than the Osher scheme.

The velocity profiles of the axial and span-wise velocity components showed excellent agreement with the measurements, mainly at 80% span, where the grid was more refined. The oscillatory pattern resulting from the vortex and blade passages was successfully captured in all three wind speed cases.

A comparison of the velocities at the rotor plane was also performed. In this case, the CFD computations proved to be consistent with the PIV located at 120% R radial station. However, some discontinuities were observed in the PIV windows at the inner parts of the blade at azimuth angles of 0 and 20 degrees. These could be due to inaccuracies in the CFD, but equally due to problems with the experiments.

Finally, a comparison between two grid densities was presented, employing sliding planes grids, where the cells at the wake had a size of 2.5%c, and a chimera grid with cell sizes of 1.5%c. Although the differences in the overall velocities, radius and position of the vortices were minimal, the chimera technique enabled a better and more localised mesh refinement. This provided better resolution of the vortex cores.

In the future, it would be interesting to look at other PIV sets from the MEXICO project, including yaw flow conditions. Comparisons with other wind turbine cases would be interesting, provided more PIV measurements become available.

8.3 Wake breakdown study

A comparison of the span-wise loads was firstly presented, for three cases with different wake resolutions, once the near wake was resolved for the MEXICO blade. The results showed that the loads were not affected by the level of wake resolution.

Using different criteria (λ_2-criterion and vorticity), the wake developed behind the MEXICO blade was identified and instabilities leading to vortex pairing from 4R downstream for wind speeds of 15m/s and 1.25R for 10m/s were observed. FFTs of the axial velocity component enabled to identify the main velocity harmonics in the wake. For the stable wake, the main frequency was the blade-passing one and where instabilities were present higher frequencies dominated.

A study on the effect of 120-degree azimuthally periodicity of the CFD domain was performed, by comparing to a 360-degree solution. Both cases showed the same location of the onset of the instabilities of the tip vortices, showing that it can be successfully captured using periodicity. Regarding the root vortices, however, the effects of periodicity were more noticeable since the azimuthal domain is much shorter in that region. Likewise, for a more detailed study of the breakdown mechanism, the full rotor provides more information about the frequency content in the wake, since there is no forced azimuthal periodicity.

A comparison of turbulence intensity with a semi-empirical model was also presented. Both solutions showed similar behaviour, except for the turbulence levels at the near wake as a result of the generation of the tip vortices, since this phenomena is not accounted for by the semi-empirical model. In addition, kinematic and field wake models were compared with the CFD solution and a model which combines the kinematic model for the near wake and the field model for the far wake was proposed, improving the agreement with the CFD solution. With the correct set of constants, it was proved that this simple model can be used to approximate the behaviour of wind turbine wakes with minimal computational cost.

The results suggest that, provided enough grid resolution is employed to capture and preserve the vortices downstream the rotor, CFD methods are able to predict instabilities on wind turbine wakes. Future work should involve time-accurate computations, to asses the evolution of the instabilities and study more in detail the dynamics of the wake breakdown. The effect of the inflow turbulence, as well as the atmospheric boundary layer, should be investigated.

8.4 Aeroelastic analysis

The MEXICO blade was employed for static aeroelastic analyses, where a single-blade domain was considered and steady-state computations were performed. A structural model for the MEXICO blade was firstly put together and the torsional stiffness was estimated from the flapwise and edgewise moments of inertia, using their average and the minimum value. Dependence on the torsional stiffness was observed for wind speeds of 10, 15 and 24m/s, not only in the deformations in torsion but also in bending. However, the former was more sensitive and the aeroelastic effects were mainly present from mid-span to the tip of the blade. Since the MEXICO blade is a relatively short blade and it has unusually high stiffness, the expected deformations were small and the approach where the torsional stiffness was assumed to be the averaged value between the flapwise and edgewise moments of inertia was the one with more realistic results. For both approaches, the aeroelastic method performed well, preserving the quality of the deformed grids. The effect of the pre-coning angle was also studied and lower deformations were observed when it was applied, in agreement with other works in the literature.

The NREL Annex XX blade was also analysed using both static and dynamically coupled aeroelastic methods. The static results showed that the main deflections were in flapping and almost no torsion was obtained. To characterise in a better way the effect of the blade flapping motion on the loads, a fully coupled CFD-CSD dynamic method was employed for wind speeds of 7m/s, where the flow was attached, and of 20m/s, where the flow was stalled. In these cases, the full wind turbine was considered, including the rotor, hub, nacelle and tower. Due to the proximity of the rotor to the tower, a deficit on the thrust and torque values was observed due to the blade passage, which was in good agreement with the experiments. The blade deformed in flapping and edgewise direction, being the former the most significant one, and the static and dynamic cases showed consistency in the mean deformations. The maximum deflections were present after the blades had passed in front of the tower and with 70 and 80 degrees of delay, at wind speeds of 7 and 20m/s, respectively. Larger deflections were obtained at 20m/s than at 7m/s wind speed. The effect of the deformations on the loads was found to be very small at 7m/s, obtaining differences of less than 1% in the averaged thrust and torque, between the rigid and elastic blades. At 20m/s, conversely, the torque on the elastic blades showed a 13% increment from the rigid ones, which was attributed to the rapid

blade oscillation. The effect of the rigid and elastic blades on the tower was also studied, showing a global reduction on the stagnation pressure, as a result of the rotor taking momentum out of the flow. Finally, the structural damping was reduced and an increase in the blade oscillation was observed, while the mean deflections were not affected.

In the future, efforts should be directed towards studying the influence of the deformed blade on the wake developed behind the wind turbine. It would also be interesting to apply this method to larger wind turbines, where the aeroelastic effects may be more pronounced. Study of the acoustics of the full wind turbine configuration should be performed too, including the assessment of the role that aeroelasticity plays in the generated noise levels.

Bibliography

[1] European wind energy association. http://www.ewea.org.

[2] http://www.cerfacs.fr/4–26336–NSMB.php.

[3] http://www.esi-cfd.com/content/view/779/140/.

[4] Icemcfd. http://www.ansys.com/products/icemcfd.asp.

[5] AcuSolve. http://www.altairhyperworks.com/Product,54,AcuSolve.aspx.

[6] J.F. Ainslie. Calculating the flowfield in the wake of wind turbines. *Journal of Wind Engineering and Industrial Aerodynamics*, 27:213–224, 1988.

[7] R.S Amano and R.J. Malloy. CFD Analysis on Aerodynamic Design Optimization of Wind Turbine Rotor Blades. *World Academy of Science*, 60:71–75, 2009.

[8] O. Axelsson. *Iterative Solution Methods*. Cambridge University Press: Cambridge, MA, 1994.

[9] K.J. Badcock, B.E. Richards, and M.A. Woodgate. Elements of Computational Fluid Dynamics on Block Structured Grids using Implicit Solvers. *Progress in Aerospace Sciences*, 36:351–392, 2000.

[10] C. Bak, F. Zhale, R. Bitsche, T. Kim, A. Yde, L.C. Henriksen, A. Natarajan, and M.H. Hansen. Description of the DTU 10 MW Reference Wind Turbine. *DTU Wind Energy Report-I-0092*, July 2013.

[11] T.K. Barlas and G.A.M. van Kuik. Review of state of the art in smart rotor control research for wind turbines. *Progress in Aerospace Sciences*, 46:1–27, 2009.

[12] B. Basara, A. Alajbegovic, and D. Beader. Simulation of Single- and Two-Phase Flows on Sliding Unstructured Meshes Using Finite Volume Method. *International Journal for Numerical Methods in Fluids*, 45(10):1137–1159, 2004.

[13] C.A. Baxevanou, P.K. Chaviaropoulos, S.G. Voutsinas, and N.S. Vlachos. Evaluation study of a Navier-Stokes CFD aeroelastic model of wind turbine airfoils in classical flutter. *Journal of Wind Engineering and Industrial Aerodynamics*, 96:1425–1443, 2008.

[14] Y. Bazilevs, M.C. Hsu, J. Kiendl, and D.J. Benson. A computational procedure for prebending of wind turbine blades. *International Journal for Numerical Methods in Fluids*, 89:323–336, 2012.

[15] Y. Bazilevs, M.C. Hsu, J. Kiendl, R. Wunchner, and K.U. Bletzinger. 3D Simulation of Wind Turbine Rotors at Full Scale. Part II: Fluid-Structure Interaction Modeling with Composite Blades. *International Journal for Numerical Methods in Fluids*, 65:236–253, 2011.

[16] A. Bechmann, N.N. Sorensen, and F. Zahle. CFD simulations of the MEXICO rotor. *Wind Energy*, 14(5):677–689, July 2011.

[17] K.H. Bergey. The Lanchester-Betz limit. *Journal of Energy*, 3:382–384, December 1979.

[18] L.O. Bernhammer and R. De Breuker. Wind Turbine Structural Model Using Non-Linear Modal Formulations. pages AIAA 2014–0715. 32nd ASME Wind Energy Symposium, National Harbor, Maryland, January 2014. .

[19] J. Bohbot, G. Grondin, A. Corjon, and DarracqD. A Parallel Multigrid Conservative Patched/Sliding Mesh Algorithm for Turbulent Flow Computation of 3D Complex Aircraft Configurations. 39th Aerospace Sciences Meeting and Exhibit, Reno, Nevada, USA, 8–11 January 2001. .

[20] J. Boussinesq. Essai sur la thorie des eaux courantes. *Mmoires prsents par divers savants l'Acadmie des Sciences*, 23(1):1–680, 1872.

[21] S-P. Breton, C.S. Watters, C. Masson, S. Gomez-Iradi, and X. Munduate. On the prediction of tip vortices in the near wake of the MEXICO rotor using the actuator surface method. *Engineering Systems Modelling and Simulation*, 4:11–26, 2012.

[22] C.W.S. Bruner. Parallelization of the Euler Equations on Unstructured Grids. *PhD thesis, Virginia Polytechnic Institute and State University, USA*, May 1996.

[23] M. Campobasso. Analysis of unsteady flows past horizontal axis wind turbine airfoils based on harmonic balace compressible Navier-Stokes equations with low-speed preconditioning. Gas Turbine Technical Congress and Exposition, June 6 –10 2011. .

[24] P.K. Chaviaropoulos, I.G. Nikolaou, K.A. Aggelis, N.N. Sorensen, J. Johansen, M.O.L. Hansen, T. Gaunaa, M. Hambraus, H.F. von Geyr, Ch. Hirsch, K. Shun, S.G. Voutsinas, G. Tzabiras, Y. Perivolaris, and S.Z. Dyrmose. Viscous and Aeroelastic Effects on Wind Turbine Blades. The VISCEL Project. Part I: 3D Navier-Stokes Rotor Simulations. *Wind Energy*, 6:365–385, July 2003.

[25] P.K. Chaviaropoulos, I.G. Nikolaou, K.A. Aggelis, N.N. Sorensen, J. Johansen, M.O.L. Hansen, T. Gaunaa, M. Hambraus, H.F. von Geyr, Ch. Hirsch, K. Shun, S.G. Voutsinas, G. Tzabiras, Y. Perivolaris, and S.Z. Dyrmose. Viscous and Aeroelastic Effects on Wind Turbine Blades. The VISCEL Project. Part II: Aeroelastic Stability Investigations. *Wind Energy*, 6:387–403, July 2003.

[26] A.J. Chorin. A Numerical Method for Solving Incompressible Viscous Flow Problems. *Journal of Computational Physics*, 2(1):12–26, August 1967.

[27] MSC.Software Corporation. MSC.Nastran 2005 Release Guide. *Macmillan*, 2005.

[28] D. Corson, D. Griffith, T. Ashwill, and F. Shakib. Investigating aeroelastic performance of multi-megawatt wind turbine rotors using CFD. 53rd AIAA/ASME/ASCE/AHS/ASC Structures, Structural Dynamics and Materials Conference,Honolulu, HI, United states, AIAA 2012-1827, 23–26 April 2012. .

[29] A. Crespo and J. Hernandez. Turbulence Characteristics in Wind-Turbine Wakes. *J. Wind Engineering and Industrial Aerodynamics*, 61(1):71– 85, 1996.

[30] A. Crespo, J. Hernandez, and S. Frandsen. Survey of Modelling Methods for Wind Turbine Wakes and Wind Farms. *Wind Engery*, 2:1–24, 2009.

[31] A. Crespo, F. Manuel, D. Moreno, E. Fraga, and J. Hernandez. Numerical analysis of wind turbine wakes. In *Proc. Delphi Workshop on Wind Energy Applications*, Delphi, 1985.

[32] F. Dehaeze. *Aeroelastic Analysis of Turbulent Rotor Flows*. PhD thesis, University of Liverpool, January 2012.

[33] F. Dehaeze and G.N Barakos. Hovering rotor computations using an aeroelastic blade model. *Aeronautical Journal*, 116(1180):621–649, June 2012.

[34] F. Dehaeze and G.N. Barakos. Mesh deformation method. *AIAA J. of Aircraft*, 49(1):82–92, January 2012.

[35] C. Depcik and B. van Leer. In Search of An Optimal Local Navier-Stokes Preconditioner. *AIAA Journal*, 2003.

[36] R.V. Chima D.L. Tweedt and E. Turkel. Preconditioning for Numerical Simulation of Low Mach Number Three-Dimensional Viscous Turbomachinery Flows. 28th Fluid Dynamics Conference, Snowmass, Colorado, June 29 –July 2 1997. .

[37] L. Dubuc, F. Cantariti, M.A. Woodgate, B. Gribben, K.J. Badcock, and B.E. Richards. A Grid Deformation Technique for Unsteady Flow Computations. *International Journal for Numerical Methods in Fluids*, 32:285–311, 2000.

[38] Y. Egorov and F. Menter. Development and Application of SST-SAS Turbulence Model in DESIDER Project. *Adv. in Hybrid RANS-LES Modelling*, 97:261–270, 2008.

[39] S.C. Eisenstat, H.C. Elman, and M. Schultz. Variational Iterative Methods for Nonsymmetric Systems of Linear Equations. *SIAM Journal of Numerical Analysis*, 20(2):345–357, 1983.

[40] FLUENT. http://www.fluent.co.uk/.

[41] V. Gleize. Low-Mach-Number Preconditioning Applied to Turbulent Helicopter Fuselage Flowfield Computation. *AIAA Journal*, 41(4), April 2003.

[42] S. Gomez-Iradi and G.N. Barakos. Computational fluid dynamics investigation of some wind turbine rotor design parameters. *Journal of Power and Energy*, 222:455–470, 2008.

[43] S. Gomez-Iradi, A. Irisarri, and X. Munduate. Summary of MexNext Task 4.1 – Standstill. *MexNext Report, ECN*, 2011.

[44] S. Gomez-Iradi and X. Munduate. A CFD Investigation of the Influence of Trip-Tape on the MEXICO Wind Turbine Blade Sections. In *The science of making torque from wind*, 2011.

[45] S. Gomez-Iradi, X. Munduate, and A. Irisarri. Task 4.1 - Standstill. In *MexNext Meeting*, Amsterdam, Netherlands, January 2011.

[46] S. Gomez-Iradi, R. Steijl, and G.N. Barakos. Development and Validation of a CFD Technique for the Aerodynamic Analysis of HAWT. *Journal of Solar Energy Engineering*, 131, August 2009.

[47] F. Grasso and A. van Garrel. Near Wake Simulation of MEXICO rotor in Axial and Yawed Flow Conditions with Lifting Line Free Wake Code. In *Wake Conference*, Gotland University, Visby, Sweden, June 2011.

[48] D.T. Griffith and T.D Ashwill. The Sandia 100-meter All-glass Baseline Wind Turbine Blade: SNL100-00. *Sandia National Laboratories Technical Report*, SAND2011-3779, June 2011.

[49] H. Guillard. Recent developments in the computation of compressible low Mach number flows. *Flow Turbulence Combust*, 76:363–369, 2006.

[50] H. Guillard and A. Murrone. On the behaviour of upwind schemes in the low Mach number limit: II. Godunov type schemes. *Computers and Fluids*, 33:655–675, 2004.

[51] H. Guillard and A. Murrone. Behaviour of upwind schemes in the low Mach number limit:III. Preconditioned dissipation for a five equation two phase model. *Computers and Fluids*, 37:1209–1224, 2008.

[52] H. Guillard and C. Viozat. On the behaviour of upwind schemes in the low Mach number limit. *Computers and Fluids*, 28:63–86, 1998.

[53] C. Gundling, H. Gopalan, B. Roget, and J. Sitamaran. A free-vortex wake diffusion model for wind turbines in steady and turbulent atmospheric inflow. In *51st AIAA Aerospace Science Meeting*, Grapevine (Dallas/Ft. Worth Region), Texas, 07–10 January 2013.

[54] S.K. Guntur, C. Bak, C. Niels, and N.N. Sorensen. Analysis of 3D stall models for wind turbine blades using data from the Mexico experiment. In *13th International conference on Wind Engineering, ICWE*, Amsterdam, Holland, July 2011.

[55] T. Guo, Z. Lu, D. Tang, T. Wang, and L. Dong. A CFD/CSD Model for Aeroelastic Calculations of Large-Scale Wind Turbines. *Sci China Tech Sci*, 56:205–211, 2013.

[56] M.M. Hand, D.A. Simms, L.J. Fingersh, D.W. Jager, J.R. Cotrell, S. Schreck, and S.M. Larwood. Unsteady Aerodynamics Experiment Phase VI: Wind Tunnel Test Configurations Available Data Campaigns. *NREL Technical Report*, December 2001.

[57] M.O.L. Hansen, J.N. Sorensen, N. Voutsinas, S. annd Sorensen, and H.Aa. Madsen. State of the art in wind turbine aerodynamics and aeroelasticity. *Progress in Aerospace Sciences*, 42:285–330, December 2006.

[58] F. Harlow and J.E. Welch. Numerical Calculation of Time-dependent Viscous Incompressible Flow of Fluid with a Free Surface. *Physics and Fluids*, 8, 1965.

[59] M. Hsu, I. Akkerman, and BazilevsY. Finite Element Simulation of Wind Turbine Aerodynamics: Validation Study using NREL Phase VI Experiment. *Wind Energy*, 2013.

[60] M. Hsu and BazilevsY. Fluid-Structure Interaction Modeling of Wind Tubines: Simulating the Full Machine. *Comput. Mech.*, 50:821–833, 2012.

[61] D. Huang. Unified computation of flow with compressible and incompressible fluid based on Roe's scheme. *Applied Mathematics and Mechanics*, 27(6):757–763, 2006.

[62] K. Hung, M. Papadakis, S-H. Wong, and S-C. Wong. Computation of Pre- and Post-Stall Flows Over Single and Multi-Element Airfoils. 36th Aerospace Sciences Meeting and Exhibit, Reno, Nevada, USA, 12–15 January 1998. .

[63] G. Iaccarino. Predictions of a Turbulent Separated Flow Using Commercial CFD Codes. *Journal of Fluids Engineering*, 123:819–828, December 2001.

[64] S. Ivanell, R. Mikkelsen, J.N. Sorensen, and D. Henningson. Stability analysis of the tip vortices of a wind turbine. *Wind Energy*, 13:705–715, 2010.

[65] K.J. Jackson, M.D. Zuteck, C.P. van Dam, K.J. Standish, and D. Berry. Innovative Design Approaches for Large Wind Turbine Blades. *Wind Energy*, 8(2):141–171, 2005.

[66] A. Jameson. Time Dependent Calculations Using Multigrid, with Applications to Unsteady Flows Past Airfoils and Wings. In *10th Computational Fluid Dynamics Conference, Honolulu, HI*, 1991. AIAA-91-1596.

[67] A. Jameson, W. Schmidt, and E. Turkel. Numerical Solutions of Euler Equations by Finite Volume Methods Using Runge-Kutta Time-Stepping Schemes. *AIAA Journal*, 81-1259, June 1981.

[68] M. Jarkowski, M. Woodgate, G. Barakos, and J. Rokicki. Towards Consistent Hybrid Overset Mesh Methods for Rotorcraft CFD. 37th European Rotorcraft Forum, Gallarate, VA, Italy, 13th Sept. - 15th Sept 2011. .

[69] M. Jarkowski, M. Woodgate, G. Barakos, and J. Rokicki. Towards Consistent Hybrid Overset Mesh Methods for Rotorcraft CFD. *International Journal for Numerical Methods in Fluids*, 74(8):543–576, 2014.

[70] J. Jeong and F. Hussain. On the Identification of a Vortex. *Journal of Fluid Mechanics*, 285:69–94, 1995.

[71] S. Jindal. Unsteady Turbulent Separated Flow Simulations on Unstructured Grids. *PhD thesis, Virginia Polytechnic Institute and State University, USA*, December 2004.

[72] I. Katic, J. Jojstrup, and N. O. Jensen. A simple model for cluster efficiency. In *Proc. EWEC'86*, Rome, 1986.

[73] H. Kim, LeeA., and S. Lee. Influence of Blade-Tower Interaction in Upwind-type Horizontal Axis Wind Turbines on Aerodynamics. *Journal of Mechanical Science and Technology*, 25(5):1351–1360, 2011.

[74] K. Kitamura, E. Shima, K. Fujimoto, and Z.J. Wang. Performance of Low-Dissipation Euler Fluxes and Preconditioned LU-SGS at Low Speeds. *Communications in Computational Physics*, 10(1):90–119, July 2011.

[75] N. Kroll, C.C. Rossow, D. Schwamborn, K. Becker, and G. Heller. MEGAFLOW A Numerical Flow Simulation Tool for Transport Aircraft Design. pages 1–20. ICAS Congress, 2002. .

[76] M.A. Lackner, N. deVelder, and T. Sebastian. On 2D and 3D potential flow models of upwind wind turbine tower interference. *Computers & Fluids*, 71:375–379, 2013.

[77] G.C. Larsen, H.A. Madsen, F. Bingol, J. Mann, S. Ott, J.N. Sorensen, V. Okulov, N. Troldborg, M. Nielsen, K. Thomsen, T.J. Larsen, and R. Mikkelsen. Dynamic wake meandering modeling. *Technical Report R-1607, Riso National Laboratory, Technical University of Denmark*, 2079.

[78] A. Le Pape and J. Lecanu. 3D Navier-Stokes Computations of a Stall-Regulated Wind Turbine. *Wind Energy*, 7(4):309–324, 2004.

[79] D. Lee. The Design of Local Navier-Stokes Preconditioning for Compressible Flow. *Journal of Computational Physics*, (144):460–483, 1998.

[80] D. Lee, B. van Leer, and J.F Lynn. A local Navier-Stokes preconditioner for all Mach and cell Reynolds numbers. *AIAA Journal*, 1997.

[81] J. Leishman and T. Beddoes. A semi-empirical model for dynamic stall. *Journal of the American Helicopter Society*, 34:3–17, 1989.

[82] X.S. Li and C.W. Gu. An All-Speed Roe-type scheme and its asymptotic analysis of low Mach number behaviour . *Journal of Computational Physics*, 227:5144–5159, February 2008.

[83] X.S. Li and C.W. Gu. On the Mechanism of Roe-type Schemes for All-Speed Flows. *arXiv:1107.3744, Cornell University Library*, 2011.

[84] X.S. Li, C.W. Gu, and J.Z. Xu. Development of Roe-type scheme for all-speed flows based on preconditioning method. *Computers and Fluids*, 38:810–817, 2009.

[85] Y. Li, K. Paik, T. Xing, and P.M. Carrica. Dynamic Overset CFD Simulations of Wind Turbine Aerodynamics. *Renewable Energy*, 37:285–298, 2012.

[86] M-S. Liou. A Sequel to AUSM: AUSM+. *Journal of Computational Physics*, 129:364–382, 1996.

[87] M-S. Liou. A Sequel to AUSM, Part II: AUSM+-up for all speeds. *Journal of Computational Physics*, 214:137–170, 2006.

[88] M-S. Liou and C.J. Steffen. A New Flux Splitting Scheme. *Journal of Computational Physics*, 107:23–39, 1993.

[89] Y. Liu and M. Vinokur. Upwind Algorithms for General Thermo-chemical Nonequilibrium Flows. pages AIAA–89–0201. 27th AIAA Aerospace Sciences Meeting including New Horizons Forum and Aerospace Exposition, January 9 – 12 1989. .

[90] T. Lutz. Near Wake Studies of the MEXICO Rotor. In *EWEA Annual Event*, Brussels, Belgium, March 2011.

[91] C. Masson, J Johansen, N.N. Sorensen, F. Zhale, H.A. Madsen, E. Politis, G. Schepers, K. Lindenburg, H. Snel, R. van Rooij, E.A. Arens, G. van Bussel, G. van Kuik, F. Meng, T. Sant, A. Knauer, G. Moe, X. Munduate, A. González, E. Ferrer, S. Gomez, G. Barakos, S. Ivanell, and S. Schreck. IEA Wind Annex XX: HAWT Aerodynamics and Models from Wind Tunnel Measurements. *NREL/TP-500-43508*, December 2008.

[92] E.H.M. Mast, L.J. Vermeer, and G.J.W. van Bussel. Estimation of the Circulation Distribution on a Rotor Blade from Detailed Near Wake Velocities . *Wind Energy*, 7:189–209, July 2004.

[93] S. McTavish, D. Feszty, and F. Nitzsche. Aeroelastic Simulations of the NREL Phase VI Wind Turbine using a Discrete Vortex Method Coupled with a Nonlinear Beam Model. pages 4256–4265. European Wind Energy Conference and Exhibition, EWEC, 2009. .

[94] S. Medida and J. Baeder. Numerical Prediction of Static and Dynamic Stall Phenomena using the $\gamma - Re_{\theta t}$ Transition Model. pages 431–454. 67th American Helicopter Society Annual Forum, Virginia Beach, VA, 3–5 May 2011. .

[95] F.R. Menter. Two-Equation Eddy-Viscosity Turbulence Models for Engineering Applications. *AIAA Journal*, 32(8):1598–1605, 1994.

[96] F.R. Menter and Y. Egorov. The Scale-Adaptive Simulation Method for Unsteady Turbulent Flow Predictions. Part 1: Theory and Model Description. *Flow Turbulence Combust*, 85:113138, 2010.

[97] F.R. Menter, R.B. Langtry, S.R. Likki, Y.B. Suzen, P.G. Huang, and S. Volker. A correlation-based transition model using local variables, part I model formulation. In *ASME Turbo Expo, Power for Land, Sea, and Air*, Vienna, Austria, 1417 June 2004.

[98] D. Micallef, M. Kloosterman, C.S. Ferreira, T. Sant, and G. van Bussel. Validating BEM, Direct and Inverse Free Wake Models with the MEXICO experiment. In *48th AIAA Aerospace Sciences meeting*, Orlando, USA, January 2010.

[99] D. Micallef, G. van Bussel, C.S. Ferreira, and T. Sant. An Investigation of Radial Velocities for a Horizontal Axis Wind Turbine in Axial and Yawed Flows. *Wind Energy*, 2012.

[100] J.A. Michelsen. Basis3D a Platform for Development of Multiblock PDE Solvers. *Technical Report AFM 92–05 Technical, University of Denmark, Lyngby*, 1992.

[101] J.A. Michelsen. Block Structured Multigrid Solution of 2D and 3D Elliptic PDEs. *Technical Report AFM 94–06 Technical, University of Denmark, Lyngby*, 1992.

[102] J-O. Mo, A. Choudhry, M. Arjomandi, R. Kelso, and Y-H. Lee. Effects of wind speed changes on wake instability of a wind turbine in a virtual wind tunnel using large eddy simulation. *J. Wind Eng. Ind. Aerodyn.*, 117:38–56, 2013.

[103] J-O. Mo, A. Choudhry, M. Arjomandi, and Y-H. Lee. Large eddy simulation of the wind turbine wake characteristics in the numerical wind tunnel model. *J. Wind Eng. Ind. Aerodyn.*, 112:11–24, 2013.

[104] J. Motta-Mena, P. Jha, R.L. Campbell, and S. Schmitz. Wind Turbine Fluid-Structure Interaction using an Actuator Line Solver and a Structural Dynamics Solver in a Tightly-Coupled Implementation. pages AIAA 2014–0717. 32nd ASME Wind Energy Symposium, National Harbor, Maryland, January 2014. .

[105] K. Nilsson, W.Z. Shen, J.N. Sorensen, S.P. Breton, and S. Ivanell. Validation of the actuator line method using near wake measurements of the MEXICO rotor. *Wind Energy*, 2014. DOI:10.1002/we.1714.

[106] S. Osher and S. Chakravarthy. Upwind Schemes and Boundary Conditions with Applications to Euler Equations in General Geometries. *Journal of Computational Physics*, 50(3):447–481, June 1983.

[107] S.A Pandya, S. Venkateswaran, and T.H. Pulliam. Implementation of Preconditioned Dual-Time Procedures in OVERFLOW. *AIAA Journal*, 0072, 2003.

[108] S.A. Pandya, S. Venkateswaran, and T.H. Pulliam. Implementation of Preconditioned Dual-Time Procedures in OVERFLOW. *AIAA Journal*, 2003.

[109] L. Pascal. Analysis of MEXICO measurements. *Wind Energy*, January 2009.

[110] U.S. Paulsen. Konceptundersgelse Nordtank NTK 500/41 Strukturelle Laster. *Technical Report I-936(DA),Riso, Roskilde, Denmark*, 1995.

[111] R. Pereira, G. Schepers, and M.D. Pavel. Validation of the Beddoes-Leishman dynamic stall model for horizontal axis wind turbines using MEXICO data. *Wind Energy*, 2012.

[112] R. Steijl, G. Barakos and K. Badcock. A framework for CFD analysis of helicopter rotors in hover and forward flight. *International Journal for Numerical Methods in Fluids*, 51(8):819–847, 2006.

[113] J. Raddatz and J.K. Fassbender. Block Structured Navier-Stokes Solver FLOWer, MEGAFLOW. *Numerical Flow Simulation for Aircraft Design*, 89:27–44, 2005.

[114] D.J. Renkema. *Validation of wind turbine wake models - using wind farm data and wind tunnel measurements*. PhD thesis, Master of Science Thesis, Delft University of Technology, 2007.

[115] P.E. Rethore, N.N. Sorensen, F. Zhale, A. Bechmann, and H.A. Madsen. CFD model of the MEXICO wind tunnel. In *EWEA Annual Event*, March 2011.

[116] P.E. Rethore, N.N. Sorensen, F. Zhale, A. Bechmann, and H.A. Madsen. MEXICO Wind Tunnel and Wind Turbine modelled in CFD. In *AIAA Conference*, Honolulu, Hawaii, USA, June 2011.

[117] F. Rieper. A low-Mach number fix for Roe's approximate Riemann solver. *Journal of Computational Physics*, 230:5263–5287, March 2011.

[118] T. Rinehart, S. Medida, S. Thomas, and J. Baeder. Computation of Two-dimensional Wind Turbine Airfoil Characteristics Using Advanced Turbulence and Transition Modeling Methods and a GPU-Accelerated Navier-Stokes Solver. pages AIAA 2014–1216. 32nd ASME Wind Energy Symposium, National Harbor, Maryland, 13–17 January 2014. .

[119] V.A. Riziotis, S.G Voutsinas, and D.I. Manolas. Aeroelastic Analysis of Pre-Curved Rotor Blades. European Wind Energy Conference and Exhibition,EWEC, 2010. .

[120] A. Rizzi, P. Eliasson, I. Lindblad, C. Hirsch, C. Lacor, and J. Haeuser. The Engineering of Multiblock-/Multigrid Software for Navier-Stokes Flows on Structured Meshes. *Wind Energy*, 22(2/3):341–367, 1993.

[121] P.L. Roe. Approximate Riemann Solvers, Parameter Vectors, and Difference Schemes. *Journal of Computational Physics*, 43(2):357–372, October 1981.

[122] A. Rosen, A. Wolf, D. Ben-Shmuel, and G. Omri. Part I. The MEXICO Project Wind Turbine Model. *Technion Research and Development Foundation*, (985), August 2011.

[123] A. Rosen, A. Wolf, D. Ben-Shmuel, and G. Omri. Part II. The MEXICO Project Wind Turbine Model. *Technion Research and Development Foundation*, (986), August 2011.

[124] B. Sanderse. Aerodynamics fo wind turbine wakes. *ECN Report*, 16, 2009.

[125] B. Sanderse, S.P. van der Pijl, and B. Koren. Review of computational fluid dynamics for wind turbine wake aerodynamics. *Wind Energy*, 14:799–819, January 2011.

[126] V. Sankaran, A. Wissink, A. Datta, J. Sitaraman, B. Jayaraman, M. Potsdam, A. Katz, S. Kamkar, B. Roget, D. Mavriplis, H. Saberi, W-B. Chen, W. Johnson, and R. Strawn. Overview of the Helios Version 2.0 Computational Platform for Rotorcraft Simulations. *AIAA Journal*, 2011.

[127] J.G. Schepers and H. Snel. Final Report of IEA Task 29, MexNext (Phase I): Analysis of MEXICO Wind Tunnel Measurements. *Technical report, ECN*, February 2012.

[128] S. Schmitz and J.J. Chattot. A Parallelized Coupled Navier-Stokes/Vortex- Panel Solver. *Journal of Solar Energy Engineering-Transactions of the ASME*, 127(4):475–487, 2005.

[129] S. Schreck, T. Sant, and D. Micallef. Rotational Augmentation Disparities in the UAE Phase VI and MEXICO Experiments. In *Torque from Wind Conference*, Heraklion, Greece, June 2010.

[130] N. Sezer-Uzol and L.N. Long. 3-D Time-Accurate CFD Simulations of Wind Turbine Rotor Flow Fields. *AIAA Journal*, 2006.

[131] W.Z. Shen, R. Sorensen, and J.N. Bak. Tip loss correction for wind turbines computations. *Wind Energy*, 8:457–475, 2005.

[132] W.Z. Shen, W.J. Zhu, and J.N. Sorensen. Actuator line/Navie-Stokes computations for the MEXICO rotor: comparison with detailed measurements. *The Science of Making Torque from the Wind*, 2010.

[133] E. Shima and K. Kitamura. Parameter-Free Simple Low-Dissipation AUSM-Family Scheme for All Speeds. *AIAA Journal*, 49(8):1693–1709, August 2011.

[134] J. Sitaraman, M. Floros, A.M. Wissink, and M. Potsdam. Parallel Unsteady Overset Mesh Methodology for a Multi-Solver Paradigm with Adaptive Cartesian Grids. 26th AIAA Applied Aerodynamics Conference, Honolulu, Hawaii, 18–21 August 2008. .

[135] H. Snel, J.G. Schepers, and B. Montgomerie. The MEXICO project (Model Experiments in Controlled Conditions): The database and first results of data processing and interpretation. *Journal of Physics*, 2007.

[136] D.M. Somers. Design and experimental results for the S809 airfoil. In *Subcontrat Report SR-440-6918*, NREL, Colorado, USA, January 1997.

[137] D.M. Somers. The S816, S817 and S818 Airfoils. *NREL Technical Report, NREL/SR-500-36333*, December 2004.

[138] J.N. Sorenen and A.M. van Kuik. General momentum theory for wind turbines at low tip speed ratios. *Wind Energy*, 14:821–839, 2011.

[139] N. Sorensen. CFD Modelling of Laminar-turbulent Transition for Airfoils and Rotors Using the $\gamma - \tilde{Re}_\theta$ Model. *Wind Energy*, 12(8):715–733, April 2009.

[140] N.N. Sorensen, A. Bechmann, and P.E. Rethore. Near wake Reynolds-averaged Navier-Stokes Predictions of the Wake behind the MEXICO rotor in Axial and Yawed Flow Conditions. *Wind Energy*, 2012. DOI:10.1002/we.1559.

[141] P. Spalart, S. Deck, M.L. Shur, K.D. Squires, M.Kh. Strelets, and A. Travin. A new version of detached-eddy simulation, resistant to ambiguous grid densities. *Theor. Comput. Fluid Dyn.*, 20:181–195, 2006.

[142] P. Spalart, W.H. Jou, M.Kh. Strelets, and S.R. Allmaras. Comments on the Feasibility of LES for Wings, and on a Hybrid RANS/LES Approach. In *Advances in DNS/LES, Columbus*, 1997.

[143] Ph. Spalart and S.R. Allmaras. A One-Equation Turbulence Model for Aerodynamic Flows. *La Recherche Aérospatiale*, (1):5–21, 1994.

[144] R. Steijl and G. Barakos. Sliding Mesh Algorithm for CFD Analysis of Helicopter Rotor-Fuselage Aerodynamics. *Int. J. Numer. Meth. Fluids*, 58:527–549, October 2008.

[145] J. Summer, C.S. Watters, and C. Masson. CFD in Wind Energy: The Virtual, Multiscale Wind Tunnel. *Energies*, 3:989–1013, May 2010.

[146] W. Sutherland. The viscosity of gases and molecular force. *Philosophical Magazine*, 5(36):507–531, 1893.

[147] A. Tadamasa and M. Zangeneh. Numerical prediction of wind turbine noise. *Renewable Energy*, pages 1902–1912, 2010.

[148] A. Tadamasa and M. Zangeneh. Numerical prediction of wind turbine noise. *Renewable Energy*, 36:1902–1912, 2011.

[149] Inc. Tecplot. Tecplot 360^{TM}, User's Manual for use with Tecplot 360^{TM} Version 2013 R1. *Tecplot, Inc.*, 2013.

[150] B.J.R. Thornber and D. Drikakis. Numerical dissipation of upwind schemes in low Mach flow. *International Journal for Numerical Methods in Fluids*, 56:1535–1541, 2007.

[151] C. Tongchitpakdee, S. Benjanirat, and L.N. Sankar. Numerical Simulation of the Aerodynamics of Horizontal Axis Wind Turbines under Yawed Flow Conditions . *AIAA Journal*, 2005.

[152] N. Troldborg, G.C. Larsen, H.A. Madsen, K.S. Hansen, J.N. Sorensen, and MikkelsenR. Numerical simulations of wake interaction between two wind turbines at various inflow conditions. *Wind Energy*, 14:859–876, 2011.

[153] N. Troldborg, J.N. Sorensen, and R. Mikkelsen. Numerical simulations of wake characteristics of a wind turbine in uniform flow. *Wind Energy*, 13:86–99, 2010. DOI: 10.1002/we.345.

[154] N. Troldborg, F. Zahle, P-E. Rethore, and N.N. Sorensen. Comparison of the wake of different types of wind turbine CFD models. In *5th AIAA Aerospace Sciences Meeting including the New Horizons Forum and Aerospace Exposition*, Nashville, Tennessee, January 2012.

[155] C. Tsalicoglou, S. Jafari, N. Chokani, and R. Abhari. RANS Computations of MEXICO Rotor in Uniform and Yawed Inflow. *Journal of Engineering for Gas Turbines and Power*, 136, January 2014. DOI:10.1115/1.4025362.

[156] E. Turkel. Preconditioning Techniques in Computational Fluid Dynamics . *Annual Review of Fluid Mechanics*, 31:385–416, 1999.

[157] G.D van Albada, B. van Leer, and W.W. Roberts. A Comparative Study of Computational Methods in Cosmic Gas Dynamics. *Astron. Astrophysics*, 108:76–84, 1982.

[158] A. van Garrel. Development of a Wind Turbine Aerodynamics Simulation Module. *ECN, ECN–C–03–079, Petten, The Netherlands*, August 2003.

[159] B. van Leer. Towards the Ultimate Conservative Difference Scheme, V. A Second Order Sequel to Godunov's Method. *J. Comp. Phys.*, 32:101–136, 1979.

[160] G.H. Vatistas, V. Kozel, and W.C. Mih. A Simpler model for concentrated vortices. *Experiments in Fluids*, 11(1):73–76, 1991.

[161] L.J. Vermeer, J.N. Sorensen, and A. Crespo. Wind turbine wake aerodynamics. *Progress in Aerospace Sciences*, 39:467–510, 2003.

[162] Q. Wang, H. Zhou, and D. Wan. Numerical Simulation of Wind Turbine Blade-Tower Interaction. *J. Marine Sci. Appl.*, 11:321–327, 2012.

[163] D.C. Wilcox. Multiscale Model for Turbulent Flows. *AIAA Journal*, 26(11):1311–1320, 1988.

[164] W.P. Wolfe and S.S. Ochs. CFD Calculations of S809 Aerodynamic Characteristics. pages 97–0973. 35th AIAA Aerospace Sciences Meeting and Exhibit, Reno, Nevada, USA, 6–9 January 1997. .

[165] W. Xudong, W.Z. Shen, W.J. Zhu, J.N. Sorensen, and C. Jin. Shape Optimization of Wind Turbine Blades. *Wind Energy*, 12(8):781–803, March 2009.

[166] H. Yang, W.Z. Shen, J.N. Sorensen, and W.J. Zhu. Extraction of airfoil data using PIV and pressure measurements. *Wind Energy*, 14(4):539–556, May 2011.

[167] D.O. Yu and O.J. Kwon. A Coupled CFD-CSD Method for Predicting HAWT Rotor Blade Performance. pages AIAA 2013–0911. 51st AIAA Aerospace Sciences Meeting, Grapvine (Dallas/Dt. Worth Region), Texas, January 2013. .

[168] D.O. Yu and O.J. Kwon. Predicting wind turbine blade loads and aeroelastic response using a coupled CFD-CSD method. *Renewable Energy*, pages 1–13, 2014.

[169] M. Zaccanti and P. Cinnella. Analysis of Preconditioning Methods for the Euler Equations. pages A99–33467 08–34. 14th Computational Fluid Dynamics Conference, June 28 –July 1 1999.

[170] F. Zhale, N.N. Sorensen, and J. Johansen. Wind Turbine Rotor-Tower Interaction Using an Incompressible Overset Grid Method. *Wind Energy*, 12:594–619, 2009.

[171] P. Zhang, S. Huang, T. Yang, and J. Li. Research on the Aeroelastic Response of Tower Effects for Great Grade Wind Turbine. *Journal of Applied Sciences*, 13(15):3042–3048, 2013.